NTNU
Norwegian University of
Science and Technology

Snow and Ice on Photovoltaic Devices

Analysis of a Challenge and Proposals for
Solutions

Maria Chiara Failla

Innovative Sustainable Energy Engineering
Submission date: September 2016
Supervisor: Bjørn Petter Jelle, BAT

Norwegian University of Science and Technology
Department of Civil and Transport Engineering

Maria Chiara Failla

Snow and Ice on Photovoltaic Devices:
Analysis of a Challenge and Proposals for Solutions

TBA4905 Building and Material Engineering,
Master's thesis

Trondheim, 15.09.2016

NTNU
Norwegian University of Science and Technology
Faculty of Engineering Science and Technology
Department of Civil and Transport Engineering

Università degli studi di Catania
Dipartimento di Ingegneria Civile e Architettura (DICAR)
C.d.L.M. Ingegneria Edile - Architettura

NTNU
Norwegian University of
Science and Technology

UNIVERSITÀ degli STUDI di CATANIA

Maria Chiara Failla

Snow and Ice on Photovoltaic Devices:
Analysis of a Challenge and Proposals for Solutions

Thesis for the Master's degree in Architectural Engineering

Trondheim, September 2016

NTNU
Norwegian University of
Science and Technology

Norwegian University of Science and Technology (NTNU)
Faculty of Engineering and Science Technology
Department of Civil and Transport Engineering

UNIVERSITÀ
degli STUDI
di CATANIA

University of Catania (UNICT)
Dipartimento di Ingegneria Civile e Architettura (DICAR)
C.d.L.M. Ingegneria Edile – Architettura

Abstract

The global photovoltaic industry is a rapidly growing and highly competitive, innovation-based sector. Norway's interest in photovoltaics has been behind other countries for a long time; however a recent impulse in the solar industry has developed, driven by the necessity of reducing buildings' impact on environment.

As a matter of fact Norwegian interest in photovoltaics leads to the study of the influence of snow on PV devices. As a consequence, different studies have been conducted to find an adequate solution to the problem.

First of all the snow condition is described through statistical data and graphs in the most populated cities of Norway: Oslo, Bergen and Trondheim. In addition the will of Norwegian industry and research to address to renewable resources is underlined. As a consequence, the motivation and the interest in this thesis' topic appear clear.

The second part of the thesis gives some guidelines about the geometric design of a PV-plant taking in consideration the accumulation of snow on the panels. Different answers are given for different plan conditions. When the modules are all located on the same shed, a high tilt angle can be more convenient than a low one, because it increases the sliding of snow. On the contrary, when panels are located on different sheds, the shading problems leads to the conclusion that a medium tilt angle is the best solution. Other indications are given regarding the division of the system electrically, through string diodes and module by-pass diodes. In conclusion this part is addresses to who is approaching in designing a new PV-plant.

The third part focuses on computation of snow loss; therefore it is applicable to existing PV systems. An application of Marion's algorithm and the PVsyst software on the ZEB Living Lab PV-plant supposed in Oslo, Bergen and Trondheim gives interesting results about the snow loss values. They are strongly related to the snow depth, solar radiation and air temperature, therefore a deep connection to the location weather data is present. The monthly snow loss percentage reaches values till 70% in Oslo, while lower percentages characterize the other sites. However the annual loss is around 3% in Oslo and Trondheim and around 1% in Bergen.

Possible solutions to avoid or reduce snow accumulation on the PV panels are investigated in the fourth chapter. Then a focus on the icephobic coatings was presented. Their characteristics, their design, their properties were studied to know how useful these elements can be to our case. Finally a spotlight on the state-of-art showed the possibilities that are nowadays offered by the market.

The fifth chapter copes with a hypothesis of simulation of icephobic coatings on the PV modules, to have an idea of their contribute in term of energy save. Moreover the fact that soiling loss is reduced as well should be taken in consideration. The simulations were conducted for the same PV-plant supposed in Oslo, Bergen and Trondheim in the third part, so that differences between the two cases were highlighted.

II

Acknowledgements

At University of Catania, all fifth year students of the Architectural Engineering course are obliged to hand in a Master's thesis. This work is written at NTNU (Norwegian University of Science and Technology) alongside Prof. Bjørn Petter Jelle (NTNU) and Prof. Luigi Marletta (University of Catania) during an Erasmus Plus project. This work has been supported by the Research Council of Norway and several partners, through the research project "Building Integrated Photovoltaics for Norway" (BIPV Norway).

First of all I would like to thank my Norwegian supervisor Prof. Bjørn Petter Jelle and my Italian supervisor Prof. Luigi Marletta, who gave me the possibility to make this relevant Master's thesis and this delicious experience in Norway. I discovered NTNU as a synergetic world, ready to welcome new ideas and proposals to improve studies and research. In this context my gratitude goes to Luca Finocchiaro, Francesco Goia, Gabriele Lobaccaro and all the other researchers and professors who helped me with scientific consultations or simple advices.

Secondly I would like to thank my family: my parents, always ready to support my new ideas; my brothers and my sister, hoping that will be inspired and encouraged by my experiences; my grandparents, who always think about me, even if they are not really keen on technology. A special thank goes to my uncle, who always believes in my will and my skills, supporting me with his love and dedication.

Last but not least, I admit that is not so easy to tolerate my continuous complaints, especially when people who listen to me know that I will go beyond all the difficulties that I find. For this reason I would like to thank all the patient friends who guided me in this path from Norway, Mattia, Giulia, Valentina, Marilena, Veronica, Luca, Fekadu, and from Italy, Chiara, Martina, Ester, Federico, Edgar. A special person who lived my strains daily is Emanuele, the most lovely and authentic person who I could hope to find next to me. He was the most distant in terms of kilometres, but the nearest one in terms of love. A huge kiss goes to all the people that I have not mentioned, but supported and believed in me in some way.

IV

Ringraziamenti

Innanzitutto vorrei ringraziare il mio relatore norvegese Bjørn Prof. Petter Jelle e il mio relatore italiano Prof. Luigi Marletta, che mi hanno dato la possibilità di svolgere un lavoro di notevole rilevanza e intraprendere questa deliziosa esperienza in Norvegia. Ho scoperto l'NTNU come un mondo sinergico, pronto ad accogliere nuove idee e proposte per migliorarsi in studi e ricerche. In questo contesto, la mia gratitudine va a Luca Finocchiaro, Francesco Goia, Gabriele Lobaccaro e tutti gli altri ricercatori e professori che mi hanno aiutato con consulenze scientifici o semplici consigli.

In secondo luogo vorrei ringraziare la mia famiglia: i miei genitori, sempre pronti a sostenere le mie nuove idee; i miei fratelli e mia sorella, sperando che saranno ispirati e incoraggiati dalle mie esperienze; i miei nonni, che mi pensano sempre, anche se trovano qualche difficoltà nell'uso della tecnologia. Un ringraziamento particolare va a mio zio, che crede sempre nella mia forza di volontà e nelle mie capacità, sostenendomi con il suo amore e la sua dedizione.

Infine, ammetto che le mie continue lamentele non sono così facili da tollerare, soprattutto quando le persone che mi ascoltano sanno che in realtà supererò facilmente tutte le difficoltà che trovo. Per questo motivo vorrei ringraziare tutti gli amici pazienti che mi hanno guidato in questo percorso, dalla Norvegia, Mattia, Giulia, Valentina, Marilena, Veronica, Luca e Fekadu, Heloie, Susanne, e dall'Italia, Chiara, Martina, Ester, Federico, Edgar. Una persona speciale che ha vissuto i miei drammi quotidiani è Emanuele, la persona più amorevole e autentica che potevo sperare di trovare accanto a me in questo percorso. E' stata la più distante in termini di chilometri, ma la più vicina in termini di amore. Un caloroso bacio va a tutte le persone che non ho menzionato, ma che mi hanno sostenuto in qualche modo, credendo in me.

Contents

List of figures

Chap.1

Chap. 2

Fig. 2.18. Sheds plane tilt versus annual energy respect to horizontal in Oslo. The orange curve represents the shading and electrical loss in a one-string configuration (plotted through PVsyst).

Fig. 2.19. Sheds plane tilt versus annual energy respect to horizontal in Oslo. The orange curve represents the shading and electrical loss in a two-string configuration (plotted through PVsyst).

Fig. 2.10. 8 Sheds plane tilt versus annual energy respect to horizontal in Oslo. The orange curve represents the shading and electrical loss in a three-string configuration (plotted through PVsyst).

Chap. 3

Fig. 3.1. Combinations of hourly irradiance and temperature for the LafWater PV system for which the snow did (red dots) or did not (blue circles) slide some amount down the PV panel. The line is an estimate of the dividing line for conditions that will (to the right of the line) or will not (to the left of the line) permit snow to slide down the PV panel or module (B. Marion et al. 2013).

Fig. 3.2. Combinations of hourly irradiance and temperature for all the PV systems for which the snow did not slide. Data to the right of the diagonal line indicate that snow expected to slide did not. PV modules were 100% covered with snow at the beginning of the hour (B. Marion et al. 2013).

Fig. 3.3. Linear relationships between the sine of b and the snow slide amount for the hours when a snow slide is estimated for roof mounted systems (blue) and ground rack-mounted PV systems with adequate ground clearance (red) (B. Marion et al. 2013).

Fig. 3.4. Scatter plot of modeled versus measured monthly PV system energy losses due to snow for November 2010–March 2011 and November 2011–March 2012. Diagonal has slope of one. Data above the diagonal indicate model estimates are too great, and vice versa (B. Marion 2013).

Fig. 3.5. . Results from the validation study using the RSF2 system in Golden, Colorado (Ryberg and Freeman 2015).

Fig. 3.6. Results from the validation study using the Forrestal system in Washington D.C and the RSF2 system in Golden Colorado (Ryberg and Freeman 2015).

Fig. 3.7. IAM function of the incident angle on solar rays on the modules (plotted by the author through PVsyst).

Fig. 3.8. PVsyst results and losses flowchart (plotted by SAM and modified by the author).

Fig. 3.9. SAM results and losses flowchart (plotted by SAM and modified by the author).

Fig. 3.10. General trends in average snow losses as a percentage of annual energy production was created (Ryberg and Freeman 2015).

Fig. 3.11. PVsyst reference system for module's azimuth and tilt angle (plotted by the author through PVsyst).

Chap. 4

Fig. 4.26. Friction coefficient determination between snow and roofing by method A (left) horizontal plane applied pulling force method and method B (right) inclined plane slip method. (Illustrations: SINTEF Building and Infrastructure) (Jelle 2013).

Fig. 4.27. A DSA30 drop shape analysis system from Kruss.

Fig.4.28. Coated sample in centrifuge set-up that evaluates ice adhesion: (1) sample, (2) aluminium beam, (3) counter-weight (S. A. Kulinich and M. Farzaneh).

Fig. 4.29. Zero-degree cone test configuration (left) and instrumented sample pile and mould in testing machine (right) (U.S. Army Corps of Engineering).

Fig. 4.30. Common methods in use to quantify the durability of the superhydrophobic/icephobic surfaces. (a) UV irradiation, (b) tape adhesion test (c) sand impact test (d) ice formation/ice removal cycles3 (e) water jet/dripping test and (f) sandpaper abrasion measurement (Sojoudi 2016).

Chap. 6

Fig. 6.1. Comparison daily energy production (kWh) versus daily snow depth (cm) for the PV-plant on the ZEB Living Lab. Data of February 2016 (from the 16th to the 26th).

List of tables

Chap. 1

Chap. 2

Chap. 3

Chap. 4

Chap. 5

Abbreviations and Nomenclature

Abbreviations

AC	alternative current
AM	air mass
ASHRAE	American society of heating, refrigerating and air-conditioning engineers
BIPV	building integrated photovoltaic
CA	contact angle
CAH	Contact angle hysteresis
CEC	California Energy Commission
CSV	comma separated value
CVD	chemical vapour deposition
DAQ	data acquisition
DC	direct current
LID	light induced degradation
EPBD	Energy Performance of Buildings Directive
EPIA	European Photovoltaic Industry Association
EPW	energy plus weather
EU	European Union
EW	east-west
HDKR	Hay, Davies, Klucher, Reindl
HMDS	hexaamethyldisilazane
IAM	incident angle modifier
LID	light induced degradation
NCDC	National Climatic Data Center
NOAA	National Oceanic and Atmospheric Administration
NREL	National Renewable Energy Laboratory
NS	north-south
NSRDB	National Solar Radiation Database
NTNU	Norwegian University of Science and Technology
NW	nanowire
OTS	octadecyltrichlorosilane
OTSF	trichloro 1H,1H2H,2H-perflurooctyl silane
POA	plane of array
PV	photovoltaic
RMS	root mean square
SAM	System Advisor Model
SMW	special marine warning
TEK	Technical Building Regulations
TMY	typical meteorological year
TF	transposition factor
UV	ultraviolet
VIS	visible
ZEB	The Research Centre on Zero Emission Buildings

Nomenclature

a	m/s^2	acceleration
A	m²	real area of contact
b_o	-	coefficient
E	MPa	Young modulus
E_E	kWh/m²	estimated daily energy production
E_L	kWh/m²	daily energy snow loss
E_{loss}	%	annual percentage loss
E_M	kWh/m²	measured daily energy production
F	%	surface fraction
F	N	applied pulling force parallel with the sample surface
F_f	N	frictional force
F_s	N	sliding force due to gravity
g	m/s^2	gravitational acceleration
G	W/m²	POA irradiance
GIT	-	ground interference term
$Glob. \; Eff.$	W/m²	global irradiance component with detraction of shading loss, IAM loss, snow loss and soiling loss
$Glob. \; IAM$	W/m²	global irradiance component
$Glob.Shad.$	W/m²	global irradiance component with detraction of only shading loss
$Glob.Snow$	W/m²	global irradiance component with detraction of shading loss, IAM loss and snow loss
H	kWh/m²	total in-plane irradiance
h	inches	drop height from array edge to ground
i	°	incident angle
J	-	ice nucleation rate
k	-	snow slide amount coefficient
J_{SC}	mA/cm²	short circuit current density
k_B	J / K	Boltzmann constant
m	kg	mass
m'	W °C /m²)	slope of line
n	-	number of snow events in a month
N	N	normal force
P	N/m²	yield pressure
P_0	kW	nameplate DC power
p_{snow}	kW	hourly power loss due to snow
P_{snow}	kW	monthly power loss due to snow
POA	kWh/m²	monthly plane of array insolation
PR_{25}	-	system performance ratio for 25°C PV module temperature
r	inches	row plane of array dimension
r_c	nm	critical nucleus radius
R	N	friction force parallel with the sample surface
RH	%	average monthly relative humidity
s	%	snow slide amount
S	N	force per unit area of contact
sc	%	hourly snow coverage
sc'	%	corrected hourly snow coverage

sd	cm, inches	daily snow depth
SD	cm, inches	monthly snow depth
sl	%	snow loss percentage
t	s	time
T	°C	PV module cell temperature
T_a	°C	ambient air temperature
T_{air}	°C	average monthly air temperature
T_{snow}	%	annual percentage loss for Truckee region
T_w	°C	irradiance-weighted PV module temperature
U	W/m² k	U-value
v	m/s	velocity
V	V	voltage
V_{OC}	V	open circuit voltage
We	-	Weber number
Wec	-	critical Weber number
WS	m/s	wind speed
x	cm	Trondheim snow depth
y	cm	Leinstrand snow depth
β	°	tilt angle
γ	1/°C	power correction factor for temperature
γ_{IA}	N	tension force ice-air
γ_{IL}	N	tension force ice-liquid
γ_{LA}	N	tension force liquid-air
γ_{SA}	N	tension force solid-air
γ_{SI}	N	tension force solid-ice
γ_{SL}	N	tension force solid-liquid
δ	-	coefficient
θ	°	contact angle
θ_{adv}	°	advancing contact angle
θ_{rec}	°	receding contact angle
θ_{C-B}	°	apparent contact angle
μ	-	friction coefficient
μ_d	-	dynamic friction coefficient
μ_s	-	static friction coefficient
ρ	Kg/m³	density
σ	N/m²	surface tension
τ	N/m²	shear stress
τ_{yy}	N/m²	critical stress
ω	1/s	rotation speed
ΔG	nm	minimum stable size a nascent ice crystal needs to be reach to initiate freezing
$\Delta G_{f,v}$	KJ	volumetric free energy difference per unit volume between water and ice

xx

1 Introduction of thesis

1.1 Background

The building sector has a large environmental impact due to soil consumption, energy consumption and emissions to the atmosphere (Pérez-Lombard et al. 2007). Nowadays the correct use of earth resources is a frequently discussed theme. In fact non-renewable resources should not be used any more, but they should be substituted progressively by renewable resources, such as geothermal energy, hydropower, wind power, nuclear power and solar energy (Kitzing et al. 2012).

Through the Energy Performance of Buildings Directive (EPBD), the EU has directed its member states to ensure that by 2020, all new buildings shall be "nearly zero energy buildings", which require a very low amount of energy that is covered by renewable resources (European Parliament 2010). In Norway, which is an associated country to the EU, the energy performance of buildings is regulated through the Technical Building Regulations (Byggteknisk forskrift, TEK). In the latest update of the regulations (TEK10, 12.11.2015) the energy efficiency requirement is at passive house level, and is set to be further tightened until a nearly zero energy building level is reached by 2020.

Solar energy is well-suited to use in buildings. Passive solar energy provides lighting and heating through windows and the building envelope. Active solar energy systems can supply electricity, heating, and cooling to buildings. Once installed, a solar energy system will supply energy without any pollution and requires minimal maintenance (Good et al. 2015).

Most of the man-made solar energy is harvested for electricity generation by photovoltaic devices. These ones are often added on the top of the building and supported by a metallic structure. Recently the study of the energetic part in a building project has become a compulsory step (Energy Performance of Building Directive 2010, Energy Efficiency Directive 2012), therefore the project of a photovoltaic (PV) system has become integrated in the building's project. As a result we assist to the development of the building integrated photovoltaic (BIPV) systems, whose elements replace parts of the conventional building materials and systems in the climate envelope of buildings, such as roofs and façades. BIPV systems replace the outer building envelope skin, thus serving simultaneously as both a climate screen and a power source generating electricity (Jelle and Breivik 2012).

1.2 PV and BIPV in Norway

The global photovoltaic industry is a rapidly growing and highly competitive, innovation-based sector. Norway's interest in photovoltaics has been behind many other countries for a long time; however a recent impulse in the solar industry has developed, driven by the necessity of reducing buildings' negative impact on the environment. Thus, a crescent interest is shown by Norway, where the government is addressing funds to renewable energy filed in view of a depletion of the oil stock (Sørensen 2015).

The development of the solar industry and research is at an early stage. Universities and research centers have recently directed their funds to this "new" field. An obvious observation about installation of PV devices in northern countries regards the limits of the energy production respects to the southern countries, due to the lower solar irradiation. Another relevant problem is the snow cover that forms in wintertime. These considerations should not overcome and delete the possibilities of installing PV devices in Norway. As a matter of fact, according to a report predicting the global market outlook for 2014-2018 published by European Photovoltaic Industry Association (EPIA), nowadays the total capacity in Norway is about 11 MW, whereas 0.6 MW was installed in 2013 (IEA 2013).

Direct solar radiation is around 85% of the total insolation. Different locations on the globe surface present different values mostly due to the area's latitude and cloud cover. As a consequence, those major limits of Norway in PV production cannot be overcome (Fig. 1.1).

The European irradiation map shows a huge difference in solar energy potential between northern and southern countries, as expected. However, Pasonen et al. (2012) underline that Nordic countries are close to countries like Germany and Belgium, which are commonly seen as much better places for solar power than the actual difference implies. In addition real production differences between Nordic and Central European countries should also take into account the higher efficiency of traditional modules at lower temperatures.

The real reason for high PV capacity in countries of Central Europe compared to Nordic countries is the difference in the feed-in tariff system, not the actual difference in irradiation (Pasonen et al. 2012). Figure 1.2 illustrates the differences in certain European cities.
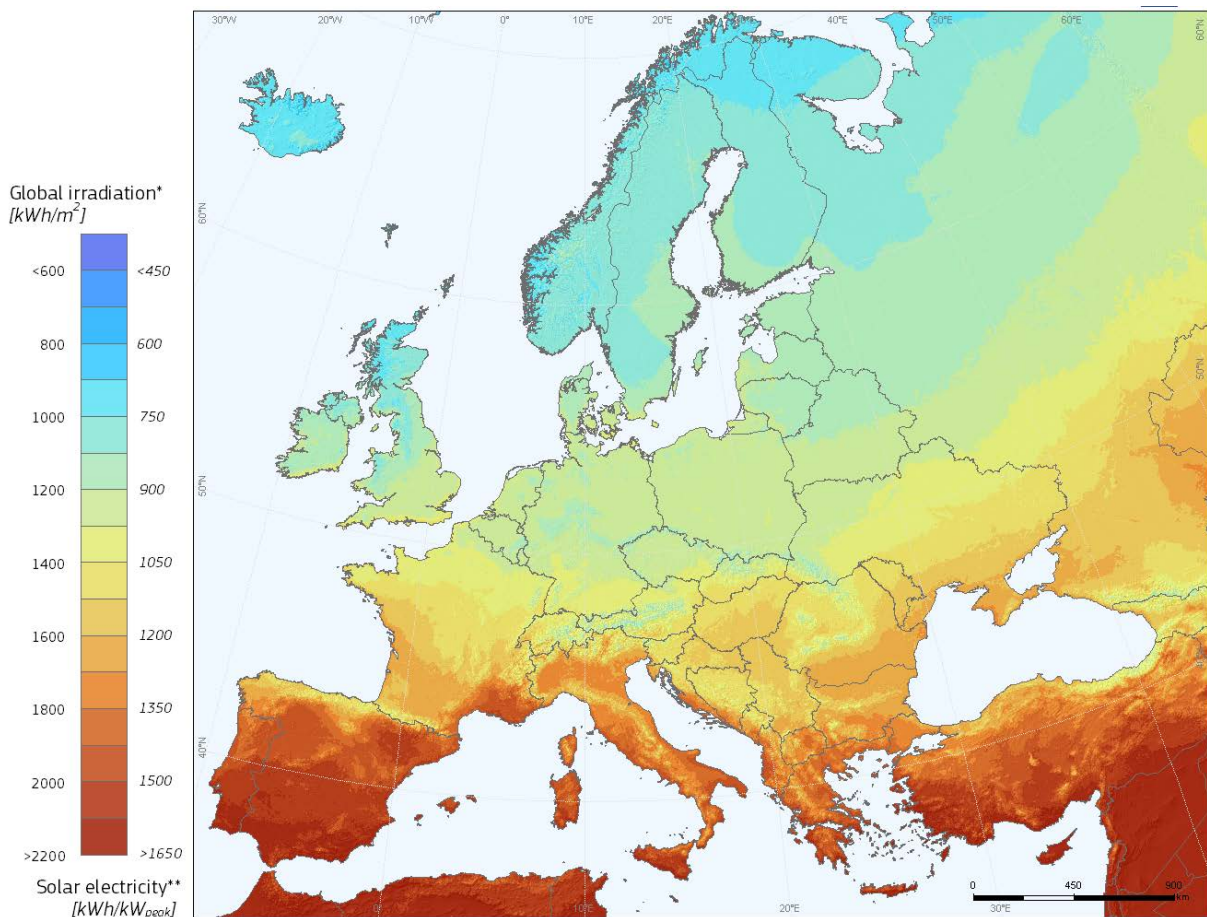
Fig. 1.1. Photovoltaic solar energy potential in European countries (PVGIS 2012).

However, a pondered PV project would bring to an adequate tilt angle of the PV modules, which will increment the beam solar radiation (Figs. 1.3 and 1.4).

Further and accurate observations have to be done considering another limiting factor for energy production: snow. A focus about it is reported in Chapter 1.3.
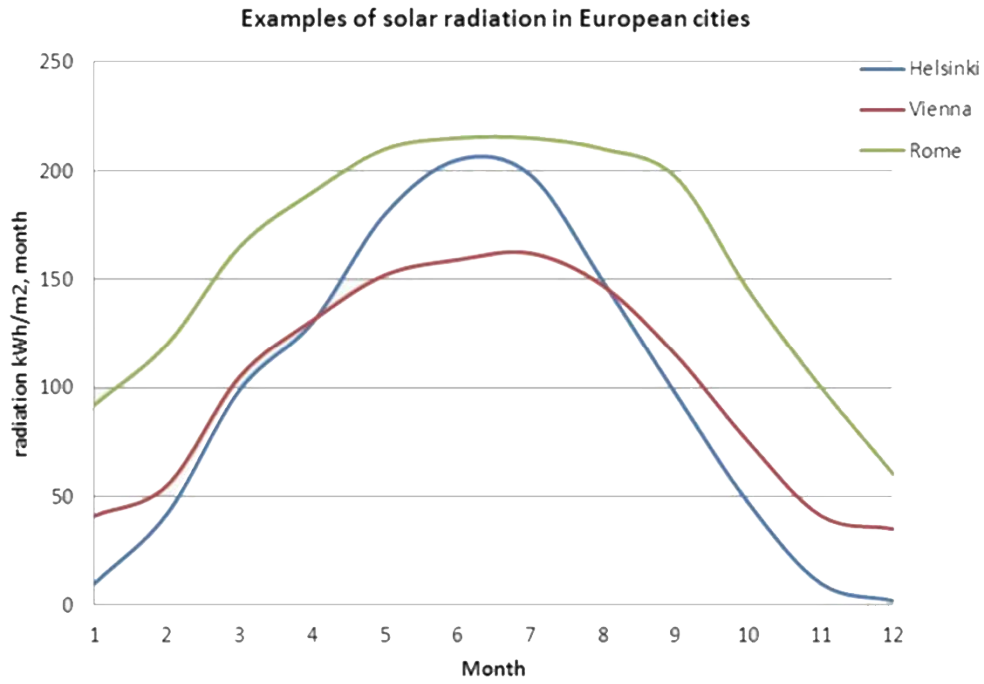
Fig. 1.2. Examples of solar radiation in European cities (Pasonen et al. 2012).

A notification should be made about the weakness of the quality of solar irradiation data in Norway, which will be used in the following work. Solar resource data is commonly based on different combinations of satellite data and ground measurements. The satellite data is usually from geostationary satellites (in orbit above the equator) which have lower accuracy at their high latitudes (Byrkjedal et al. 2013).

Fig. 1.3. Global irradiation and solar electricity potential in Norway of horizontally-mounted photovoltaics modules (PVGIS 2012).
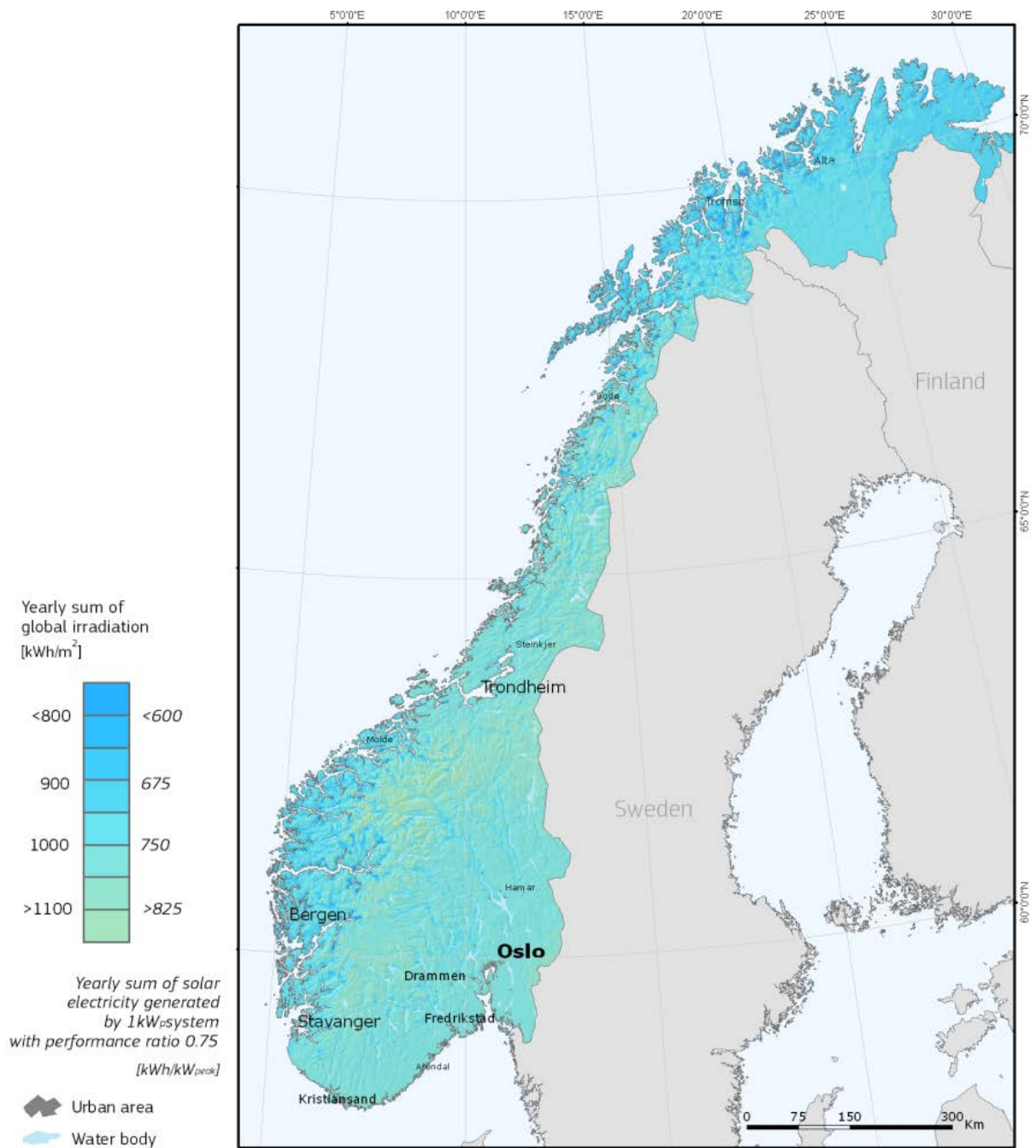
Fig. 1.4. Global irradiation and solar electricity potential in Norway of optimally inclined photovoltaics modules (PVGIS 2012).

1.3 Snow in Norway

Norwegian winter weather is characterized by frequent snowfalls. If the surface of a PV module is not cleaned and free to capture solar irradiation, the system's performance can be highly compromised. Another consideration regards the available solar irradiation, which is lower due to the snow flakes and clouds that limit it (Gardiner 1987).

Norway's snow depth map shows different average values over the country due to morphological and climate characteristics of each geographical location (Fig. 1.5), as a consequence different snow loss values of the PV systems would be present in each area. The major interest is focused on the most populated cities (more than 150 000 citizens), where most of PV resources are: Oslo, Bergen and Trondheim. Snow map shows lower values of snow depth in Bergen because of mitigate weather due to North Sea presence, although Oslo and Trondheim do not have so much less snow depth values.
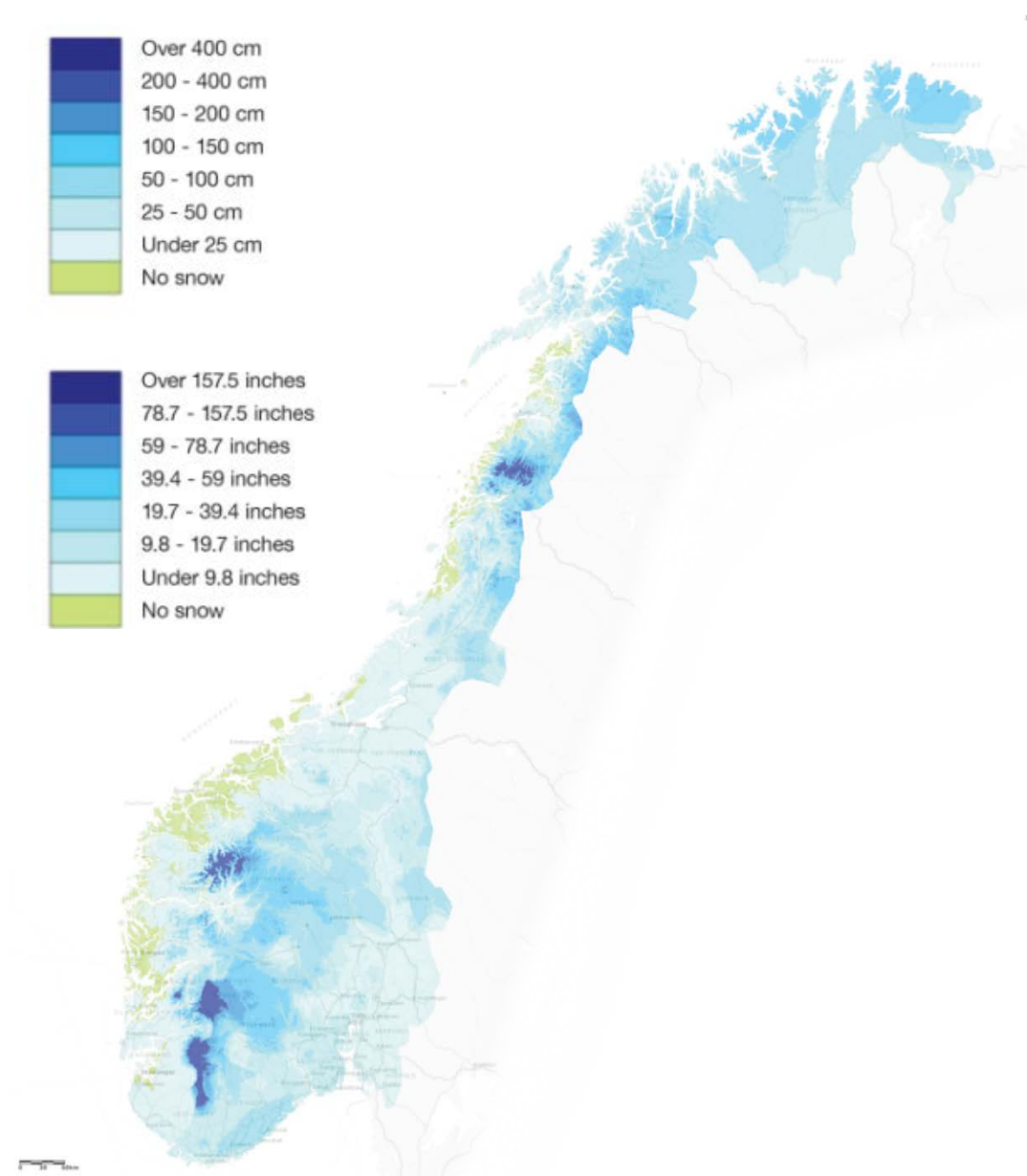
Fig. 1.5. Snow depth map showing values on the 18th of February 2015 (cm, inches) in Norway (seNorge).

Table 1.1 shows average snow depth values per month in Oslo, Bergen and Trondheim. Figure 1.6 represents snow depth trends during the winter in the same cities. This data was furnished by NOAA (National Oceanic and Atmospheric Administration) division in NCDC (National Climatic Data Center) in U.S., accessing to national database of Norwegian Meteorological Institute by eKlima service. Detailed average daily snow depth data is given in Appendix A.

Table 1.1. Average snow depth values per month in Oslo, Bergen and Trondheim (cm/day) (eKlima, Norwegian Meteorological Institute).

	Oslo	Bergen	Trondheim
November	1	0	0
December	5	2	1
January	11	5	5
February	18	4	9
March	19	2	6
April	4	0	0

In particular, only recently a meteorological station was installed in Trondheim at Voll to collect snow depth data. As a consequence, only this winter data is available, even if some days are often missing (Appendix B). This data was furnished by NOAA, accessing to the national database of Norwegian Meteorological Institute by eKlima service. Statistical snow depth data can be obtained for Leinstrand, a small city 15 km south of Trondheim with an older weather station; in fact Norwegian Meteorological Institute collected weather data there since 1960.
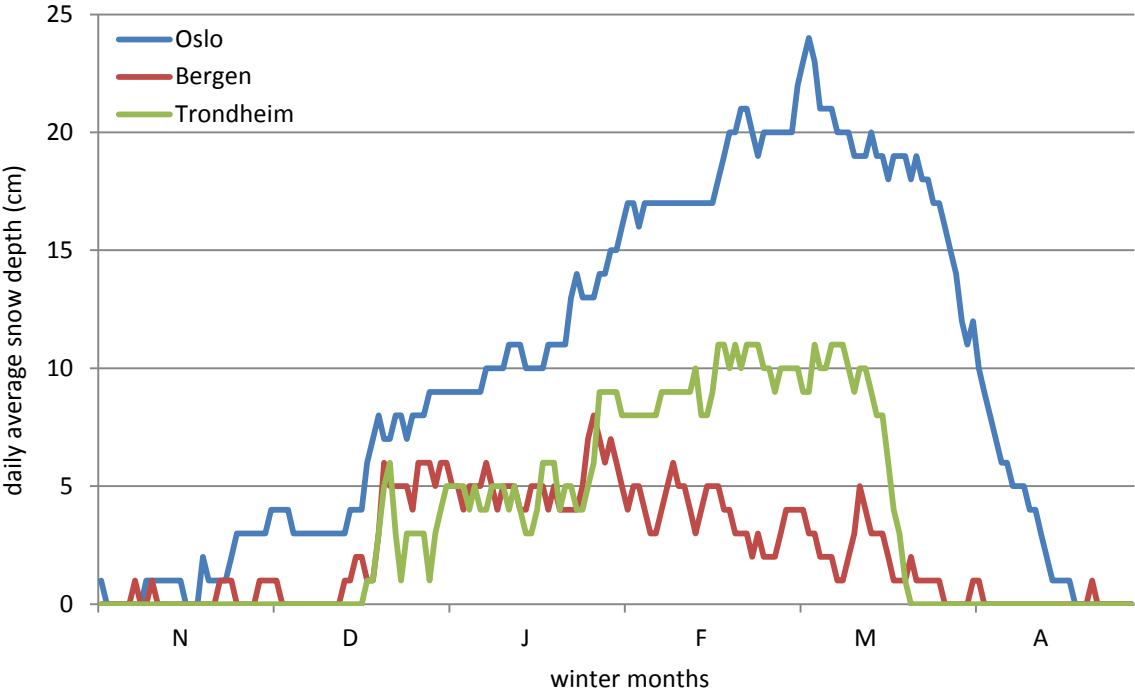
Fig. 1.6. Snow depth trends in the wintertime in Oslo, Bergen and Trondheim (eKlima, Norwegian Meteorological Institute).

A comparison between last winter snow depth data from Trondheim and Leinstrand showed a similarity between the two cities (Fig. 1.7).
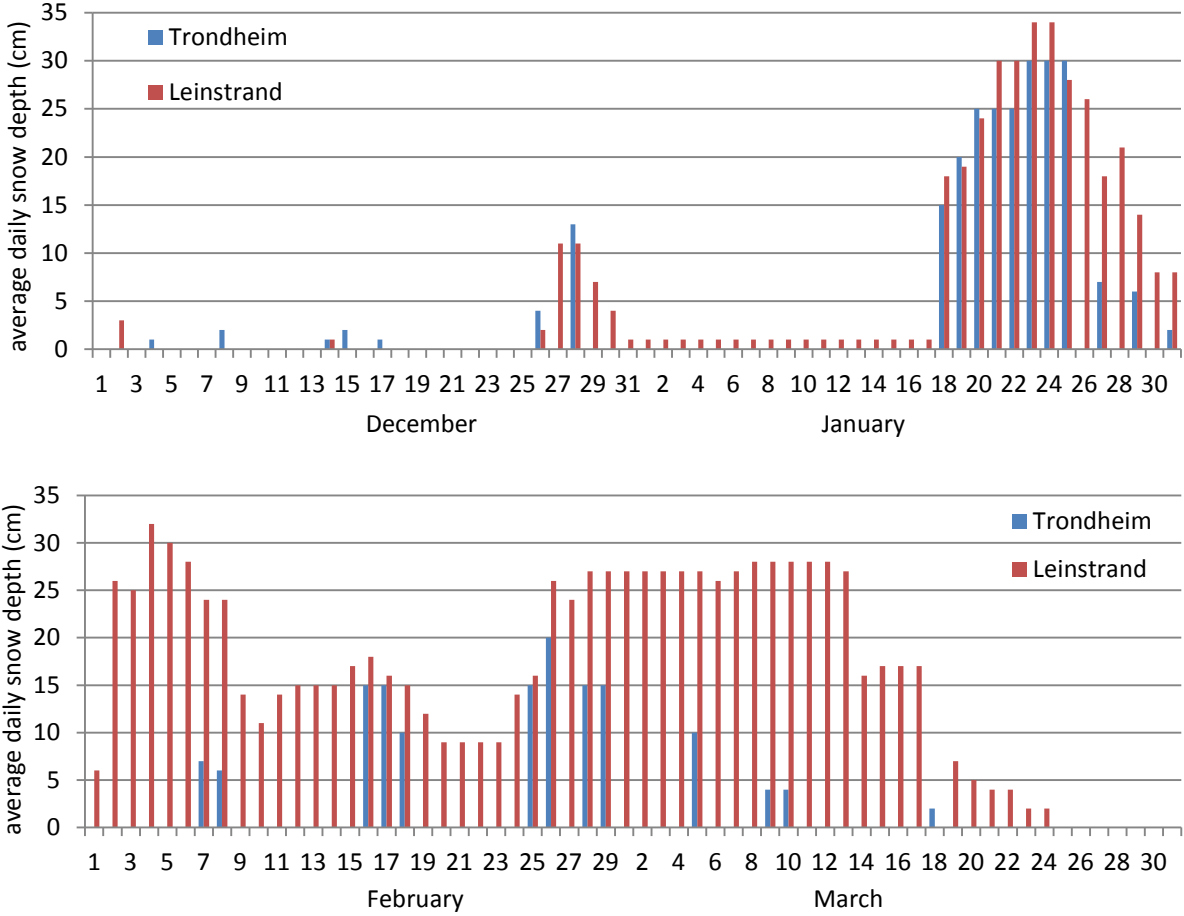
Fig. 1.7. Comparison between average daily snow depth data (cm) of Trondheim and Leinstrand from November 2015 to March 2016. Trondheim data was often missing. Data furnished by Norwegian Meteorological Institute.

As far as Trondheim is concerned, the main data intervals were used to create a linear correlation with Leinstrand data in the same time periods (Fig. 1.8). Leinstrand statistical snow depth data were then corrected through an equation found to obtain statistical Trondheim snow depth data:

$$y = 0.5065x - 0.4895 \qquad (1.1)$$

where x is Trondheim snow depth data and y is Leinstrand snow depth data.

Results are plotted in Appendix B.
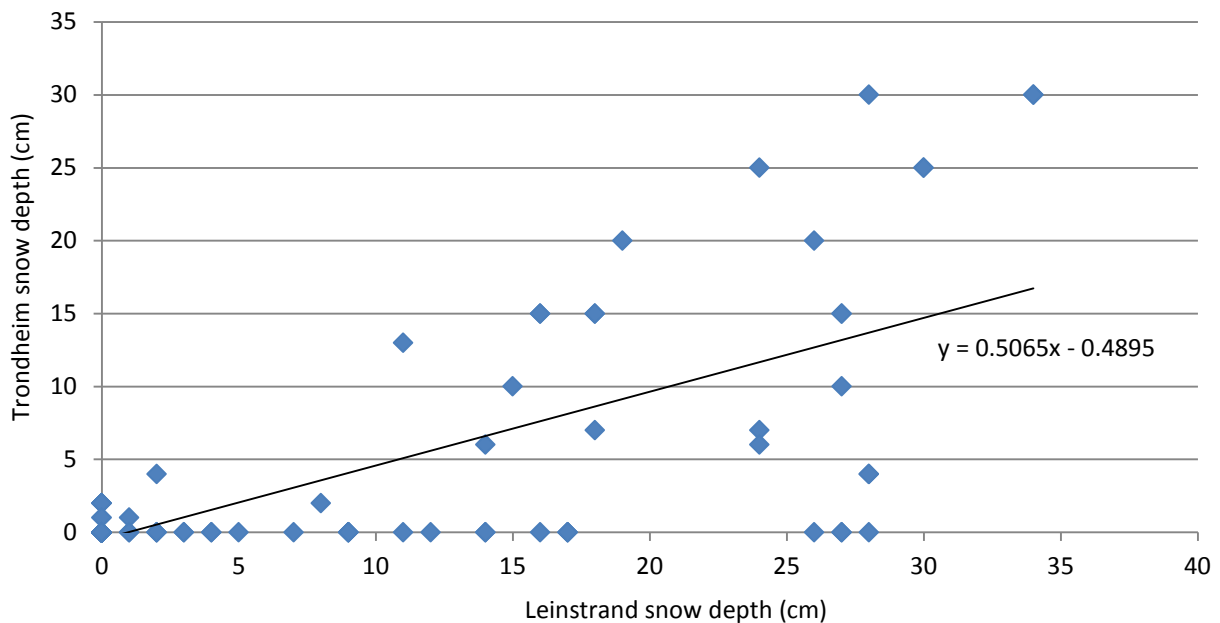
Fig. 1.8. Linear correlation between main intervals of snow depth data (cm) of Trondheim and Leinstrand from November 2015 to March 2016. Data furnished by Norwegian Meteorological Institute.

Snow is one of the major causes of energy production loss for photovoltaic devices in northern countries. As a matter of fact in coldest months snow creates even a total coverage of modules that does not allow any electricity production. However, despite common beliefs, northern countries have great energy potential also in winter time, due to high albedo values caused by snow reflections (Scharmer and Greif 2000). As a matter of fact, 74% of PV resources were installed in countries that experience some amount of snowfall (Becker et al. 2007).

Albedo describes solar radiation that has been reflected from non-atmospheric surfaces e.g. ground, asphalt. Common albedo values in the cities are 10-20%, due to the asphalt and buildings' reflection. An exception is in very snowy conditions which can sometimes raise the percentage of reflected radiation quite high. Fresh snow reflects 80 to 90% of the solar radiation striking it. When there is still snow on the ground in March, the reflected radiation portion of the total radiation can be 25% (Colgan and Wiltse 2010).

1.4 Case study

The PV-plant used in this research is the one set on the ZEB (The Research Centre on Zero Emission Buildings) Living Lab roofs. This building is located in NTNU (Norwegian University of Science and Technology) campus and has a notable relevance, because it was designed as a multipurpose experimental test facility. That is the reason why it was chosen as a case study in this thesis. This paragraph is going to deepen it.

The ZEB Living Lab

The ZEB Living Lab was designed to carry out experimental investigations on interactions between users and low (zero) energy buildings (Figs. 1.9 and 1.10). The primary aim of the ZEB Living Laboratory was thus to realize a building that is representative, as a typology, of

the most common Norwegian dwelling – the single family house – and to demonstrate how CO2-neutral construction can be realized in the Norwegian climate (Finocchiaro et al. 2014).

Fig. 1.9. The ZEB Living Lab at NTNU (Norwegian University of Science and Technology) in Trondheim (Finocchiaro et al. 2014).
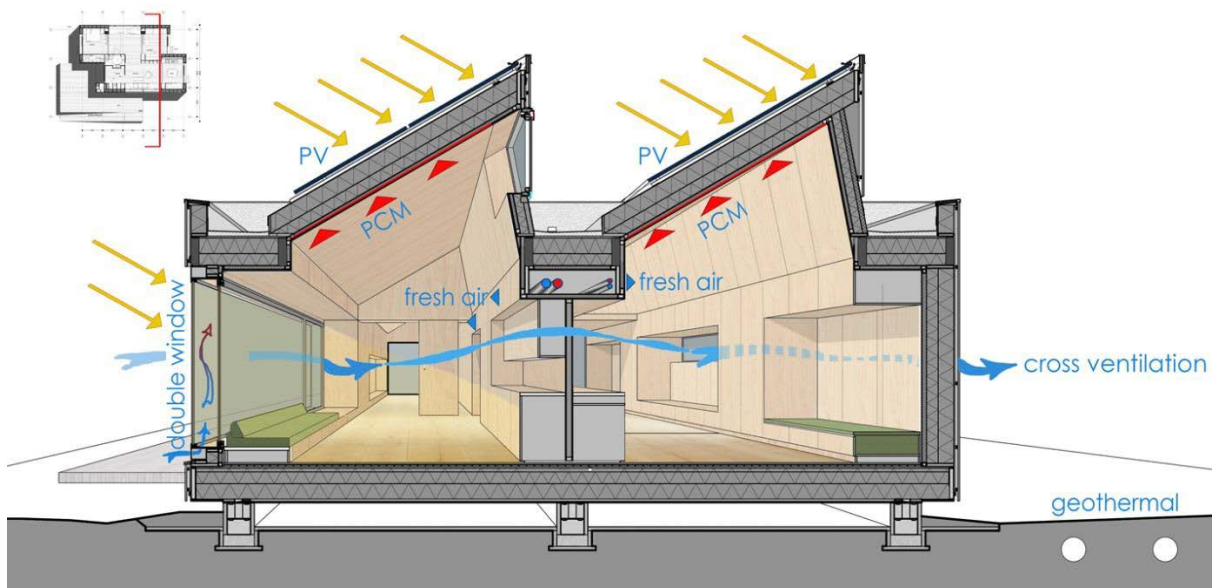
Fig. 1.10. A section of the building that shows the interaction and operation of the strategies applied (Finocchiaro et al. 2014).

The ZEB Living Lab is designed to minimize energy demand for its operation and to harvest solar energy. The aim of the project was to satisfy building energy demand on yearly basis by collecting solar energy through passive measures and active technologies. Active systems used are a solar collector field (SCL), solar thermal panels (STP) and photovoltaic roofs PVR). The energy flow within the building plant, including on-site renewable energy supply, is schematically illustrated in Figure 1.11 (Goia et al. 2015).

12
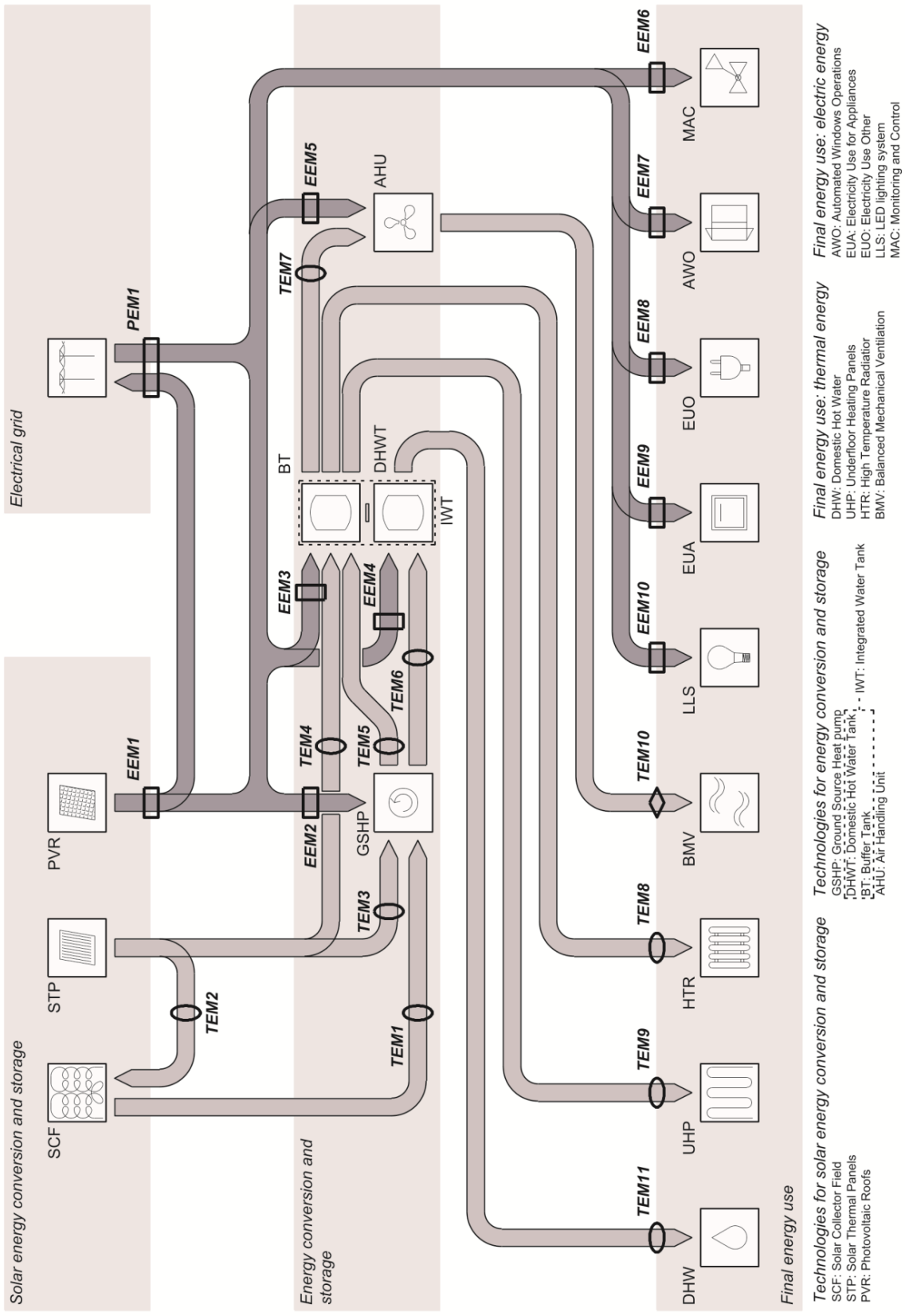
Fig. 1.11. Thermal and electrical energy/power flow within the ZEB Living Laboratory; technologies and devices for energy conversion and storage; associated monitoring system (Goia et al. 2015).

13

The ZEB Living Lab was projected as a test facility equipped by a monitoring system of the energy and environmental performance of the building. The following tasks are given to monitor by the data acquisition (DAQ) system technologies (Goia et al. 2015):

- environmental quantities, both indoor (air temperature, humidity ratio and pressure; CO_2 concentration; diffuse illuminance) and outdoor (air temperature, humidity ratio, and pressure; wind velocity; global solar irradiance on different planes and illuminance);
- users patterns and occupants' habits (rooms occupancy, windows/shading systems opening/displacement; use and control of appliances and lighting system);
- energy use for heating, ventilation, domestic hot water, artificial lighting, appliances and other uses;
- solar energy exploitation (by PV roofs and façade-integrated solar thermal panels) and energy from the grid;
- efficiency in conversion and storage of energy for different uses.

BIPV-plant on the ZEB Living Lab

The photovoltaic system on ZEB Living Lab is located on the two tilted roof areas. The roof tilt is 30° and south-facing.

The solar cell system on ZEB Living Lab consists of 48 modules, equally distributed on the two roofs. Roof length is divided into four rows; the first three from the top are covered by modules in the landscape orientation. Each PV row is made up by 8 modules (Fig. 1.12). The PV system is organized into four strings of 12 modules. The middle row of modules is split between the upper and the lower string.
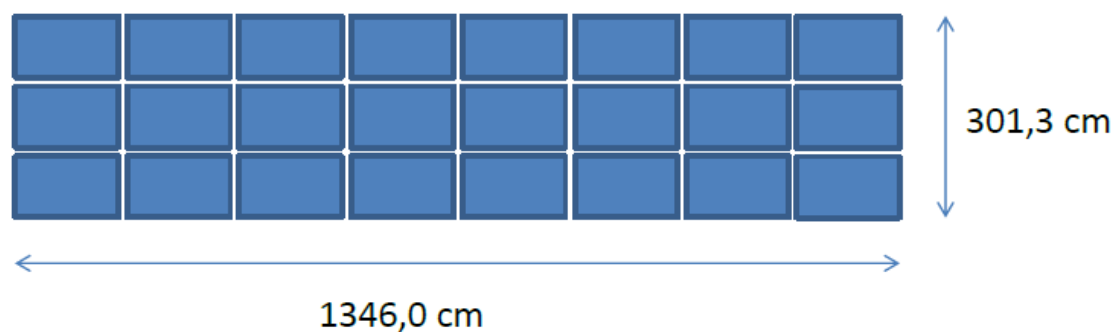
Fig. 1.12. Scheme representing PV system configuration per roof (Johannessen 2013).

Modules are REC 260PE by REC company. Each module has 60 polycrystalline silicon (poly-Si) solar cells, with three bypass diodes. The nominal power for one module is 260 Wp, with a total installed power of 11.48 kWp. The rated efficiency of the modules is 15.8%. The gross modules area is 1.65 m² (1 m x 1.65 m), resulting in a total installed area of 79.2 m². The module weight is 18 kg, which means a total weight of 864 kg, or 10.9 kg/ m²installation. Detailed information is shown in the Appendix C.

One inverter is installed per roof, thus two inverters in total. Inverters are Sunny Boy 5000 TL-21 MS basic by SMA company. Inverter's maximum DC power is 5.25 kW and the efficiency is ranking between 96.5% and 97%. Inverter data sheet is attached in Appendix C.

The mounting system is InterSole SE from Renusol (Fig. 1.13). The PV modules are mounted on aluminium profiles, which are fastened with screws on top of a HDPE membrane. The lower part on both roofs is covered by tar roofing (Appendix C).

Fig. 1.13. Left: The installation of the PV modules on the InterSole system. The HDPE membrane is visible on the middle part of the roof. Right: A close-up of the aluminium profiles and the membrane (Good 2015).

Since the PV system does not replace any other part of the building envelope (the roof would have been weather-proof without it) the system can only be referred to as semi-integrated. The PV system does replace other roofing material, but it is the membrane and not the PV modules that act as the climate shield. The backside ventilation on this system is probably better on this system than on fully integrated systems, thanks to the 49 mm gap between the PV panel and the roof membrane (Good 2015).

The performance of the PV modules are measured through the inverter system, and sent via the SMA Sunny WebBox to SMA's server. The WebBox is located on the wall directly to the right in the technical room. Voltage, current and power from the modules are measured, and the data is available at down to 15 minute intervals. A SensorBox from SMA is also connected to the WebBox. The SensorBox includes a solar radiation sensor, a module

temperature sensor, and a wind sensor. The SensorBox is located on the north roof. Measurement data from the PV system is available through the SMA web interface Sunny Portal, which can be accessed at: http://www.sunnyportal.com (Good 2015).

The module temperatures on three modules are also measured by thermocouples. A weather station is installed on the south roof of the building (Fig. 1.14). Access to data from the thermocouples and weather station is not possible through the SMA interfaces, but is possible through the ZEB Living Lab monitoring system.

Fig. 1.14. Weather station installed on the south roof of the ZEB Living Lab (Good 2015).

Limitations of the results

A particular benefit of using ZEB Living Lab as case study is that it has been (and will be) the subject of several other studies, which means that there is a significant amount of data to build on. A disadvantage of using case studies is that the results have limited validity for other cases, especially buildings that are not similar to the presented cases.

In winter time PV panels installed on the ZEB Living Lab are often subjected to snow cover affecting energy production (Fig. 1.15), as a consequence the analysis previously conducted have a great importance to it. However this building presents specific geometrical and technique conditions that make those values indicative, but not reliable.

Figure 1.16 shows a cross section of the ZEB Living Lab. The roof was designed with a tilted part and a plane part. In this specific case the geometry of the building strongly influences snow deposition; in fact the plane part of the roof represents an excellent place for snow to accumulate, leading to a permanent snow cover of lowest PV rows in coldest months. As a consequence the snow on the higher rows is prevented to slide off the modules.

16

This phenomenon was taken in consideration when the building was designed; in fact the lowest part of the roof has no modules installed. However the snow precipitation is far more intense than the expected and the PV modules result prevented to produce any energy because of snow obstruction.

Fig. 1.15. ZEB Living Lab after a snowfall in late January 2015 (Good 2016).
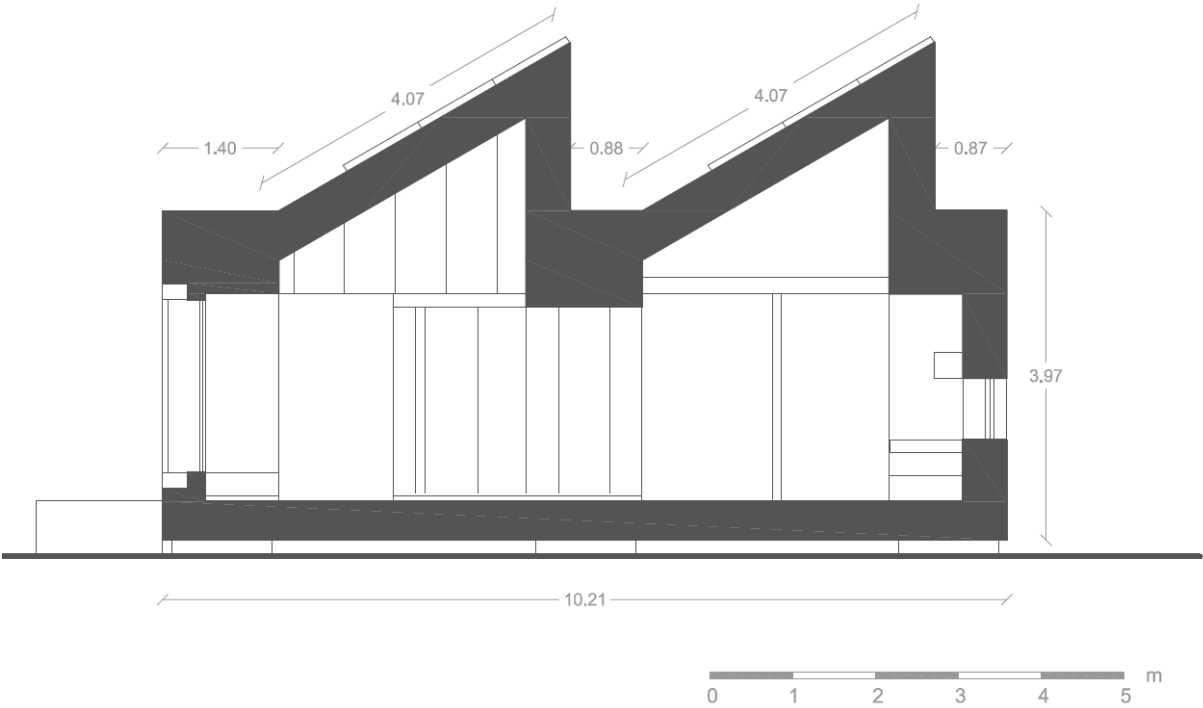
Fig. 1.16. ZEB Living Lab's roof design and measurement.

Further observations highlighted another problem that impedes the snow sliding is the module frame. Sometimes the snow cover sticks to the frame and slides off only partially (Fig. 1.17).

Fig. 1.17. ZEB Living Lab after a snowfall in late November 2015 (Good 2016).

In conclusion the results of the analysis conducted in the previous chapter have a general validity. While the ZEB Living Lab PV-plant is subjected to different conditions that need further study.

1.5 Thesis statement

As a matter of fact, Norwegian interest in photovoltaics leads to the study of the influence of snow on PV devices. As a consequence, different studies have been conducted to find an adequate solution to this challenge.

An overview to the possible solutions to the problem of snow and ice removal leads to different answers. The most realizable and practise ones seem to be the architectural and material solutions.

The module tilt angle not only affects snow and ice accumulation on a PV module, but, through gravity, it determines the force motivating the snow or ice to slide off the module. The tendency of snow or ice to slide off the module is related to the sine of the module tilt angle. Therefore, an optimal tilt angle should be chosen to design PV-array, in order to favourite the snow sliding and increase the energy harvesting. The architectural solution will be one of the themes analysed in this thesis.

Engineering and chemistry research is now focusing on new nano materials that can be manipulated to obtain specific desired properties. The main strength is to create an icephobic surface, which could overcome various problems in different fields, including photovoltaic surfaces. Investigating this theme will be another goal of this thesis.

The two solutions will be analysed through the use of different tools. A great help will be furnished by energy simulations, developed through the software PVsyst.

In summary the thesis develops first coping with the optimisation of the system that favours the snow sliding. After consideration about PV projects, a second analysis regards the quantification of energy production loss due to the presence of the snow. At this point an overview of the solutions to reduce or eliminate snow from the modules is necessary. After the investigation of a valid solution, its influence on the values of energy production should be investigated.

In conclusion this thesis addresses four goals:

1) Suggest some guidelines to design a PV system at snowy locations.
2) Quantify energy loss due to snow coverage through models.
3) Investigate the characteristics of icephobic materials and state-of-the-art solutions.
4) Quantify the energy loss reduction produced by icephobic coatings.

1.6 Thesis structure

The thesis is structured as follows:

Chapter 1: The general background where this study is introduced. Information about irradiation and snow depth values help to understand the conditions of PV production in Norway and the need for solving the snow challenge. Finally a spotlight about the case study is presented.

Chapter 2: The study focuses on the design of a PV-plant geometrically. The architecture of the system can be optimized favouring the sliding of the snow off the modules. Different cases should be analysed, considering different geometries desired for various roofs applying BIPV systems. In addition a study of the electrical loss due to the system design could lead to an adequate choice about the division of the systems in strings and the introduction of by-pass diodes.

Chapter 3: The aim of this chapter is to model snow loss. An overview of different models is given. Then one of them is integrated with the output given by PV simulation. This new model is applied to a case study: the ZEB Living Lab in Trondheim. Finally, the system is supposed also in Oslo and Bergen to analyse the various results given by the different snow conditions.

Chapter 4: An overview of different solutions to snow cover is presented. It is followed by an analysis of icephobic materials: properties, nano design, and application challenges. A state-of-the-art review concludes this chapter, focusing on what is now commercially offered by companies on the market.

Chapter 5: An application of icephobic coatings in the simulations in presented. Results of the ZEB Living Lab supposed in Oslo, Trondheim and Bergen are discussed.

Chapter 6: In this chapter considerations about previous results are presented. The case study offered the possibility to analyse energy production data for only the last winter. However, observations and proposals for further studies are given.

Appendix: The entire appendix material is included in this section.

1.7 References

Arnstad-utvalget, «Energieffektivisering av bygg. En ambisiøs og realistisk plan mot 2040 Kommunal» («Energy efficiency of buildings. An ambitious and realistic plan toward 2040").- og moderniseringsdepartementet/Ministry of Local Government and Modernisation, 2010.

G. Becker, "An approach to the impact of snow on the yield of grid connected PV systems", Bavarian Association for the Promotion of Solar Energy, Munich, 2007.

Ø. Byrkjedal, A.L. Løvholm, S. Liléo, "Resource mapping of solar energy - An overview of available data in Norway", Kjeller Vindteknikk, Report KVT/OB/2013/R046, 2013.

R. Colgan and N. Wiltse, "Performance of photovoltaic arrays", GW Scientific Ben La Rue, Siemens Greg Egan, Remote Power, 2010.

eKlima, Norwegian Meteorological Institute, eklima.met.no

European Parliament, Directive 2010/31/EU of the European Parliament and of the Council of 19 May 2010 on the energy performance of buildings, Directive 2010/31/EU, Brussels, 2010.

L. Finocchiaro, F. Goia, S. Grynning, A. Gustavsen, "The ZEB Living Lab: a multi-purpose experimenral facility", Gent Expert Meeting, Ghent University, Belgium, 2014.

Forskrift om tekniske krav til byggverk (Byggteknisk forskrift), Kommunal- og moderniseringsdepartementet/Ministry of Local Government and Modernisation FOR-2010-03-26-489, Lovdata, 2015.

B. G. Gardiner, "Solar radiation transmitted to the ground through cloud in relation to surface albedo", *J. Geophys. Res.,* **92**, 4010–4018, 1987.

F. Goia, L. Finocchiaro, A. Gustavsen, "The ZEB Living Laboratory at the Norwegian University of Science and Technology: a zero emission house for engineering and social science experiments", Passivhus Norden – Sustainable Cities and Buildings, Copenhagen, 2015.

C. Good, I. Andresen, A. G. Hestnes, "Solar energy for net zero energy buildings. A comparison between solar thermal, PV and photovoltaic-thermal (PV/T) systems". *Solar Energy*, **122**, 986-996, 2015.

C. Good, "The photovoltaic system on the ZEB Living Lab", 2015.

C. Good, "Photovoltaic-thermal systems for zero emission residential buildings", PhD thesis, NTNU, Faculty of Architecture and Fine Arts, Department of Architectural Design, History and Technology, 2016.

IEA (2013). PVPS Report Shapshot of Global PV 1992-2013. In IEA Photovoltaic Power System Programme (ed.). 11 pp.

B.P. Jelle and C. Breivik, "State-of-the-art building integrated photovoltaics", *Energy Procedia*, **20**, 68-77, 2012.

E. Johannessen, "ZEB Living Lab – Takintegrert PV-system", Solbes report, 2013.

L. Kitzing, C. Mitchell, P. E. Morthorst, "Renewable energy policies in Europe: converging or diverging?", *Energy Policy*, **51**, 192-201, 2012.

R. Pasonen, K. Mäki, R. Alanen, K. Sipilä, "Artic solar energy solutions", VTT Technology Report, **15**, 2012.

L. Pérez-Lombard, J. Ortiz, C. Pout, "A review on building energy consumption information", *Energy and Buildings*, **40**, 394–398, 2007.

PVGIS, Photovoltaic Geographical Information System, European Commission, Scientific tools and databases, 2012.

K. Scharmer, J. Greif, "European Solar Radiation Atlas: fundamentals and maps", Ecole des Mines de Paris, Paris, 2000.

Å. L. Sørensen, "Solar energy use and regulations in Norway", Solar energy in urban planning, Norsk solenergiforening, 2015.

SeNorge, senorge.no.

National Weather Service, "Snow measurement guidelines for National Weather Surface Observing Programs", U.S. Department of Commerce National Oceanic and Atmospheric Administration, September 2013.

2 Designing a PV and BIPV system in snowy areas

2.1 Abstract

This work presents an analysis of how geometrical and electrical optimisation increases the energy production of a photovoltaic (PV) and building integrated photovoltaic (BIPV) plants. The study is focusing on snowy places, to find an optimal orientation of modules that concerns the sliding of the snow in winter time.

The software PVsyst is implemented with several tools that let an optimal orientation of the modules. They do not take in consideration the snow cover in the winter time, though. In snowy places the bulk of snow that deposits on the modules can constitute a serious limit to energy production. Several studies have been conducted regarding the relation between the snow slide amount and the surface tilt angle. In conclusion the aim of this study is to compare different results to consider the presence of the snow in designing a PV or BIPV plant.

Further considerations are given considering the case when the system is organized not just in one row of modules, but in several rows of modules. In this case the PV-plant design should be determined taking into account the self-shading problem. Finally the study analyses also the optimisation of electrical aspects, leading to a reduction of electrical loss due to snow.

The design optimisation of a PV system is related to the location where the plant is set. As a consequence, the choice of a case study is necessary. However, the methodology maintains a general validity, so that it can be repeated for other locations. In this study the simulations are conducted considering three different cities in Norway: Oslo (59°55'; 10°45'), Bergen (60°39'; 5°33') and Trondheim (63°26'; 10°23').

2.2 Introduction

The optimal design of photovoltaic (PV) system is a topic that has been analyzed widely before (Yadav and Chandel 2013, Idowu et al. 2013, Benghamen 2011, Ahmad and Tiwari 2009). The main question is about choosing the right tilt angle of the modules, in order to increase the beam component of the solar radiation.

Other aspects to be considered are introduced if the system is organized not just in one row of panels, but in several rows of panels. In this case the PV-plant design should be determined taking into account the self-shading problem. In fact shading presence will lead to the annulment of the beam component, provoking the so-called "shading loss" in the energy production (Yang et al. 2012, Honsberg and Bowden 2011).

Actually, this term usually refers not only to the near shading causes, but also to the far shading. As a consequence, an important discussion regards the fact that the PV system's production will be affected deeply if the plant is installed near high buildings, trees, chimneys, antennas and so on.

The "shading loss" can be reduced if the system is rationally divided into strings, equipped by blocking diodes. When a diode is installed in series with a string of modules, it performs a blocking function and prevents backflow down the module string. If one string becomes severely shaded, or if there is a short circuit in one of the modules, the blocking diode prevents the other strings from losing current backwards down the shaded or damaged string. The shaded or damaged string is "isolated" from the others, and more current is sent on to the load (Prontes 2013, Solar-Facts 2012).

Another problem caused by shading is the hot-spot heating. It occurs when there is one low current solar cell in a string of at least several high short-circuit current solar cells. One shaded cell in a string reduces the current through the good cells, causing the good cells to produce higher voltages that can often reverse bias the bad cell. Bypass diodes are a standard addition to any crystalline PV module. The bypass diodes' function is to eliminate the hot-spot phenomena which can damage PV cells and even cause fire if the solar radiation on the PV cells in a module is not uniform. The bypass diodes are usually placed on sub-strings of the PV module, one diode per up to 20 PV cells. This configuration eliminates the creation of hot-spots and enables the PV modules to operate with high reliability throughout their lifetime. In conclusion, a standard 60 cell PV module is usually built from 3 substrings, each protected by a bypass diode (Deutsche Gesellschaft für Sonnenenergie 2008; Sargosis Solar & Electric 2014).

Taking into account the presence of the snow on the PV-plant could lead to different answers in the architectural optimisation of the system. In fact, the variation of the tilt angle is related to the variation of the snow amount that slides off the panels (NAIT 2015, Bayard 2015).

A recent study was conducted by a group of researchers on a test bed in Michigan (Heidari et al. 2015). The aim was to develop a model to predict how snowfalls affect energy generation. A relationship between the tilt angle of the panels and the snow coverage was highlighted by Tim Townsend, principal engineer for solar services with DNV GL. A clear relation between the tilt angle and the amount of snow sliding off the panels was showed by Marion et al. (2013), who developed an accurate satellite analysis. The results found were then used to predict PV-plant snow loss.

The choice of the tilt angle is an important step in designing a PV-plant, but it is even more important in designing a building integrated photovoltaic (BIPV) plant. In this case the project of the PV system is integrated in the building's project, because BIPV elements replace parts of the conventional building materials and systems in the climate envelope of buildings, such as the roofs and facades (Jelle and Breivik 2012). As a consequence, in most cases defining a tilt angle leads to determine the inclination of the roof.

The disposition of the panels in different sheds is not typical of BIPV systems, but some examples are present e.g. ZEB (The Research Centre on Zero Emission Buildings) Living Lab at Norwegian University of Science and Technology (NTNU) campus in Trondheim. However, the ground-mounted arrays are usually arranged into more sheds if the space is sufficient, therefore considerations about self-shading problems have a more general character, referring also to PV systems.

The electrical loss due to shading respect the total energy production concerns PV and BIPV panels, because they are caused by self-shading and far shading. Therefore, the analysis of this problem would be beneficial for a careful design of a PV and BIPV system.

The aim of this study is to present some considerations about PV and BIPV system design in snowy place, highlighting the geometrical and electrical aspects. The study will be conducted using various tools available in the PVsyst programme, integrated with observation of Marion's study to consider the influence of the snow.

Marion's relation has a general validity, but the design optimisation of a PV system is related to the location where the plant is set. As a consequence, the choice of a case study is necessary. However, the methodology maintains a general validity, so that it can be repeated for other locations. In this study the simulations are conducted considering three different cities in Norway: Oslo (59°55'; 10°45'), Bergen (60°39'; 5°33') and Trondheim (63°26'; 10°23').

2.3 Methodology

2.3.1 PVsyst tools

Once defined an external environment of the project, several options in the PVsyst software can help to optimize plant orientation. These ones can be accessed by several places in the software (PVsyst 6 Help):

1. During the definition of the project's parameters, the "Orientation" choice offers the possibility to see the optimum tilt and azimuth angle to catch the maximum beam irradiation in the "Fixed tilted plane" option. There is the possibility to analyse the sheds' influence on the "Unlimited sheds" option, where the geometry of the system leads to a different optimum tilt angle. Finally this sheet also considers the electrical effect of the partition of the modules into different strings.

2. In "Tools" / "transposition factor", several graphs showing the convenience of optimum angles previously described can be plotted.

3. During the definition of the project's parameters, the "Near shading" choice leads to the building of a 3D scene with the real measures of the plant. At this point the

shadows that are automatically calculated by the software can be used in the energy production simulation as "linear shading" or "according to module strings" with a definition of the electrical effect fraction, obtaining the same results of the above described procedure 1. The addition option is the consideration of the presence of a module bypass diodes in the computation.

2.3.2 Geometrical optimisation

One shed

The first hypothesis is to have all the modules set on the same shed (rows as called by PVsyst), so that no shading occurs.

The PVsyst software gives the possibility to determine the optimum tilt and azimuth angle of the modules in three different cases: over a year, in the summer (April-September) and in the winter (October-March). Then the global irradiance of the collector plane is calculated for these three different situations.

The orientation optimisation is calculated by the software considering the transposition factor (TF), that is the ratio of the incident irradiation (GlobInc) on the plane and the horizontal irradiation (GlobHor).

The optimisation in the winter leads to the highest tilt angle, because of lower solar altitude angle; whereas the optimisation in the summer leads to the lowest tilt angle, due to the higher solar altitude angle. Solar angles are represented in the solar diagrams for Oslo, Trondheim and Bergen, given in Figs. 2.1 - 2.3.
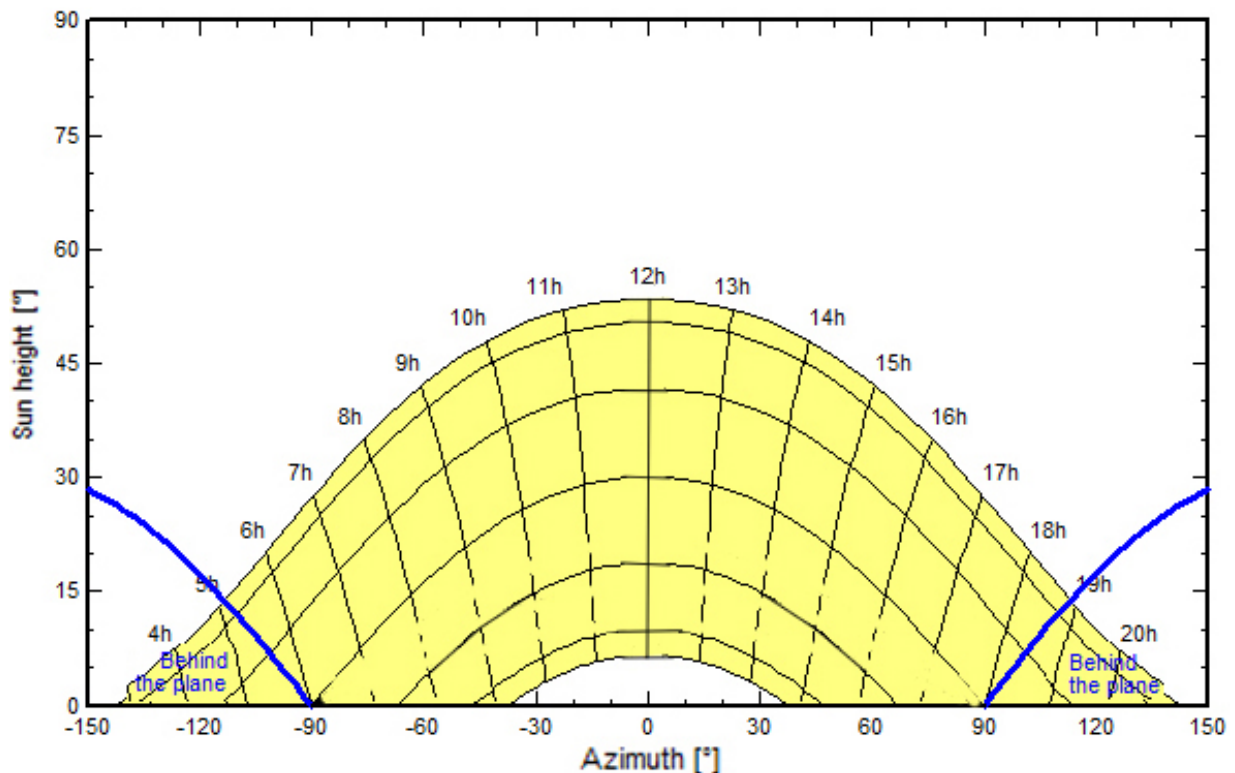
Fig. 2.1. Sun paths diagram of Oslo (59°55'; 10°45') (plotted through PVsyst).
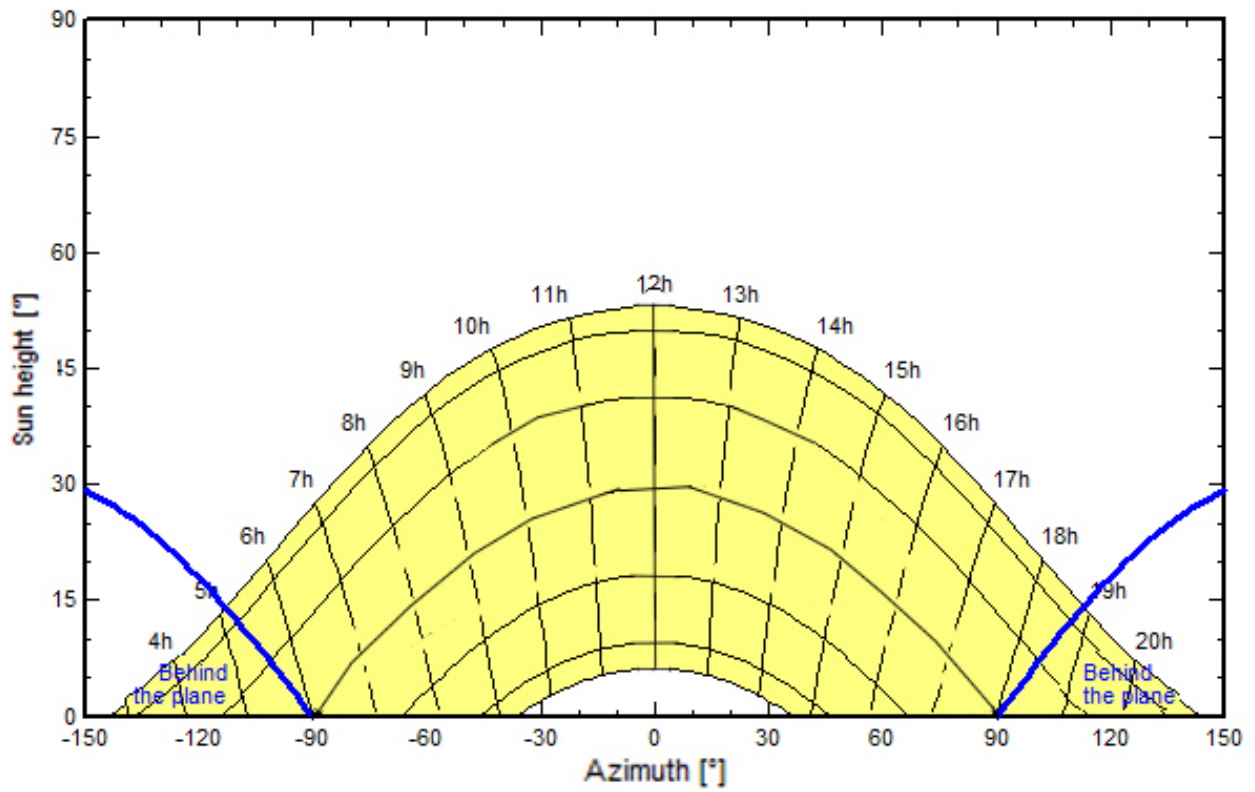
Fig. 2.2. Sun paths diagram of Bergen (60°39'; 5°33') (plotted through PVsyst).
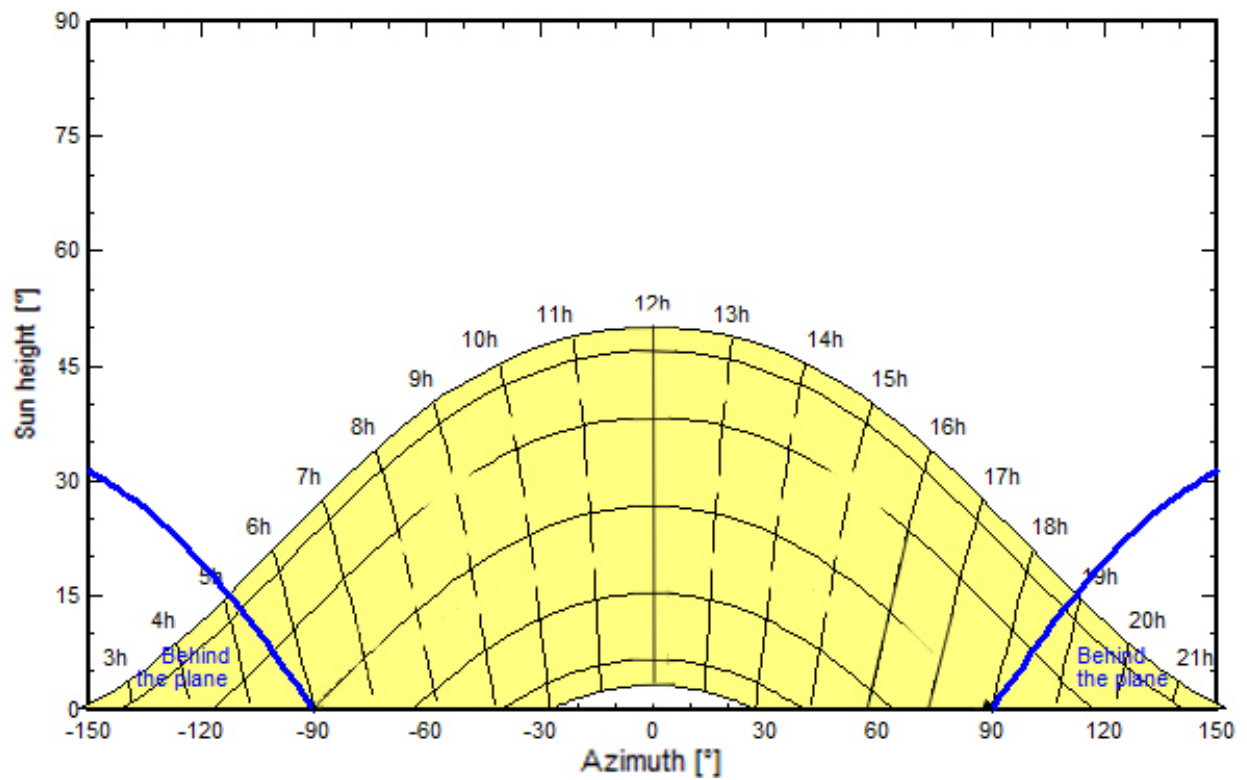
Fig. 2.3. Sun paths diagram of Trondheim (63°26'; 10°23') (plotted through PVsyst).

30

The snow coverage can be considered on the plane from December to March in these Norwegian cities. Details about snow depth values are described in Table 1, Fig. 1.6 and Appendix 1. Therefore, snow coverage is present only in half on the months considered in wintertime from PVsyst.

The module's tilt angle influences the sliding of the snow from the panels (Report by Northern Alberta Institute of Technology 2015, Heidari et al. 2015, Bayard 2015). This phenomenon was studied in detail by Marion et al. (2013). Six PV systems situated with different tilt angle (from 15° to 35°) and different array types (roof-mounted and rack ground-mounted) were monitored in different locations (Colorado and Wisconsin, U.S.) to collect PV performance data. Key data recorded were snow depth, digital images of the PV arrays to assess snow coverage and plane-of-array (POA) solar irradiance.

This research led to an interesting result, which is a different linear relationship between snow amount sliding away and the sine of the tilt angle β for roof-mounted systems and ground rack-mounted systems (Fig. 2.4).
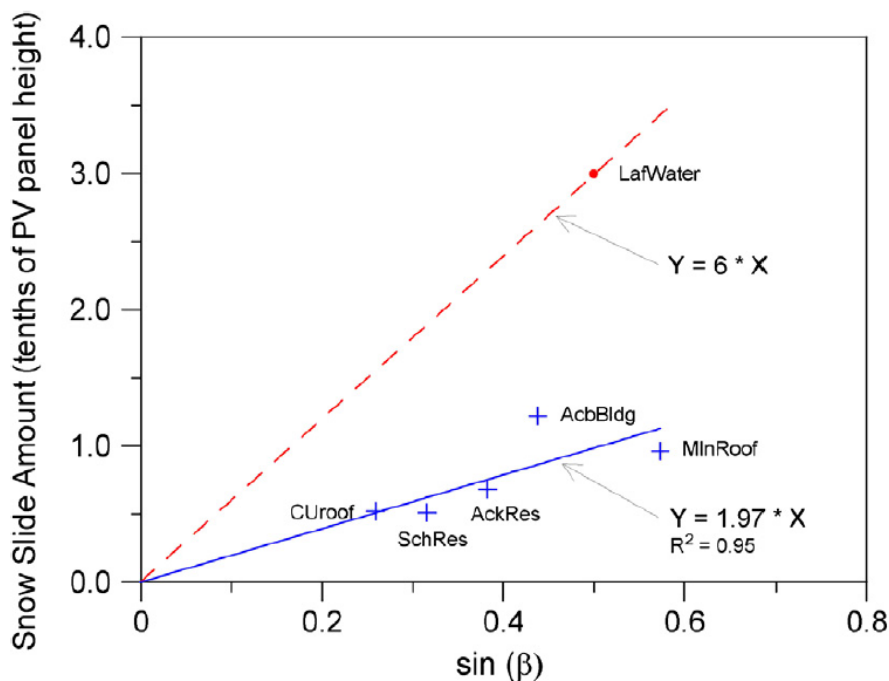
Fig. 2.4. Scatter plot of modelled versus measured monthly PV system energy losses due to snow for November 2010 – March 2011 and November 2011 – March 2012. The diagonal has a slope of one. Data above the diagonal indicate that model estimates are too large, and vice versa (Marion et al. 2013).

Snow slide amount s (tenths of PV panel height) is equal to (Marion et al. 2013):

$$s = k \sin \beta \qquad\qquad (2.1)$$

where k is a coefficient (1.97 for roof-mounted systems; 6 for ground rack-mounted systems) and β is the tilt angle in degree.

Considering snow cover in the selected months proportionally to the tilt angle, other results may be found about energy production. The calculation assumes that a part of the energy production is obstructed when snow cover is on the module surface.

Unlimited sheds

If the PV system is organized into more sheds, the shadow problem will be present.

After inserting the geometrical dimensions of the PV-plant, such as the number of sheds, the pitch, the collector band width, the top and bottom inactive band measures, PVsyst can recalculate the optimum tilt angle of the modules considering the shading. A shading loss will always be present, but it will be minimized by the right choice of the tilt angle.

The previous computation can be executed if the pitch measure is already established. This is the case of the roof-mounted PV or BIPV, where the distance between the rows cannot be too great.

Other analyses are conducted attempting to reach an optimum pitch distance. This is the case of photovoltaic fields, where modules are sets into several sheds. The shading loss cannot be overcome, but a very low value can be reached.

2.3.3 Electrical optimisation

Finally, some evaluations regarding the energy saved inserting some electrical devices will be performed.

After inserting the geometrical settings previously listed, the software requires the number of strings per row. It develops some graphs showing the mutual shading factor, function of the profile angle. The mutual shading factor is 50% when the array is made up by only two rows, 66% for three rows and so on. The profile plane is the plane passing through a horizontal line perpendicular to a given azimuth, and the sun. We call profile angle, related to a given azimuth, the angle formed by the profile plane and the horizontal plane. This is the characteristic angle describing the shadows limited by a horizontal line.

The linear effect plotted on the graphs shows the decreasing trend of the mutual shading factor till the limit profile angle. The limit profile angle is the sun angle that does not create any shadow on the module (Fig. 2.5).

If the software is asked to consider the electrical effect, it means that the collector band width is divided into the desired number of strings. The electrical effect curve will show a mutual shading factor higher than the one with the linear effect (Fig. 2.5).

However, increasing the number of strings the Mutual Shading factor will be reduced (Fig. 2.5 - 2.7). Supposing an infinite number of rows the electrical effect would be equal to the linear effect (Fig. 2.8).

Considering the width of the collector band as a fix data, the number of strings will be equal to the number of rows of modules that suit in the collector band in a landscape position. The dimension of the short side of a module is generally 1 m.

Values of electrical loss are plotted in the flowchart simulation results. They can be compared in the different cases, changing the strings number.
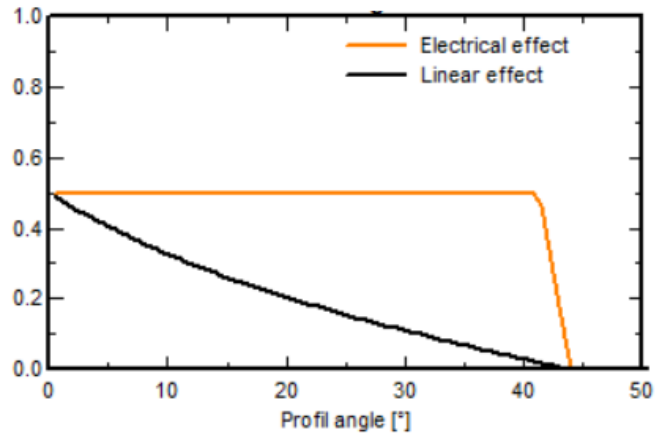
Fig. 2.5. Mutual shading factor versus profile angle. PV system with two sheds divided into two strings (plotted through PVsyst).
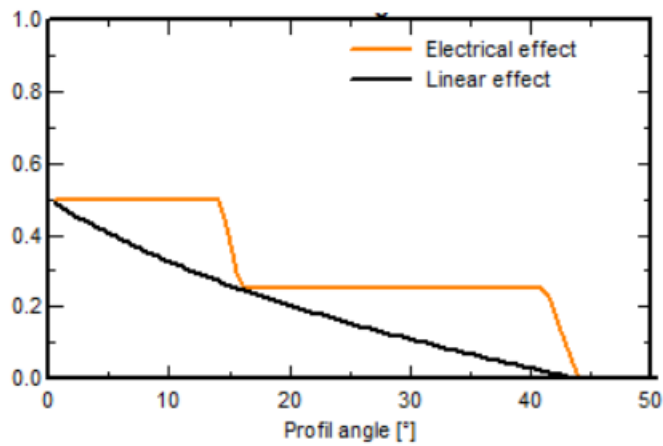
Fig. 2.6. Mutual shading factor versus profile angle. PV system with two sheds divided into four strings (plotted through PVsyst).
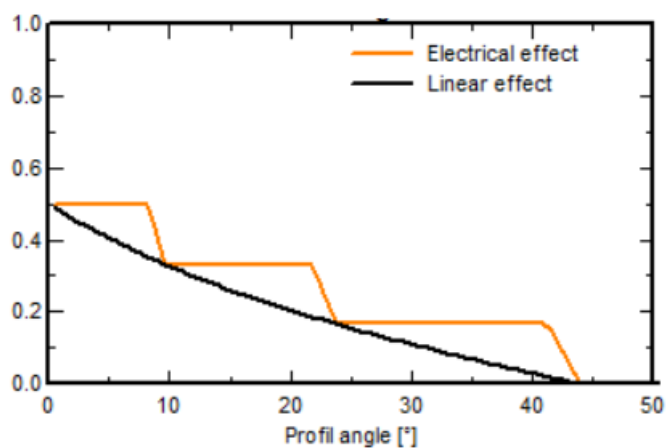
Fig. 2.7. Mutual shading factor versus profile angle. PV system with two sheds divided into six strings (plotted through PVsyst).
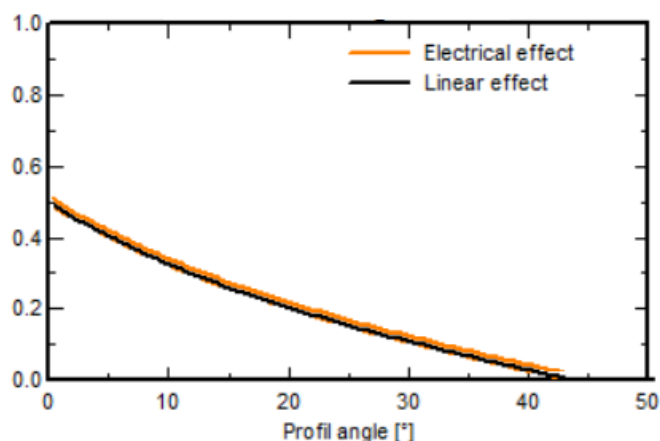
Fig. 2.8. Mutual shading factor versus profile angle. PV system with two sheds divided into infinite strings. The electrical effect graph nearly identifies the linear effect graph (plotted through PVsyst).

One last consideration related to the electrical problems regards the presence of by-pass diodes into the modules. Their function has already been explained in paragraph 2.1. If the presence of the diodes is indicated in the sheet "Near shading" of the software, the influence on the total energy production is calculated and computed in the electrical loss in the flowchart results with all the other types of loss. The simulations can be repeated changing the number of by-pass diodes per module to analyse the variation of the total electrical loss.

2.4 Results

2.4.1 Geometrical optimisation

One shed

The study about tilt optimisation gave similar results for Oslo, Bergen and Trondheim (Tables 2.1 - 2.3).

Table 2.1. Tilt optimisation for Oslo photovoltaic devices over a year, in the summer (April-September) and in the winter (October-March).

Oslo Tilt angle 42°, nominal POA 879 kWh/m²	Optimisation over a year	Summer	Winter
Transposition factor	1.21	1.1	1.81
Loss respect to the optimum (%)	0	-1	-7.4
Global radiation on collector plane (kWh/m²)	1065	816	249
Oslo Tilt angle 32°, nominal POA 879 kWh/m²	Optimisation in summer	Year	Winter
Transposition factor	1.11	1.2	1.68
Loss respect to the optimum (%)	0	-1.1	-14.4
Global radiation on collector plane (kWh/m²)	825	1054	230

Oslo **Tilt angle 67°, nominal POA 879 kWh/m²**	Optimisation in winter	Year	Summer
Transposition factor	1.96	1.13	0.97
Loss respect to the optimum (%)	0	-7.2	-12.5
Global radiation on collector plane (kWh/m²)	298	988	710

Table 2.2. Tilt optimisation for Bergen photovoltaic devices over a year, in the summer (April-September) and in the winter (October-March).

Bergen **Tilt angle 43°, nominal POA 747 kWh/m²**	Optimisation over a year	Summer	Winter
Transposition factor	1.23	1.1	1.87
Loss respect to the optimum (%)	0	-1.1	-7.3
Global radiation on collector plane (kWh/m²)	965	739	227
Bergen **Tilt angle 33°, nominal POA 747 kWh/m²**	Optimisation in summer	Year	Winter
Transposition factor	1.12	1.22	1.73
Loss respect to the optimum (%)	0	-1.1	-14.4
Global radiation on collector plane (kWh/m²)	747	955	210
Bergen **Tilt angle 68°, nominal POA 747 kWh/m²**	Optimisation in winter	Year	Summer
Transposition factor	2.02	1.15	0.99
Loss respect to the optimum (%)	0	-6.6	-11.8
Global radiation on collector plane (kWh/m²)	245	902	660

Table 2.3. Tilt optimisation for Trondheim photovoltaic devices over a year, in the summer (April-September) and in the winter (October-March).

Trondheim **Tilt angle 45°, nominal POA 879 kWh/m²**	Optimisation over a year	Summer	Winter
Transposition factor	1.28	1.13	2.17
Loss respect to the optimum (%)	0	-1	-8.3
Global radiation on collector plane (kWh/m²)	1124	849	275
Trondheim **Tilt angle 35°, nominal POA 879 kWh/m²**	Optimisation in summer	Year	Winter
Transposition factor	1.15	1.27	1.99
Loss respect to the optimum (%)	0	-1.3	-16
Global radiation on collector plane (kWh/m²)	859	1110	252
Trondheim **Tilt angle 70°, nominal POA 879 kWh/m²**	Optimisation in winter	Year	Summer
Transposition factor	2.37	1.2	1
Loss respect to the optimum (%)	0	-6.6	-12.5
Global radiation on collector plane (kWh/m²)	300	1050	750

The recorded nominal plane-of-array (POA) solar irradiance over a year has the same value for Oslo and Trondheim (879 kWh/m²), but a lower one for Bergen (747 kWh/m²). The reason could be attributed to the different climate conditions of the three areas e.g. Bergen is a very rainy city in Norway, thus cloud cover influences the irradiation values.

The optimisation in the winter leads to a higher tilt angle than optimisation in summer, because of different Earth position in its orbit round the Sun. As a result the transposition factor is maximized because diffuse component grows compared to the direct one.

Figures 2.9 - 2.11 show the optimisation of plane tilt and plane azimuth to obtain the maximum Transposition Factor in the whole year, summer and winter in Trondheim. Graphs for Oslo and Bergen are plotted in Appendix D. The optimisation for plane azimuth can be considered approximately 0°, which means the modules are facing the South.

In general, the tilt optimisation during the whole year can be considered generally the most convenient. In this case the global radiation on the collector plane obviously reaches the highest values. However, they are not too far from the values reported in case of optimisation in the summer. While the values for the winter optimisation are much lower (Tables 2.1 - 2.3).

The comparison between the three cities shows results very similar between each other, but they lead to one last consideration. The tilt angle needs to be higher for both winter and summer to gain more solar irradiation when modules are placed at locations with higher latitudes (Tables 2.1 - 2.3), because of inclination of Earth axis.
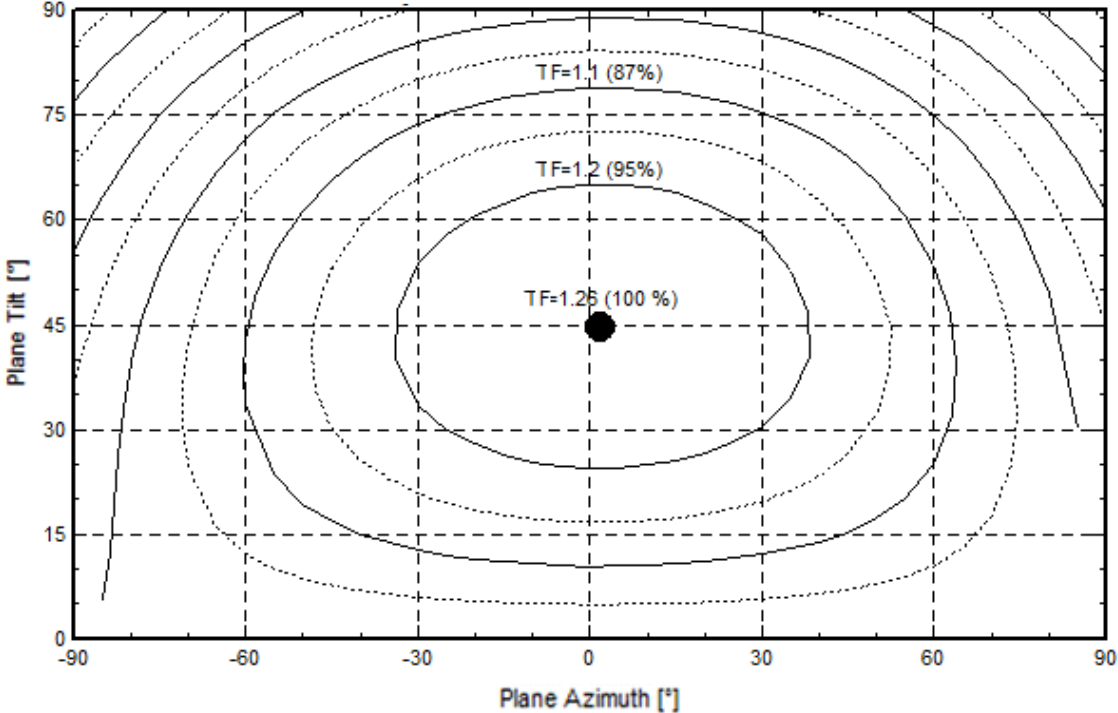
Fig. 2.9. Transposition factor variation as function of plane tilt and plane azimuth. Values during the whole year for Trondheim (plotted through PVsyst).
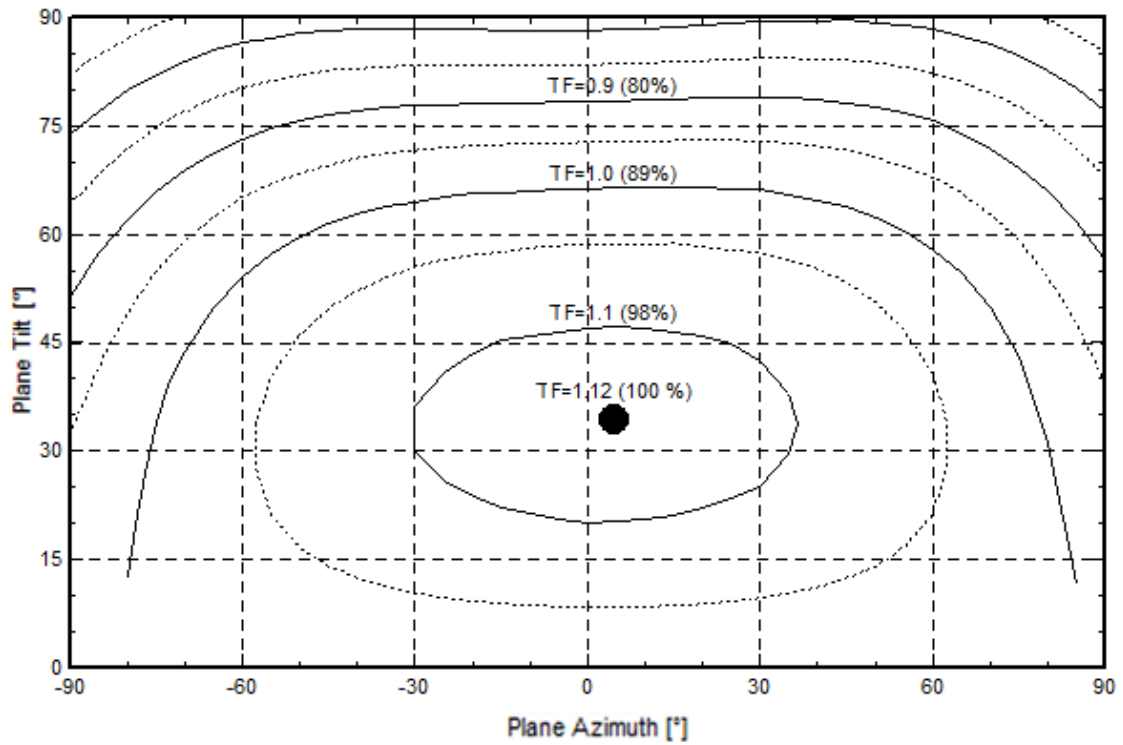
Fig. 2.10. Transposition factor variation as function of plane tilt and plane azimuth. Values during the summer for Trondheim (plotted through PVsyst).
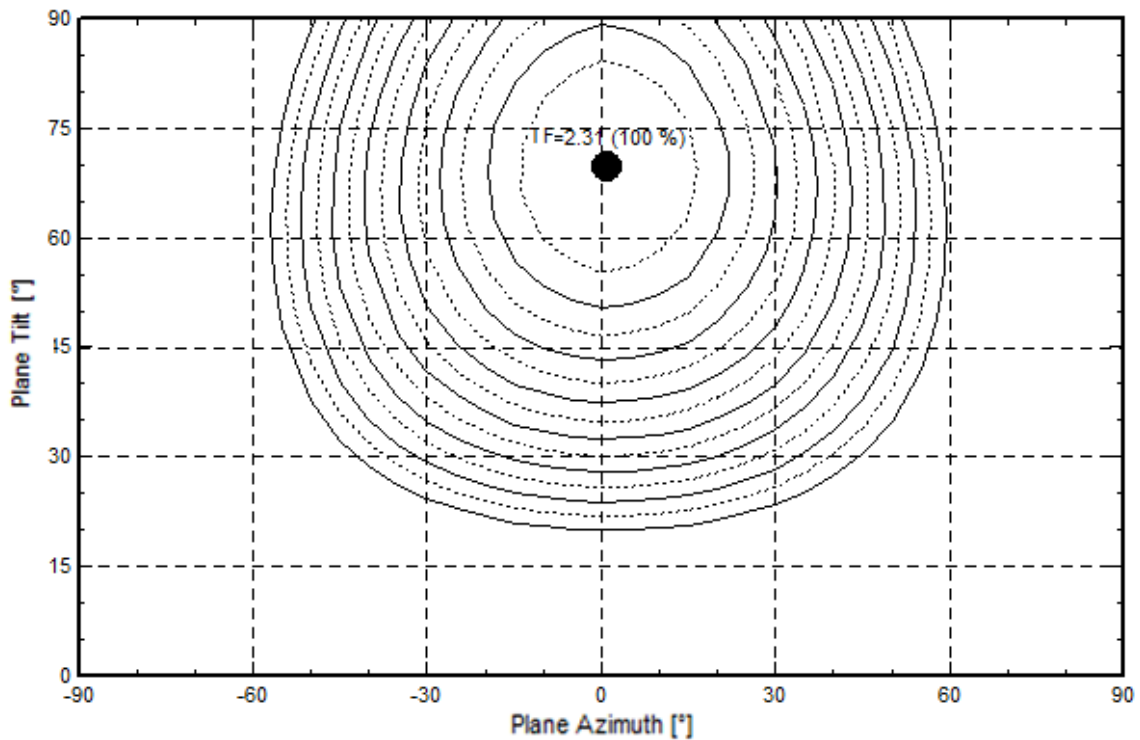
Fig. 2.11. Transposition factor variation as function of plane tilt and plane azimuth. Values during the winter for Trondheim (plotted through PVsyst).

The gain of the global component on the tilted plane compared to the global on a horizontal plane over a year in the different cases is summarized in Table 2.4).

Table 2.4. Percentage of solar irradiation gained tilting the plane for Oslo, Bergen and Trondheim.

	Oslo	Bergen	Trondheim
Optimisation over a year (%)	21	10	28
Optimisation in summer (%)	20	9	26
Optimisation in winter (%)	12	3	19

The previous results are altered if the snow coverage is considered in the global irradiation calculations. Assuming the same air temperature, snow depth values and number of days with snow, we can refer to graph given in Fig. 2.4 to recompute the previous percentages by considering a snow cover during half of the winter period proportional to the tilt angle of the plane. The new results can be summarized in Table 2.5.

Table 2.5 shows that the tilt angle chosen with the whole year optimisation is still the most adequate. However, similar results are obtained with the winter tilt angle. On the contrary, the summer tilt angle is the less convenient. These new results are due to the fact that a higher tilt angle helps the snow to slide from the panels.

Table 2.5. Percentage of solar irradiation gained tilting the plane for Oslo, Bergen and Trondheim. Snow cover during the winter time is considered.

	Oslo	Bergen	Trondheim
Optimisation over a year (%)	12	1	18
Optimisation in summer (%)	8	0	14
Optimisation in winter (%)	12	1	17

In conclusion, a project of PV-plant design should consider the presence of the snow during the winter months. In fact, this factor would lead to higher tilt angles. The study of Norwegian cities has been performed by choosing a moderate tilt angle, satisfying the optimisation over the whole year. However, similar values of irradiation gains have been reached also with a winter optimisation.

This study has been conducted for cities where snow cover is only from December to February, but different results could be obtained at locations where the snow period is longer. In that case, an optimum winter tilt angle could be chosen.

Unlimited sheds

When solar panels are placed on more sheds, the mutual shading obstructs part of the beam solar component, creating the so-called "shading loss" of energy production. The more the modules are tilted the more the shading loss grows. As a result, in this case a PV-array design with winter tilt angle is not advised, while the optimisation of tilt angle over a year should be taken into consideration.

The optimum tilt angle for the different cases of Oslo, Bergen and Trondheim previously found are now updated taking into account the presence of shadows (Table 2.6). The Table 2.6 also reports the shading loss associated with the different cases, considering a pitch of 5 m.

Table 2.6. Optimum angles calculated for a situation with and without shadows with the related shading loss for Oslo, Bergen and Trondheim.

	Optimum angle (without shadows)	Shading loss	Optimum angle (with shadows)	Shading loss
Oslo	42°	10.20%	32°	6.40%
Bergen	43°	10.80%	33°	7.90%
Trondheim	45°	12.80%	35°	9.70%

Figures 2.12 - 2.14 show the trend of the sheds plane tilt as function of the energy production over a year. The curve in green represents the trend of energy production related to the tilt angle. When shades are considered, the black curve represents the new values. We can notice how the vertex of the first curve is shifted to a lower tilt angle in the second curve. The difference on the y-axes of the two curves represents the shading loss.
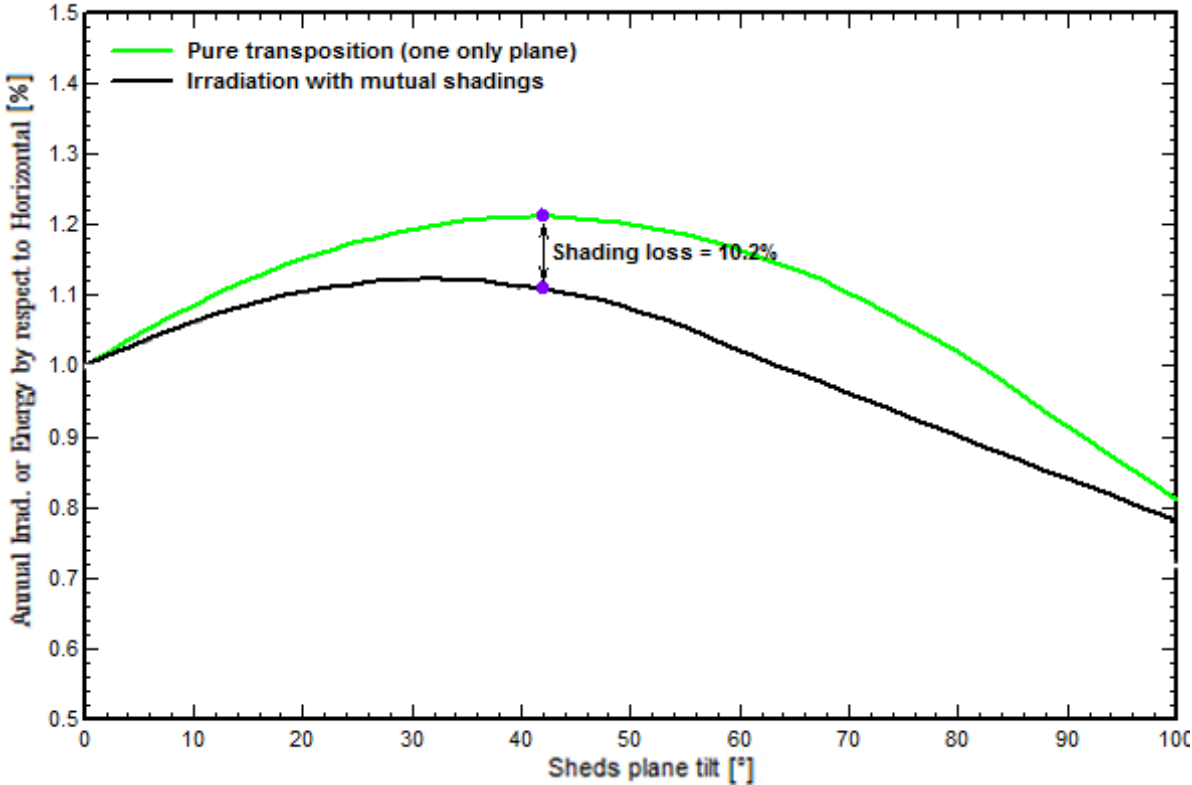
Fig. 2.12. Sheds plane tilt versus annual energy respect to horizontal in Oslo (plotted through PVsyst).
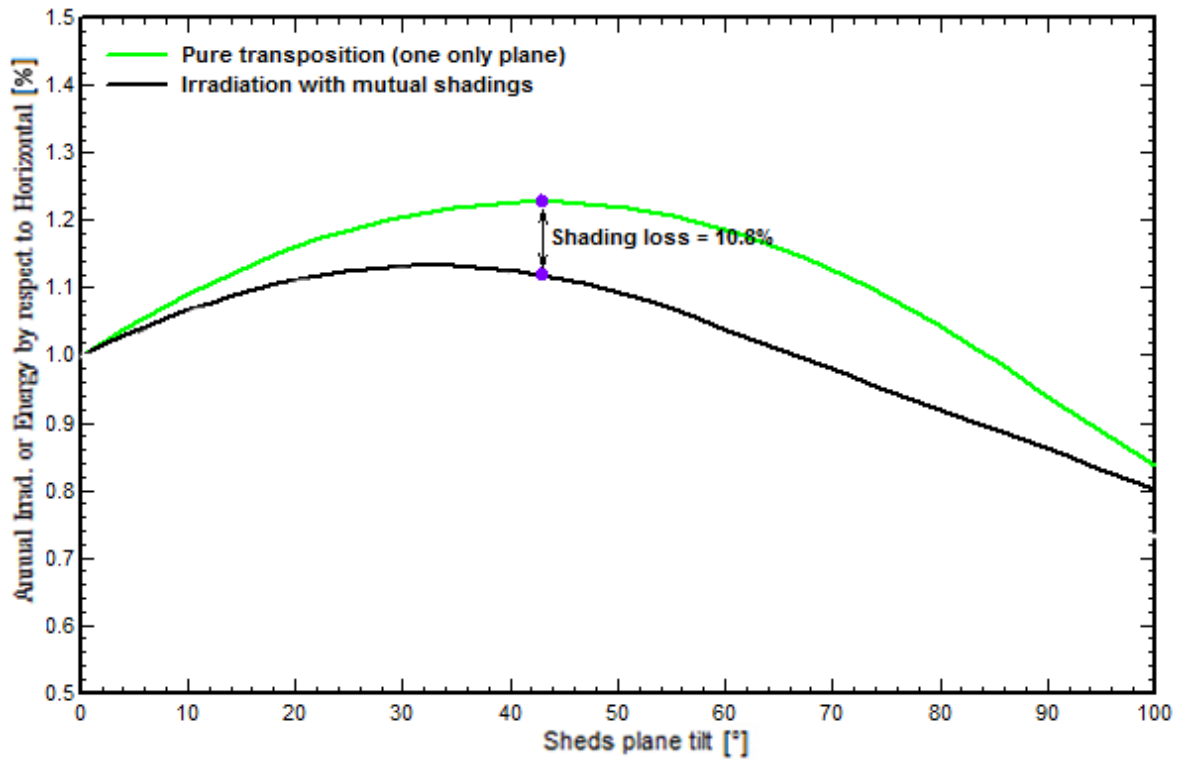
Fig. 2.13. Sheds plane tilt versus annual energy respect to horizontal in Bergen (plotted through PVsyst).
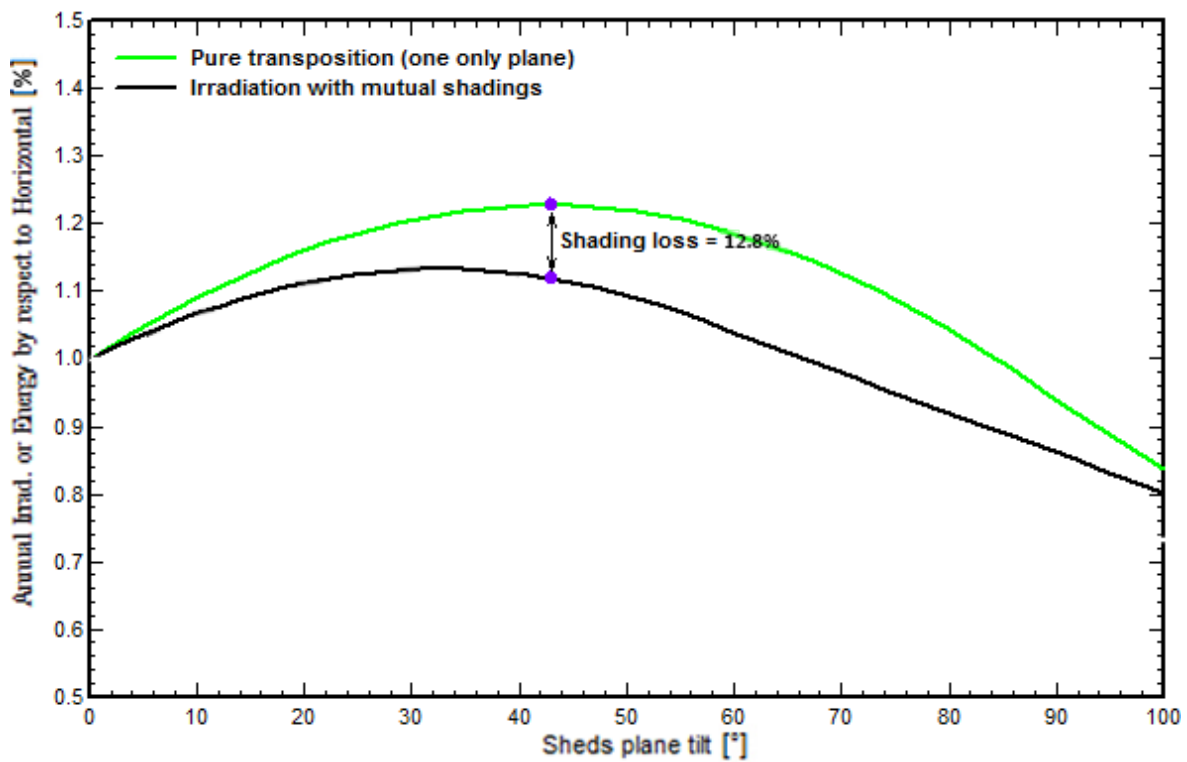
Fig. 2.14. Sheds plane tilt versus annual energy respect to horizontal in Trondheim (plotted through PVsyst).

The loss due to shading in the different months of the year with the new tilt configurations is represented in the Figs. 2.15 - 2.17. The limit profile angle is slightly different in the three cities. The graphs show how in the winter months the profile angle is lower; as a consequence the shading loss is increased.
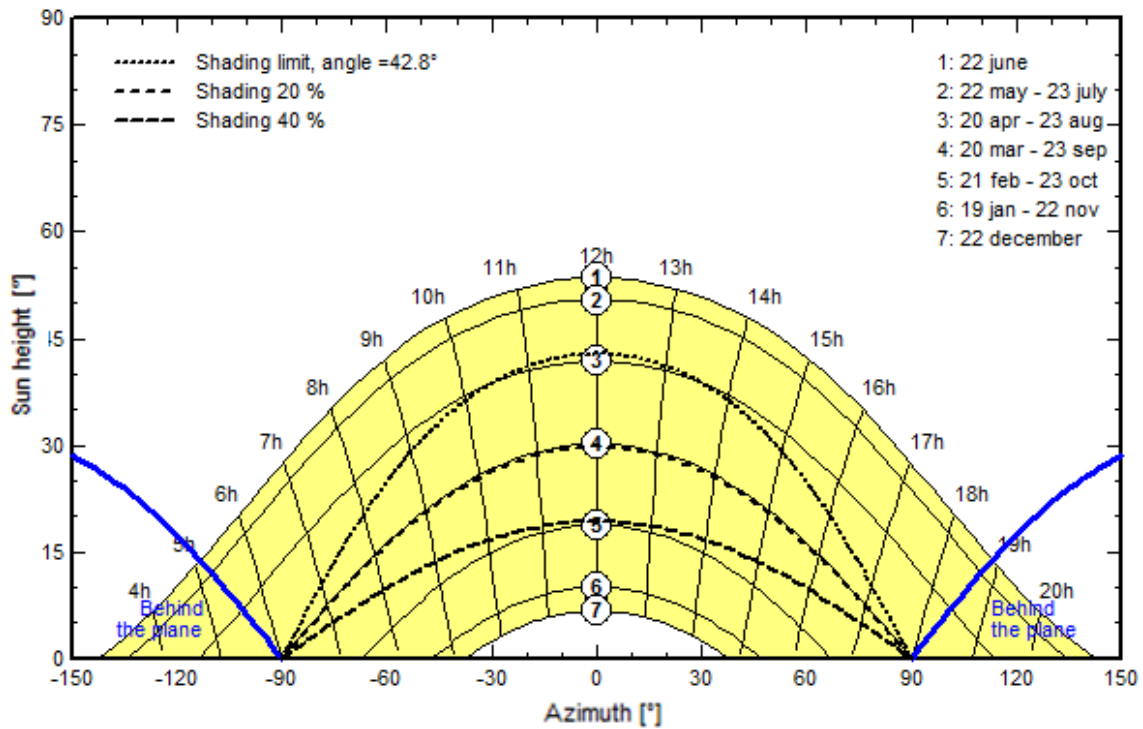
Fig. 2.15. Shed mutual shading in Oslo (59°55'; 10°45') in the sun paths diagram (plotted through PVsyst).
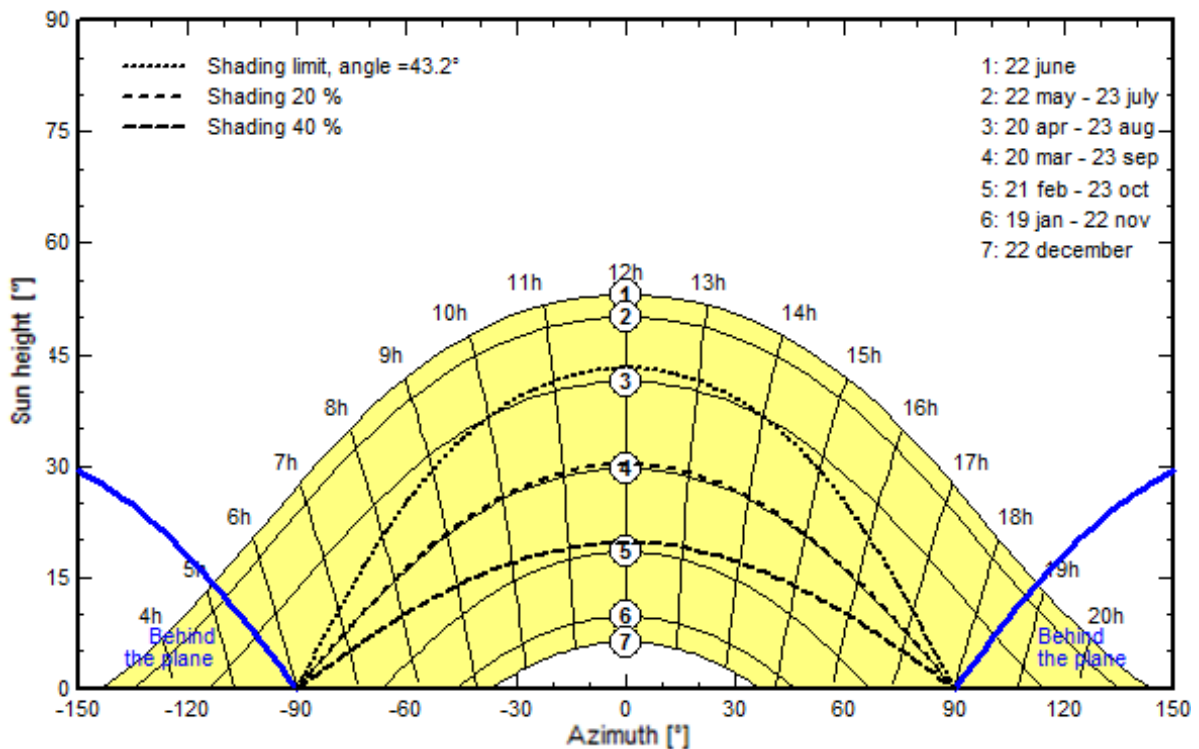
Fig. 2.16. Shed mutual shading in Bergen (60°39'; 5°33') in the sun paths diagram (plotted through PVsyst).
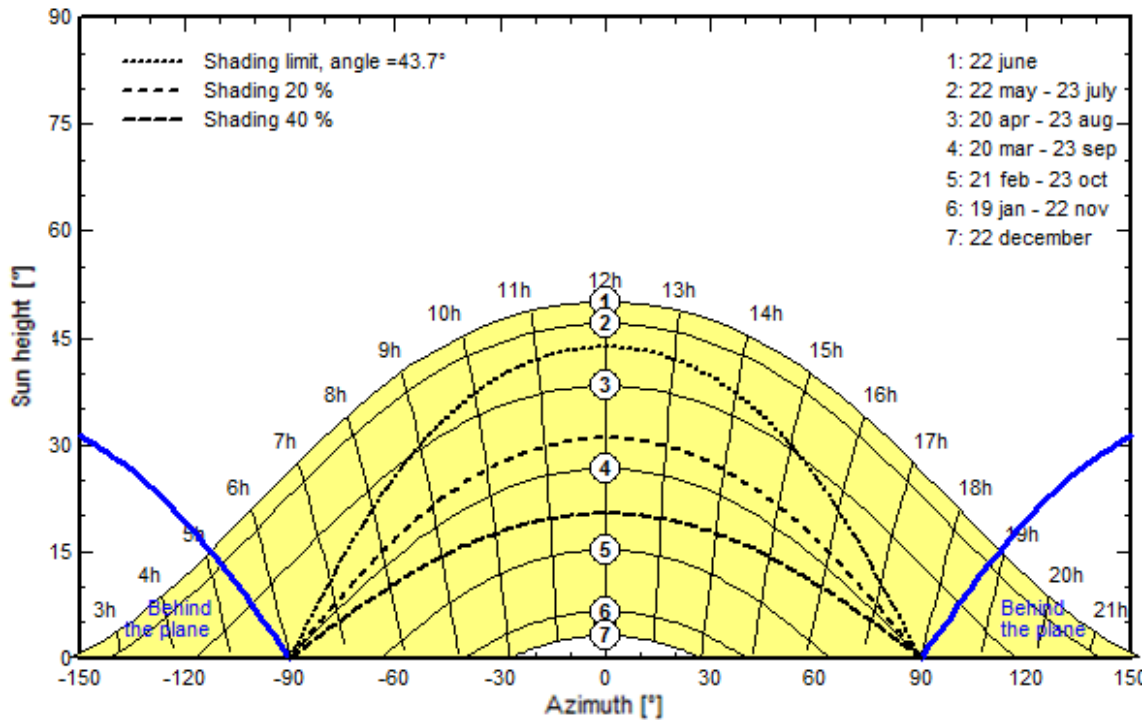
Fig. 2.17. Shed mutual shading in Trondheim in the sun paths diagram (plotted through PVsyst).

One last analysis has been conducted on the case with more sheds. Maintaining the previous tilt configuration (42°, 43°, 45° for Oslo, Bergen and Trondheim, respectively), the optimal distance between the sheds has been searched. A total avoidance of the shadows cannot be achieved; nevertheless the shadow loss can be reduced till values lower than 2%. The pitch distances to achieve this condition are collected in Table 2.7.

Table 2.7. Pitch distance to minimize the shading loss at defined tilt configuration in Oslo, Bergen and Trondheim.

	Tilt angle (°)	Pitch distance (m)
Oslo	42	18
Bergen	43	19
Trondheim	45	20

The calculated pitch distances in Table. 2.7 show very high values. Any rack-mounted or ground-mounted PV or BIPV plant could not respect these values because of obvious space limitations. Therefore, the most adequate solution is to consider the new configurations with lower tilt angles.

2.4.2 Electrical optimisation

The shading study will now be completed with electrical loss due to shading. As previously explained, PVsyst introduces the string diodes and module by-pass diodes in the simulations. The computation of electrical loss is added to the one of shading loss, therefore the final energy production varies.

The first analysis has been conducted changing the number of strings in the PV-plant configuration. Figs. 2.18 - 2.20 show how the curve, representing the shadow and electrical losses, suggests another optimum tilt angle, sliding its vertex to higher tilt angles.

Increasing the number of strings, the electrical loss decreases (Table 2.8). Similarly the orange curve rises in the graphs, towards the black one. In fact, electrical loss due to shading is being reduced, but not the shading loss (Fig. 2.18, 2.19, 2.20).
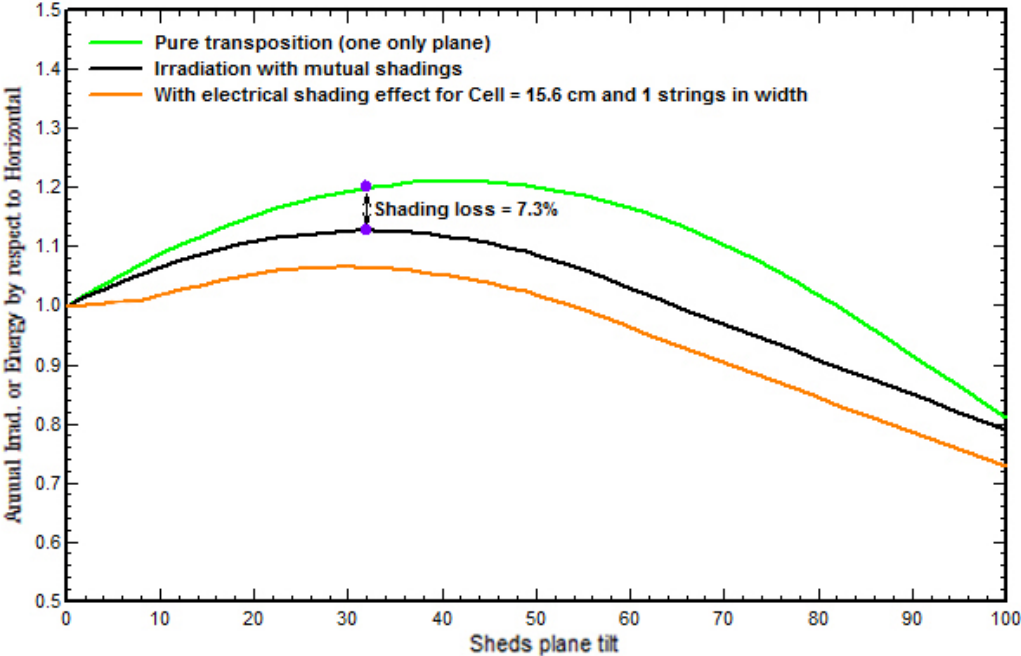
Fig. 2.18. Sheds plane tilt versus annual energy respect to horizontal in Oslo. The orange curve represents the shading and electrical loss in a one-string configuration (plotted through PVsyst).
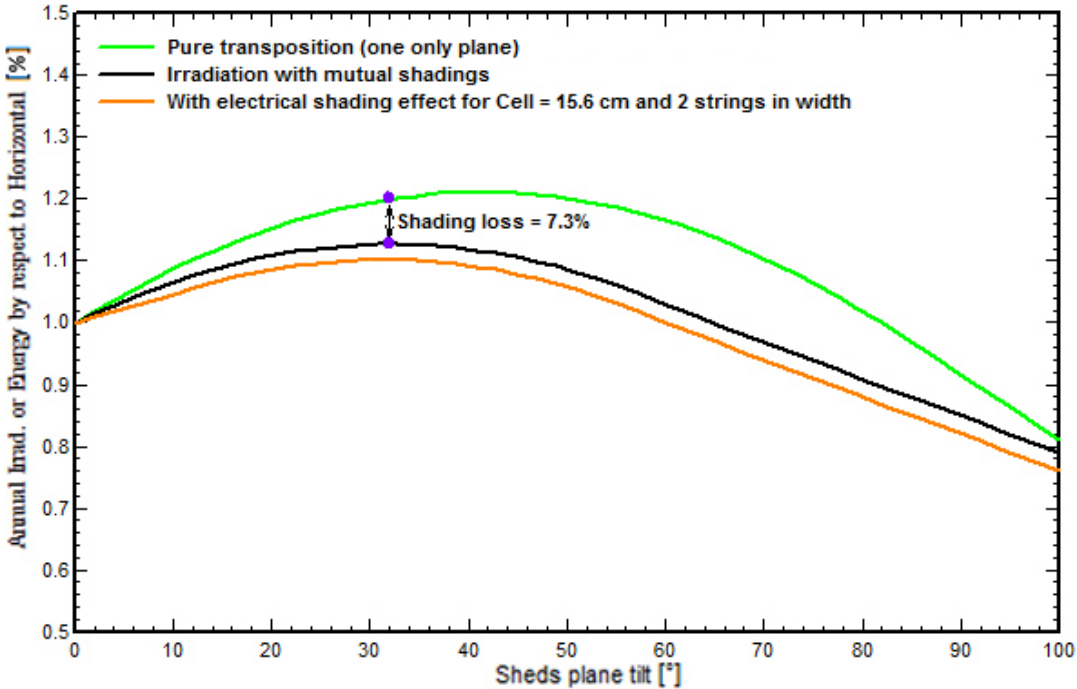
Fig. 2.19. Sheds plane tilt versus annual energy respect to horizontal in Oslo. The orange curve represents the shading and electrical loss in a two-string configuration (plotted through PVsyst).
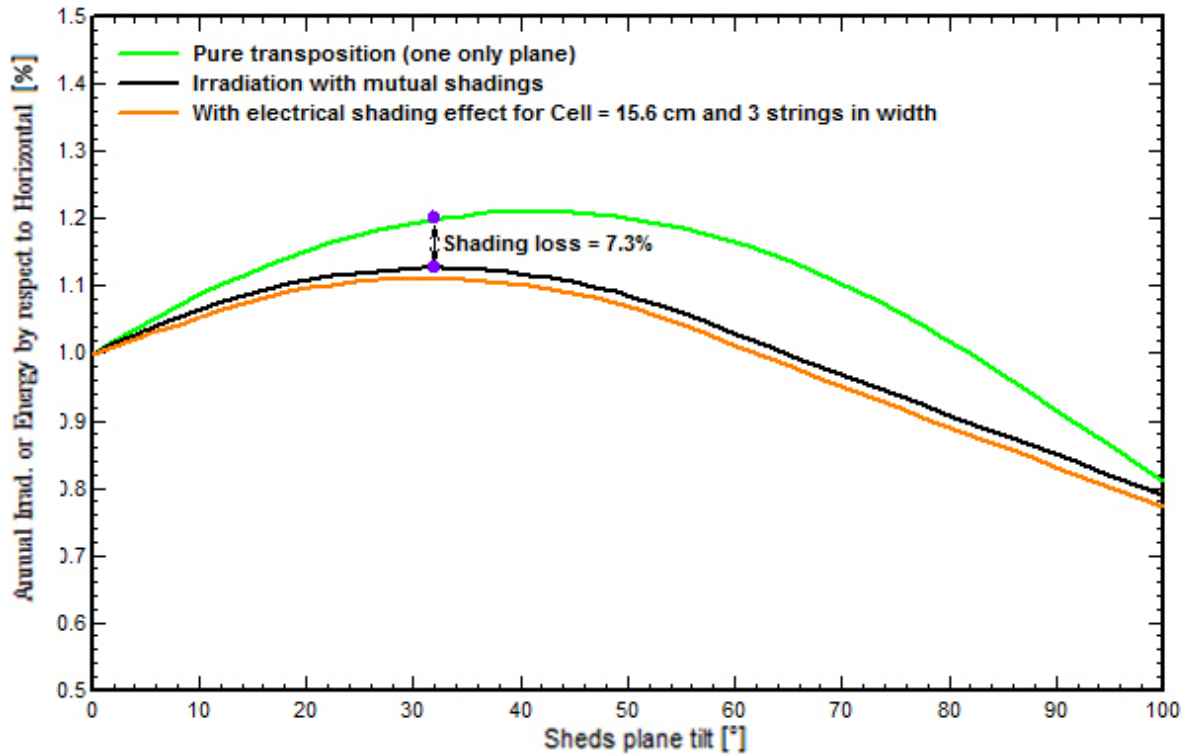
Fig. 2.20. Sheds plane tilt versus annual energy respect to horizontal in Oslo. The orange curve represents the shading and electrical loss in a three-string configuration (plotted through PVsyst).

In conclusion, the division of module rows into strings with diodes optimizes the system due to the limitation of the electrical loss due to shading.

Table 2.8. Electrical loss due to shading function of the tilt angle of the modules in Oslo, Bergen and Trondheim.

	Oslo		Bergen		Trondheim	
	Opt. angle	Elec. loss	Opt. angle	Elec. loss	Opt. angle	Elec. loss
1 string	29°	5.6%	30°	3.6%	30°	16.4%
2 strings	30°	2.3%	31°	1.4%	32°	7.2%
3 strings	31°	1.3%	32°	0.9%	34°	4.9%
Inf. strings	32°	0%	33°	0%	35°	0%

The second analysis has been conducted changing the number of module by-pass diodes in the PV-plant configuration. The electrical loss was calculated considering the previous system with 3 string diodes. The effect of the module diodes is summed to the effect of the string diodes in the electrical loss values.

The simulations were launched considering the same system with a variable number of module diodes (1, 2, 3). The values of electrical loss are summarized in Table 2.9.

Table 2.9. Electrical loss of PV systems with 1,2,3 bypass diodes placed in Oslo, Bergen and Trondheim.

	Oslo (%)	Bergen (%)	Trondheim (%)
1 diode	1.3	0.9	4.9
2 diodes	1.2	0.8	4.6
3 diodes	1.1	0.8	4.1

The use of module bypass diodes is definitely beneficial for the PV-plant because reduces the electrical effect due to the presence of shadows.

2.5 Conclusions

A study of the influence of snow in designing a photovoltaic (PV) plant geometrically and electrically has been conducted.

In snowy places the optimum tilt angle of the modules should be calculated considering the snow cover during the wintertime. A higher tilt angle can lead to energy benefits because of the increment of snow sliding off the panels.

The analysis of a Norwegian case study showed that to harvest the maximum solar energy during the whole year a moderate tilt angle is the most beneficial, but slightly superior of an elevated tilt angle. The same study conducted at locations where the snowfalls period is longer and solar irradiation in winter time is more intensive would lead to a preference of high tilt angles.

If a building integrated photovoltaic (BIPV) roof plant is considered, the choice could also lead to a high tilted roof. In fact the solar irradiation is surely more required during the winter than in the summer, so that the necessity of heating is reduced.

Considering the case of a PV system organized into more sheds, the tilt angle should not be too high because it would increase the energy loss due to shading. A new optimum tilt angle has to be recalculated taking into account the shadows.

The last considerations regard the reduction of electrical loss due to shading. In fact, the study showed how the division of the PV-plant into strings with diodes and the use of bypass diodes in the modules increased the energy production.

2.6 References

M. J. Ahmad, G. N. Tiwari, "Optimisation of tilt angle for solar collector to receive maximum radiation", *The Open Renewable Energy Journal*, **2,** 19-24, 2009.

K. Bayard, "Three tips for designing solar arrays in snowy areas", *SolarDock*, 2015, available at www.solardocks.com/designing-solar-for-snow/

M. Benghamen, "Optimisation of tilt angle for solar panel: case study for Madinah, Daudi Arabia", *Applied Energy*, **88**, 1427-1433, 2011.

N. Heidari, J. Gwamuri, T. Townsend, J. M. Pearce, "Impact of snow and ground interference on photovoltaic electric system performance, *IEEE Journal of Photovoltaics*, **5** (6), 1680-1685, 2015.

C. Honsberg, S. Bowden, Hot Spot Heating. URL: http://pveducation.org/pvcdrom/modules/hot-spot-heating, 2011.

O. S. Idowu, O. M. Olarenwajy, O. I. Ifedayo, "Determination of optimum tilt angles for solar collectors in low-latitude tropical region", *International Journal of Energy and Environmental Engineering*, **4** (29), 2013.

B.P. Jelle and C. Breivik, "State-of-the-art building integrated photovoltaics", *Energy Procedia*, **20**, 68-77, 2012.

A. K. Yadav, S. S. Chandel, "Tilted angle optimisation to maximize incident solar radiation: a review", *Renewable and Sustainable Energy Reviews*, **23**, 503-513, 2013.

H. Yang, H. Wang, M. Wang, "Investigation of the relationship between reverse current of crystalline silicon solar cells and conduction of bypass diode", International Journal of Photoenergy, 1–5, 2012.

B. Marion, R. Schaefer, H. Caine, G. Sanchez, "Measured and modelled photovoltaic system energy losses from snow for Colorado and Wisconsin locations", *Solar Energy,* **97**, 112-121, 2013.

Northern Alberta Institute of Technology (NAIT), Alternative Energy Program, Solar Photovoltaic Reference Array Report, March 2015.

I. Prontes, "What Is a Blocking Diode?" http://www.ehow.com/about_4697360_what-blocking-diode.html, 2013, accessed on the 9th of August.

PVsyst 6 Help, Project Design > Plane Orientation > Orientation Optimisation, http://files.PVsyst.com/help/orientation_optimisation.htm, accessed on the 9th of August.

Sargosis Solar & Electric, "How Shade Affects a Solar Array". http://sargosis.com/articles/science/how-shade-affects-a-solar-array/, 2012, accessed on the 9th of August.

Solar-Facts, "Blocking and by-pass diodes used in solar panels". http://www.solar-facts.com/panels/panel-diodes.php, 2012, accessed on the 9th of August.

Solar-Facts, "Blocking and by-pass diodes used in solar panels", http://www.solar-facts.com/panels/panel-diodes.php, 2012, accessed on the 9th of August.

3 Modeling snow loss

3.1 Abstract

One of the major causes that limit the energy production of photovoltaic (PV) devices in high-latitude countries is the snow coverage in wintertime. The energy loss due to the presence of snow on the modules is thus called "snow loss".

Marion et al. (2013) developed an algorithm to predict snow cover on PV panels. Its utility is connected to the possibility of calculating snow loss of a photovoltaic (PV) system, which is not negligible in Nordic countries. This algorithm was implemented in System Advisor Model (SAM) by National Renewable Energy Laboratory (NREL), a U.S. software that presents several limits in components and weather databases and PV models. PVsyst is a software widely used for PV simulations. It offers several tools and enables a more accurate description of the plant.

A new method was used to calculate snow losses. It is based on Marion's algorithm, whose results are integrated in PVsyst ones. The method was applied to the system mounted on the ZEB (The Research Centre on Zero Emission Buildings) Living Lab, a building set in the Norwegian Institute of Science and Technology (NTNU) campus in Trondheim. The same plant was supposed to be in Oslo and Bergen, so that other simulations were launched considering different weather conditions to compare results.

50

3.2 Introduction

3.2.1 Background

One of the major causes that limit the energy production of photovoltaic devices in high-latitude countries is the snow coverage in wintertime. The energy loss due to the presence of snow on the modules is called "snow loss". This one is often considered generically as "soiling loss", together with dirt and dust (Maghami et al. 2016). This approximation can be done in countries were a thin snow coverage that soon melts can be neglected, whereas in high-latitude countries snowfall is a serious problem to take in consideration.

In recent years scientists have tried to predict snowfall and to model snow presence on PV panels, in order to evaluate snow influence on production. Different results have been collected, because snowfall frequency is strongly affected by climate and location. Other difficulties are due to the variability of snow accumulation phenomenon (Pfister and Schneebeli 1999; Becker et al. 2007), influenced by weather and array design factors:

- wind speed,
- type of snow,
- global radiation,
- ambient temperature and module temperature,
- atmospheric humidity (microclimate),
- inclination of the horizontal,
- surface properties,
- type of mounting system (specific characteristics),
- set-up of the modules,
- distance of the modules to the ground.

Concerning type of snow factor, snow and ice can accumulate on a PV array in a number of physical forms (Ross 1995):

- dry snow deposition, characterized by low moisture content;
- wet snow accretion, characterized by high moisture content;
- rime, which occurs when supercooled water droplets impinge on a structure and freeze before forming a continuous liquid layer;
- glaze, which occurs when rain or supercooled water droplets deposit on a structure and freeze after forming a continuous liquid layer;
- hoarfrost, which occurs when supercooled or supersaturated water vapour encounters a nucleating surface and forms crystals.

In general, dry snow melts off, slides off or blows off PV panels fairly quickly, and thus is not considered the major problem for PV energy production. On the contrary, a wet snowfall followed by very cold weather appears most likely to result in a long-lived deposit of snow on the array. Rime may accumulate in the late autumn and not melt off until the spring, effectively stopping the PV energy production for the winter. Glaze does not appear to be a serious problem in the operation of PV arrays, since it transmits considerable light and, in most places, is followed by warm temperatures. Finally hoarfrost formation is an event that occurs rarely (Ross 1995).

In conclusion snow accumulation on a plane is a phenomenon hard to predict. Scientists have developed different models simplifying it, in general taking into account only few of the previous factors and considering a generic kind of snow. In spite of all these approximations,

researchers have created some reliable models. These ones can be studied and improved to perform realistic applications, modifying them concerning the case studied.

3.2.2 Modeling snow loss

3.2.2.1 Literature review

The first study about snow effects was performed by Brench (1979) in Utah. A simple linear empirical correlation was used to determine expected PV output and to evaluate snowfall losses. Different daily loss values were found for snow depth higher and lower than one inch for 30° and 40° tilted modules.

Ross (1995) developed a C++ code to predict module temperature. Snow coverage is assumed to start to clear when the module reaches a temperature of 0°C, as a consequence energy production is set different to zero.

A study to evaluate the impact of snow on the yield of grid-connected PV systems was conducted by Becker et al. (2006) in Munich. A PV-plant was installed and energy production had been monitored for six years. As a result the yearly lost yield by snow covered modules was estimated to be between 0.3 and 2.7%. As far as energy loss values are strongly connected to PV panels' collocation, this result cannot be generalized.

A PV test bed with different-inclinations modules was installed in California near Lake Tahoe by Powers et al. (2010). The aim of the study was to create a model that predicted snow loss in function of module's tilt angle and snow depth values. A first result reached was an empirical correlation:

$$T_{snow} = 0.1 * sd * \cos^2 \beta \tag{3.1}$$

where T_{snow} is the annual percentage loss for Truckee region (%), sd is snow depth (inches) and β is the tilt angle of the module (°).

Observation of Truckee's test bed data collection has continued for another year. At the end of this period researchers generalized the model to make it applicable also in other locations (Townsend and Powers 2012):

$$E_{loss} = 5.7 * 10^4 * Se' * \cos^2 \beta * GIT * \frac{RH}{T_{air}^2 * POA^{0.67}} \tag{3.2}$$

where E_{loss} is the annual percentage loss (%), Se' is the six-week rolling average of Se (inches), β is the tilt angle of the module (°), GIT is the ground interference term, RH is the average monthly relative humidity (%), T_{air} is the average monthly air temperature (°C), POA is the monthly plane of array insolation (kWh/m²).

Se and GIT are defined as:

$$Se = \frac{SD * (1 + \frac{1}{n})}{2} \tag{3.3}$$

$$GIT = 1 - 0.5^{(-\delta)} \tag{3.4}$$

where SD is monthly snow depth (inches), n is the number of snow events in a month and δ is another coefficient:

$$\gamma = \frac{r * Se' * \cos\beta}{\frac{h^2 - Se'^2}{2} * \tan\alpha} \tag{3.5}$$

where r is the row plane of array dimension (inches), h is the drop height from array edge to ground (inches) and β is the piled snow angle (assumed 40°).

Andrews et al. (2013) monitored a multi-angle and multi-technology PV system to understand the effects of snowfall on the performance of PV systems. Snow loss was derived by comparison between predicted and actual output of photovoltaic devices. Prediction was developed through a model previously described by the same authors (Andrews et al. 2012), that uses as input data measured global and diffuse irradiation, meteorological data (ambient temperature, relative humidity, wind speed, precipitation), module performance and module temperature. Accumulation and shedding of snow on modules was analyzed through time-lapse digital photography. Townsend and Powers energy loss model (2012) was applied to data collected by Andrews et al. (2013). It was found that this algorithm tended to under-predict the effects of snowfall on the system.

3.2.2.2 Marion's snow model

Considerable progress in snow loss prediction has been done by Marion et al. (2013). Six PV systems situated with different tilt angle (from 15° to 35°) and different array types (roof-mounted and rack ground-mounted) were monitored in different locations (Colorado and Wisconsin) to collect PV performance data. Key data recorded were also: snow depth, digital images of the PV arrays to assess snow coverage and plane-of-array (POA) solar irradiance.

The measured energy snow loss E_L was obtained by the following:

$$E_L = E_E - E_M \tag{3.6}$$

where E_E is an estimated energy production value and E_M is the measured energy production value.

The estimation of energy production is determined through another equation, previously found by Marion et al. (2013):

$$E_E = P_0 * H * PR_{25} * [(1 + \gamma * (T_w - 25)] \tag{3.7}$$

where P_0 is the nameplate DC power (kW), H is the total in-plane irradiance (kWh/m²), PR_{25} is system performance ratio for 25°C PV module temperature, γ is power correction factor for temperature ($°C^{-1}$) and T_w is irradiance-weighted PV module temperature (°C).

PR_{25} was empirically determined when snow was absent as function of daily irradiance for each PV system observed.

The irradiance-weighted PV module temperature is determined by:

$$T_w = \left(\sum T_i * G_i\right) / \left(\sum G_i\right) \tag{3.8}$$

where G is the POA irradiance (W/m²), T is PV module cell temperature (°C) and i is the index for individual hourly measurement.

The PV module cell temperature is calculated by (King et al. 2004):

$$T = G * e^{-3.56 - 0.075 * WS} + T_a + G * 3/1000 \qquad (3.9)$$

where WS is wind speed (m/s) and T_a is ambient air temperature (°C).

The modeled energy snow loss is found following the pseudo code described in Table 3.1.

Table1 3.1. Pseudo code used in Marion et al. (2013) snow model.

INPUT	Yesterday's and today's snow depth (sd), today's daytime hourly values for *G, Ta*, and *WS*
OUTPUT	Calculated daily energy production for "with snow" (E_w) and "without snow" (E_{w0})
Step 1	If today's sd > yesterday's sd Set PV snow amount = 10 tenths (100% snow) Else Set PV snow amount = Yesterday's end amount
Step 2	Initialize daily energy productions E_w and E_{w0} to zero
Step 3	For each daytime hour:
Step 4	If *Ta - G/m' > 0* Decrease PV snow by Fig.3.3 amount. (where *m'* is the slope of line from Fig. 3.1, that is -80 W °C /m²)
Step 5	Determine number of PV strings with PV modules not covered with snow
Step 6	Model energy produced for *G, Ta*, and *WS* for PV strings with PV modules not covered with snow, add to *Ew*
Step 7	Model energy produced for *G, Ta,* and *WS* for a no snow condition, add to E_{w0}
Step 8	OUTPUT E_w and E_{w0}
Step 9	GOTO next day

The discriminating equation

$$Ta - G/m' > 0 \qquad (3.10)$$

used to predict snow sliding phenomenon was found combining hourly POA irradiance (*G*) and air temperature (*Ta)* with hourly digital images taken of snow coverage on the rack ground mounted PV system (Fig. 3.1). *m'* is the slope of line from Fig. 1, that is -80 W °C /m². On the contrary, roof-mounted PV system respected this equation only from 25% to 50% of times. In fact, once arrays were partially uncovered, the accumulated snow at the base of the panels impeded further snow sliding (Fig. 3.2).

Fig. 3.1 summarizes snow sliding information about two different phenomena that leave snow on a PV surface: insufficient frictional forces and freezing.
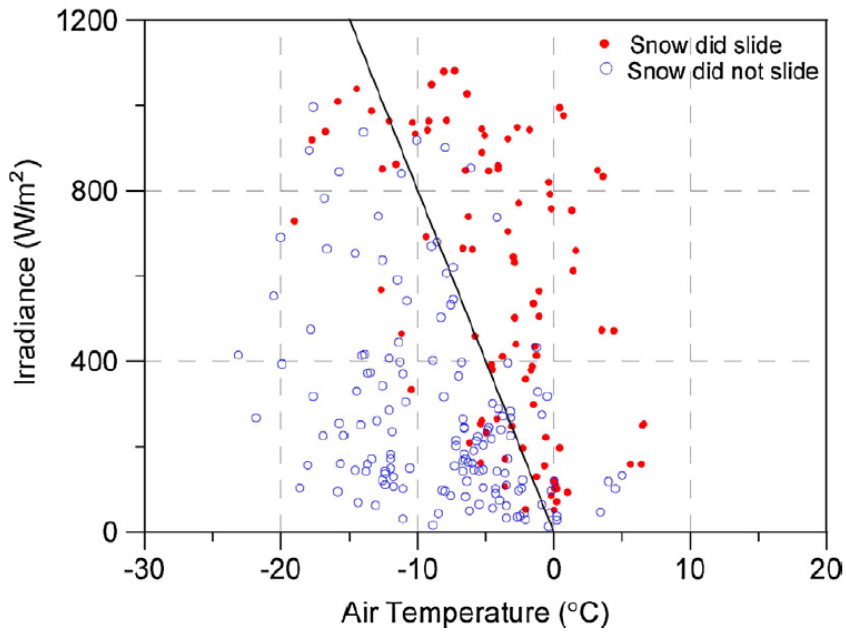
Fig. 3.1. Combinations of hourly irradiance and temperature for the LafWater PV system for which the snow did (red dots) or did not (blue circles) slide some amount down the PV panel. The line is an estimate of the dividing line for conditions that will (to the right of the line) or will not (to the left of the line) permit snow to slide down the PV panel or module (Marion et al. 2013).
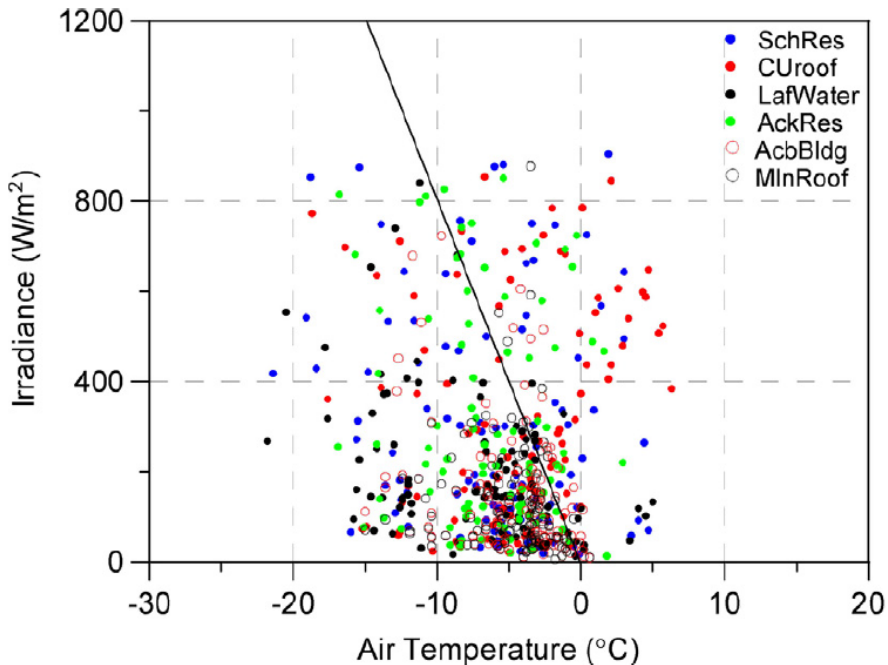
Fig. 3.2. Combinations of hourly irradiance and temperature for all the PV systems for which the snow did not slide. Data to the right of the diagonal line indicate that snow expected to slide did not. PV modules were 100% covered with snow at the beginning of the hour (Marion et al. 2013).

55

In the first case snow sliding occurs when the sliding force due to gravity F_s is greater than the frictional force F_f. These two can be explicated by:

$$F_s = mg \sin \beta \tag{3.11}$$

$$F_f = \mu \, mg \, \cos \beta \tag{3.12}$$

where m is the mass of snow, g is the acceleration of gravity, β is the tilt angle and μ is the static coefficient of friction of wet or dry snow.

In conclusion snow slides when

$$\mu < \tan \beta \tag{3.13}$$

In the second case snow sliding occurs when the module-snow interface temperature reaches 0°C and the snow-ice begins melting. When it melts, snow slides away because coefficient of friction is low enough.

Fig. 3.3 shows a different linear relationship between snow amount sliding away and the sine of the tilt angle β for roof-mounted systems and ground rack-mounted systems.
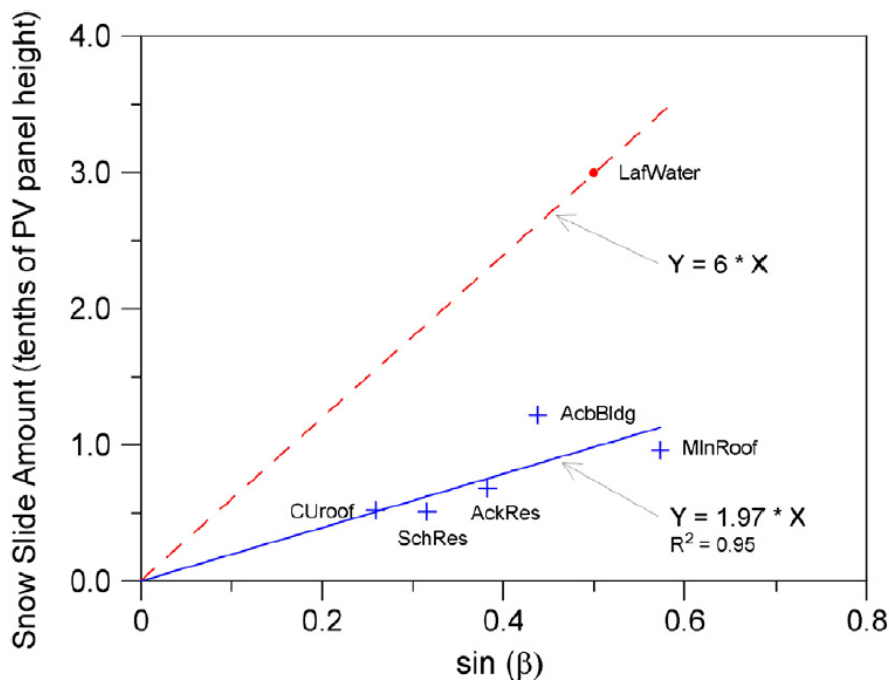
Fig. 3.3. Linear relationships between the sine of b and the snow slide amount for the hours when a snow slide is estimated for roof mounted systems (blue) and ground rack-mounted PV systems with adequate ground clearance (red) (Marion et al. 2013).

Snow slide amount s (tenths of PV panel height) is equal to:

$$s = k \sin \beta \tag{3.14}$$

where k is a coefficient (1.97 for roof-mounted systems; 6 for ground rack-mounted systems) and β is the tilt angle.

In the first case these empirical relationships are confirmed by the previous explanation. In the second case we can consider that in winter time increasing β raises the POA irradiance and, as a consequence, snow temperature.

Marion's model was validated through a comparison between measured and modeled monthly loss (Fig. 3.4). On average the model worked well, with a standard deviation of the differences between the two losses equal to 10.5%.
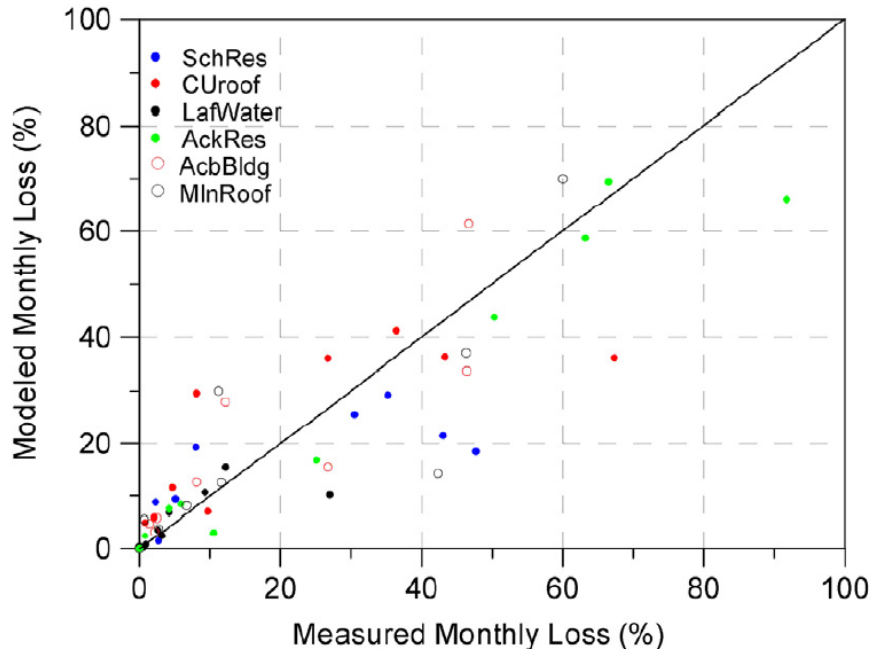
Fig. 3.4. Scatter plot of modeled versus measured monthly PV system energy losses due to snow for November 2010–March 2011 and November 2011–March 2012. Diagonal has slope of one. Data above the diagonal indicate model estimates are too great, and vice versa (B. Marion 2013).

3.2.2.3 Implementation of Marion's model in System Advisor Model

Nowadays different computer software are used to predict energy production of photovoltaic devices (PVsyst, Solarius, RETScreen, etc.). Although they base their prediction on a sophisticated calculus, they are not able to evaluate energy loss due to snow. The first PV software that has been integrated with PV snow loss model is System Advisor Model (SAM) by National Renewable Energy Laboratory (NREL) (Ryberg and Freeman 2015).

Sam was implemented with Marion's model as following (Ryberg and Freeman 2015):

"At the beginning of each day, the model checks to see if a snowfall has occurred during that day. If it has, the model assumes that the PV array being simulated will be completely covered by snow. If a new snowfall is not detected, the coverage is left at its value at the end of the previous day. For each hour in the day, the array will remain covered unless the plane of array irradiance and ambient temperature are sufficient to allow some of the accumulated snow to slide off the PV array. More specifically, snow sliding will only occur so long as the following inequality is satisfied:

$$Ta - G/m' > 0 \qquad (3.10)$$

where *Ta* represents the ambient temperature, *G* represents the plane of array irradiance, and *m* represents Marion's empirically defined value -80 W/(m² °C). If the model determines that sliding is possible during a particular hour, then the amount of the PV array that will be exposed in that hour, measured in tenths of a row's total height (see Fig. 3.3), is a function of the PV system's tilt.

The amount that will be exposed, in tenths of total row height, can be found using:

$$s = 1.97 * \sin \beta \tag{3.15}$$

The 1.97 constant in this equation was experimentally determined by Marion et al. (2013) for roof-mounted systems in units of tenths of PV row height per hour, and will be referred to as the sliding coefficient. At the end of the hour during which the calculation permits sliding, the initial PV snow coverage will be decremented by the snow slide amount. Finally, given the new height of snow relative to the PV row's total height, and the configuration of PV strings in a row, the number of PV strings within the system which are not covered with snow is determined. These modules are allowed to operate normally while the energy production of the covered strings is set to zero. The model then moves on to the next hour in the day and repeats this process."

Marion's model implementation was completed preventing the coverage from going below 0% and including threshold values for minimum depth and minimum change in depth (delta), in order to reduce data measurement uncertainty) (Ryberg and Freeman 2015).

SAM snow loss calculus is allowed by the 1961-1990 National Solar Radiation Database (NSRDB) data set integrated in the software. This data set contains hourly meteorological weather data (including daily snow depth measurements) for 239 locations across the United States, collected since 1961 till 1990.

Marion's model was validated on energy production data collected by Forrestal system, located on the James Forrestal Building in Washington, D.C., and the RSF2 system, located on NREL's Research Support Facility in Golden, Colorado, with tilted angle of 0° and 10° respectively. Monthly energy has been simulated and measured; the comparison is displayed in Fig. 3.5 and 3.6.

Error calculations have been performed using:

$$Error = \frac{Simulated - Measured}{Measured} * 100\% \tag{3.16}$$

while reduction in absolute annual error were calculated using:

$$\begin{aligned} Abs.\ Annual\ Error \\ = \frac{(|Without\ Model| - |With\ Model| * Measured\ Monthly\ Energy}{Measured\ Annual\ Energy} \end{aligned} \tag{3.17}$$
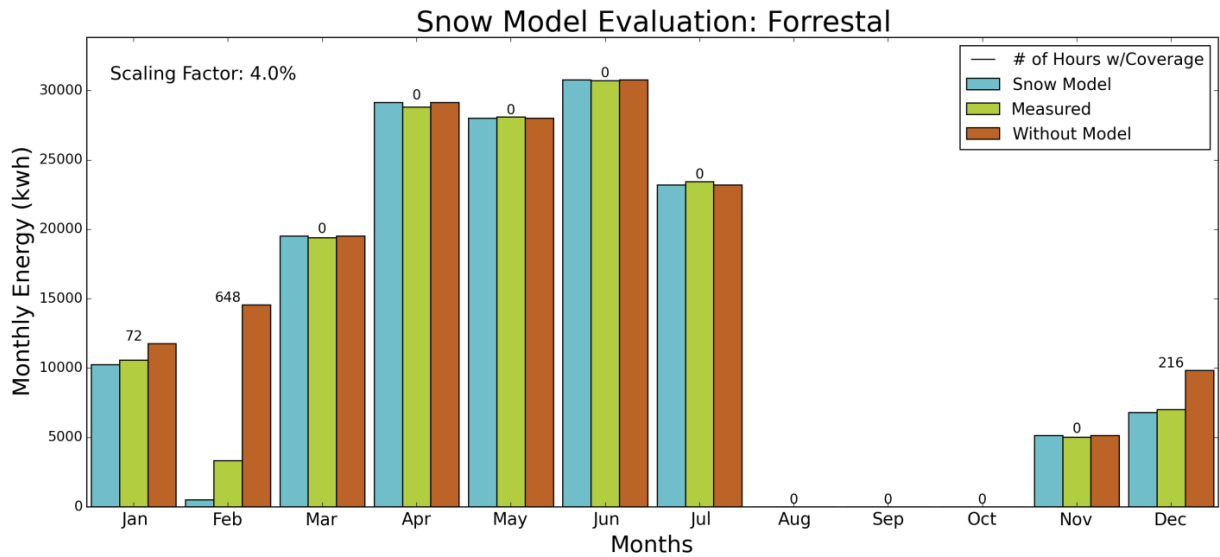
Fig. 3.5. Results from the validation study using the RSF2 system in Golden, Colorado (Ryberg and Freeman 2015).
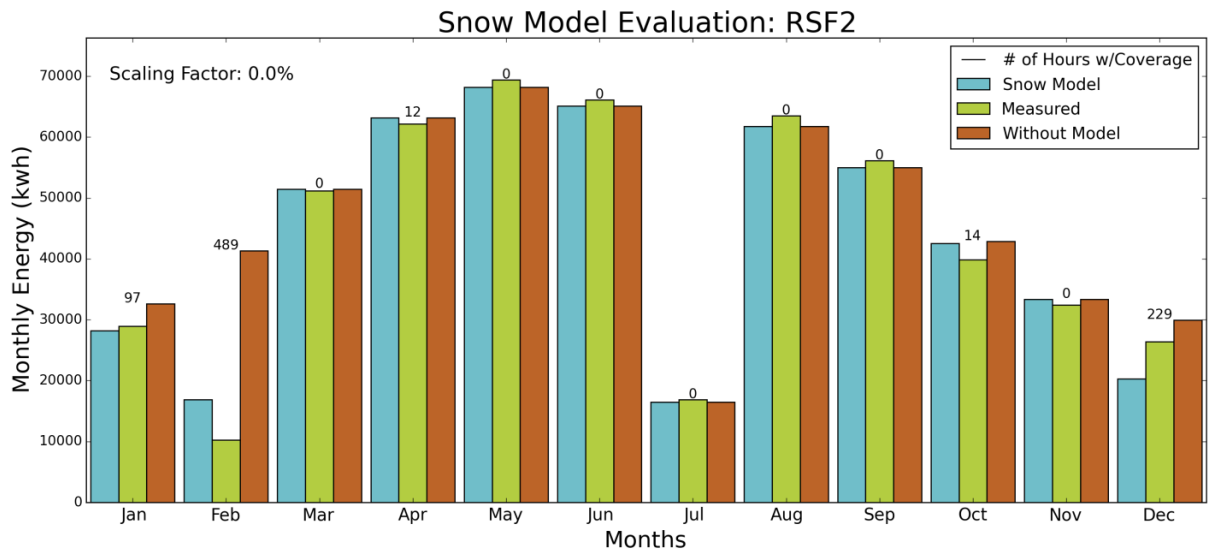
Fig. 3.6. Results from the validation study using the Forrestal system in Washington D.C and the RSF2 system in Golden Colorado (Ryberg and Freeman 2015).

Results in Table 3.2 show over-prediction and under-prediction energy estimation on a monthly, daily or hourly basis, while annual results are more faith to reality. As a matter of fact Marion's model is strongly reliable only on an annual scale, a monthly study can always be helpful to obtain approximate values.

Table 3.2. Monthly and annual errors with and without snow model (Ryberg and Freeman 2015).

		January	February	December	Annual
Forrestal	With model (%)	-2.9	-85.0	-3.0	-1.0
	Without model (%)	11.3	337.6	40.4	9.9

	Absolute Annual Error Reduction (%)	0.6	5.4	1.7	8.0
RSF2	With model (%)	-2.4	64.3	-23.2	-0.1
	Without model (%)	12.7	302.1	13.4	7.3
	Absolute Annual Error Reduction (%)	0.6	4.7	-0.5	7.2

3.2.2.4 Conclusions

Limitations of Marion's model have been listed by the authors. Some approximations were done because of lack of information, such as the extent of ice formation at the snow-module interface, the effect of age and freeze-thaw cycles on snow properties, snow depth on the PV array and snow density, wind effects and so on (Marion et al. 2013).

Different array types (roof-mounted and rack ground-mounted) are subjected to different relationships between snow slide amount and tilt angle, as shown in Fig. 3.3. Observation has focused especially on roof-mounted system, while only a PV system was rack ground-mounted, as a consequence empirical relationship is less reliable in this case. A considerable difference is present because roof-mounted systems are generally not subjected to snow accumulation on horizontal planes, which could partially cover module surfaces.

SAM's software provides a considerable help in calculating snow loss. The implementation of Marion's model permits to obtain hourly snow coverage percentage just entering meteorological input data, such as hourly ambient temperature (°C), hourly POA after shading (W/m²) and daily snow depth (cm), and system design input data, such as module tilt angle (°). Meteorological data can be easily set choosing a weather file from NREL solar resource library or uploading a new one from your own computer in the "Location and Resource" sheet.

In reality SAM develops calculus in the "Photovoltaic Residential" page only if some other information about the PV system is given, because it is set to give results as annual energy production (kWh), capacity factor (%), energy yield (kWh/kW), performance ratio. Therefore, snow loss can be calculated only through the other models that SAM is implemented with, to find the energy production values. In addition snow loss is give only as a yearly value; as a consequence monthly values cannot be checked.

Analyzing in detail SAM results, information about hourly snow coverage are found, but it is influenced by the shading model, due to the fact that Marion's algorithm is implemented with "POA after shading".

3.2.3 Modeling a PV system

A software commonly used to do photovoltaic simulation is PVsyst. It is the most accurate and sophisticated software existing on the market, because it is implemented with several models that let to use different tool to study an existing PV system and to design a new one. PVsyst does not give the possibility to calculate the snow loss, though.

A comparison between SAM and PVsyst was performed to see which one would be most suitable to perform a reliable PV simulation. The first paragraph is going to describe how

SAM let the description of a PV-plant though the input pages of version 2 (14.03.2016). The second paragraph is going to do the same with PVsyst version 6.47 (15.07.2016). Finally the results in the flowcharts are compared.

3.2.3.1 Input parameters in SAM

This paragraph will be structured following the same name and order of the input sheets present in the software interface.

Location and resources

The software refers to the NREL National Solar Radiation Database (NSRDB), which can also be updated through the website. Weather file can also be uploaded from the computer data, but only TMY2 (typical meteorological year 2), TMY3 (typical meteorological year 3), epw (energy plus weather), SMW (special marine warning), CSV (comma separated value) files are admitted.

However, several problems are observed in founding a complete European weather file. NREL created a weather file database with snow depth data for only American locations, while the European ones derive from the Official Energy Plus library (https://energyplus.net/weather/simulation), not often containing snow depth information.

The software offers the possibility to choose between three sky diffuse models: isotropic, HDKR (Hay, Davies, Klucher, Reindl) and Perez. Albedo values can be entered manually per month.

Module

A module has to be chosen in the "Module" sheet by the "CEC (California Energy Commission) Performance Module Database" or the "Sandia PV Array Performance Module Database". However, the software is developed in the U.S., as a consequence these databases contain specifications about American products, which are different from the ones used in Europe.

A solution would be to choose American modules from these databases with similar characteristics to the used in the real PV system, taking in consideration a suitable margin of error. Another solution would be to insert specifications required from the "Simple Efficiency Module Model", "CEC Performance Model with User Entered Specifications", "IEC61853 Single Diode Model" menu. This one will lead to another approximate calculus, compared to using a product from a database.

Inverter

An inverter has to be chosen in the "Inverter sheet" by the "Inverter CEC Database". For the same reasons that have been explained previously, the required specifications will frequently be insert in the "Inverter Datasheet" and "Inverter Part Load Curve" menu.

System design

System sizing have to be specified (modules per string, strings in parallel and number of inverters). Each PV sub-array can be defined with number of strings, tilt angle (°), azimuth angle (°) and ground coverage ratio factor. However, there is no possibility to design particular configurations, such as a module row split in two strings.

Shading and Snow

External Shading can be designed through a 3D Shade Calculator or through a Shade Loss Table, while Self Shading are calculated through module's dimension and number of module along side of row and along bottom of row. Snow losses are calculated just ticking a box in the same sheet.

Losses

For a detailed calculus losses can be defined in this sheet: irradiance losses (soiling), DC (Direct Current) losses (module mismatch, diodes and connections, DC wiring, tracking error, nameplate, DC power optimizer loss), AC (Alternative Current) losses (AC wiring, set-up transformer).

Not any tool helps in evaluating the loss entity. SAM just gives the possibility to introduce some values.

Further sheets

Some other sheets are present ("Lifetime", "Battery Storage", "System Costs", "Financial Parameters", "Incentives", "Electricity Rates", "Electric Load"), but information in them will not influence energy calculus.

The software interface with all the previously-mentioned sheets is shown in the images in Appendix E.

3.2.3.2   Input parameters in PVsyst

The following paragraphs are going to show the software possibilities. They are especially focusing on the input given to launch the simulations.

Weather parameters

This software contains a large database of weather files. Some of them have data in hourly values (Meteonorm, Satellight, US TMY 2/3, Solar Prospector, Canadian EPW, SolarAnywhere, Helioclim-3, SolarGIS climData) and some others in monthly values (Meteonorm, NASA-SSE, SolarGIS iMaps, PVGIS-E SRA, Helioclim-1, Ratscreen).

If the considered city is not present in the database, PVsyst gives the possibility to create a new "site", with latitude, longitude, altitude and time zone information. Weather data of the new site can be uploaded through a weather file, as far as it has one of the extensions of the files previously mentioned.

Finally albedo values should be defined monthly or yearly.

The simulation was performed for Oslo, Bergen and Trondheim as "sites". The weather files and albedo values inserted are the same used in SAM.

"Site", "Meteo" and "Albedo" define a "Project". The following information regards the creation of a "variant" to the "Project".

Orientation

The software allows the study of different kinds of orientation: fixed tilted plane, seasonal tilt adjustment, tracking two axis, tracking tilted or horizontal NS (north-south) axis, tracking horizontal axis EW (east-west), tracking vertical axis, tracking sun-shields, double orientation, unlimited sheds, unlimited sun-shields.

As far as fixed orientations are concerned, PVsyst is implemented with a tool that shows the tilt optimisation.

System Design

This sheet gives the possibility to insert specifications about system geometry and to choose module and inverter data sheet from the PVsyst database. The database is very wide and easily updated, therefore every kind of modules and inverters can be found. However, the software allows to modify the present modules and inverter to every necessity. Screenshots showing the parameters that can be modified are plotted in Appendix F.

Detailed losses

The thermal behaviour is characterized by a thermal loss factor designed here by U-value, which can be split into a constant component Uc and a factor proportional to the wind velocity Uv:

$$U \;=\; Uc \;+\; Uv \cdot WS \tag{3.18}$$

where U stands for U-values (W/m²·k) and WS is the wind speed (m/s).

The ohmic loss in the DC circuit can be generally indicated through a value. The software offers also a more detailed computation through information about average length and section of the wires in the string module connexions and from the main box to inverter.

The ohmic loss can be applied also to the AC circuit, if the wires length is significant, and to the external transformer, if it is present.

The LID (light induced degradation) loss is the degradation of crystalline silicon modules in the first operating hours by respect to the manufacturing flash test STC (Standard Test Conditions) values.

The mismatch loss has been computed by PVsyst through a tool that refers to the PV-array design.

The soiling loss can be indicated though a value monthly or yearly.

The IAM (incident angle modifier) loss is computed through the ASHRAE (American society of heating, refrigerating and air-conditioning engineers) model, considering

$$IAM = 1 - b_o \left({}^{1}\!/_{\cos i} - 1\right) \tag{3.19}$$

where i is the incident angle and b_o is a coefficient equal to 0.05.

The IAM graph (Fig. 3.7) can be modified manually, defining the single points. In addition this PVsyst tool let to investigate the IAM effect on beam, diffuse and albedo solar component.
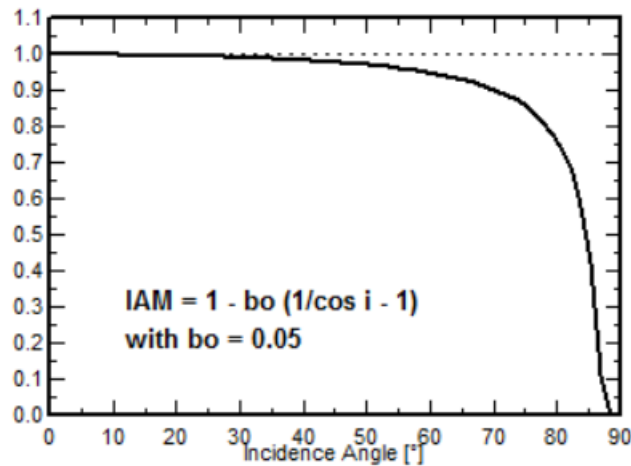
Fig. 3.7. IAM function of the incident angle on solar rays on the modules (plotted by the author through PVsyst).

Finally the software is implemented also with Fresnel and Sandia models to compute IAM loss, which can be set by the users.

PVsyst presents other sheets, where values about degradation factor, unavailability of the system and auxiliaries energy losses can be insert.

Further sheets

Some other sheets are present ("Economic evaluation" and "Miscellaneous tools"), but information in them will not influence energy calculus. The software interface with all the previously-mentioned sheets is shown in the images in Appendix F.

3.2.3.3 Comparison between SAM and PVsyst results and loss flowchart

Figures 3.8 and 3.9 show how the two software plot the results in the loss flowchart. Differences are explained in the following paragraphs.

From nominal POA to DC

SAM takes into account only the shading and soiling loss; while PVsyst cares also about the IAM loss.

Nominal DC energy

SAM considers the snow loss, which should be considered previously.

The PV loss due to irradiance level and temperature and the LID loss in PVsyst can be summarize only in the module loss in SAM. IAM loss can also be computed in this voice, but it should have been counted previously.

PVsyst counts the electrical loss related to shading.

The ohmic loss in PVsyst corresponds to the DC wiring in SAM.

The module mismatch in PVsyst is divided into module mismatch and diodes and connection in SAM.

Net DC energy

SAM computes inverter power clipping, inverter power consumption, inverter nighttime consumption and inverter efficiency.

PVsyst computes inverter loss during operation, inverter loss over nominal inverter power, inverter loss due to power threshold, inverter loss over nominal inverter voltage and inverter loss due to voltage threshold.

AC energy

This part was not considered in this study.

_____ kWh/m²	**Horizontal global irradiation**
	Global incident in coll. plane
	Near Shadings: irradiance loss
	IAM factor on global
	Soiling loss factor
____ kWh/m² *___ m² coll.	**Effective irradiance on collectors**
efficiency at STC = _____%	PV conversion
_____ kWh	**Array nominal energy (at STC effic.)**
	PV loss due to irradiance level
	PV loss due to temperature
	Shadings: Electrical Loss acc. to strings
	LID - Light induced degradation
	Module array mismatch loss
	Ohmic wiring loss
_____ kWh	**Array virtual energy at MPP**
	Inverter Loss during operation (efficiency)
	Inverter Loss over nominal inv. power
	Inverter Loss due to power threshold
	Inverter Loss over nominal inv. voltage
	Inverter Loss due to voltage threshold
_____ kWh	**Available Energy at Inverter Output**
_____ kWh	**Energy injected into grid**

Fig. 3.8. PVsyst results and losses flowchart (plotted by SAM and modified by the author).

65

Fig. 3.9. SAM results and losses flowchart (plotted by SAM and modified by the author).

3.2.3.4 Conclusions

SAM is a user-friendly software that let an easy comprehension of the requirements needed to develop the computation. Its simplifications produce a too approximate model, though. For instance a comparison with PVsyst software would highlight the fact that "System Design" sheet does not let to describe the geometry entirely and the bypass diodes presence, and that losses can be studied far more in detail than what is allowed in "Shading and Snow" and "Losses" sheets.

In conclusion SAM is a useful software due to the fact that it is implemented with the snow loss model. However, a whole photovoltaic system simulation would produce more reliable results with PVsyst.

3.2.4 Proposed research

Marion's model can be recognized as the most reliable algorithm existing in literature as far as snow coverage calculation is concerned. Information regarding snow-module interface, the effect of age and freeze-thaw cycles on snow properties, snow depth on the PV array and snow density, wind effects and so on are still lacking in literature, but the model can produce adequate results even without them.

Implementation in SAM can be helpful, but this software presents some lacks in modeling PV systems. The algorithm that obtains the hourly snow coverage is implemented using "POA after shading", therefore this calculus is influenced by the shading model used in SAM. The energy produced with snow coverage and snow loss percentage can be calculated more faithfully using PVsyst software, which would let a better consideration of PV components and energy loss on the DC and AC side.

Finally weather file can be obtained accessing to other databases, which would give complete information about considered location.

In conclusion, an Excel file that connects SAM's results with PVsyst results is the best solution to obtain a reliable answer.

The purpose of this research is to determine the impact of snow on energy production of PV panels, through PV energy production that considers snow presence and snow loss percentage values. The research will look at the effect of winter conditions such as ice accumulation and snowfalls on photovoltaic solar panels. As previously highlighted, results are strongly connected to the location's weather conditions, as a consequence a case study have to be chosen to develop the research. However, the methodology maintains a general validity, so that it can be repeated for other locations.

3.3 Methodology

3.3.1 Case study

Most of the studies concerning snowfall have been performed in U.S. because of the rigid climate in many regions and the strong interest of the government in the energy field. Thus a map showing general trends in average snow losses as a percentage of annual energy production was created (Fig. 3.10).
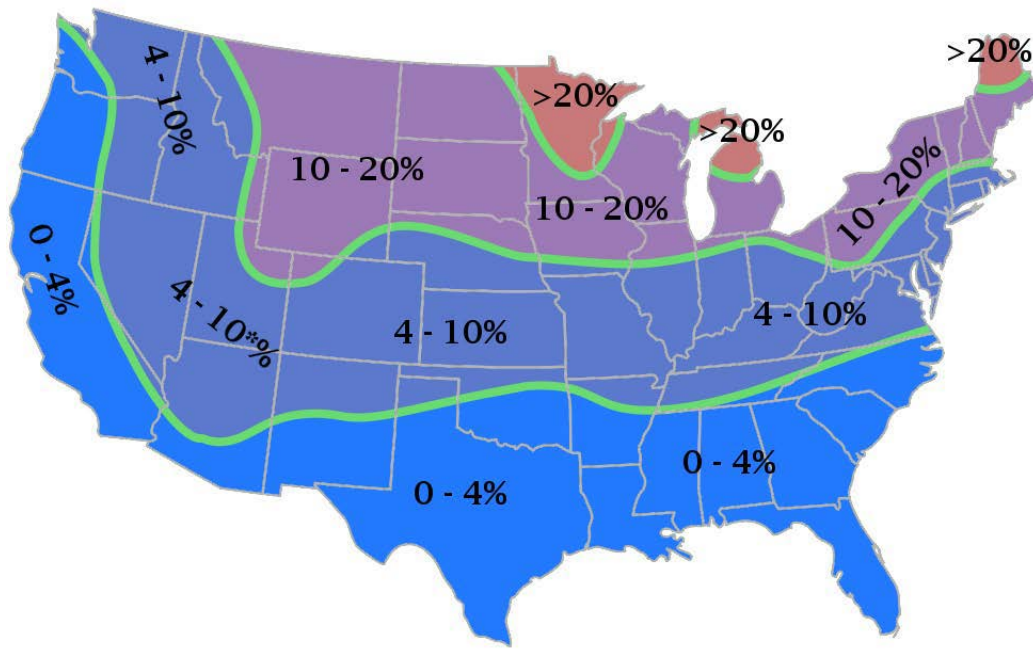
Fig. 3.10. General trends in average snow losses as a percentage of annual energy production was created (Ryberg and Freeman 2015).

Some studies were conducted also in Europe, but a map showing snow losses does not exist. Mediterranean countries do not cope with snow problem because of favourable weather, but Continental and Scandinavian countries are actually affected by snowfalls.

A growing interest is shown by Norway, where government is addressing funds to renewable energy filed in view of a depletion of oil stock. The development of the solar industry is at an early stage, but the consideration of the great energy potential in winter time due to high albedo values caused by snow reflections promotes an advancing research in PV devices (Scharmer and Greif 2000). Therefore, an evaluation of PV energy losses due to snow coverage would be useful to estimate the effective production of PV devices.

Norway's snow depth map show different values over the country due to morphological characteristics of each location (Fig. 1.5), as a consequence different snow loss values would be present in each area. The major interest is focused on the most populated cities (more than 150 000 citizens), where most of PV resources are: Oslo (59°55'; 10°45'), Bergen (60°39'; 5°33') and Trondheim (63°26'; 10°23'). Snow map shows lower values of snow depth in Bergen because of mitigate weather due to North Sea presence; whereas Oslo and Trondheim have similar snow depth values.

The following research is applied to these cities. The same PV-plant can be supposed in Oslo, Trondheim and Bergen, so that the influence of snow depth values on the snow loss in shown. In addition a general knowledge in the values of snow influence on PV production would be a great help to Norwegian research.

3.3.2 Simulation assumption

3.3.2.1 PV-plant characteristics

The PV-plant that is used in the simulations is a roof-mounted system on the ZEB (The Research Centre on Zero Emission Buildings) Living Lab building at Norwegian University of Science and Technology (NTNU) in Trondheim. It is located on the two 30°-tilted roofs and south facing areas.

The solar cell system on ZEB Living Lab consists of 48 modules, equally distributed on the two roofs. Roof length is divided into four rows; the first three from the top are covered by modules in the landscape orientation. Each PV row is made up by 8 panels. The PV system is organized into four strings of 12 modules. The middle row of modules is split between the upper and the lower string.

Modules are REC 260PE by REC company. Each module has 60 polycrystalline silicon (poly-Si) solar cells, with three bypass diodes. The nominal power for one module is 260 Wp, with a total installed power of 11.48 kWp. The rated efficiency of the modules is 15.8%. The gross modules area is 1.65 m² (1 m x 1.65 m), resulting in a total installed area of 79.2 m². The module weight is 18 kg, which means a total weight of 864 kg, or 10.9 kg/ m² installation. Detailed information is shown in Appendix C.

One inverter is installed per roof, thus two inverters in total. Inverters are Sunny Boy 5000 TL-21 MS basic by SMA company. Inverter's maximum DC power is 5.25 kW and the efficiency is ranking between 96.5% and 97%. Inverter data sheet is attached in Appendix C.

3.3.2.2 Climate and context

The weather data about Oslo and Bergen was taken from Energy Plus library. Trondheim weather file was developed by NTNU researchers, who make it available on the university's website.

These weather files did not have any information about snow depth values, though. Therefore, a statistical analysis was performed on the data furnished by National Oceanic and Atmospheric Administration (NOAA) division in National Climatic Data Center (NCDC) in U.S., accessing to the national database of Norwegian Meteorological Institute by eKlima service. Values are accessible at Appendix A.

Trondheim data was not sufficient for a statistical analysis. In fact a meteorological station was installed in Trondheim at Voll to collect snow depth data only last year. As a consequence a linear correlation with Leinstrand data, a small city 15 km far from Trondheim with an ancient weather station, was performed. Further information is described in Appendix B.

Albedo values were set up monthly to take into account the amplification of light reflections due to the presence of the snow, as indicated in Table 3.3:

Table 3.3. Albedo values for snowy areas.

Jan	Feb	Mar	Apr	May	Jun	Jul	Aug	Sep	Oct	Nov	Dec
0.82	0.82	0.75	0.55	0.20	0.20	0.20	0.20	0.20	0.20	0.20	0.82

The previous values have been chosen consulting the range of albedo values for different conditions proposed by PVsyst (Table 3.4):

Table 3.4. Albedo values for different environmental conditions.

Urban environment	0.14 - 0.22
Grass	0.15 – 0.25
Fresh grass	0.26
Fresh snow	0.82
Wet snow	0.55 – 0.75
Dry asphalt	0.09 – 0.15
Wet asphalt	0.18
Concrete	0.25 – 0.35
Red tiles	0.33
Aluminium	0.85
Copper	0.74
New galvanized steel	0.35
Very dirty galvanized	0.08

The sky diffuse model used by the software is the Perez model.

3.3.2.3 PVsyst setup and results

The following paragraphs are showing the software possibilities concerning our necessities. They are especially focusing on the input given to launch the simulations.

Weather parameters

The simulation was performed for Oslo, Bergen and Trondheim as "sites". The weather files and albedo values inserted are the same used in SAM.

Orientation

In this case the input is given just in "Fixed Tilted Plane" sheet. Tilt angle and azimuth angle have the following values respectively: 30° and 0°. Reference system is shown in Fig. 3.11.
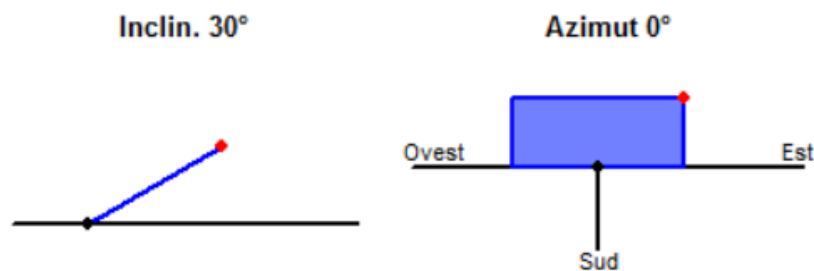
Fig. 3.11. PVsyst reference system for module's azimuth and tilt angle (plotted by the author through PVsyst).

System Design

The modules and inverter datasheet were found easily (Fig. 3.12).

Fig. 3.12. ZEB Living Lab's PV system design in PVsyst (screenshot of PVsyst 6).

Detailed losses

Studying PVsyst proposed values and considering ZEB Living Lab PV system as a semi-integrated one because of 49 mm gap, parameters used to determine the thermal behaviour were 22.5 W/(m² K) for *Uc* value and 0 W/(m² K) for *Uv* value because of 0 / m/s for *WS*.

The ohmic loss in the DC circuit was generally indicated as 1.5%.

The PV-plant on the Living has not been analysed yet to define the module quality loss, therefore the value used is 0%.

The LID loss was set to 1.5%, value taken from the module specifications.

The mismatch loss was computed by PVsyst through a tool that refers to the PV-array design.

The soiling loss was assumed to be 1%, referring to Marion et al. (2005), who recommend derate factors of 0.95 for soiling, with values ranging from 0.75 to 0.98. They mentioned that soiling is site- and weather-dependent. Areas with high-traffic, high pollution and infrequent rain are the most susceptible, but Norwegian cities do not fit with this description.

The IAM loss is computed automatically through the ASHRAE model.

The losses values used are summarized in Table 3.5:

Table 3.5. Losses values set in PVsyst to describe the PV-plant for the ZEB Living Lab.

DC wiring	1.50%
AC wiring	0.00%
Set-up transformer	0.00%
Module quality	0.00%
Light Induced Degradation (LID)	1.50%
Module mismatch	1.00%
Soiling loss	1.00%
Degradation factor	0.40%/year

Horizon

In this case no input was set up as external shadings, because light obstacles are too far from the building considered.

Near shadings

The ZEB Living Lab PV system was represented in the software through a 3D drawing program. Then shadows were calculated in the simulation through the Shading Factor table. The simulations were launched "according to module strings", setting the "fraction for electrical effect" as 100%.

Module layout

In this case the PV system was designed distributing 8 modules per row. Each sub-array is made up by 3 rows. The 3 rows are divided into two strings; in fact the central one is split in two. Information about the presence of 3 by-pass diodes per module was also given.

PVsyst results

Principal results are listed in the report produced by the software (Appendix G). In addition every computation result can be accessed through tables and graphs yearly, monthly and daily.

3.3.3 Integration of snow loss in PVsyst results

Marion's snow cover algorithm was used to obtain results regarding the same PV-plant supposed in Oslo, Trondheim and Bergen. Energy simulations about it were launched also in PVsyst and the final flowchart results were integrated with snow cover values, so that snow loss and final energy production were computed.

Marion's algorithm was set using *Glob. IAM* values (W/m²) to derive snow coverage. That is global irradiance component with detraction of shading and IAM losses. In reality *Glob.Shad.*, global irradiance component with detraction of only shading loss, should have been used, but hourly values were not made available by the software.

The steps followed to find the snow loss percentage are summarized as the following:

1. Set a new project in PVsyst considering the weather data and the plant characteristics.
2. Launch the simulation, obtaining yearly flowchart results and hourly *Glob.IAM*.
3. Use the *Glob.IAM* and the other hourly data in the weather file to execute Marion's algorithm:

Step 1	If today's sd > yesterday's sd Set PV snow amount = 10 tenths (100% snow) Else Set PV snow amount = Yesterday's end amount
Step 2	Initialize daily energy productions E_w and E_{w0} to zero
Step 3	For each daytime hour:
Step 4	If $Ta - Glob.IAM/m' > 0$ Decrease PV snow by Fig.3.3 amount. (where m' is the slope of line from Fig. 3.1, that is -80 W °C /m²)

4. Calculate hourly snow coverage (sc') considering the presence of module by-pass diodes.

5. Hourly power loss due to snow p_{snow} (kW) is calculated using the following equation:

$$p_{snow} = sc' * Glob.IAM \qquad (3.20)$$

where sc' is corrected sub-array snow cover (%) and $Glob.IAM$ is global irradiance component with detraction of shading and IAM losses as computed by PVsyst (W/m²).

6. p_{snow} is summed hour by hour and day by day to obtain monthly power loss P_{snow} (kWh).

7. Snow loss percentage sl (%) is determined diving P_{snow} (kWh) per monthly $Glob.IAM$ (kWh):

$$sl = \frac{P_{snow}}{Glob.IAM} \qquad (3.21)$$

8. $Glob.IAM.$ is then reduced by snow loss to obtain $Glob.Snow$.

9. Soiling percentage is detracted from $Glob.Snow$ to have the $Glob.Eff$.

10. Net DC energy is finally obtained considering irradiance loss, temperature loss, electrical loss due to shadings, light induced degradation. Module array mismatch loss and ohmic wiring loss. Gross AC energy takes into account inverter parameters: efficiency, nominal power, power threshold, nominal voltage and voltage threshold.

11. PVsyst flowchart can be updated with new values, considering also snow loss, so that final energy production can be computed.

3.4 Results

3.4.1 PV-plant for the ZEB Living Lab in Trondheim

The main results about the PV-plant mounted on the ZEB Living Lab roofs are described by the PVsyst flowchart (Table 3.6, Appendix G).

Table 3.6. PVsyst results for the PV-plant on the ZEB Living Lab in Trondheim.

Nominal POA			
879 kWh/m²	+26.30%	global incident	1 110 kWh/m²
	-6.45%	shading	1 039 kWh/m²
	-3.37%	IAM factor	1 004 kWh/m²
	-1.00%	soiling	994 kWh/m²
			12 401 kWh
Nominal DC energy	-1.65%	loss due to irradiance	12.197 kWh
994 kWh/m²	-0.79%	loss due to temperature	12 100 kWh
79 m²	-2.87%	electrical loss due to shadings	11 753 kWh
	-1.50%	light induced degradation	11 577 kWh
	-1.00%	module array mismatch loss	11 461 kWh
	-0.70%	ohmic wiring loss	11 380 kWh
Net DC energy	-3.75%	inverter efficiency	10 953 kWh
11 380 kWh	-0.39%	inverter over nominal power	10 911 kWh
	0.00%	power threshold	10 911 kWh
	0.00%	nominal inverter voltage	10 911 kWh
	0.00%	voltage threshold	
gross AC energy			
10 911 kWh			

The results are not relevant as energy production at other locations of Europe, but they are coherent to the nominal irradiance and the other loss values.

A deeper analysis was run on the snow loss computation. The application of the steps showed in the previous list, lead to the monthly power loss P_{snow} (kWh) and snow loss percentage sl (%), showed in Table 3.7.

Table 3.7. Global irradiance after shading and IAM losses (kWh), monthly power loss (kWh) and snow loss percentage (%) of the PV-pant on the ZEB Living Lab in Trondheim.

	$Glob.IAM$ (kWh)	P_{snow} (kWh)	sl (%)
January	876	204	23
February	3 010	898	30
March	7 292	803	11
April	10 228	0	0
May	12 497	0	0
June	12 084	0	0
July	11 835	0	0
August	9 668	0	0

September	6 377	0	0
October	3 300	0	0
November	1 066	0	0
December	443	80	18
Year	78 674	1 985	3

The final percentage seems to be a value not too high. The reason is related to the easy sliding of snow off the panels (Fig. 3.3).

The results in Table 3.7 were applied to PVsyst in the flowchart, considering the loss due to snow after the shading and IAM factor losses. The $Glob.Inc.$ decreased by these ones and soiling losses is called by the software "global effective irradiance" ($Glob.Eff.$). This quantity is the nominal DC energy. The new results are showed in Table 3.8.

Finally, the consideration of the other losses at the DC side (Table 3.9 and 3.10) bring to the creation of a PVsyst flowchart with new values (Table 3.11).

In conclusion the annual energy production decreased from 10.911 kWh to 10.451 kWh.

Fig. 3.13. ZEB Living Lab after a snowfall in late November 2015 (Good 2016).

Table 3.8. Global after shading, IAM and snow, global effective irradiance (kWh) of the PV-pant on the ZEB Living Lab in Trondheim.

	$Glob.Snow$ (kWh)	$Glob.Eff.$ (kWh)
January	8	8
February	27	27
March	82	82
April	129	127
May	158	155
June	153	150
July	149	146
August	122	120

September	81	79
October	42	41
November	13	13
December	5	5
Year	968	952

Table 3.9. Monthly energy values from nominal DC energy to net DC energy of the PV-pant on the ZEB Living Lab in Trondheim.

	GlobEffSTC	Irradiance	Temperature	ShdElec	LID	MisLoss	OhmLoss
	kWh	kWh	kWh	kWh	kWh	kWh	kWh
J.	106	104	103	99	98	97	96
F.	333	327	325	298	293	290	289
M.	1 023	1 006	998	912	899	890	884
A.	1 580	1 554	1 541	1 463	1 441	1 427	1 416
M.	1 930	1 898	1 883	1 864	1 836	1 818	1 803
J.	1 866	1 836	1 821	1 821	1 794	1 776	1 761
J.	1 828	1 798	1 784	1 783	1 756	1 738	1 724
A.	1 493	1 469	1 457	1 415	1 394	1 380	1 370
S.	985	969	961	913	899	890	885
O.	510	501	497	464	457	452	450
N.	168	165	164	158	156	154	154
D.	57	56	56	54	53	52	52
Yr	11 878	11 682	11 590	11 243	11 074	10 964	10 883

Table 3.10. Monthly energy values from net DC energy to gross AC energy of the PV-pant on the ZEB Living Lab in Trondheim.

	EOutInv	ENPInv
	kWh	kWh
January	91	91
February	277	276
March	852	849
April	1 367	1 361
May	1 739	1 732
June	1 696	1 689
July	1 660	1 654
August	1 319	1 314
September	851	848
October	430	428
November	145	144
December	49	48
Year	10 474	10 433

Table 3.11. Results about the PV-plant on the ZEB Living Lab in Trondheim after the consideration of snow loss.

Nominal POA			
879 kWh/m²	+26.30%	global incident	
	-6.45%	shading	
	-3.37%	IAM factor	
	-1.00%	soiling	
	-3.00%	snow	952 kWh/m²
Nominal DC energy	-1.65%	loss due to irradiance	
952 kWh/m²	-0.79%	loss due to temperature	
79.2 m²	-2.87%	electrical loss due to shadings	
	-1.50%	light induced degradation	
	-1.00%	module array mismatch loss	
	-0.70%	ohmic wiring loss	10 900 kWh
Net DC energy	-3.75%	inverter efficiency	
10 900 kWh	-0.39%	inverter over nominal power	
	0.00%	power threshold	
	0.00%	nominal inverter voltage	
	0.00%	voltage threshold	10 451 kWh
gross AC energy			
10 451 kWh			

3.4.2 Comparison between Oslo, Bergen and Trondheim

The methodology previously explained was followed to obtain results for Oslo and Bergen as well. Simulations in PVsyst and SAM were launched setting Oslo and Bergen weather files, considering the same PV-plant characteristics.

Table 3.12 and 3.13 report the monthly power loss P_{snow} (kWh) and snow loss percentage sl (%) in Oslo and Bergen. The previous Table 3.7 gives the values of Trondheim.

Table 3.12. Global IAM (kWh), monthly power loss (kWh) and snow loss percentage (%) of the PV-plant on the ZEB Living Lab in Oslo.

	$Glob.IAM$ (kWh)	P_{snow} (kWh)	sl (%)
January	1 140	811	71
February	2 174	665	31
March	5 600	613	11
April	8 167	183	2
May	12 346	0	0
June	12 628	0	0
July	12 373	0	0
August	9 744	0	0

September	5 791	0	0
October	3 327	0	0
November	1 219	23	2
December	588	299	51
Year	75 098	2 594	3

Table 3.13. Global IAM (kWh), monthly power loss (kWh) and snow loss percentage (%) of the PV-plant on the ZEB Living Lab in Bergen.

	$Glob. IAM$ (kWh)	P_{snow} (kWh)	sl (%)
January	648	19	20
February	1688	47	14
March	3892	134	1
April	6874	204	0
May	11530	312	0
June	10984	319	0
July	9668	312	0
August	7898	246	0
September	4527	146	0
October	2665	84	0
November	816	31	5
December	362	11	6
Year	61552	475	1

Marion's algorithm applied to the same PV-plant supposed in different Norwegian cities gave different results to the different weather conditions in them. Table 3.14 shows snow loss values per month in Oslo, Bergen and Trondheim.

Table 3.14. Snow loss (%) values of ZEB Living Lab PV-plant supposed in Oslo, Bergen and Trondheim. The year value (*) is an energy-weighted percentage as it takes into account the solar radiation energy distribution throughout the year. The month values are the energy loss with respect to the energy in the specific month.

	Oslo (%)	Bergen (%)	Trondheim (%)
January	71	20	23
February	31	14	30
March	11	1	11
April	2	0	0
May	0	0	0
June	0	0	0
July	0	0	0
August	0	0	0
September	0	0	0
October	0	0	0
November	2	5	0
December	51	6	18
Year *	3	1	3

Fig. 3.14. Monthly snow loss (%) values of ZEB Living Lab PV-plant supposed in Oslo, Bergen and Trondheim.

Table 10 shows a low value of year energy loss, compared to the month ones, due to the fact that the solar radiation is in summer months is more generous. However, energy is more requested in winter; hence, the interest in knowing winter energy values.

Bergen values are lower than other cities, while Oslo and Trondheim show similar results. In particular the Oslo case has a higher loss in January and December. The reason why is contained in the weather data (Figs. 3.14 - 3.16).

Global irradiance after shading and IAM losses has the lowest trend in Bergen for all the winter. Oslo values are higher than Trondheim ones in November, December and January, but not in February and March (Fig. 3.14). However, from November to January values of solar radiation are really low, due to the few hours per day of light and the frequent snow cover.

Average air temperature is between 1°C and 4°C in wintertime in Bergen. While Oslo and Trondheim show lower values (Fig. 3.15). The air temperature seems to be quite similar during the whole winter, except from January, when Oslo's average temperature is around -4°C.

Average snow depth data are similar in Bergen and Trondheim. The trend in Trondheim rises only in February and March. While Oslo's curve shows double values of snow depth (Fig. 3.16).
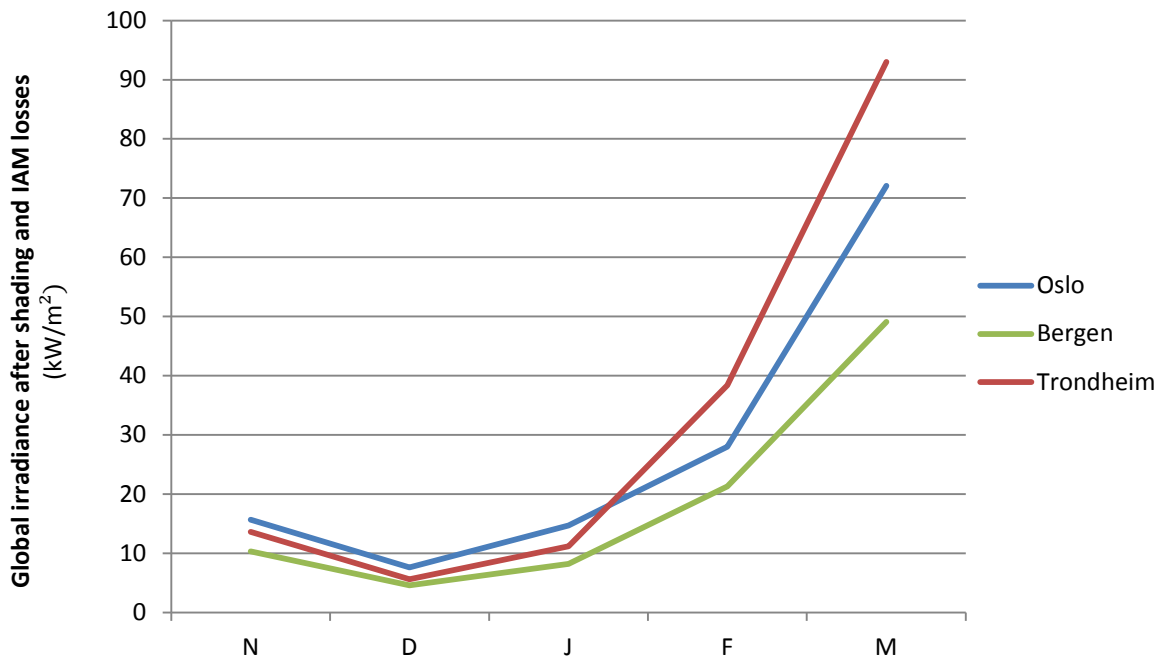
Fig. 3.15. Global irradiance after shading and IAM losses (kWh/m^2) in Oslo, Bergen and Trondheim. Values from the 1st of November to the 31th of March.

In conclusion Bergen's weather is less rigid than in the other cities, therefore snow loss values are lower. Oslo and Trondheim have similar weather conditions, but Oslo snow depth trend proves a massive and increasing presence of snow till February.
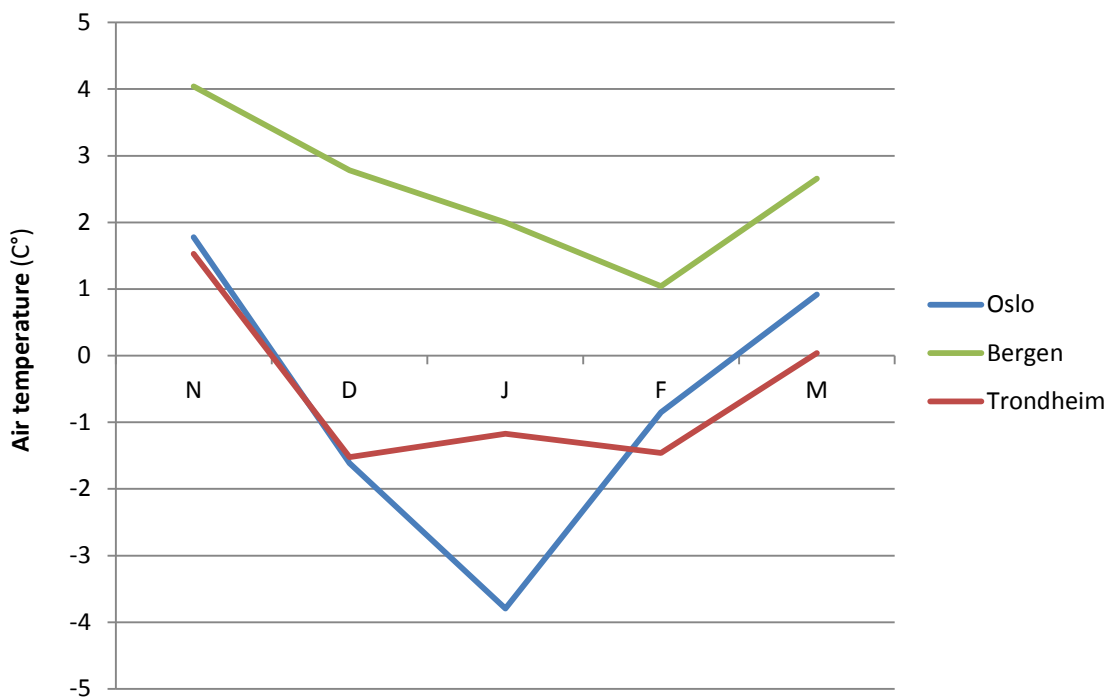
Fig. 3.16. Air temperature (C°) in Oslo, Bergen and Trondheim. Values from the 1st of November to the 31th of March.
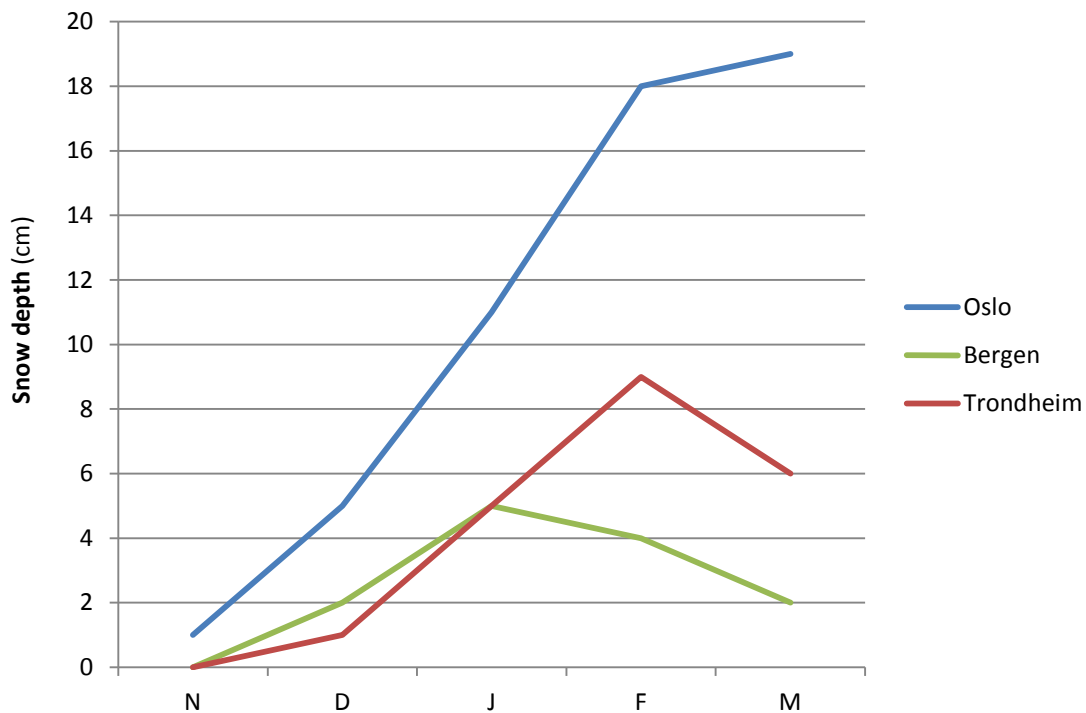
Fig. 3.17. Snow depth (cm) in Oslo, Bergen and Trondheim. Values from the 1st of November to the 31th of March.

3.5 Conclusions and further research

Marion et al. (2013) developed an algorithm to predict snow coverage on photovoltaic panels. Its utility is connected to the possibility of calculating the energy loss due to snow coverage on a PV system, henceforth called snow loss, which is not negligible in Nordic countries. This algorithm was implemented in System Advisor Model (SAM) by National Renewable Energy Laboratory (NREL), an U.S. software that presents several limits in components and weather databases and PV models. PVsyst is a software widely used for PV simulations. It offers several tools and allows a more accurate description of the plant.

A new method was used to calculate snow losses. It is based on Marion's algorithm, whose results are integrated in PVsyst. The method was applied to the system mounted on the ZEB Living Lab, a building set in the Norwegian Institute of Science and Technology (NTNU) campus in Trondheim. The same plant was assumed to be in Oslo and Bergen, so that other simulations were launched considering different weather conditions to compare the results.

Snow loss percentage can reach very high values in the winter months, even more than 50%. However, the year value is around 1% in Bergen and around 3% in Oslo and Trondheim, which is not unimportant. The year value is an energy-weighted percentage as it takes into account the solar radiation energy distribution throughout the year. The month values are the energy loss with respect to the energy in the specific month.

The lowest snow loss values were found in Bergen, which reaches the maximum in January with 20% loss. This result is due to the lower solar radiation, air temperature and snow depth.

Oslo and Trondheim present more similar results because of similar weather conditions. Note that, Oslo reaches a snow loss value of 71% in January and 51% in December, due to an increasing snow depth trend.

These results were obtained through simulations, as a consequence they are not expected to predict the exact values of loss, but they give an idea of the trends. Simulations are based on statistical weather data, therefore results are considered reliable.

Marion's algorithm was developed on PV-plant set in Colorado and Wisconsin. After that it was validated by NREL on the Forrestal system in Washington D.C. Results show over-prediction and under-prediction energy estimation on a monthly, daily or hourly basis, while annual results are more faith to reality. As a matter of fact Marion's model is strongly reliable only on an annual scale, a monthly study can always be helpful to obtain approximate values.

Further observation of the behaviour on snow on panels could lead to a more accurate and detailed model. For example, that also the formation and melting of ice of the panel can be predicted and considered as a different phenomenon.

Other uncertainties are due to the different answers of the sliding of snow on the module frames. Sometimes snow sticks on them; therefore, the panel is partially covered. This phenomenon should be investigated further as well.

Marion's model is applied considering roof-mounted systems. The systems observed did not present any obstacle to the sliding of snow. Therefore, chimneys, roof-windows, antennas, etc., may invalidate to a certain degree some of the model's results.

As a result, the ZEB Living Lab PV-plant was chosen as case study; however, results cannot be considered faithful for it. The geometry of this building is unusual, because of two plane parts next to the tilted roof. These ones make the snow accumulate on them, so that an obstacle is created to the sliding of snow. In conclusion in this case snow loss values are far higher than simulation results. Nevertheless simulations gave useful results about a generic PV-plant set in Oslo, Trondheim and Bergen.

3.6 References

R. Andrews, A. Pollard, J. Pearce, "The effects of snowfall on solar photovoltaic performance", *Solar Energy,* **92**, 84–97, 2013.

R. Andrews, A. Pollard, J. Pearce, "A new method to determine the effects of hydrodynamic surface coatings on the snow shedding effectiveness of solar photovoltaic modules", *Solar Energy Materials &Solar Cells,* **113**, 71–78, 2013.

G. Becker, B. Schiebelsberger, W. Weber, "An approach to the impact of snow on the yield of grid connected pv systems", Bavarian Association for the Promotion of Solar Energy, 2007.

B. L. Brench, "Snow-Covering Effects on the Power Output of Solar Photovoltaic Arrays", DOE DE-AC02-76ET20279, 1979.

C. Good, "Photovoltaic-thermal systems for zero emission residential buildings", PhD thesis, NTNU, Faculty of Architecture and Fine Arts, Department of Architectural Design, History and Technology, 2016.

M. R. Maghami, H. Hizam, C. Gomes, M. A. Radzi, M. I. Rezadad, S. Hajighorbani, "Power loss due to soiling on solar panel: a review", *Renewable and Sustainable Energy Reviews*, **59**, 1307-1316, 2016.

B. Marion, J. Adelstein, K. Boyle, "Performance parameters for grid-connected PV systems", *Proc 31st IEEE PVSEC*, Lake Buena Vista, FL, USA, Jan 3-7, 2005.

B. Marion, R. Schaefer, H. Caine, G. Sanchez, "Measured modeled photovoltaic system energy losses from snow from Colorado and Wisconsin locations", *Solar Energy*, **97**, 112-121, 2013.

R. Pfister, M. Schneebeli, "Snow accumulation on boards of different sizes and shapes", *Hydrological Processes,* **13**, 2345–2355, 1999.

L. Powers, J. Newmiller, T. Townsend, "Measuring and modeling the effect of snow on photovoltaic system performance", 38th IEEE PVSC, 2010.

D. Ryberg and J. Freeman, "Integration and validation and application of a PV snow coverage model in SAM", Technical Report, NREL/TP-6A20-64260, 2015.

M. Ross, "Snow and Ice Accumulation on Photovoltaic Arrays: An Assessment of the TN Conseil Passive Melting Technolog", Division Report EDRL 95-68 (TR), 1995.

K. Scharmer, J. Greif, "European Solar Radiation Atlas: fundamentals and maps", Ecole des Mines de Paris, Paris, 2000.

T. Townsend et L. Powers, "Solar Winter Output Assessment: Measuring Snow-related Losses", DNV Kema Energy and Sustainability, 2012.

PVSYST Help 6, http://files.PVsyst.com/help/ Pveducation, http://pveducation.org/

4 Icephobic coatings

4.1 Abstract

Development of icephobic surfaces is becoming a research topic of considerable attention in different fields because of various possible applications: power lines, plane wings, wind turbines, etc. The design of a transparent, anti-reflective, robust and durable icephobic coating would increase the energy production of photovoltaic devices in winter time.

The aim of this study is to introduce icephobic surfaces, since the explanation of wetting behaviour to the detailed analysis of the meaning of "icephobicity". In addition the nano-design of existing water-repellent and icephobic surfaces will be investigated, to establish the properties that should be reached to create an icephobic surface applicable on photovoltaic devices. After that, a spotlight is pointed on the robustness and durability problems. Finally the conclusions and the state-of-the-art of useful coatings for photovoltaic applications are presented.

4.2 Introduction

4.2.1 Background

The growing interest of Nordic countries in photovoltaic devices leads to another relevant topic: snow. Snow in its various forms deposits on the module surface in wintertime, preventing the collection of solar radiation. The entity of the problem depends on the PV-plant geometry and material properties and on the location's weather characteristics.

Traditionally, roofs have been designed to keep the snow in its place on top of the roofs. However, solar cell roofs should ideally have no snow covering the cells, in order to maximize the solar cell energy production (Jelle 2013).

The natural snow and ice removal from the PV panel is due to complex phenomena. When the surface of a PV module has a higher temperature than the snow and ice set on it, the transfer of heat will cause the melting of ice and snow. For tilted panels, water will run down them. Melting is produced also by increasing of snow and ice temperature, due to the solar irradiation (Ross 1995).

4.2.2 Solutions to snow and ice removal

Different solutions can be mentioned and proposed to intensify the snow and ice removal from PV surfaces, in order to increase the system's energy production. The solutions prosed do not concern the consume of additional energy. Furthermore the snow sliding off the solar cells on the roofs, should not constitute a danger to people walking next to the building or an obstacle to building entrances, pathways, etc. (Jelle 2013).

Manual clearing is not considered a possibility because it was observed that human error is often responsible for the breakage of equipment (Ross 1995).

The architectural solution

The panel tilt angle not only affects snow and ice accumulation on a PV panel, but, through gravity, it determines the force motivating the snow or ice to slide off the panel. The tendency of snow or ice to slide off the panel is related to the sine of the panel tilt angle (Ross 1995).

Further observation studies have been conducted recently by Marion at al. (2013). Six PV systems situated with different tilt angle (from 15° to 35°) and different array types (roof-mounted and rack ground-mounted) were monitored in different locations (Colorado and Wisconsin) to collect PV performance data. This research lead to an interesting result. A linear relationship was found between snow amount sliding away and the sine of the tilt angle β for roof-mounted systems and ground rack-mounted systems.

In conclusion an optimal tilt angle should be chosen to design PV-array, in order to favourite the snow sliding and increase the energy harvesting.

The wind solution

Miscellaneous studies treating computer simulations of snowdrift and snow accumulation regarding buildings have been carried out. Bang et al. (1994), Tominaga et al. (2009) and Okaze et al. (2010) focused on finding methods for simulations of wind and snowdrift around

building construction. Such and similar investigations may give ideas as how to utilize the wind to remove snow from solar cell panels (Jelle 2013).

The water solution

Another idea consists in applying water in such a way that from the beginnings now and ice will not stick to the panel surface. Notice that the water application must not require any energy consumption (Jelle 2013).

The material solution

Modifications of the panel surfaces may easily alter the snow friction (Ross 1995).

The wettability of the surfaces has been studied for a long time, to try to create water-repellent and self-cleaning surfaces. Researchers created interesting solutions thank to the possibility of designing the surfaces at a nano-scale.

The repellent-answer of a surface to the presence of snow and ice was defined "icephobicity". Literally it means "fear of the ice" and it refers to the formation and accumulation of ice and snow on the solar panels (Hejazi et al. 2013). This phenomenon has been investigated in the recent years, trying to design a successful icephobic surface. The observation of water-repulsion phenomenon constituted a great help in that way.

4.2.3 Conclusion and chapter statement

An overview to the possible solutions to the problem of snow and ice removal leads to different answers. The most realizable and practise ones seem to be the architectural and material solutions.

The first one has been deeply investigated in Chapter 2. The second one is going to be explored in this chapter.

The first part of the study will set theory of the behaviour of water and ice on a surface, as far as this phenomenon has something in common with icephobicity. The wettability of the surfaces has been studied for a long time, to try to create water-repellent surfaces; therefore it can help in the comprehension of icephobicity.

The second part of the chapter will focus on water-repellent and icephobic design of surfaces, to establish the properties that they should have to reach icephobic behaviour.

The third part of the study will introduce the robustness and durability problem.

Finally the conclusions and the state-of-the-art are presented.

4.3 Icephobicity

4.3.1 Definition

"Icephobic" is a new term that has been introduced only in the recent years, so different meanings are given to it by researches. Finally Hejazi et al. (2013) established a definition related to the three anti-icing properties: freezing prevention or delay of condensed water vapour, freezing prevention or delay of incoming water and weak solid to ice adhesion strength. This phenomenon will be detailed in the following chapters.

The anti-icing properties are described by two different parameters. The first one is the median nucleation temperature T_N at which ice nucleates in a sessile water droplet placed on a surface when entire droplet/surface/surrounding gas system is cooled in a slow, quasi-steady manner. The second one is the average nucleation delay time τ_{av}, that refers to the average time required for ice to nucleate in a supercooled droplet when the droplet is maintained at the thermal equilibrium with its surroundings.

4.3.2 Nucleation

The classical nucleation theory shows that when an amount of liquid is exposed to temperature below its equilibrium state, it will stay in a supercooled state for some amount of time, until it reaches a certain temperature. In those conditions a very small volume of liquid will start crystallizing, so that the freezing process begins.

The crystallization process consists of two major events: nucleation and crystal growth. Nucleation is the step where the solute molecules dispersed in the solvent start to gather into clusters, on the nanometer scale. When stability is reached, these stable clusters constitute the nuclei. However, when the clusters are not stable, they dissolve. Crystal growth is the step where the clusters need to reach a critical size in order to become stable nuclei. The critical size is

$$r_c = \frac{2\gamma_{IL}}{\Delta G_{f,v}} \qquad\qquad 1(4.1)$$

where γ_{IL} is the ice-water interfacial energy and $\Delta G_{f,v}$ is the volumetric free energy difference per unit volume between water and ice. The nucleation theory also shows that the roughness radius of curvature R has a strong bearing on ice nucleation when its value is near the critical nucleus radius r_c.

Depending upon the conditions, supersaturation can drive to predominant nucleation or crystal growth over the other, and as a result, crystals with different sizes and shapes are obtained. Once the supersaturation is exhausted, the solid–liquid system reaches equilibrium and the crystallization is completed.

Nucleation is called "heterogeneous" if it occurs at nucleation sites on surfaces in the system and "homogeneous" if it occurs away from a surface. In most situations heterogeneous nucleation is more common than homogeneous nucleation. In fact the first one reduces the nucleation barrier by lowering the surface energy cost of forming a nucleus (ΔG). It can be altered through the parameters of ice–water contact angle θ_{IL} and roughness radius of the curvature R. Another parameter to be considered is the contact area A between the droplet and the surface. To delay icing in a supercooled droplet on a surface it should be minimized.

Ice nucleation rate (J) is used to understand the role of ice nucleation in crystallization events:

$$J = K^{\left(\frac{-\Delta G}{k_B T}\right)} \qquad\qquad (4.2)$$

where J is a kinetic prefactor representing the attraction of free water molecules to a forming ice embryo, ΔG is the minimum stable size a nascent ice crystal needs to be reach to initiate freezing and k_B is the Boltzmann constant.

4.3.3 Moisture condensation

When the air temperature drops below the dew point, water vapour in the air becomes liquid and condensation occurs. Therefore, an icephobic property is avoiding or delaying moisture condensation so that freezing of that liquid cannot occur.

Frosting is the process of water desublimation onto a cold surface, often forming small ice crystals. Frost usually forms during winter nights when temperature drops and melts quickly in sunlight of the day.

4.3.4 Snow

Snow consists of flake of crystalline ice, formed in clouds and fallen to ground via precipitation. Snow will form at temperature below 0°C, but it can fall even when the ambient air temperature is above the freezing point (Andenæs et al. 2015).

Therefore, another icephobic property is avoiding the deposition of snow on the surface, so that its adhesion to it will not occur. This one affected by many factors such as the surface's roughness and composition, as well as the atmospheric temperature and wind velocity. The temperature of the ground also alters the adhesion behaviour of snow, below -1°C or -2°C the snow is dry but above that, a thin layer of water covers the ice, creating wet ice with properties between that of ice and water.

4.3.5 Ice adhesion

Ice is water that freezes on a surface at a temperature below 0°C. Ice is visually transparent with a high transmittance of solar radiation, but unless quickly melted it can compromise the effect of the solar panel's coating.

Once freezing process is completed, another icephobic characteristic that surfaces may have is low solid-ice adhesion. It depends on the nature of the substrate, the ice and the mode of fracture (Fillion et al. 2014). Another physical factor that affects ice adhesion to a surface is particle size, as shown lately.

Ice can undergo two different mode of fracture, as shown by Nosonovsky and Hejazi (2012): opening crack (mode I) and edge sliding crack (mode II), which correspond to reaching the normal (τ_{xy}) and shear loading (τ_{yy}) (Fig. 4.1).
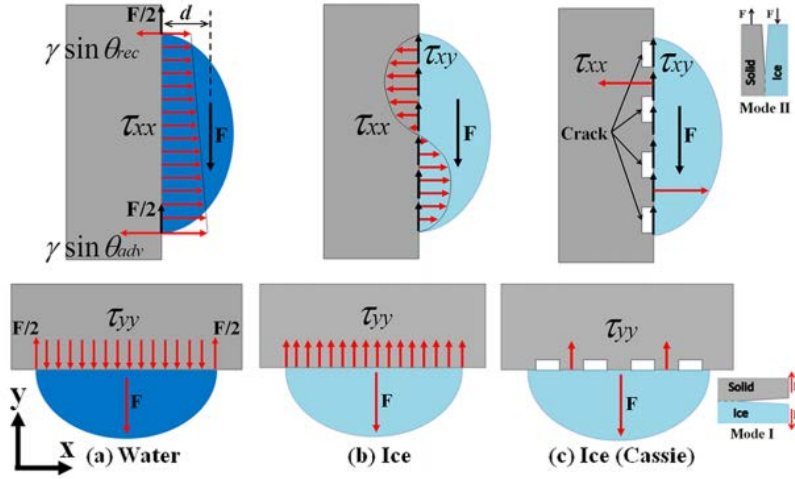
Fig. 4.1. Cracking mode I (opening crack) and II (edge sliding crack) between the surface and water (a), ice (b) and ice in a Cassie-Baxter state (c) (Nosonovsky et Hejazi 2012).

For instance the shear loading is defined as

$$\tau_{yy} = \sqrt{\frac{EG}{\pi a}} \tag{4.3}$$

where τ_{yy} is the critical strength above which the fracture occurs, E is Young modulus, G is surface energy and a is the crack length.

The surface energy can be explicit by the following equation

$$G = \gamma_{IA}(1 + \cos\theta) \tag{4.4}$$

and

$$\cos\theta = (\gamma_{SA} - \gamma_{SI})/\gamma_{IA} \tag{4.5}$$

where θ is the contact angle (CA), γ_{IA} is the tension force ice-air, γ_{SA} is the tension force solid-air and γ_{SI} is the tension force solid-ice.

When the crack is opening only the receding value matters, so equation (4.3) becomes

$$\tau_{yy} = \sqrt{\frac{EG_{rec}}{\pi a}} \tag{4.6}$$

where G_{rec} is the surface energy of the crack and it is given by

$$G_{rec} = \gamma_{IA}(1 + \cos\theta_{rec}) \tag{4.7}$$

where θ_{rec} is the receding angle and γ_{IA} is the tension force ice-air.

93

4.3.6 Icephobic surfaces

Icephobic surfaces are being designed to reduce ice adhesion and to delay water freezing on them. Physical characteristics desired for icephobic surfaces are often the same that water-repellent surface have. Water repulsion is a phenomenon that has been intensively studied for much more decades, so answers to this research could be found in surfaces that already exists. Therefore, next chapters investigate water repulsion phenomenon and surfaces specialized in that role.

4.4 Water repulsion

4.4.1 Wetting behaviour on a solid surface

The contact angle θ is the angle where a liquid–vapour interface meets a solid surface. A given system of solid, liquid, and vapour at a given temperature and pressure has a unique equilibrium contact angle.

A surface is called "hydrophilic" if contact angle is less than 90° and "hydrophobic" if contact angle is more than 90°, as shown in Fig. 4.2.
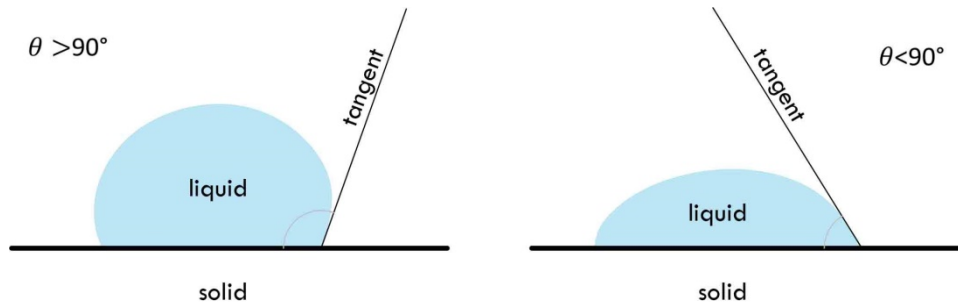
Fig. 4.2. Hydrophobic (left) and hydrophilic (right) behaviour of a water droplet on a generic surface.

For a smooth and chemically homogeneous solid surface, the contact angle θ of a drop can be calculated theoretically. First the balancing the vertical components of interfacial tension forces is developed:

$$\gamma_{LA} \cos \theta + \gamma_{SL} = \gamma_{SA} \qquad (4.8)$$

where γ_{LA} is tension force liquid-air, γ_{SA} is tension force solid-air and γ_{SL} is the tension force solid-liquid (Fig. 4.3).
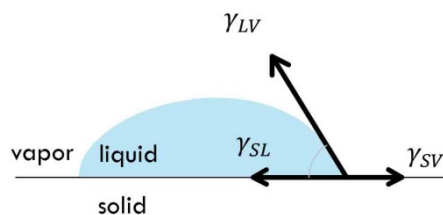
Fig. 4.3. Tension forces (γ_{LA}: liquid-air, $\gamma_{SA:}$ solid-air and γ_{SL}: solid-liquid) created by a water droplet on a generic surface.

From (4.8) Young equation is easily found:

$$\cos\theta = \frac{\gamma_{SA} - \gamma_{SL}}{\gamma_{LA}} \tag{4.9}$$

If solid-air interfacial energy is higher than the solid-liquid interfacial energy ($\gamma_{SA} > \gamma_{SL}$), $\cos\theta$ will be positive, so $0° < \theta < 90°$ and the liquid is said to "partially wet the surface". If solid-air interfacial energy is lower than the solid-liquid interfacial energy ($\gamma_{SA} < \gamma_{SL}$), $\cos\theta$ will be negative, so $90° < \theta < 180°$ and the liquid is said to "not wet the surface".

Therefore, the surface hydrophobicity increases with the decreasing value of the surface free energy of the solid-air interface (γ_{SA}). Further increase of the hydrophobicity requires manipulation of the surface topography.

Considering a rough surface, when a drop deposits on a surface and the bottom penetrates in the asperities, it is called in a Wenzel state (Fig. 4.4). The increase of the surface roughness, due to the presence of the texture, amplifies the natural response of the surface to the presence of water. The apparent contact angle is described by the Wenzel equation:

$$\cos\theta_W = r\cos\theta \tag{4.10}$$

where θ_W is the apparent contact angle, observed by a microscope, r is the ratio between the true surface area over the projected area, θ is the contact angle.
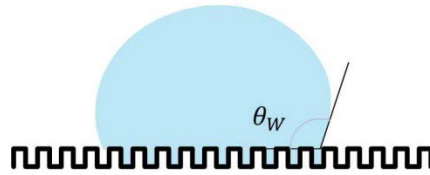
Fig. 4.4. Water droplet on a generic surface in a Wenzel state.

As the surface roughness of the surface hydrophobicity increases, it becomes unlikely for water to completely follow the surface topography of a hydrophobic substrate. Air may be trapped between water and the surface texture. This condition in called Cassie-Baxter state (Fig. 4.5) and it is described by the Cassie equation:

$$\cos\theta_{C-B} = f_1\cos\theta_1 + f_2\cos\theta_2 \tag{4.11}$$

where θ_{C-B} is the apparent contact angle, observed by a microscope, θ^1, θ^2 are the contact angles on two different kind of materials and f^1, f^2 are the surface fractions of material 1 and 2, respectively.
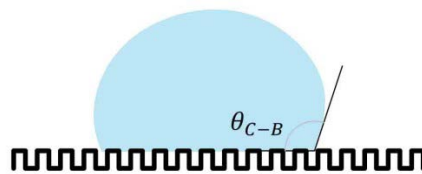
Fig. 4.5. Water droplet on a generic surface in a Cassie-Baxter state.

Most likely the transition from Cassie-Baxter to Wenzel state is an irreversible process, since the droplet in Wenzel state in more energy favourable.

There are five techniques that can be employed to measure the contact angle: static or sessile drop method, tilted-drop measurement, Wilhemly plate method, captive air bubble method and capillary rise method. The static or sessile drop method and tilted-drop measurement are the most common.

In the static or sessile drop method the experiment normally calls for the successive addition of fluid droplets. The largest possible drop that can stay without increasing the interfacial area between the drop and the solid has a contact angle called "advancing contact angle" (θ_{adv}). As the volume is removed from the drop, the contact angle formed just before the droplet recedes is referred to as the "receding contact angle" (θ_{rec}), as shown in Figure 4.6.

Fig. 4.6. Static drop method to measure the advancing θ_{adv} (left) and receding θ_{rec} (right) contact angle of a water droplet on a generic surface.

In the tilted-drop measurement a droplet is added to a surface with an increasing tilted angle. The advancing and receding angles are measured when the droplet reaches a point where it almost moves (Fig. 4.7). This technique is useful to measure both the receding and advancing contact angles at the same time.
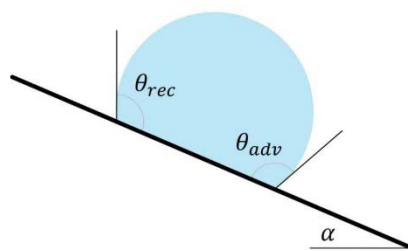
Fig. 4.17. Tilted-drop method to measure the advancing θ_{adv} and receding θ_{rec} contact angle of a water droplet on a generic surface.

The difference between the advancing and the receding angle is called "contact angle hysteresis" (Fig. 4.8).
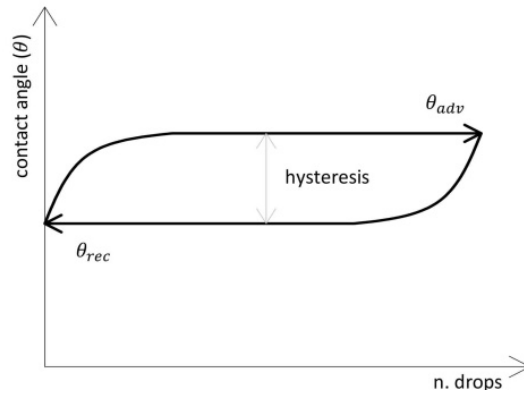
Fig. 4.8. Measurement of the contract angle hysteresis in a number of drops versus contact angle θ value graph.

Another parameter to consider to define wettability of surface is contact time. When a drop impacts a solid without wetting it, it can fully bounce, with a remarkable elasticity. We measure how long the drop remains in contact with the solid during the shock, a question which is reminiscent of the famous Hertz problem (contact time of a solid ball bouncing on a solid), but raised here for a liquid ball. Our findings may help quantifying the efficiency of water repellent surfaces. The way a water drop of radius R deforms during its impact on a highly hydrophobic solid principally depends on its impinging velocity v. The Weber number

$$We = \frac{\rho R v^2}{\sigma} \qquad (4.12)$$

compares the kinetic and surface energies of the drop, noting the density ρ and the surface tension σ. The higher We, the larger the deformations during the shock.

4.4.2 Superhydrophobic surface

Surfaces that exhibit apparent contact angle greater than 150° and contact angle hysteresis lower than 10° are called "superhydrophobic" surfaces. These surfaces have attracted significant attention within the scientific community over the last two decades because of their unique water-repellent and self-cleaning properties (Fig. 4.9). In fact a droplet that rolls off on a surface has the ability to drag the dirt away (Midtal and Jelle 2013).
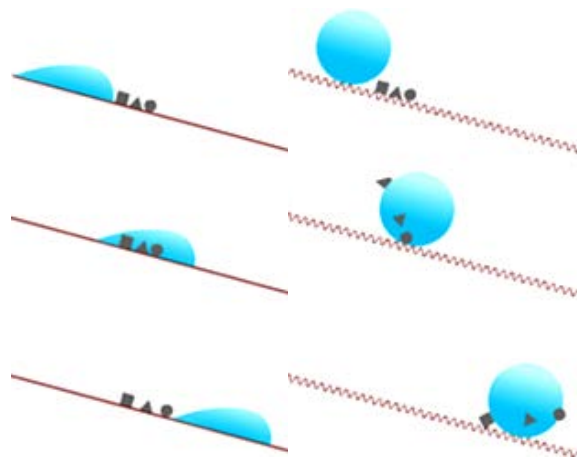
Fig. 4.9. Water carries dust particles away much more efficiently on a hydrophobic surface (right) than on a hydrophilic surface (left) (http://www.hk-phy.org/atomic_world/lotus/lotus02_e.html)

Superhydrophobic droplets usually are in a Cassie-Baxter state, which is reached when a surface is highly rough. Therefore, research focused on designing a texture that has these properties, referring also to superhydrophobic existing natural surfaces as the lotus leaf.

Until now, procedures of roughening the surfaces followed by hydrophobization or transforming low-surface-energy materials into rough surfaces have been commonly used to produce superhydrophobic surfaces. Numerous approaches have been attempted, including wax solidification, lithography, vapour deposition, templating technique, polymer reconformation, sublimation, plasma etching, electrospinning, sol-gel processing, electrochemical methods, hydrothermal synthesis, metal-assisted etching, layer-by-layer deposition and one-pot reaction. Some of these methods are here explained, referring to an overview made in 2010 by Xue et al. and synthetize in Table 4.1, other methods have been described by Xu Deng (2013).

Table 4.1. Hydrophobization methods analysed by interaction between substrates and coatings, roughness formation and type of hydrophobization (Xue et al. 2010).

Method	Interaction between substrates and coatings	Roughness formation	Hydrophization
Covalent layer-by-layer assembly	Covalent bonding	Nanoparticle-induced micro/nanostructure	Using low-surface-energy chemicals
Polymer film roughening	Polymer film itself as substrate or polymer binding	Phase-separation-induced porous structure of a multicomponent mixture	Hydrophobic polymer itself
Chemical vapour deposition	Covalent binding and/or polymer binding	Growth of nanostructures by polymerization	Polymerized structure itself
Sol-gel process	Covalent binding and/or adhesion	Rough coating	Using low-surface-energy chemicals
Hydrothermal synthesis	Covalent binding	Hydrothermal growth of nanostructures	Using low-surface-energy chemicals
Coating with composites of nanoparticles	Covalent bonding and/or polymer binding	Nanoparticle-induced micro/nanostructured	Using low-surface-energy chemicals or hydrophobic polymers

The most used methods are here described.

Layer-by-layer assembly is a versatile way to modify surfaces, usually through the construction of a film of nanoparticles. The interaction between the first layer and the substrate is activated by residual functional groups, marked by letters A and C, which react with low-surface-energy agents for covalent hydrophobization (Fig. 4.10) (Xue et al. 2010).
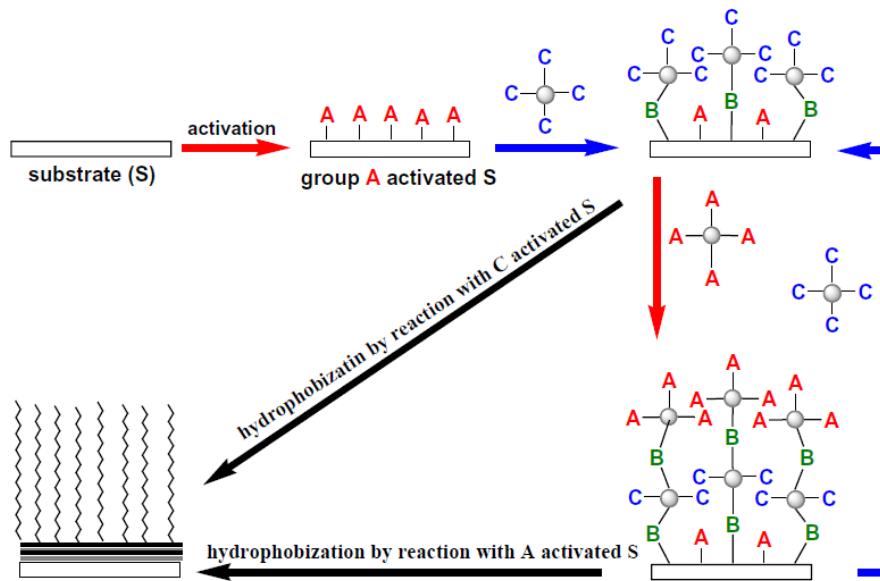
Fig. 4.10. Generic process of the covalent layer-by-layer assembly (Xue et al. 2010).

In polymer film roughening cooling or solvent evaporation can make a stable mixture go unstable. This mixture will separate into two phases, one of which might be a solid, so a lotus-like structure with micro and nano papillae is created (Xue et al. 2010).

In the method of chemical vapour deposition (CVD) gaseous reactants are deposited onto a substrate to form a non-volatile solid film. Changing the gaseous reactants and the reaction conditions different morphologies can be realized on the substrate (Xue et al. 2010).

Sol–gel processing is a method of synthesizing gels and nanoparticles. It is used to crate protective coatings, thin films and fibres, nanoscale powders. The surface roughness can be easily changed by alterating the composition of the reaction mixture (Xue et al. 2010).

Hydrothermal synthesis usually includes two steps (Fig. 4.11). First, ZnO micro/nanostructures are grown in a basic solution of Zn2+ on the target substrate, which might have been pretreated by ZnO seeding. Then polymers and small molecules hydrophobize ZnO layer. This wet chemical route could be applied to a variety of substrates, such as silicon wafers, glasses and even polymer surfaces, regardless of their irregular shapes or curved surfaces. (Xue et al. 2010)
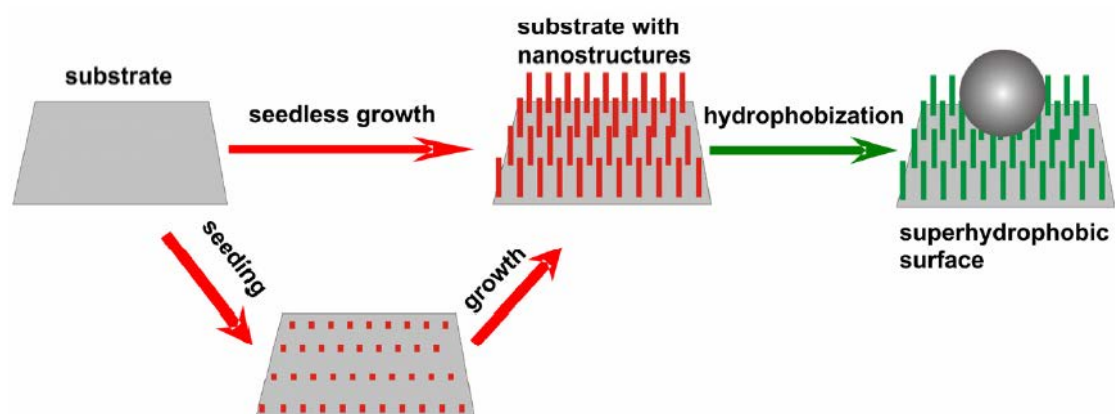
Fig. 4.11. Generic process of the hydrothermal synthesis (Xue et al. 2010).

To improve the coating rate and the durability of superhydrophobicity, particles or/and textile substrates are usually modified by introduction of functional groups, such as carboxyl, amino, epoxy and hydroxyl groups. In this way, the particles can covalently react with each other and with the textile fibers to form a firm coating. The remaining functional groups on the coating surface can then facilitate further hydrophobization with low-surface-energy materials. (Xue et al. 2010)

Templating is a direct way to replicate 2D or 3D patterns or shapes of a surface. The surface to be templated is covered with a suitable material, typically a polymer. This material is removed when the shape of the template is defined. However, this method is not suitable for many materials, especially for inorganic materials. (Xu Deng 2013)

Plasma-based etching processes are other hydrophobization methods. Roughness is created polishing the surface matrix, which reacts in different ways to plasma. This method can generate uniform roughness at large scale, but it is quite energy consume and expensive. (Xu Deng 2013)

Electrospinning is a method to generate continuous ultrathin fibres with micrometer and sub-micrometer diameters from a variety of polymeric materials. (Xu Deng 2013)

In photolithographic approaches, a photoactive polymer layer is irradiated by UV, X-ray and e-beam light which passes through a featured mask. Then the polymer is submitted to other processes until it reaches the desired roughness. This method is not used industrially because it is still very expensive. (Xu Deng 2013)

The metal-assisted etching process on Si surfaces involves deposition of metal nanoparticles 8Au, Pt, Ag, etc.) on the Si surface and etching of the metal coated Si in HF/oxidant solutions. The metal particle density will decide the roughness of the surface.

4.4.3 Superhydrophobic surfaces for photovoltaic panels

As discussed previously, many approaches to fabricate superhydrophobic surfaces are based on certain roughness and surface is covered by low surface energy material. However, the mechanical stability is the most challenging problem for these surfaces. In fact nano-roughness can be easily destroyed by external force. Moreover the adhesion of the coating to the substrate is usually weak.

For photovoltaic applications high transparency is another characteristic that these surfaces should have. In general, transmittance decreases with increasing roughness, especially if the roughness exceeds the wavelength of light. So reducing the roughness below a certain value, to achieve high transparency is another challenge.

Therefore, some experiments have been done on solar cells in order to obtain a superhydrophobic, transparent and anti-reflective layer are here reported. Moreover these devices have been tested in the long-term period, to verify the long-lasting efficiency of these surfaces. The following study are analysed and compared between each other to understand which is the most efficient surface treatment that could undergo also icephobicity tests.

4.4.3.1 Investigating different surface nanopatterns

J. Son et al. (2011) executed two nanopatterning methods on glass surfaces to obtain a solution with nanopillars and a solution with nanoholes, as it is shown in Figure 4.12. In the nanopillars process the glass surface is covered with a mask of Ni. This 10 nm –thick layer is annealed al 600°C for 5 min to obtain randomly distributed nanoparticles with diameters less than 100 nm. After a plasma-reactive etching process the glass substrate is transformed in nanopillars array. At the end the nanoparticles are removed (Fig. 4.12.a).

In the nanoholes process the glass surface is covered with a mask of Al. This 200 nm –thick layer is anodized and pore widened for 80 min in a phosphoric acid to obtain randomly distributed holes with diameters from 50 to 70 nm with ~100 nm of spacing. After a dry etching process the glass substrate is transformed in nanoholes array. At the end the Al layer is removed through anodized aluminium oxide removal (AAO) removal (Fig. 4.12.b).
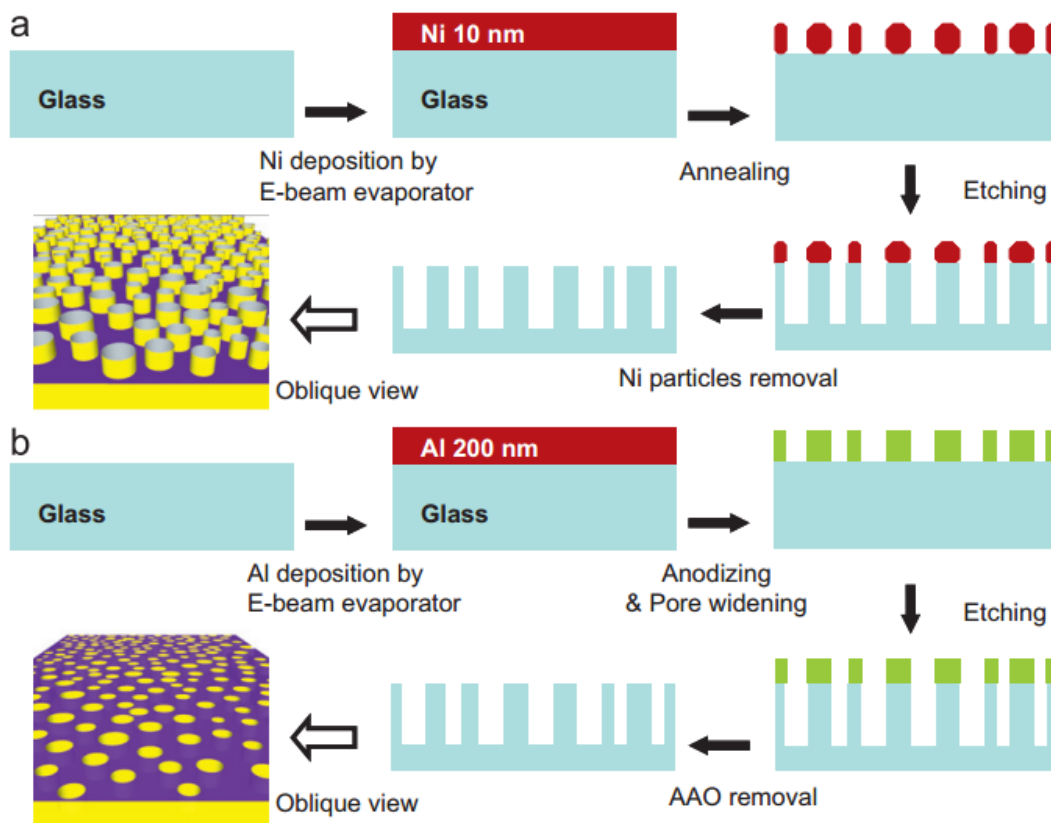
Fig. 4.12. Nanopatterning methods with nanopillars (a) and nanoholes (b) (Son et al. 2011).

Then different hydrophilic, hydrophobic, superhydrophilic and superhydrophobic surfaces where obtained through different treatments of the surfaces. Focusing on superhydrophobic ones, patterned and bare glass was exposed to PFTS in a desiccator under vacuum for 5 h that created a gas-phase evaporation.

Surface morphology was investigated by a SEM. Bare glass exhibits a CA of 125°, while patterned exhibits CA of 170° and 167° for nanopillars and nanoholes treatments respectively. The superhydrophobic character is reached because these patterns leave trapped air between

water and the nanostructural surface, so contact area is reduced and water undergo a Cassie-Baxter state.

The transmittance parameter is about 95% between 500 nm and 700 nm for both nanopatterned surfaces. It decreases to 94% between 400 nm and 500 nm and between 700 nm and 100 nm. With the PFTS treatment the transmittance is reduces only between 400 and 600 nm, much more drastically in nanoholes surface than in nanopillars surface. However, transmittance results greater than the condition of simple glass surface, which presents a quite constant value of 92%. In conclusion this treatment improves also the anti-reflective properties of the glass surface (Fig. 4.13).
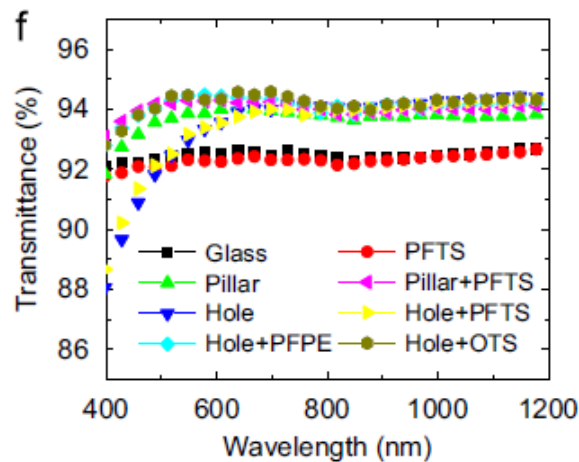
Fig. 4.13. Wavelenght (nm) versus transmittance (%) for different coatings (pillar, hole, hole+PFPE, PFTS, pillar+PFTS, hole+PFTS, hole+OTS) on glass sample (Son et al. 2011).

The durability of the different coatings on solar panels was tested by exposing them from 3 months (12 weeks) on the roof of a 35 m –tall building in Singapore (1° 18' N). The average temperature was 23°C and the precipitation was of an average of 195 mm monthly. The solar panel had a tilting angle of 23°.

There was a constant decrease of the contact angle that brought to 150° for nanoholes with PFTS, to 140° for nanopillars with PFTS. The self-cleaning effect of the PFTS treatment fades away gradually because of the sticky dirt on the surfaces (Fig. 4.14.b).

Transmittance was quite constant at 400 nm for both the coatings. There was a 2% decrement al 800 nm, though. The optical transmission is affected by the dirt particles on the panels as well. The efficiency and the short circuit current of the solar cells are closely related to the reduction of the optical transmission. The PFTS nanopatterned glass shows a decrease in efficiency of 2.62% after 12 weeks, that is quite low compared to the efficiency decrease of bare glass (7.79%) (Fig. 4.14. c,d).

In conclusion patterned glass with nanopillars seems a good way to create a superhydrophobic and anti-reflective glass for efficient solar cells. Next step will be to improve the design of these nanopillars.
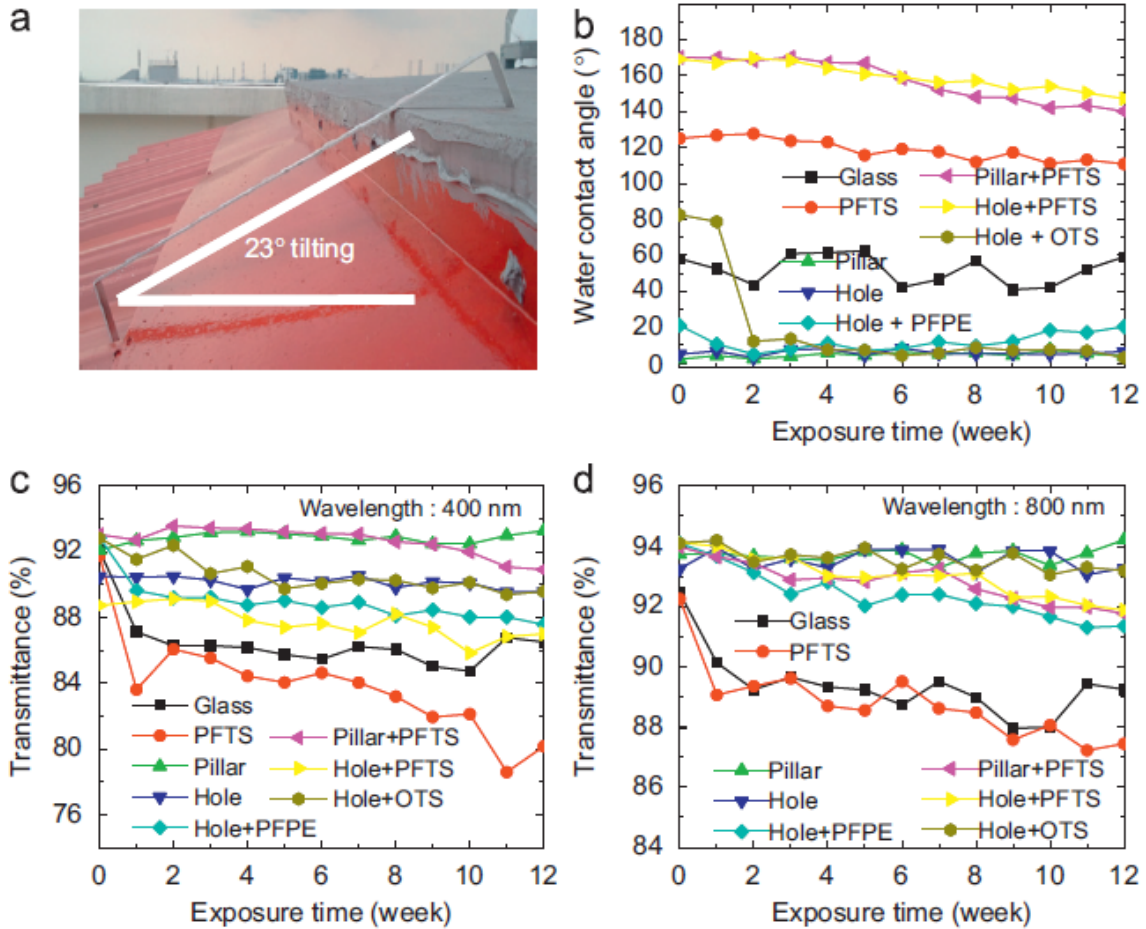
Fig. 4.14. (a) Tilting angle of photovoltaic devices in outdoor test. (b) Exposure time (week) versus water contact angle (°) for different surface coatings. (c) Exposure time (week) versus transmittance (%) for different surface coatings at wavelength 400 nm. (d) Exposure time (week) versus transmittance (%) for different surface coatings at wavelength 800 nm.

4.4.3.2 Investigating surface treatments

The same group of researchers (J. Son et al. 2013) used a different anodizing method to create a 6x6 inch^2 area Al film on a dielectric substrate using grid line contacts. The proposed anodizing method can be considered as an alternative technique for the fabrication of large area nanostructures, which can find applications in the photovoltaic industry.

Five different locations on a textured glass were individuated for samples. The optical transmittance from 550 nm to 1000 nm is 2-3% higher for patterned glass than for un-patterned glass, reaching also 95% (Fig. 4.15).
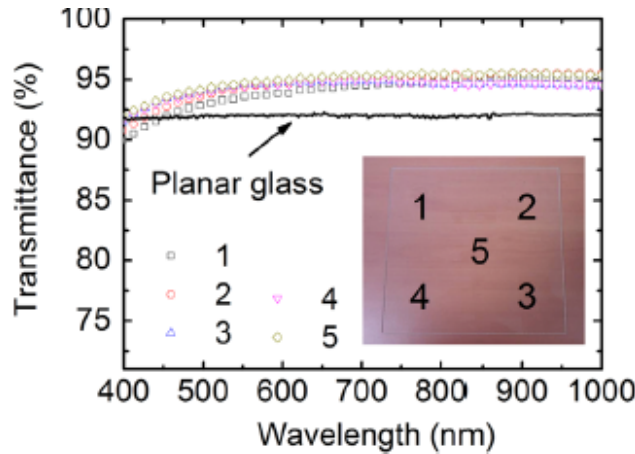
Fig. 4.15. Wavelenght (nm) versus transmittance (%) for different 5 different treatments on glass sample (Son et al. 2011).

5x5 crystalline solar cells were tested indoor with a solar simulator under AM 1.5 illumination, and outdoor, on the roof of a ~30 m tall building at the National University of Singapore for 4 months with an inclination of 20°. Major improvement is observed for the short circuit current (Isc) increasing from 1.956 Å (with planar glass) to 2.178 Å (with AR glass) due to the enhanced optical transmission of the front glass, so the AR glass cell shows 11.34% higher Isc than that of the planar glass cell. Due to the increased Isc, the power conversion efficiency (ηeff) increases from 7.9% to 8.57% (Fig. 4.16).
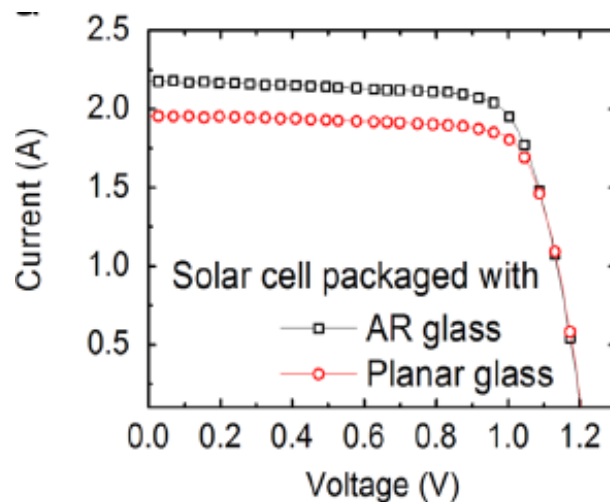
Fig. 4.16. Voltage (V) versus current (A) curves of the solar cells with an anti-reflective or planar front glass (Sakhuja et al. 2014).

Graphs of short circuit current show a quite constant value over 100 days. No measurements of contact angle were done. However, the constant efficiency of the solar cells in the long period suggests a self-cleaning property of the surface.

4.4.3.3 Investigating surface nanopattern roughness

The same process of the previous experiment was repeated by M. Sakhuja et al. (2014). A planar glass layer was provided with nanopillars high from 100 nm to 800 nm. Different cases

were study to see the influence of the height of nanopillars (planar glass, 100 nm, 200nm, 400 nm, 800 nm)on the variation of the CA and the transmission values (Fig. 4.17).
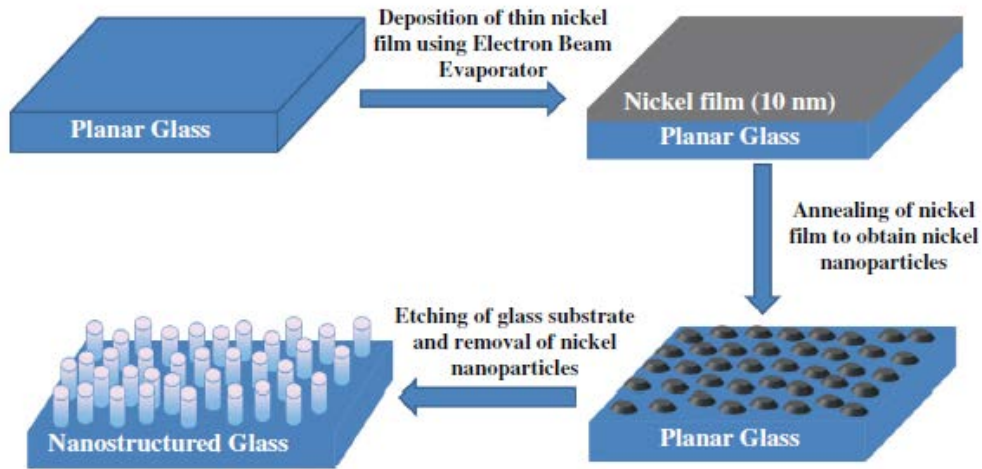
Fig. 4.17. Process to fabricate nanostructured glass samples (Sakhuja et al. 2014).

In this case, the contact angle decreases when the height of nanostructures increases. It was demonstrated that it should be the contrary, but in this case the capillary effect is very strong. The surface free energy has a similar value to the liquid free energy, so the surface becomes hydrophilic.

Transmission reached a value of 96% for 200 nm-high nanopillars between 600 nm and 1000 nm and then falls to 92% at 400 nm. This nanostructure has shown the best optical transmission. 100 nm-high nanopillars have a constant value of 93%. While 400 nm-high and 800 nm-high nanopillars present lower values of transmission that decrease drastically below 80% at 400 nm. In conclusion the ideal height for nanopillars is 200 nm (Fig. 4.18.a).

The growth of optical transmission is in contrast with the value of CA, which decreases with higher nanostructures (Fig. 4.18.b).
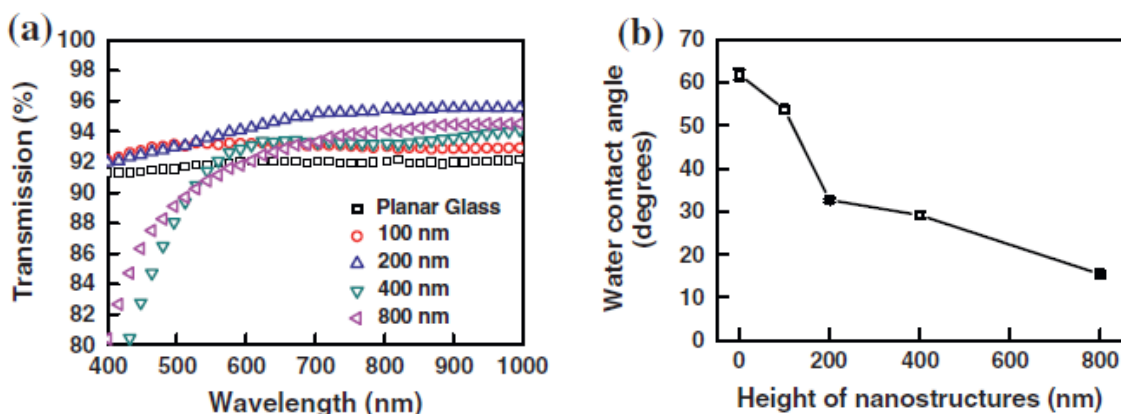
Fig. 4.18. (a) Wavelenght (nm) versus transmission (%) for coatings with different pillars heights (0 nm, 100 nm, 200 nm, 400nm, 800 nm) (a) Height of nanostructures (nm) versus water contact angle (°) (Sakhuja et al. 2014).

Furthermore durability of coatings on solar panels was tested by exposing them from 3 months (12 weeks) on the roof of a 35 m –tall building in Singapore (1° 18' N). The planar and nanostructured glass samples were mounted flat (0°) and also inclined at 10° and 20°.

A decrease in CA was shown after the first two week. In particular the 20°-tilted surface after 12 weeks demonstrated a decrement of only 2° CA.; while for the planar glass the best behaviour was for the flat one (Fig. 4.19. d).

Concerning optical transmission, there was a decrease for all the nanopatterned surfaces. After 2 weeks 200 nm-high nanopillars surface showed a ~3% decrease with 0° inclination, a ~2% decrease with 10° inclination and ~2% decrease with 20° inclination.

The inclination of 10° and 20° leads for these solar panels to a decrement in efficiency of 0.5% and 1% respectively because of the less illumination. Considering the dust accumulation, the efficiency decrement is 3% and 2.5%, though. In conclusion in this case the best solution seems to be the 20°-tilted panel (Fig. 4.19).
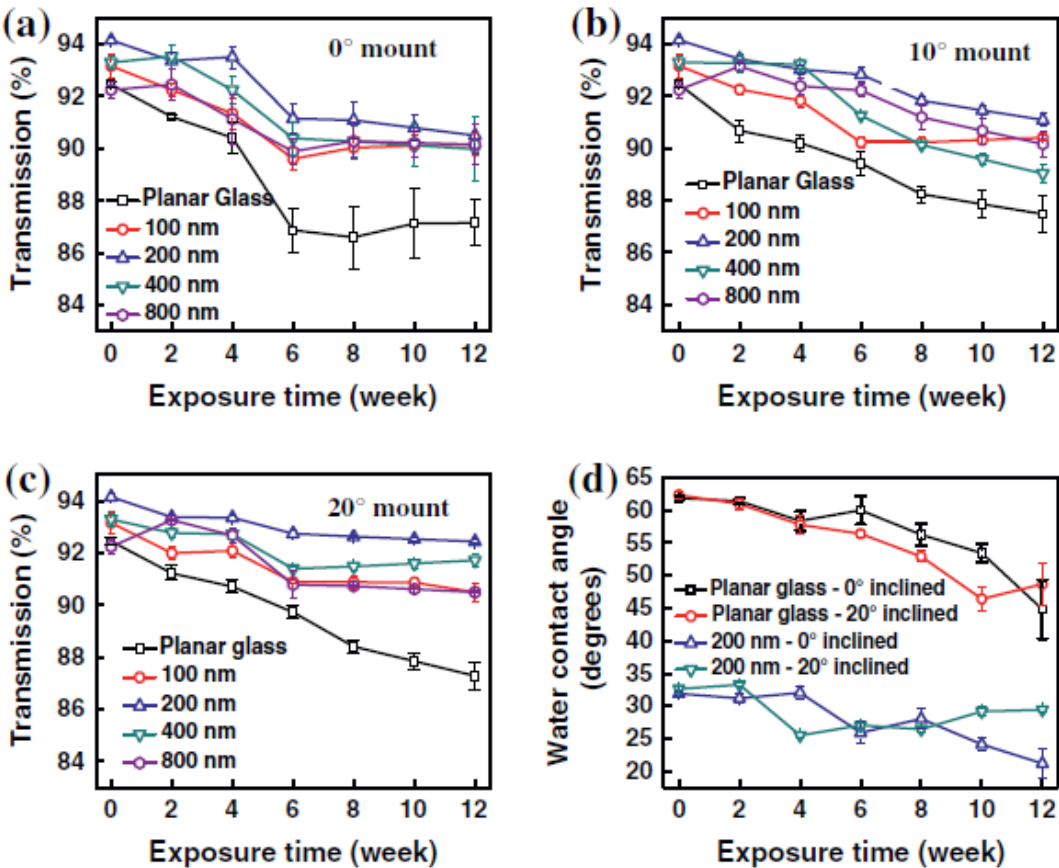
Fig. 4.19. (a) Exposure time (week) versus transmittance (%)for coatings with different pillars heights (100 nm, 200 nm, 400nm, 800 nm) for 0°-tilted panel. (b) Exposure time (week) versus transmittance (%) for coatings with different pillars height for 10°-tilted panel. (c) Exposure time (week) versus transmittance (%) for coatings with different pillars heights for 20°-tilted panel. (d) Exposure time (week) versus water contact angle (%) for planar glass tilted at 0° and 20° and for nanostructured (200 nm height) glass tilted at 0° and 20°.

At the end mini solar modules of 39.75 cm^2 were fabricated with planar and nanostructured glass and were monitored outdoor for 5 weeks. The first one had a reduction in short circuit

current density and efficiency by 5 mA/cm^2 and 2% respectively, while the second one showed better performances: reduction in short circuit current density was 1 mA/cm^2 and reduction in efficiency was 0.3% (Fig. 4.20).

In conclusion a glass surface that is treated as previously described to design a nanostructure with 200 nm–high nanopillars will provide self-cleaning and anti-reflective properties, leading to efficient and durable solar cells.
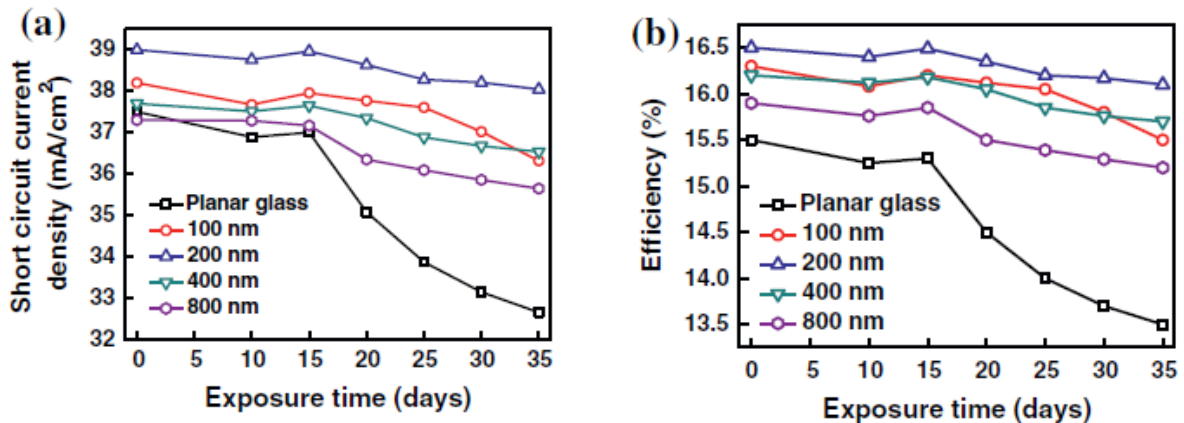
Fig. 4.20. (a) Exposure time (days) versus short circuit current density (mA/cm2) for coatings with different pillars heights (0 nm, 100 nm, 200 nm, 400nm, 800 nm). (b) Exposure time (days) versus efficiency (%) for coatings with different pillars heights (0 nm, 100 nm, 200 nm, 400nm, 800 nm) (Sakhuja et al. 2014).

4.4.3.4 Coatings on organic solar cells

Silica nanoparticles were hydrophobized with different surfactants by Šiffalovič et al. (2014): HMDS (hexaamethyldisilazane), OTS (octadecyltrichlorosilane), OTSF (trichloro 1H,1H2H,2H-perfluorooctyl silane). The morphology of the layer is characterized by an average thickness and a RMS roughness of the nanometer size, as shown in Table 4.2. This solution can easily be applied as coating granting contact angle values larger than 170°. It means that the water droplets remain in a Cassie-Baxter state because of the air trapped between the surface and the water.

Table 4.2. Parameters (average thickness and RSM roughness) of the deposited nanoparticles coatings on glass functionalized with different surfactants (Šiffalovič et al. 2014).

Surfactant type	Average thickness	RMS roughness
HDMS	602	147
OTS	513	96
OTSF	1351	1351

The rough surface brings advantages also for the optical parameters, as far as the reflectance in the visible region decreases from an average value of 7.5% (uncoated glass) to an average value of 6.5% (OTS coating). The minimum is reached at around 1100 nm with a value of ~6%; however, for photovoltaic applications a minimum in visible region would be more appropriate (Fig. 4.21).
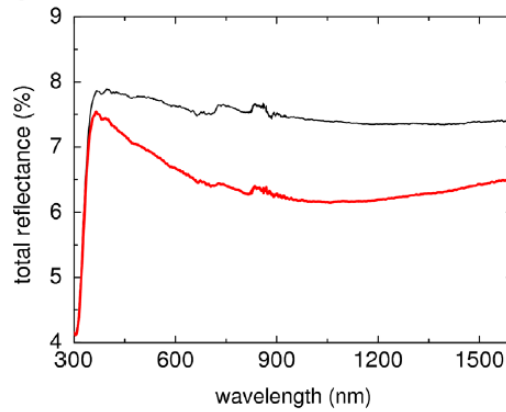
Fig. 4.21. Wavelenght (nm) versus total reflectance (%) measured at the incidence angle of 8° from the surface normal (uncoated glass - thin line, OTS functionalized monolayer coating - thick line) (Šiffalovič et al. 2014).

The coatings with OTS functionalized were applied on the front glass supporting the organic PV structure by dissolution in toluene and spincoating in ambient atmosphere. Three monolayer coating with different surfactant concentration were designed. These organic photovoltaic devices were tested in a solar simulator with 1.5 AM illumination and 100 mW/cm^2 power. Short circuit current density of superhydrophobic coatings and efficiency had a larger value than the one untreated glass, as showed in Table 4.3 and Figure 4.22.

In particular sample 3 showed an increment of ~5% of short circuit current density and an increment of ~3.2% of efficiency. Observing these results, it was found that nanoparticle cluster size should be reduced to a size of ~100 nm to create a more efficient coating. Deposition of this coating could be experimented also on silica solar cells to understand the different value of efficiency that this process would lead to.

Table 4.3. Parameters (short circuit current density and efficiency) of the photovoltaic device spincoated with OTS functionalized nanoparticles under different conditions as determined from the I-V curves (Šiffalovič et al. 2014).

Superhydrophobic coating	Short circuit current density [mA/cm^2]	Efficiency
None	6.33	2.13
#1	6.54	2.19
#2	6.72	2.26
#3	6.64	2.20
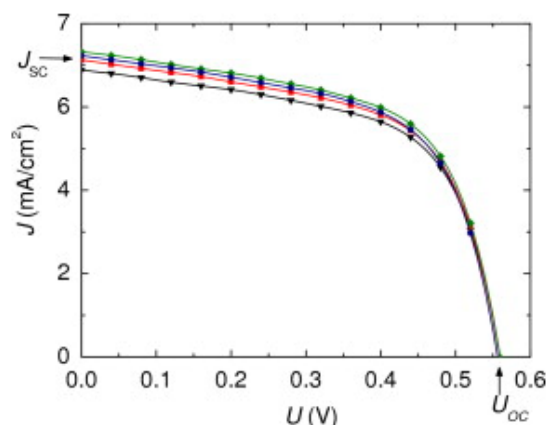
Fig. 4.22. Voltage (U) versus short circuit current density (J) under illumination of the uncoated photovoltaic device (triangles) and the device spincoated with OTS functionalized nanoparticles under different conditions as specified in Table 4.3. The coating labeling is the same as in Table 4.3 (#1—squares, #2—diamonds, #3—circles).

Durability of these nanostructured is one of the most challenging topics. Lifetime of these coatings was demonstrated to be around one month. After this period the layer can be removed and re-deposited as Verho et al. (2010) explained.

4.4.3.5 ZnO NWs on organic solar cells

Hiralal et al. (2014) reported another experiment on organic photovoltaic device. This time the authors created a ZnO nanowires coating to deposit by metalorganic chemical vapour on a glass substrate. Nanowires exhibit a diameter of 20-60 nm and a length of ~450 nm (Fig. 4.23).
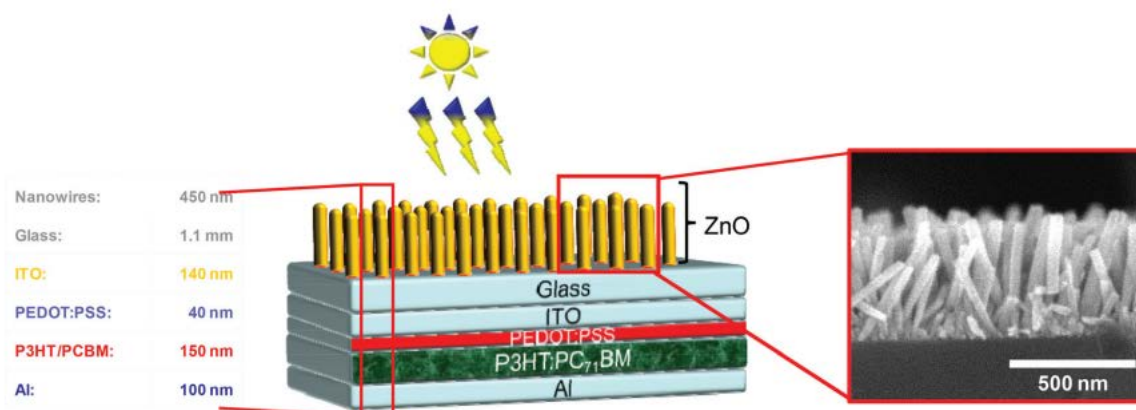
Fig. 4.23. Structure of the fabricated photovoltaic device (not to scale). The inset shows a scanning electron microscope image of the ZnO NWs. (Hiralal et al. 2014).

Organic cells showed high and constant transmittance in the visible range (~95%) and good absorbance in the UV. The coating is used as a UV-barrier, demonstrating a 50% reduction in the rate of degradation of the polymers under accelerated lifetime testing, as shown in Fig. 4.24 a,b.
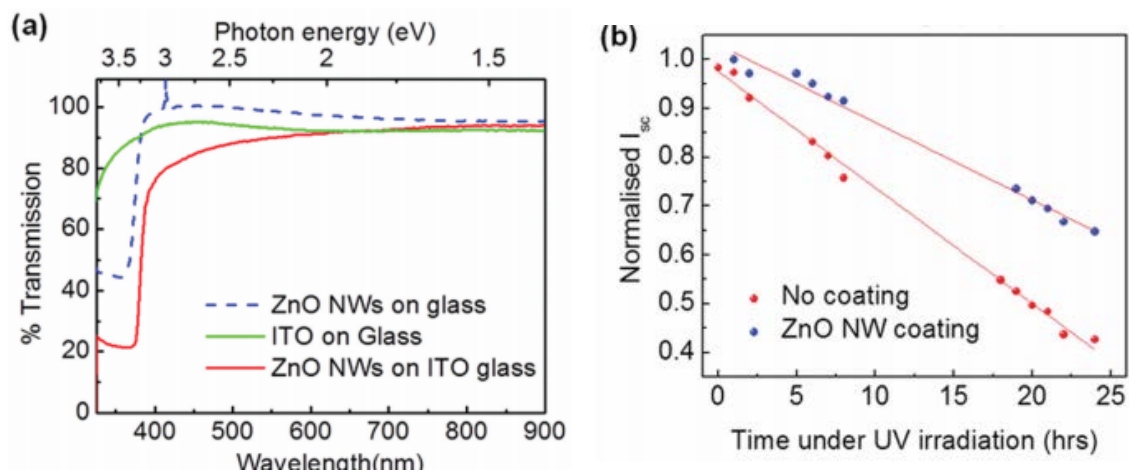
Fig. 4.24. (a) Transmission spectra of bare ITO glass, and 450 nm ZnO NWs on bare and ITO coated glass measured with a Thermoelectron UV-VIS spectrometer and (b) normalised short circuit current of P3HT– PCBM cells degraded by exposing constantly to a high intensity UV lamp.

The OPV cells were tested for different angle of incidence of the light, tilting the solar cells at 0°, 30° and 60°, to find the J-V characteristics. Efficiency reached a value of ~17% at normal incidence for the NW samples. The short circuit current increased for ~1 mA/cm^2 for every inclination of the panels, reaching values of 7.21±0.52 mA/cm^2. Efficiency reached larger values as well, as showed in Figure 4.25 and Table 4.4.

Table 4.4. Power conversion effiency for different angle from normal incidence (Hiralal et al. 2014).

	0°	30°	60°
No coating	2.30	2.25	2.00
ZnO – Worst of Batch	2.45	2.35	2.35
ZnO – Best of Batch	2.70	2.60	2.70
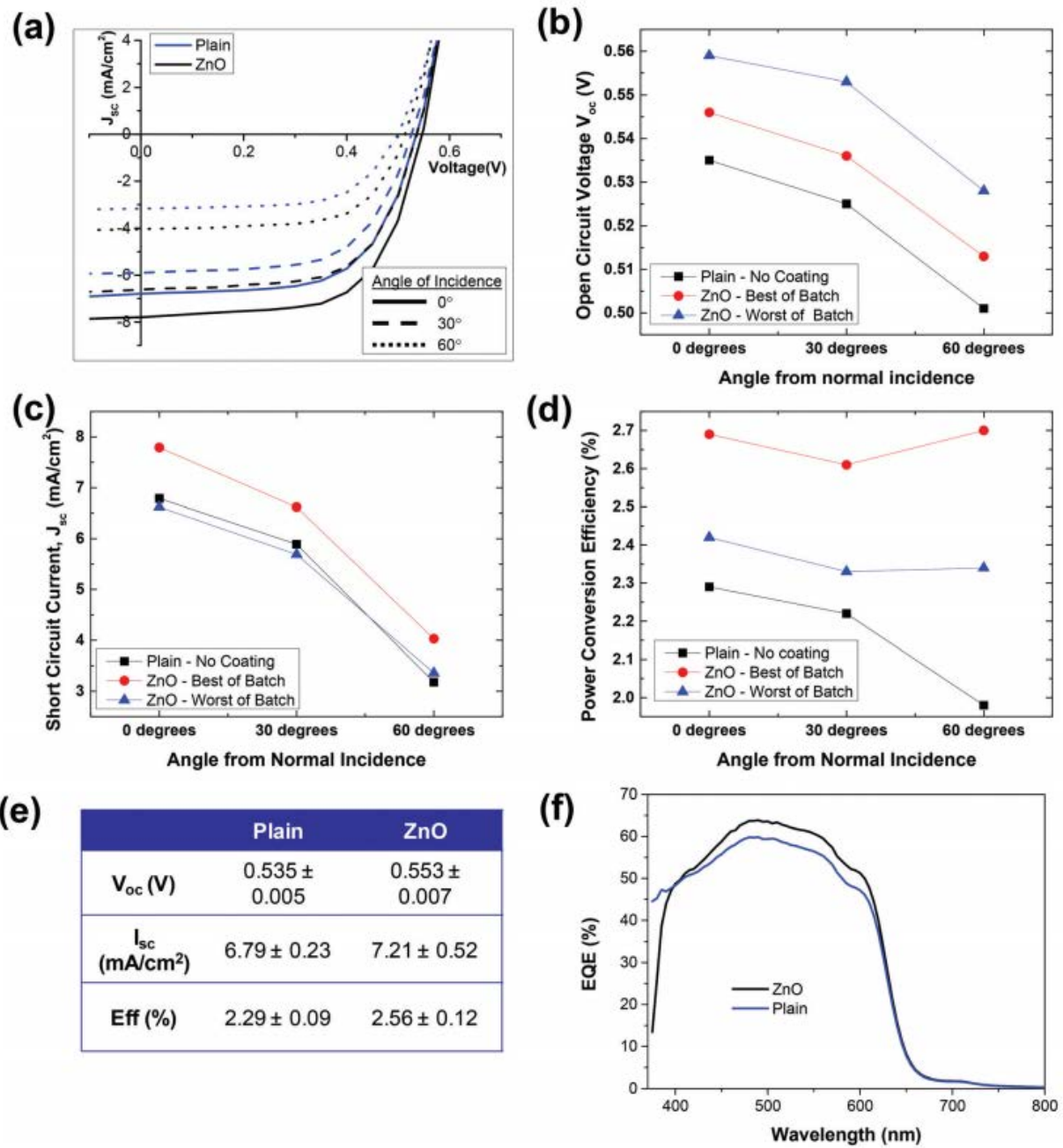
Fig. 4.25. (a) J–V characteristics of NW solar cells, (b) open circuit voltage, (c) short circuit currents and (d) efficiencies of the cells at various incidence angles of light. Note the efficiencies are corrected for light intensity change with tilt, (e) table showing average values and standard deviation for the samples measured and (f) comparison of the external quantum efficiency (EQE) of representative samples (Hiralal et al. 2014).

Superhydrophobic features can be obtained treating the ZnO NW with a layer of a hydrophobic molecule, that increases the CA from 16° to 152°.

4.4.3.6 Comments and comparison between tests

In conclusion research in the Department of Electrical and Computer Engineering in National University of Singapore (NUS) firstly focused on different types of nanopatterning (2011): nanopillars and nanoholes. Tests showed a better superhydrophobicity and anti-reflection of the surface with nanopillars. The behaviour of the layer was investigated also on PV panels for 12 weeks in outside test. Secondly the anodizing method that resulted successful in creation of nanopillars was modified and experimented on different samples with nanoholes pattern (2013). This time only anti-reflectivity and durability of the samples were tested, though. Recently these researchers investigated the most efficient nanopillars height (2014), but surfaces treatments created a surface less transparent and hydrophobic than one realized in 2011.

Therefore, the most efficient solution seems to be a surface covered by nanopillars with RMS of 200 nm, wide less than 100 nm and spacing 100 nm.

The other two tests that have been analysed refer to surfactants treatment (Šiffalovič et al. 2014) and ZnO NW on glass layer (Hiralal et al. 2014), that is then added on organic solar cells. These surfaces showed high values of CA and transmittance, durability tests highlighted the weakness of these roughness treatments, though.

In Table 4.5 the characteristics of these coatings and the results of tests are summarized:

Table2 4.5. Comparison between different surface treatments: coatings used on PV devices and submitted to durability test (Tr: transmission, CA: contact angle, RMS: roughness root-mean-square, d: diameter, s: spacing).

Article	Tr	CA	geometry	RMS	d	s
Jaesung Son et al., 2011	95%	170°	Nanopillars	200 nm	<100 nm	100 nm
Jaesung Son et al., 2013	95%	-	Nanoholes	400 nm	80 nm	100 nm
Sakhuja et al., 2014	94%	30°	Nanopillars	200 nm	<100 nm	100 nm
Šiffalovič et al., 2014	93%	170°	Nanoparticles	680 nm	50 nm	
Hiralal et al., 2014	95%	152°	ZnO NW	450 nm	30-60 nm	100 nm

4.4.3.7 Other examples

Researchers have been focusing on looking for an anti-reflective, water-repellent coating or treatment for PV. Often they have not investigated durability and robustness of the solar cells, though. However, these solutions could be analysed and completed with durability, robustness and icephobicity tests. Table 4.6 reports some of the most efficient coatings that have been created.

Table 4.6. Comparison between different surface treatments: coatings used on PV devices.

	Title	Author	Date	Method
1	Low-cost, flexible and self-cleaning 3D nanocone anti-reflection films for high-efficiency photovoltaics	Kwong-Hoi Tsui et al.	2014	coating with composites of nanoparticles
2	Fabrication of highly transparent self-cleaning protection films for photovoltaic systems	Seon-Hwan Lee et al.	2012	lithography process
3	Hybridizing ZnO Nanowires with	Yan Liu et al.	2012	hydrothermal

Micropyramid Silicon Wafers as Superhydrophobic High-Efficiency Solar Cells		synthesis	

	Transmittance	Contact Angle	Geometry	RMS
1	95-96%	156-157°	Nanopillars	325 nm
2	96%	152°	Nanocones	1000 nm
3	97%	171°	Micropyramids + ZnO NW	800 nm

Finally other studies have been done on glass, to try to create a superhydrophobic, transparent and/or antireflective surface. In some case also durability and robustness have been tested (Table 4.7).

Table 4.7. Comparison between different surface treatments: coatings used on glass surfaces and submitted to durability tests.

	Title	Author	Date	Method
1	Optically transparent superhydrophobic TEOS-derived silica films by silylation method	Sanjay Latthe et al.	sept 2009	sol-gel process
2	Transparent, superhydrophobic and wear-resistant coatings on glass and polymer substrates	Daniel Ebert et al.	july 2012	coating with composites of nanoparticles
3	Superhydrophobic antireflective coating with high transmittance	Shing-Dar Wang et al.	2013	sol-gel process
4	Durable superhydrophobic and anti-reflective surfaces for trimethylsilanized silica nanoparticles-based sol-gel processing	Michele Manca et al.	2009	sol-gel process

	Transmittance	Contact Angle	Geometry	RMS
1	84-90%	147-162°	Nanocluster	200 nm
2	87-93%	154-165°	Nanoparticles	45-84 nm
3	91-97%	158°	Nanopyramids	25 nm
4	93%	168°	Nanoparticles	90-120 nm

In conclusion superhydrophobicity is deeply related to surface roughness, that can be achieved through different geometry (nanoparticles, nanopyramids, nanowires, nanopillars, etc.) realized by different chemical treatments. Almost all studies quantify roughness using root-mean-squared (RMS) or average roughness (R_a).

Although roughness is often described only by parameters that individuate the height variation of the surface, recent studies have shown that horizontal changes in roughness play a

significant role in determining the hydrophobicity of the surface (Kwun Lun Cho et al. 2010). The fractal dimension is a parameter that quantifies the roughness of the surface across all length scale, providing information also on horizontal planes.

Several studies have shown that an increasing roughness provides an increasing contact angle, but a decreasing transmittance; therefore a compromise should be reached. Kwun Lun Cho et al. (2010) demonstrated that the surface design should present RMS<200 nm and R_a>2.6 to grant CA>165°, sliding angle <1° and Tr>90%.

4.5 Icephobic surfaces

Icephobicity is a term that has been recently introduced, therefore a unique definition is still missing. As a consequence superhydrophobic surfaces might or might not be suitable for icephobic applications (Sojoudi et al. 2016).

4.5.1 Ice nucleation mechanism and freezing delay

Eberle et al. (2014) concluded that nanostructuring of substrates enhanced icephobicity. Therefore, they tested different nanoscaled textures with RMS between 0.1 nm and 100 nm on both hydrophobic and hydrophilic surfaces at temperature down to – 25 °C. Test results were positive to both hydrophobic and hydrophilic surfaces: ice nucleation is stopped at lower temperatures than the reference aluminium substrate. To justify this behaviour a hydration layer was postulated to exist between the forming ice nucleus and the solid surface, therefore affecting θ_{IW} and the nucleation rate of ice.

Schutzius et al. (2014) found that the nucleation temperature is relatively insensitive to surface nanoroughness, when surfaces have only a fraction of the area occupied with nanoscale pits below $10r_c$ (a critical stable radius). They claimed also that designing a surface composed of an array of nanoscale pits with small asperities. In fact the energy barrier for ice nucleus formation is increased if the radius of curvature of the rough bumps is kept in contact with water smaller than the smallest stable ice nuclei. Surface roughness can maximize the solid-air fraction of the surface, reduce the wetted area fraction and so delay ice nucleation.

Schutzius et al. (2014) found also that that for droplet impact minimizing the contact time between substrate–supercooled water reduces the probability of droplet freezing. One way to minimizing the contact time is to design properly the roughness of the surface.

Daniel et al. (2013) observed a critical transition temperature, above which impacting droplets could rebound, to be 20°C to 25°C. Below this transition temperature, the droplet froze within a time less than the Rayleigh contact time:

$$t_c = 2.65 \sqrt{\frac{\rho R^3}{\sigma}} \tag{4.13}$$

Jung et al. (2011) tested both hydrophilic and superhydrophobic surfaces in order to evaluate the delayed freezing of supercooled droplets at – 20 °C (temperature for both droplet and surface) and therefore the icephobicity. The hydrophilic surface with nanometer scaled roughness (1.4-6 nm) exhibited the highest icing delay. A rough hydrophobic surface may reduce the amount of liquid that stays in contact with the surface because of his properties, though. In conclusion hydrophobic surfaces decrease the possibility of water to freeze, while hydrophilic surfaces with nanoscaled roughness delay the freezing of supercooled droplets. Therefore, icephobic coatings should be designed aiming to both these characteristics.

114

4.5.2 Moisture condensation

Varanasi et al. (2010) highlighted the transition from Cassie-Baxter to Wenzel state with decreasing surface temperature in a humid environment. This passage verifies when vapour condensates in the air pockets between rough surface and droplet and then it starts freezing because of low temperature. Frost formation can alter the wetting properties of a rough superhydrophobic surface, making it increasingly hydrophilic.

Wang et al. (2013) have tested the superhydrophobicity of surfaces at temperature of -10°C and relative humidity of 85–90%. In these conditions droplet rebounced off the surface easily under a critical value of Weber number (We_c). The value of We was found to be higher for superhydrophobic surfaces with hierarchical structures as compared to solely micro- or nanostructured superhydrophobic surfaces.

Drop impact is a critical aspect from superhydrophobic surface because the liquid meniscus may penetrate the surface texture, displacing the entrapped gas/air, causing the drop to stick on the surface (Schultzius et al. 2015). A solution to this problem can be found designing nanotextured, closed-cell geometries (Schultzius et al. 2015).

When a drop impacts on a surface, a vapour layer is generated at the solid-liquid interface. This one acts as a thermal insulator and can help droplets to rebounce off the surface. This layer can be crated sublimating surfaces at temperature below -79°C (Schultzius et al. 2015).

In conclusion in this context icephobicity refers to the ability of surfaces to prevent or delay formation of frost and sometimes to the ability of textured surfaces to prevent the Cassie-to-Wenzel transition during supercooling or during Wenzel ice formation. This one can be reached by superhydrophobic surfaces, because frost growth can be delayed via self-removal of condensed water micro-droplets (Sojoudi et al. 2016).

4.5.3 Snow

Nakajima (2004) reported that the sliding characteristics of dry snow refer to solid-solid friction; on the contrary the sliding characteristics of wet snow refer to solid-liquid friction. He concluded that sliding of dry snow is accelerated on a superhydrophobic surface and sliding of wet snow is accelerated on a hydrophilic surface. Sliding characteristics of wet snow can be controlled by introducing hydrophilic channels to a superhydrophobic surface. This could be the solution to create surfaces with a reversible superhydrophobic and superhydrophilic character for all anti-snow adhesion applications.

Two methods for measuring the friction coefficient between snow and roofing were investigated in SINTEF laboratory (SINTEF method 169, 2008). Both static (starting, resting) and dynamic (sliding, motional, kinetic) friction coefficients are treated in Method A "Friction Coefficient Determination between Snow and Roofing by Horizontal Plane Applied Pulling Force Method" and Method B "Friction Coefficient Determination between Snow and Roofing by Inclined Plane Slip Method".

Method A (horizontal plane) gives the static and dynamic friction coefficient between the roofing and packed snow, also in case of an underlayer of ice. The principle for method A is measurement of how large applied pulling force is necessary in order to pull a snow sample along a horizontal roofing (Fig. 4.26.a) .The friction coefficient μ for the roofing is given by the following:

$$\mu = \frac{R}{N} = \frac{F}{G} = \frac{F}{mg} = \frac{a}{g} = \frac{v^2}{2gx} = \frac{2x}{gt^2} \tag{4.14}$$

where R = friction force parallel with the sample surface, N = normal force on the sample surface, F = applied pulling force parallel with the sample surface, G = mg = gravitational force, m = mass of sample, g = 9.81 m/s^2= gravitational acceleration, a = acceleration of sample, x = distance the sample travels during time t, v = velocity of sample after time t, t = time (Jelle 2013).

The friction coefficient μ is found for each single measurement by dividing the applied pulling force F by the snow sample weight G. The static friction coefficient μ_s is normally determined from the maximum measured applied pulling force before the snow sample begins to slide. The dynamic friction coefficient μ_d is normally determined from the mean value of the applied pulling force along a given sliding distance. In general $\mu_s > \mu_d$.

Method B (inclined plane) gives the static friction coefficient between the roofing and packed snow, also in case of an underlayer of ice. The friction coefficient μ for the roofing is given by the following:

$$\mu = \frac{R}{N} = \tan \theta \tag{4.15}$$

where R is the friction force parallel with the sample surface, N is the normal force on the sample surface, θ is the slip angle, that is the angle of inclination between horizontal plane and inclined plane when the snow sample begins to slip the inclined plane (Jelle 2013).

The principle for method B is measurement of how large inclination angle between the horizontal plane and inclined plane which is necessary for a snow sample to start sliding downwards the roofing (Fig.4.26.b)

Fig. 4.26. Friction coefficient determination between snow and roofing by method A (left) horizontal plane applied pulling force method and method B (right) inclined plane slip method. (Illustrations: SINTEF Building and Infrastructure) (Jelle 2013).

Jelle (2013) observed that the applied force decreases as the number of slides increases. An explanation could be that the surface is becoming smoother. Tests on different surfaces were experimented to find recommended maximum slip angles and friction values. The recommended maximum slip angle for solar cell panels is 3°, a value the author stresses is open for discussion and change, because of the presence of adhesive forces that often make this value insufficient..

4.5.4 Ice adhesion

As we said (Novosovsky et al. 2012), the crack is opening in mode II when the critical shear strength is given by (4.6). While superhydrophobic surfaces have low shear strength because of high contact angle θ and low value of receding contact angle θ_{rec} , icephobic surfaces have high contact angle θ and high value of receding contact angle θ_{rec}.

Hejazi et al. (2013) tried to create a parallelism between the definition of superhydrophobicity and icephobicity. The high CA and low surface energy of a superhydrophobic surface corresponds to low solid-ice adhesion and low solid strength for an icephobic surface. Moreover low CAH corresponds to low shear strength in icephobic surfaces, while high CA corresponds to low normal strength. In conclusion Hejazi et al. (2013) suggested a definition for an icephobic surface: "a surface that delays ice formation from condensed or incoming water in the situation where normally ice would form and/or it has weak shear and normal adhesion strength to ice (100 kPa)".

Another parameter to consider is contact area a. In fact the Cassie wetting state can decrease the shear strength by introducing voids between the solid surface and water/ice, which serve as microcracks (stress concentrators) and increase a. Consequently, some superhydrophobic surfaces can have strong ice adhesion if they do not provide sufficiently large voids at the interface.

4.5.5 Requirements for icephobicity

Table 4.8 (Schultzius et al. 2015) synthetizes the different textures that have been tests and the relative advantages/disadvantages:

Table 4.8. Icephobic surfaces and their associated advantages and disadvantages (Schultzius et al. 2015).

Icephobic surfaces	Description	Advantages	Disadvantages
Untextured	Surfaces exhibiting relatively high receding contact angle.	Reduce ice adhesion. Reduce condensation and nucleation rate.	No clear ice nucleation strategy; therefore, ice will form. External forces must be used to remove ice.
Single-tier texture	Nanotexture: Hydrophobic surfaces exhibiting high resistance to drop impalement or promoting quasiliquid layers/confinement effects.	Can resist droplet impalement. Can also promote quasi-liquid layers and confinement effects. Can maintain non-wetting state during condensation.	May have an increased nucleation temperature (compared with multitier case).
	Microtexture: hydrophobic surfaces exhibiting high apparent contact angle values and low liquid adhesion.	Low-droplet adhesion, so it can repel supercooled droplets. Lower nucleation temperature due to	Cannot control condensation; susceptible to flooding. May not reduce ice adhesion, surface is damaged

Multi-tier texture	Hydrophobic surfaces consisting of a combination of macro-, micro-, nano-scale features, with each scale. affecting/addressing an important process during transport and phase change.	reduced solid-liquid contact area.	during ice removal.
		Microscale texture can reduce droplet adhesion and nucleation temperature by promotingan air layer underneath it.	Currently, drop impact resistance and contact time reduction applies to speeds $<10\ ms^{-1}$. Contact time reduction through macrotexturing only applies to $We<60$.
		Micro/nanoscale texture can resist droplet impalement during dynamic impact and has a lownucleation temperature. It may also promote spontaneous droplet jumping.	
		Macro/micro/nano-scale textures can resist drop impalement, have a low nucleation temperature, and reduce droplet impact contact time.	

In conclusion superhydrophobic surfaces seem to have suitable characteristics to respond to icephobic requirements, as far as the surface has a nanometer scale roughness, possibly with a hierarchical structure, which grants for large voids between the solid surface and water/ice. These requirements will avoid the transitions from Cassie-Baxter to Wenzel state, which leads to the lock of ice in the surface.

Therefore, transparent, anti-reflective superhydrophobic surfaces for solar cells that have been analysed in the former chapters should have also good icephobic properties. To confirm this statement, they should undergo icephobicity tests, such as the SINTEF Method 169 that has been previously described.

4.5.6 Testing methods

Different parameters are taken in consideration to evaluate icephobic behaviour; as a consequence different tests are performed to study materials' answer to water, snow and ice at different temperatures.

As showed in the previous chapter, contact angle is commonly measured through the static drop method. A needle places a water droplet on a surface though a computer-controlled liquid dispenser system. After the needle is removed, an optical goniometer measures the static CA and displays the results on a connected computer (Fig. 4.27).
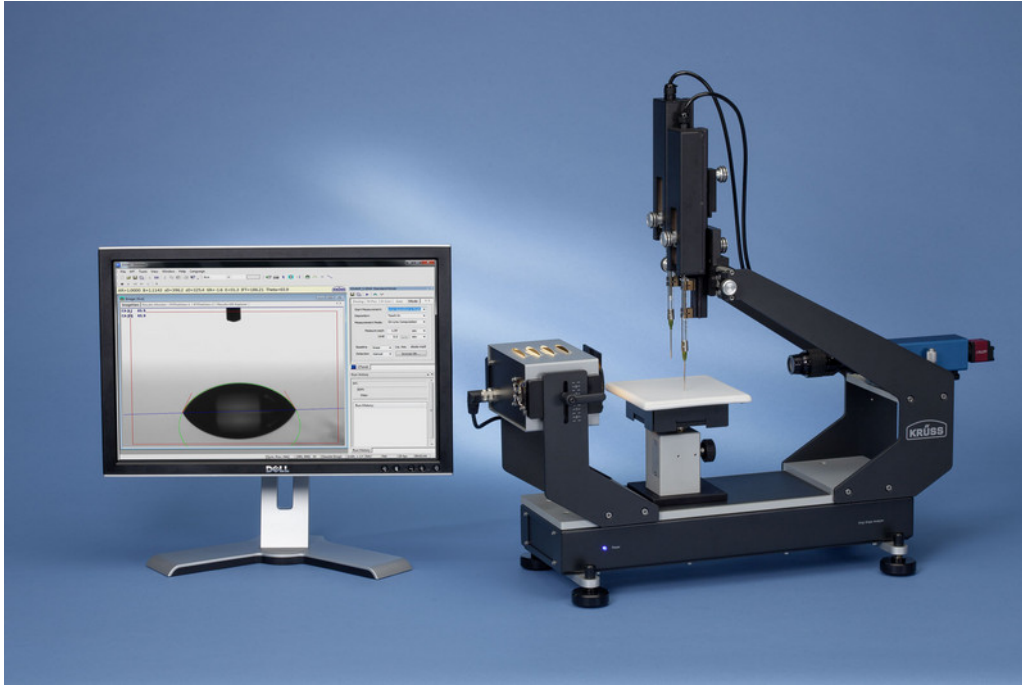
Fig. 4.27. A DSA30 drop shape analysis system from Kruss.

Tilted-drop method is used to evaluate contact angle hysteresis. A plane is tilted through a mechanical device till the drop is going to slide. At that moment an optical goniometer is employed to measure the advancing and receding contact angle. The different between these values gives the CAH.

Measuring ice adhesion is not as straightforward as measuring water contact angles, as there are no standardized and commercially available instruments available that are designed for measuring solid-solid adhesion strengths. Different groups have therefore come up with their own solutions.

In the spin test samples are usually places on an aluminium plate in a wind chamber, where micro-droplets are sprayed at a subzero temperature in order to simulate the presence of freezing rain. Then samples are spun inside a centrifuge (Fig. 4.28) to determine the rotational speed at which detachment of the ice cylinder occur. The ice adhesion strength can be evaluated by assuming that the adhesive force is equal to the centrifugal force

$$F = mr\omega^2 \tag{4.17}$$

where m is the ice mass, r is the beam radius and ω is the rotational speed at the moment of detachment, that is detected with sensors embedded in the walls of the centrifuge. Lastly, the shear stress τ can be calculated by dividing the calculated force by the contact area A of ice on the sample:

$$\tau = \frac{F}{A} \tag{4.18}$$
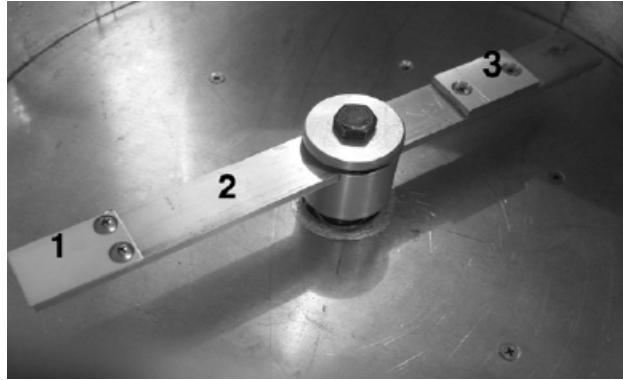
Fig. 4.28. Coated sample in centrifuge set-up that evaluates ice adhesion: (1) sample, (2) aluminium beam, (3) counter-weight (S. A. Kulinich and M. Farzaneh).

In the cone test a pile of the material to test or an aluminium pile coated with a candidate icephobic material is built (Fig. 4.29). The pile is placed in a machine, where it is left to freeze for several hours at a certain temperature. At a later time the pile is loaded at a constant rate until the ice-pile bond fails at a certain load. The measured load is then divided for the contact area A, equal to the lateral surface of the cylinder, to find the shear stress.
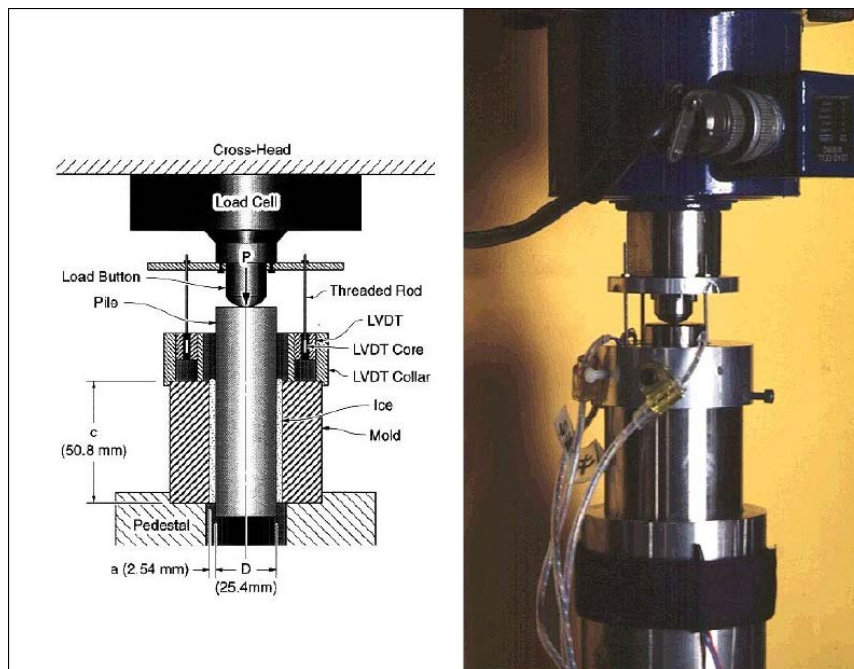
Fig. 4.29.Zero-degree cone test configuration (left) and instrumented sample pile and mould in testing machine (right) (U.S. Army Corps of Engineering).

Ice adhesion is evaluated also through icing/deicing cycles and measured not in kilopascal, but in number of cycles.

Other parameters are used to evaluate icephobicity: nucleation temperature (°C) and nucleation delay (h) to analyse ice nucleation delay, droplet impact contact time and droplet impact impalement resistance (ms^(-1)) to analyse droplet mobility. In any case Hejazi's definition (2003) made ice adhesion the parameter most commonly-used parameter to estimate icephobic performances.

120

4.6 Robustness and durability

Nano-roughness can easily be destroyed by external force, so that the panel efficiency would drastically drop down. Prolonged service life time is also desired for the practical use of these icephobic surfaces, because of the harsh environmental conditions involved in the photovoltaic applications. Superhydrophobic/ icephobic should provide enough resistance to mechanical impact (in the form of scratches, abrasions or high speed impacts) and to decomposition by some portion of the solar spectrum, that can verify frequently in outdoor conditions. This topic has received less attention in the literature to date, but it should become a research priority with the associated problem of icephobicity.

There are no standard procedures to quantify the durability of superhydrophobic/icephobic surfaces. The following image (Fig. 4.30) shows the most common characterization techniques employed to quantify mechanical and UV durability of superhydrophobic/ icephobic surfaces, including UV irradiation (a), tape adhesion test (b), sand impact/abrasion test (c), ice formation/ice removal cycles (d), water jet/dripping test (e) and sandpaper abrasion test (f). A more complete summary of the common characterization techniques is listed in the following table. In addition to the abovementioned tests, pencil hardness test, wipe test, ultra-sonication, solution/solvent immersion and thermal tests have also commonly been employed to characterize the durability of superhydrophobic/icephobic surfaces (Sojoudi 2016).
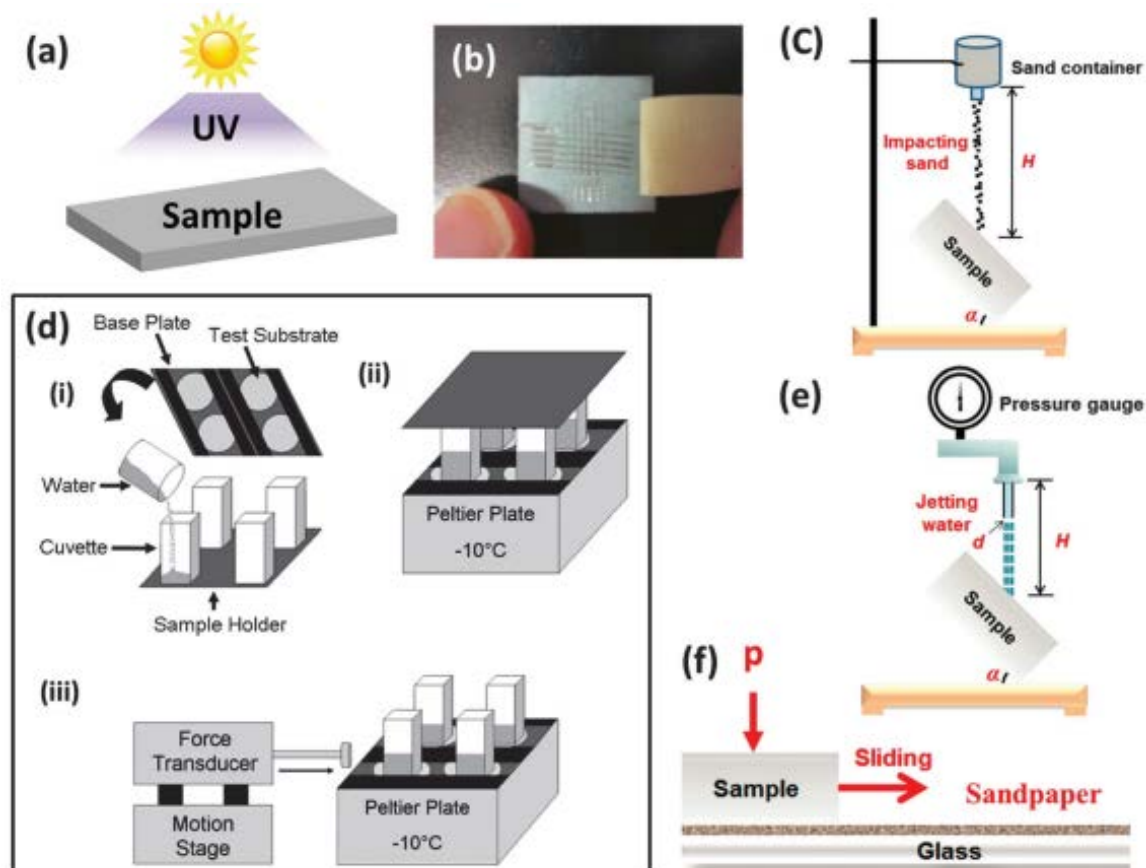
Fig. 4.30. Common methods in use to quantify the durability of the superhydrophobic/icephobic surfaces. (a) UV irradiation, (b) tape adhesion test (c) sand impact test (d) ice formation/ice removal cycles3 (e) water jet/dripping test and (f) sandpaper abrasion measurement (Sojoudi 2016).

4.7 State-of-the-art and further research

T. M. Schutzius and al. (2015) collected some of the ice adhesion results obtained by researchers in icephobic surfaces design. The lowest values were ranking between 15 and 60 kPa. In this classification all type of surfaces are mentioned, though. But our research is focusing on transparent coating applicable on photovoltaic devices.

The most recent achievement has been obtained by Golovin et al. (2016), who designed coatings with ice adhesion values even inferior to 0.2 kPa and to 10 kPa after robustness and durability tests. These ones are even transparent and applicable on glass. In conclusion Golovin's results can be revolutionary in the ice engineering field.

Till now this low values of ice adhesion have been achieved only by some researchers, though. Some years are necessary to have these products purchasable on the market.

Coatings that are already on the market are usually liquids that must be applied through rolling, brushing or spraying on different kind of substrates. Data sheets usually refers to ice adhesion to show the efficiency of the product, that reaches values around 20-80 kPa (Appendix H).

Using information contained in the data sheet collected, future research can lead to energetic simulations of photovoltaic devices with icephobic coatings. They would show the energy gain and the economic advantages produced by the coatings.

Another proposal for future work is to collect some of these products that have already been designed in order to test them on photovoltaic devices and to compare results between each other. This could show what the most efficient solution is and lead to more capable coatings.

4.8 References

E. Andenæs, B.P. Jelle, K. Ramlo, T. Kolås, J. Selj and S.E. Foss, "The influence of snow and ice coverage on the energy generation from photovoltaic solar cells", Master's thesis, NTNU, 2015.

B. Bang, A. Nielsen, P.A. Sundsbø, T. Wiik, "Computer simulation of wind speed, wind pressure and snow accumulation around buildings (SNOW-SIM)", *Energy and Buildings,* **21**, 1994.

K. L. Cho, I. I. Liaw, A. H. F. Wu, R. N. Lamb, "Influence of roughness on a transparent superhydrophobic coating", *J. Phys. Chem. C*, **114** (25), 11228-11233, 2010.

D. Daniel, M. N. Mankin, R. A. Belisle, T.-S. Wong, J. Aizenberg, "Lubricant-infused micro/nano-structured surfaces with tunable dynamic omniphobicity at high temperatures", *Applied Physics Letter*, **102**, 231603, 2013.

P. Eberle, M.K. Tiwari, T. Maitra and D. Poulikakos, "Rational nanostructuring of surfaces for extraordinary icephobicity", *Nanoscale*, **6**, 4874-4881, 2014.

D. Ebert, B. Bhushan, "Transparent, superhydrophobic and wear-resistant coatings on glass and polymer substrates", *Langmuir*, **28** (31), 11391-11399, 2012.

R.M. Fillion, A.R. Riahi and A. Edrisy, "A review of ice prevention in photovoltaic devices by surface engineering", *Renewable and sustainable energy reviews*, **32**, issue C, 797-809, 2014.

K. Golovin, S. P. R. Kobaku, D. H. Lee, E. T. DiLoreto, J. M. Mabry, A. Tuteja, "Designing durable icephobic surfaces", *Sci. Adv.,* **2***,* 2016.

V. Hejazi, K. Sobolev and M. Nosonovsky, "From superhydrophobicity to icephobicity: forces and interaction analysis", *Scientific Reports*, **3**, 2194, 2013.

P. Hiralal, C. Chien, N. N. Lal, W. Abeygunasekara, A. Kumar, H. Butt, H. Zhou, H. E. Unalan, J. J. Baumberg, G. A. J. Amaratunga, "Nanowire-based multifunctional antireflection coatings for solar cells", *Nanoscale*, **6**, 14555-14562, 2014.

B.P. Jelle, "The challenge of removing snow downfall on photovoltaic solar cell roofs in order to maximize solar energy efficiency- Research opportunities for the future", *Energy and Buildings*, **67**, 334-351, 2013.

S. Jung, M. Dorrestijn, D. Raps, A. Das, C.M. Megaridis and D. Poulikakos, "Are superhydrophobic surfaces best for icephobicity?", *Langmuir 2011*, **27**, 3059-3066, 2011.

L. Kitzing, C. Mitchell, P. E. Morthorst, "Renewable energy policies in Europe: converging or diverging?", *Energy Policy*, **51**, 192-201, 2012.

S. A. Kulinich et M. Farzaneh, "On ice-releasing properties of rough hydrophobic coatings", *Cold Regions Sciences and Technology,* **65**, 60-64, 2011.

S. Latthe, H. Imai, V. Ganesan, C. Kappenstein, A. V. Rao, "Optically transparent superhydrophobic TEOS-derived silica films by silylation method", *J. Sol-Gel Sci Technology*, **53**, 208-215, 2010.

S.-H. Lee, K.-S. Han, J.-H. Shin, S.-Y. Hwang, H. Lee, "Fabrication of highly transparent self-cleaning protection films for photovoltaic systems", *Progress in Photovoltaics*, 21 (5), 1056-1062, 2013.

Y. Liu, A. Das, S. Xu, Z. Lin, C. Xu, Z. L. Wang, A. Rohatgi, C. P. Wong, "Hybridizing ZnO Nanowires with Micropyramid Silicon Wafers as Superhydrophobic High-Efficiency Solar Cells", *Adv. En. Mater.*, **2** (1), 47-51, 2012.

M. Manca, A. Cannavale, L. De Marco, A. S. Aricò, R. Cingolani, G. Gigli, "Durable superhydrophobic and antireflective surfaces by trimethylsilanized silica nanoparticles-based sol-gel processing", *Langmuir,* **25** (11), 6357-6362, 2009.

B. Marion, R. Schaefer, H. Caine, G. Sanchez, "Measured modeled photovoltaic system energy losses from snow from Colorado and Wisconsin locations", *Solar Energy*, **97**, 112-121, 2013.

A. J. Meuler et al., Relationships Between Water Wettability and Ice Adhesion, *ACS Appl. Mater. Interfaces*, **2** (11), 3100-3110, 2010.

K. Midtal, B.P. Jelle, "Self-cleaning glazing products: a state-of-the-art review and future research pathways", *Solar Energy and Solar Cells*, **109**, 126-141, 2013.

A. Nakajima, "Design of transparent hydrophobic coating", *J. Ceram. Soc. Jpn.*, **112**, 533–540 , 2004.

M. Nosonovsky, V. Hejazi, "Why superhydrophobic surfaces are not always icephobic", *ACS Nano*, **6** (10), 8488–8491, 2012.

T. Okaze, A. Mochida, Y. Tominaga, Y. Ito, H. Yoshino, "CFD prediction of snow-drift around a cube using two transport equations for drifting snow density", Proceedings of The Fifth International Symposium on Computational Wind Engineering (CWE2010), Chapel Hill, North Carolina, USA, 2010.

L. Pérez-Lombard, J. Ortiz, C. Pout, "A review on building energy consumption information", *Energy and Building*, **40**, 394–398, 2007.

K. Ramlo, B.P. Jelle, E. Andenas, T. Kolas and P.M. Stenstad, "The robustness and durability of photovoltaic cell surfaces attempting to avoid snow and ice formation", Master's thesis, 2015.

M. Ross, "Snow and Ice Accumulation on Photovoltaic Arrays: An Assessment of the TN Conseil Passive Melting Technolog", Division Report EDRL 95-68 (TR), 1995.

M. Sakhuja, J. Son, H. Yang, C. Bhatia and A.J. Danner, "Outdoor performance and durability testing of antireflecting and self-cleaning glass for photovoltaic applications", *Solar Energy*, **110**, 231-238, 2014.

T.M. Schutzius, S. Jung, T. Maitra, P. Eberle, C. Antonini, C. Stamatopoulos and D. Poulikakos, "Physics of Icing and Rational Design of Surfaces with Extraordinary Icephobicity", *Langmuir*, **31**, 4807-4821, 2015.

P.Šiffalovič, M. Jergel, M. Benkovičová, A. Vojtko, V. Nádaždy, J. Ivančo, M. Bodík, M. Demydenko, E. Majková, "Towards new multifunctional coatings for organic photovoltaics", *Solar energy materials and solar cells*, **125**, 127-132, 2014.

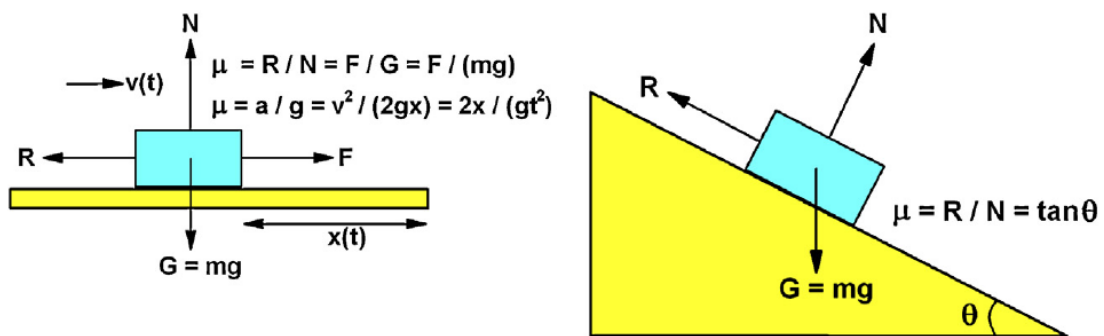SINTEF Method 169, Measurement of friction between snow and roofing, Method A – Friction coefficient determination between snow and roofing by horizontal plane applied pulling force method, Method B – Friction coefficient determination between snow and roofing by inclined plane slip method, 2008.

H. Sojoudi, M. Wang, N. D. Boscher, G. H. McKinley, K. K. Gleason, "Durable and scalable icephobic surfaces: similarities and distinction from superhydrophobic surfaces", *Soft Matter*, **12**, 1938-1963, 2015.

J. Son, S. Kundu, L. Verma, M. Sakhuja, A. Danner, C. S. Bhatia, H. Yang, "A practical superhydrophilic self-cleaning and anti-reflective surface for outdoor photovoltaic applications", *Solar energy materials and solar cells*, **98**, 46-51, 2012.

J. Son, M. Sakhuja, A. Danner, C. S. Batia, H. Yang, "Large scale antireflective glass texturing using grid contacts in anodization methods", *Solar Energy Materials and Solar Cells.*, **116**, 9-13, 2013.

Y. Tominaga, T. Okaze, A. Mochida, M. Nemoto, Y. Ito, "Prediction of snow-drift around a cube using CFD model incorporating effect of snow particles on turbulent flow", Proceedings of The Seventh Asia-Pacific Conference on Wind Engineering, Taipei, Taiwan, 2009.

K.-H. Tsui, Q. Lin, H.-T. Chou, Q. Zhang, H. Fu, P. Qi, Z. Fan, "Low-cost, flexible and self-cleaning 3D nanocone anti-reflection films for high-efficiency photovoltaics", *Adv. Mater.*, **26** (18), 2805-2811, 2014.

U.S Army Corps of Engineers, "Progress in Evaluating Surface Coatings for Icing Control at Corps Hydraulic Structures", *Ice Engineering*, ERDC/CRREL Technical Note 03-4, October 2003.

K. K. Varanasi, T. Deng, J. D. Smith, N. Bhate, "Frost formation and ice adhesion on superhydrophobic surfaces", *Applied Physics Letter*, **97**, 234102, 2010.

T. Verho, C. Bower, P. Andrew, S. Franssila, O. Ikkala, R.H. Ras, "Mechanically durable superhydrophobic surfaces", *Sci. Technol. Adv. Mater.*, **23** (5), 673-678, 2010.

S.-D. Wang, Y.-Y. Shu, "Superhydrophobic antireflective coating with high transmittance", *J. of Coat. Tech. and Res.*, **10** (4), 527-535, 2013.

Y. Wang, J. Xue, Q. Wang, Q. Chen, J. Ding, "Verification of icephobic/anti-icing properties of a superhydrophobic surface", *ACS Appl. Mater. Interfaces*, **5** (8), 3370–3381, 2013.

C. Xue, S. Jia, J. Zhang and J. Ma, "Large-area fabrication of superhydrophobic surfaces for practical applications: an overview", *Sci. Technol. Adv. Mater.*, **11** (3), 033002, 2010.

L. Ye, Y. Zhang, X. Zhang, T. Hu, R. Ji, B. Ding, B., Jiang, "Sol–gel preparation of SiO2/TiO2/SiO2–TiO2 broadband anti-reflective coating for solar cell cover glass", *Solar Energy Materials and Solar Cells*, **111**, 160-164, 2013/4.

Directive 2010/31/EU of the European Parliament and of the Council of 19 May 2010 on the energy performance of buildings.

Directive 2012/27/EU of the European Parliament and of the Council of 25 October 2012 on energy efficiency, amending Directives 2009/125/EC and 2010/30/EU and repealing Directives 2004/8/EC and 2006/32/EC Text with EEA relevance.

126

5 Modeling icephobic coatings

5.1 Abstract

Icephobic surfaces are becoming a research topic of considerable attention in different fields because of various possible applications: power lines, plane wings, wind turbines, etc. The design of a transparent, anti-reflective, robust and durable icephobic coating would increase the energy production of photovoltaic (PV) devices in winter time.

The aim of this paper is to simulate the presence of icephobic coatings on the modules surface, so that energy simulations can be launched. The results would let us know the energy gain that is achieved through the use of these devices.

The simulations are based on snow loss model developed by Marion et al. (2013), results given by PVsyst simulations and considerations about friction and adhesion phenomena on the surfaces.

The study is applied to the system mounted on the ZEB (The Research Centre on Zero Emission Buildings) Living Lab, a building set in the NTNU (Norwegian Institute of Science and Technology) campus in Trondheim. The same plant was supposed to be in Oslo and Bergen, so that other simulations were launched considering different weather conditions to compare results.

5.2 Introduction

5.2.1 Background

The growing interest of Nordic countries in photovoltaic devices leads to another relevant topic: snow. Snow in its various forms deposits on the module surface in wintertime, preventing the collection of solar radiation. The entity of the problem depends on the PV-plant geometry and material properties and on the location's weather characteristics.

Traditionally, roofs have been designed to keep the snow in its place on top of the roofs. However, solar cell roofs should ideally have no snow covering the cells, in order to maximize the solar cell energy production (Jelle 2013).

The natural snow and ice removal from the PV panel is due to complex phenomena. When the surface of a PV module has a higher temperature than the snow and ice set on it, the transfer of heat will cause the melting of ice and snow. For tilted panels, water will run down them. Melting is produced also by increasing of snow and ice temperature, due to the solar irradiation (Ross 1995).

5.2.2 Icephobic coatings

Icephobic coatings are proposed to intensify the snow and ice removal from PV surfaces, in order to increase the system's energy production (Jelle 2013).

The wettability of the surfaces has been studied for a long time, to try to create water-repellent and self-cleaning surfaces. Researchers created interesting solutions thank to the possibility of designing the surfaces at a nano-scale.

The repellent-answer of a surface to the presence of snow and ice was defined "icephobicity". Literally it means "fear of the ice" and it refers to the formation and accumulation of ice and snow on a surface (Hejazi et al. 2013). This phenomenon has been investigated in the recent years, trying to design a successful icephobic surface.

The research began with the study superhydrophobic surfaces, which are characterized by a contact angle higher than 150°. They have suitable characteristics to respond to icephobic requirements, as long as the surface has a nanometer scale roughness, possibly with a hierarchical structure, which grants for large voids between the solid surface and water/ice. These requirements will avoid the transitions from Cassie-Baxter to Wenzel state, which leads to the lock of ice in the surface (Schultzius et al. 2015).

Hejazi et al. (2013) tried to create a parallelism between the definition of superhydrophobicity and icephobicity. The high CA and low surface energy of a superhydrophobic surface corresponds to low solid-ice adhesion and low solid strength for an icephobic surface. Moreover low CAH corresponds to low shear strength in icephobic surfaces, while high CA corresponds to low normal strength. In conclusion Hejazi et al. (2013) suggested a definition for an icephobic surface: "a surface that delays ice formation from condensed or incoming water in the situation where normally ice would form and/or it has weak shear and normal adhesion strength to ice (100 kPa)".

In conclusion icephobic coatings are characterized by different parameters, but the one that is usually taken as a reference is the ice adhesion.

5.2.3 Conclusion and chapter statement

Icephobic coatings constitute a real answer to the snow accumulation on the photovoltaic panels.

The research in this field has developed only recently because of the progress on the nanometer scale. However, it has grown rapidly, leading some universities and research centres to design efficient icephobic coatings.

The most recent achievement has been obtained by Golovin et al. (2016), who designed coatings with ice adhesion values even inferior to 0.2 kPa and to 10 kPa after robustness and durability tests. These ones are even transparent and applicable on glass. Therefore, Golovin's results can be revolutionary in the ice engineering field.

Till now this low values of ice adhesion have been achieved only by some researchers, though. Some years are necessary to have these products purchasable on the market.

Coatings that are already on the market are usually liquids that must be applied through rolling, brushing or spraying on different kind of substrates. Data sheets usually refers to ice adhesion to show the efficiency of the product, that reaches values around 20-80 kPa (Appendix H).

The aim of this report is to launch energetic simulations of photovoltaic devices supposing icephobic coatings on their surfaces referring to the information contained in the data sheet collected, so that the energy gain and the economic advantages produced by the coatings are shown.

5.3 Methodology

5.3.1 Snow loss model

Snow accumulation on a plane is a phenomenon hard to predict. In spite of several approximations, Marion et al. (2013) created a reliable model, which determines snow coverage (%) based on air temperature (°C), POA irradiation (W/m^2) and snow depth (cm). As a consequence snow loss can be easily calculated. Further information is contained in paragraph 3.1.2.2.

In 2015 Marion's model was implemented in SAM, a user-friendly software that let an easy comprehension of the requirements needed to develop the calculus. Its simplifications produce a too approximate model, though. However, a whole photovoltaic system simulation would produce more reliable results with another software called PVsyst, even if it does not consider snow loss. A deeper analysis is conducted in chapter 3.1.3.

A new methodology was set up to determine the impact of snow on energy production of PV panels, through PV energy production that considers snow presence and snow loss percentage values. An Excel file that connects Marion's model results with PVsyst results is a solution that leads to a reliable answer.

Marion's algorithm was set using *Glob. IAM* values (W/m²) to derive snow coverage. That is global irradiance component with detraction of shading and IAM losses. In reality *Glob.Shad.*, global irradiance component with detraction of only shading loss, should have been used, but hourly values were not made available by the software.

The steps followed to find the snow loss percentage are summarized as the following:

1. Set a new project in PVsyst considering the weather data and the plant characteristics.
2. Launch the simulations, obtaining yearly flowchart results and hourly *Glob.IAM*.
3. Use the *Glob.IAM* and the other hourly data in the weather file to execute Marion's algorithm:

Step 1	If today's sd > yesterday's sd Set PV snow amount = 10 tenths (100% snow) Else Set PV snow amount = Yesterday's end amount
Step 2	Initialize daily energy productions E_w and E_{w0} to zero
Step 3	For each daytime hour:
Step 4	If *Ta - G/m' > 0* Decrease PV snow by Fig.3.3 amount. (where *m'* is the slope of line from Fig. 3.1, that is -80 W °C /m²)

4. Calculate hourly snow coverage (sc') considering the presence of module by-pass diodes.

5. Hourly power loss due to snow p_{snow} (kW) is calculated using the following equation:

$$p_{snow} = sc' * Glob.IAM \qquad (3.20)$$

where sc' is corrected sub-array snow cover (%) and $Glob.IAM$ is global irradiance component with detraction of shading and IAM losses as computed by PVsyst (W/m²).

6. p_{snow} is summed hour by hour and day by day to obtain monthly power loss P_{snow} (kWh).

7. Snow loss percentage sl (%) is determined diving P_{snow} (kWh) per monthly $Glob.IAM$ (kWh):

$$sl = \frac{P_{snow}}{Glob.IAM} \qquad (3.21)$$

8. $Glob.IAM.$ is then reduced by snow loss to obtain $Glob.Snow$.

9. Soiling percentage is detracted from $Glob.Snow$ to have the $Glob$.Eff.

10. Net DC energy is finally obtained considering irradiance loss, temperature loss, electrical loss due to shadings, light induced degradation. Module array mismatch loss and ohmic wiring loss. Gross AC energy takes into account inverter parameters: efficiency, nominal power, power threshold, nominal voltage and voltage threshold.

11. PVsyst flowchart can be updated with new values, considering also snow loss, so that final energy production can be computed.

5.3.2 Icephobic coating model

5.3.2.1 Friction and adhesion

The classic rules of sliding friction were discovered by Leonardo da Vinci in 1493, but they remained in his notebooks (Hutchings 2016). Amontons (1732), Forest de Bélidor (1737), Euler (1750) and Desaguliers (1724, 1734) continued the study of this topic, but a great contribute was given by Coulomb (1785).

The force of dry friction is the force resisting the relative motion of solid surfaces, fluid layers, and material elements sliding against each other. It is governed by the model:

$$F_f \leq \mu\, F_n \tag{5.1}$$

where F_f is the force of friction exerted by each surface on the other, parallel to the surface, in a direction opposite to the net applied force; μ is the coefficient of friction, which is an empirical property of the contacting materials; F_n is the normal force exerted by each surface on the other, directed perpendicular (normal) to the surface.

The Coulomb friction F_f may take any value from zero up to $\mu\, F_n$, and the direction of the frictional force against a surface is opposite to the motion that surface would experience in the absence of friction. Thus, in the static case, the frictional force is exactly what it must be in order to prevent motion between the surfaces; it balances the net force tending to cause such motion. In this case, rather than providing an estimate of the actual frictional force, the Coulomb approximation provides a threshold value for this force, above which motion would commence. This maximum force is known as traction.

There are different interpretations of the causes of this force. The Galilean mechanical interprets the bumps between the contact surfaces as the cause of the friction force. Recently the sliding friction was shown to be mainly due to the phenomena of adhesion (chemical bond) between the molecules that make the surfaces contact each other.

Bowden and Tabor (1950, 1964) explained the adhesion theory of friction. When surfaces are loaded against each other, they make contact only at the tips of the asperities. Due to the fact that the real contact area is small, the pressure over the contacting asperities is assumed high enough to cause them to deform plastically. This plastic flow of the contacts causes an increase in the area of contact, until the real area of contact is just sufficient to support the load.

Under these conditions for on ideal elastic-plastic material

$$N = A\, P \tag{5.2}$$

where A is the real area of contact, P is the yield pressure and N is the normal load.

When the surfaces are in contact, adhesion takes place and microwelds are formed because of high pressure. A force S per unit area of contact is necessary to shear the junction.

The friction strength is

$$F = A\, S \tag{5.3}$$

Considering (5.2) and (5.3), the following are obtained:

$$F = \frac{N}{P} S \tag{5.4}$$

$$F/N = S/P \tag{5.5}$$

In conclusion the friction coefficient is defined as:

$$\mu = \frac{F}{N} = \frac{S}{P} \tag{5.6}$$

Thus this theory explains two laws of friction:

- friction is independent of the apparent area of contact;
- friction force is proportional to the load.

Tests performed on several materials showed that two surfaces adhere strongly each other leading to a sharp increase in the coefficient of friction when the surfaces contact are thoroughly cleaned and smoothed. As a result, if the surfaces present several asperities, they lock each other mechanically; if the two surfaces are smooth, the intermolecular cohesive forces are involved chemically.

In conclusion frictional force can be generically approximated to adhesion force.

5.3.2.2 Considerations about Marion's graph

In Step 4 of Table 3.1, it is showed that Marion's algorithm follows this rule (par. 3.1.2.2):

"If $Ta - G/m' > 0$
Decrease PV snow by Fig.3.3 amount.
(where m' is the slope of line from Fig. 3.1, that is -80 W*°C /m²)"

Fig. 3.3 shows a linear relationship between the sine of β and the snow slide amount. It was found observing five roof-mounted systems and one ground rack-mounted system.

Two cases were considered for how snow remains on PV modules: frictional forces and freezing to the PV module (Marion et al. 2013).

In the first case snow sliding occurs when the sliding force due to gravity F_s is greater than the frictional force F_f. These two can be explicated by:

$$F_s = mg \sin\beta \tag{3.11}$$

$$F_f = \mu mg \cos\beta \tag{3.12}$$

where m is the mass of snow, g is the acceleration of gravity, β is the tilt angle and μ is the static coefficient of friction of wet or dry snow.

In conclusion snow slides when

$$\mu < \tan\beta \tag{3.13}$$

In the second case snow sliding occurs when the module-snow interface temperature reaches 0°C and the snow-ice begins melting. When it melts, snow slides away because coefficient of friction is low enough.

Fig. 3.3. Linear relationships between the sine of β and the snow slide amount for the hours when a snow slide is estimated for roof mounted systems (blue) and ground rack-mounted PV systems with adequate ground clearance (red) (Marion et al. 2013).

Fig. 3.3 shows that snow slide amount s (tenths of PV panel height) is equal to:

$$s = k \sin \beta \tag{3.14}$$

where k is a coefficient (1.97 for roof-mounted systems; 6 for ground rack-mounted systems) and β is the tilt angle.

In frictional forces case these empirical relationships are confirmed by the previous explanation. In the freezing case we can consider that in winter time increasing β increases the POA irradiance and, as a consequence, snow temperature.

The combination of. (5.6) and (3.13) leads to the following condition that determines the snow sliding:

$$\frac{S}{P} < \frac{sin\beta}{cos\beta} \tag{5.7}$$

At this point the relationship between the cohesion force and the $sin\beta$ is evident.

Icephobic coatings that are already on the market have been studied to have a full comprehension of their characteristics. Data sheets usually refer to ice adhesion parameter to show the efficiency of the product. Common values are around 40-80 kPa (Appendix H: NuSil). Tests made on bare glass showed that ice adhesion can be assumed around 400 kPa (Chernyy et al. 2014). In conclusion it is around 85% reduced.

136

The term S contains the value of word of adhesion. For the previous reasons, to simulate the presence on an icephobic coating on a photovoltaic surface S can be approximately reduced by 85%.

As a consequence, considering (5.7), $sin\beta$ is divided for 0.15.

It means that the k coefficient in (3.14) is now 13.3 for roof-mounted systems.

In conclusion simulations where launched producing this change in the Marion's algorithm.

5.3.3 Case study

This application is executed in continuum to the one in Chap. 3, therefore the same case study was chosen. The methodology is applied to the PV-plant installed on the ZEB Living Lab's roofs in Trondheim, supposed also in Oslo and Bergen.

The choice of the same case study let a comparison between the energy harvest with and without the use of icephobic coatings.

5.4 Results

5.4.1 PV-plant on the ZEB Living Lab in Trondheim, Oslo and Bergen

The main results about the PV-plant mounted on the ZEB Living Lab roofs are described by the PVsyst flowchart (Table 5.1, Appendix G).

Table 5.1. PVsyst results about the PV-plant on the ZEB Living Lab in Trondheim.

Nominal POA			
879 kWh/m²	+26.30%	global incident	1 110 kWh/m²
	-6.45%	shading	1 039 kWh/m²
	-3.37%	IAM factor	1 004 kWh/m²
	-1.00%	soiling	994 kWh/m²
			12 401 kWh
Nominal DC energy	-1.65%	loss due to irradiance	12 197 kWh
994 kWh/m²	-0.79%	loss due to temperature	12 100 kWh
79 m²	-2.87%	electrical loss due to shadings	11 753 kWh
	-1.50%	light induced degradation	11 577 kWh
	-1.00%	module array mismatch loss	11 461 kWh
	-0.70%	ohmic wiring loss	11 380 kWh
Net DC energy	-3.75%	inverter efficiency	10 953 kWh
11 380 kWh	-0.39%	inverter over nominal power	10 911 kWh
	0.00%	power threshold	10 911 kWh
	0.00%	nominal inverter voltage	10 911 kWh
	0.00%	voltage threshold	
gross AC energy			
10 911 kWh			

The results as not relevant as energy production in other location of Europe, but they are coherent to the nominal irradiance and the other loss values.

A deeper analysis was run on the snow loss computation. The application of the steps showed in the previous list, lead to the monthly power loss P_{snow} (kWh) and snow loss percentage sl (%), showed in Table 5.2.

Table 5.2. Global irradiance after shading and IAM losses (kWh), monthly power loss (kWh) and snow loss percentage (%) of the PV-pant on the Living Lab in Trondheim.

	$Glob.IAM$ (kWh)	P_{snow} (kWh)	sl (%)
January	876	87	10
February	3 010	537	18
March	7 292	113	2
April	10 228	0	0
May	12 497	0	0
June	12 084	0	0
July	11 835	0	0
August	9 668	0	0
September	6 377	0	0
October	3 300	0	0
November	1 066	0	0
December	443	55	12
Year	78 674	791	1

The results in Table 5.2 were applied to PVsyst in the flowchart, considering the loss due to snow after the shading and IAM factor losses. The $Glob.Inc.$ decreased by these ones and soiling losses is called by the software "global effective irradiance" ($Glob.Eff.$). This quantity is the nominal DC energy. The new results are showed in Table 5.3.

Finally, the consideration of the other losses at the DC side (Tables 5.4 and 5.5) bring to the creation of a PVsyst flowchart with new values (Table 5.6).

In conclusion the annual energy production decreased from 10.911 kWh to 10.616 kWh.

Table 5.3. Global after shading, IAM and snow, global effective irradiance (kWh) of the PV-pant on the ZEB Living Lab in Trondheim.

	$Glob.Snow$ (kWh)	$Glob.Eff.$ (kWh)
January	10	10
February	31	31
March	91	91
April	129	127
May	158	155
June	153	150
July	149	146
August	122	120
September	81	79
October	42	41
November	13	13
December	5	5
Year	983	967

Table 5.4. Monthly energy values from nominal DC energy to net DC energy of the PV-pant on the ZEB Living Lab in Trondheim.

	GlobEffSTC	Irradiance	Temperature	ShdElec	LID	MisLoss	OhmLoss
	kWh	kWh	kWh	kWh	kWh	kWh	kWh
J.	124	122	121	117	115	114	114
F.	390	383	380	353	348	344	343
M.	1 131	1 113	1 104	1 019	1 003	993	987
A.	1 580	1 554	1 541	1 463	1 441	1 427	1 416
M.	1 930	1 898	1 883	1 864	1 836	1 818	1 803
J.	1 866	1 836	1 821	1 821	1 794	1 776	1 761
J.	1 828	1 798	1 784	1 783	1 756	1 738	1 724
A.	1 493	1 469	1 457	1 415	1 394	1 380	1 370
S.	985	969	961	913	899	890	885
O.	510	501	497	464	457	452	450
N.	168	165	164	158	156	154	154
D.	61	60	60	57	57	56	56
Yr	12 066	11 867	11 774	11 427	11 255	11 143	11 062

Table 5.5. Monthly energy values from net DC energy to gross AC energy of the PV-pant on the ZEB Living Lab in Trondheim.

	EOutInv	ENPInv
	kWh	kWh
January	107	107
February	329	328
March	952	948
April	1 367	1 361
May	1 739	1 732
June	1 696	1 689
July	1 660	1 654
August	1 319	1 314
September	851	848
October	430	428
November	145	144
December	52	52
Year	10 646	10 605

Table 5.6. Results about the PV-plant on the ZEB Living Lab in Trondheim after the consideration of snow loss.

Nominal POA			
879 kWh/m²	+26.30%	global incident	
	-6.45%	shading	
	-3.37%	IAM factor	
	-1.00%	soiling	
	-1.00%	snow	967 kWh/m²
Nominal DC energy	-1.65%	loss due to irradiance	
967 kWh/m²	-0.79%	loss due to temperature	
79.2 m²	-2.87%	electrical loss due to shadings	
	-1.50%	light induced degradation	
	-1.00%	module array mismatch loss	
	-0.70%	ohmic wiring loss	10 900 kWh
Net DC energy	-3.75%	inverter efficiency	
11 073 kWh	-0.39%	inverter over nominal power	
	0.00%	power threshold	
	0.00%	nominal inverter voltage	
	0.00%	voltage threshold	10 616 kWh
gross AC energy			
10 616 kWh			

The methodology previously explained was followed to obtain results for Oslo and Bergen as well. Simulations in PVsyst and SAM were launched setting Oslo and Bergen weather files, considering the same PV-plant characteristics.

Tables 5.7 and 5.8 report the monthly power loss P_{snow} (kWh) and snow loss percentage sl (%) in Oslo and Bergen.

Table 5.37. Global IAM (kWh), monthly power loss (kWh) and snow loss percentage (%) of the PV-pant on the ZEB Living Lab in Oslo.

	$Glob.IAM$ (kWh)	P_{snow} (kWh)	sl (%)
January	1 140	470	41
February	2 174	93	4
March	5 600	72	1
April	8 167	11	0
May	12 346	0	0
June	12 628	0	0
July	12 373	0	0
August	9 744	0	0
September	5 791	0	0
October	3 327	0	0
November	1 219	11	1
December	588	296	50
Year	75 098	953	1

Table 5.8. Global IAM (kWh), monthly power loss (kWh) and snow loss percentage (%) of the PV-pant on the ZEB Living Lab in Bergen.

	$Glob.IAM$ (kWh)	P_{snow} (kWh)	sl (%)
January	648	19	20
February	1 688	47	14
March	3 892	134	1
April	6 874	204	0
May	11 530	312	0
June	10 984	319	0
July	9 668	312	0
August	7 898	246	0
September	4 527	146	0
October	2 665	84	0
November	816	31	5
December	362	11	6
Year	61 552	475	1

Marion's algorithm applied to the same PV-plant supposed in different Norwegian cities gave different results to the different weather conditions in them. Table 5.9 shows snow loss values per month in Oslo, Bergen and Trondheim.

Table 5.9. Snow loss values of ZEB Living Lab PV-plant supposed in Oslo, Bergen and Trondheim.

	Oslo	Bergen	Trondheim
January	71	20	23
February	31	14	30
March	11	1	11
April	2	0	0
May	0	0	0
June	0	0	0
July	0	0	0
August	0	0	0
September	0	0	0
October	0	0	0
November	2	5	0
December	51	6	18
Year	3	1	3

Bergen values are lower than other cities, while Oslo and Trondheim show similar results. In particular the Oslo case has a higher loss in January and December. The reason why is explained in chapter 3.2.2.

The results previously reported show the presence of the snow loss even with the use of icephobic coating. It is now reduced, though.

5.4.2 Comparison with the base case

In this paragraph monthly snow loss percentage of are reported for Oslo, Trondheim and Bergen to compare the case without icephobic coating, studied in Chap. 3.2, to the case with icephobic coating (Tables 5.10 - 5.12).

Table 5.10. Snow loss values of ZEB Living Lab PV-plant supposed in Oslo with and without the use of icephobic coatings.

	without coating (%)	with coating (%)	Difference (%)
January	71	41	30
February	31	4	26
March	11	1	10
April	2	0	2
May	0	0	0
June	0	0	0
July	0	0	0
August	0	0	0
September	0	0	0
October	0	0	0
November	2	1	1
December	51	50	0
Year	3	1	2

Table 5.11. Snow loss values of ZEB Living Lab PV-plant supposed in Bergen with and without the use of icephobic coatings.

	without coating (%)	with coating (%)	Difference (%)
January	20	13	7
February	14	7	7
March	1	0	1
April	0	0	0
May	0	0	0
June	0	0	0
July	0	0	0
August	0	0	0
September	0	0	0
October	0	0	0
November	5	0	5
December	6	0	6
Year	1	0	0

Table 5.12. Snow loss values of ZEB Living Lab PV-plant supposed in Trondheim with and without the use of icephobic coatings.

	without coating (%)	with coating (%)	Difference (%)
January	23	10	13
February	30	18	12
March	11	2	9
April	0	0	0

May	0	0	0
June	0	0	0
July	0	0	0
August	0	0	0
September	0	0	0
October	0	0	0
November	0	0	0
December	18	12	6
Year	3	1	2

The previous results show a remarkable reduction of snow loss monthly, from 50% to 100%. On an annual base snow loss was reduced from 3% to 1% in Oslo and Trondheim and from 1% to 0% in Bergen.

5.5 Conclusions and further research

The simulation of application of icephobic coatings on photovoltaic (PV) surface gave noticeable results, which suggest a certain utility of this solution to the accumulation of snow on the PV panels.

In addition in this simulation the icephobic coatings considered are characterized by the same efficiency of the ones that are currently on the market. Nevertheless researchers are continuously obtaining coatings with better performances, which will soon developed by companies. As a result, the advantage of applying icephobic coating could be even increased.

Another consideration concerns the fact that icephobic coatings have often also water-repellent properties. As previously showed (Chap. 4.3.2), these coatings have also an anti-soiling nature, that would reduce the soiling loss and increase the final PV energy production.

The simulations were carried out considering Marion's model, as a result limitations of it should be considered. Further information is contained in Chap. 3.4. The simulation of icephobic coatings was led modifying Marion's model through physical considerations, as a consequence additional approximations were made. However, simulations are always conducted considering a range of error. They pretend not to give exact results, but to provide an idea about results trend.

Icephobic coating are employed in different fields, such as aviation, hydraulics, etc. However, they are mostly applied on wing of planes and wind turbines. The few products realized till now have been tests mostly on these devices. A proposal for future work is to collect some icephobic coatings that have already been designed in order to test them on photovoltaic devices and observe the real behaviour of snow on these surfaces, varying panel's tilt angle, coating's substrate and external climatic conditions. In that way the model used in this simulations could also be validated.

5.6 References

G. Amontons, "De la résistance causée dans les machines, Mémoires de l'Académie Royale", A, Histoire de l'Académie Royale des Sciences, 206-227, 1732.

B. F. Bélidor, "Architecture Hydraulique, ou l'art de conduire, d'élever et de ménager les eaux", Jombert, Paris, 1737.

S. Chernyy, M. Järn, K. Shimizu, A. Swerin, S. U. Pedersen, K. Daasbjerg, L. Makkonen, P. Claesson, J. Iruthayaraj, "Superhydrophilic polyelectrolyte brush layers with imparted anti-icing properties: effect of counter ions", *ACS Appl. Mater. Interfaces*, **6**, 6487-6496, 2014.

C. A. Coulomb, " Théories des Machines Simples, en ayant égard au frottement de leurs parties et à la roideur des cordages, Mémoire de Mathématique et de Physique de l'Académie Royale", X, Paris, 161-342, 1785.

J. T. Desaguliers, "A Course of Experimental Philosophy", vol.1, London, 1734.

J. T. Desaguliers, "Some Experiments concerning the Cohesion of Lead", Philosophical Transactions of Royal Society, 33, 345-347, 1724.

D. Dowson, "History of Tribology", Professional Engineering Publishing, 1997.

L. Euler, "Histoire de l'Académie Royale à Berlin", IV, 313, 1750.

B. Forest de Bélidor, "Richtige Grund-Sätze der Friction-Berechnung" ("Correct Basics of Friction Calculation"), 1737.

K. Golovin, S. P. R. Kobaku, D. H. Lee, E. T. DiLoreto, J. M. Mabry, A. Tuteja, "Designing durable icephobic surfaces", *Sci. Adv., 2*, 2016.

V. Hejazi, K. Sobolev and M. Nosonovsky, "From superhydrophobicity to icephobicity: forces and interaction analysis", *Scientific Reports*, **3**, 2194, 2013.

I. M. Hutchings, "Leonardo da Vinci's studies of friction ", *Wear*, **360-361**, 51-66, 2016.

B.P. Jelle, "The challenge of removing snow downfall on photovoltaic solar cell roofs in order to maximize solar energy efficiency- Research opportunities for the future", *Energy and Buildings*, **67**, 334-351, 2013.

B. Marion, R. Schaefer, H. Caine, G. Sanchez, "Measured modeled photovoltaic system energy losses from snow from Colorado and Wisconsin locations", *Solar Energy*, **97**, 112-121, 2013.

M. Ross, "Snow and Ice Accumulation on Photovoltaic Arrays: An Assessment of the TN Conseil Passive Melting Technolog", Division Report EDRL 95-68 (TR), 1995.

T.M. Schutzius, S. Jung, T. Maitra, P. Eberle, C. Antonini, C. Stamatopoulos and D. Poulikakos, "Physics of Icing and Rational Design of Surfaces with Extraordinary Icephobicity", *Langmuir*, **31**, 4807-4821, 2015.

L. Xua Anh, "Dynamics of Mechanical Systems with Coulomb Friction (Foundations of Engineering Mechanics)", Springer, 2003.

6 Conclusions of thesis

6.1 Thesis achievements

The problem of snow on photovoltaic devices in Norway was investigated in all its aspect.

First of all the snow condition was described through statistical data and graphs in the most populated cities of Norway: Oslo, Bergen and Trondheim. In addition the will of Norwegian industry and research to address to renewable resources was underlined. As a consequence, the motivation and the interest in this thesis' topic appear clear.

The second part of the thesis gave some guidelines about the geometrical design of a PV-plant taking in consideration the accumulation of snow on the panels. Different answers were given for different plan conditions. When the modules are all located on the same shed, a high tilt angle can be more convenient than a low one, because it increases the sliding of snow. On the contrary, when panels are located on different sheds, the shading problems led to the conclusion that a medium tilt angle is the best solution. Other indications were given regarding the division of the system electrically, through string diodes and module by-pass diodes. In conclusion this part is addresses to who is approaching in designing a new PV-plant.

The third part focused on computation of snow loss; therefore, it is applicable to existing PV systems. An application of Marion's algorithm and the PVsyst software on the ZEB Living Lab PV-plant supposed in Oslo, Bergen and Trondheim gave interesting results about the snow loss values. They are strongly related to the snow depth, solar radiation and air temperature, therefore a deep connection to the location weather data is present. The monthly snow loss percentage reaches values till 70% in Oslo, while lower percentages characterize the other sites. However, the annual loss is around 3% in Oslo and Trondheim and around 1% in Bergen.

Possible solutions to avoid or reduce snow accumulation on the PV panels were investigated in the fourth chapter. Then a focus on the icephobic coatings was presented. Their characteristics, their design, their properties were studied to know how useful these elements can be to our case. Finally a spotlight on the state-of-art showed the possibilities that are nowadays offered by the market.

The fifth chapter coped with a hypothesis of simulation of icephobic coatings on the PV modules, to have an idea of their contribute in term of energy save. Moreover the fact that soiling loss is reduced as well should be taken in consideration. The simulations were conducted for the same PV-plant supposed in Oslo, Bergen and Trondheim in the third part, so that differences between the two cases were highlighted.

6.2 Further research

The several instruments and meters installed on the ZEB Living Lab could conduct to an interesting study about the influence of snow on the PV energy production in this specific case. Unfortunately many of these instruments have been activated only recently, therefore data collected is not sufficient yet. However, a monitoring of these values for a couple of years should be enough to conduct this experiment.

The aim of this research could be to evaluate the influence of snow coverage on energy production, as the one conducted in this thesis. However, this study would be strongly related to the case study of the ZEB Living Lab, for the reasons previously explained. Moreover a validation through collected data would test the reliability of the methodology.

The ZEB Living Lab is equipped with a weather station that collects data about wind speed, wind direction, dry bulb temperature, dew point temperature, relative humidity, barometric pressure, solar radiation every 30 seconds.

The SMA inverter is connected to the SensorBox, which provides measurement data through the SMA WebBox. Data related to input and output power from inverter let to define its efficiency curve. At this point simulations can be launched considering the real behaviour of the inverter.

The PV energy production is recorded daily and collectable at the SMA Sunny Portal, accessible via internet.

Snow depth is collected and published by local weather station. However, the collection of this data does not require any special instrument; therefore, it can be effectuated easily. Snow depth measurements are taken as long as there is snow on the ground. Determine the total depth of snow, sleet, or ice on the ground. This is a combination of snowfall and snow that was already on the ground. This observation is taken once a day at the scheduled time of observation with a measuring stick.

In conclusion all the instruments are already set. The research could be conducted easily as soon as the data is sufficient.

Data collected in the last winter are often lacking and not sufficient. It did not let any in-depth analysis, a comparison between snow depth values and daily energy production in one case was possible, though. Fig. 6.1 shows how energy production decreases when snow depth increases.
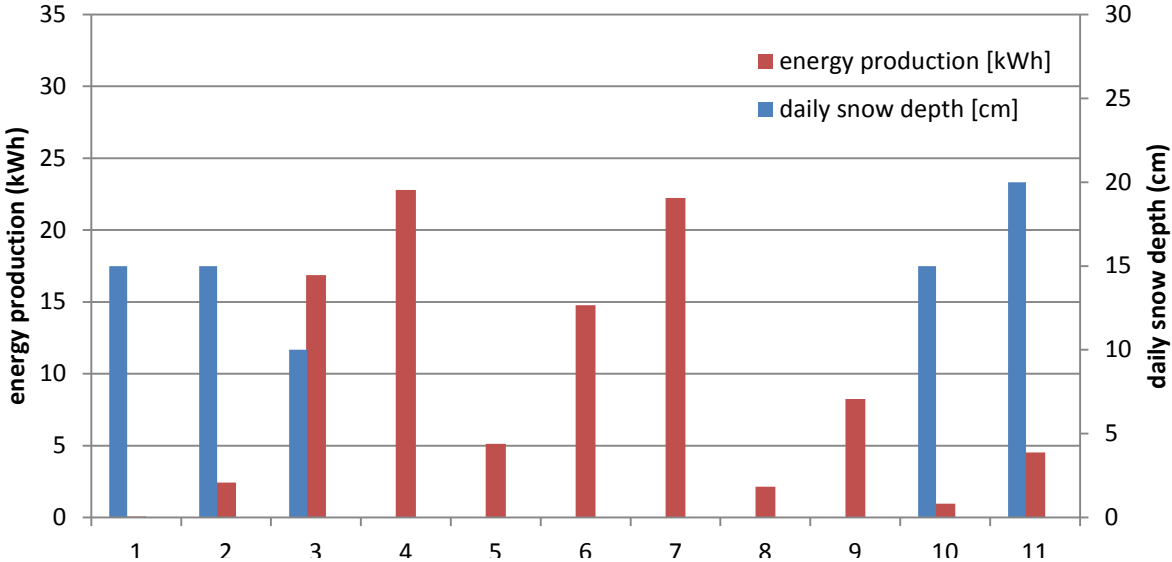
Fig. 6.1. Comparison daily energy production (kWh) versus daily snow depth (cm) for the PV-plant on the ZEB Living Lab. Data of February 2016 (from the 16th to the 26th).

The first analysis should be conducted in the spring and summer months, when the PV panels are surely free from snow. The second analysis can be conducted in the winter months, when PV panels are coved by snow. A comparison between these two would lead to the evaluation of the snow influence.

148

The methodology to follow is summarized in the following list:

1) The weather data collected over a whole year is inserted in a weather file hourly (epw file).
2) Information about the PV-plant is set in a PVsyst project accurately.
3) The inverter efficiency curve is defined considering the results collected by the SMA Sensor Box.
4) The simulation is launched.
5) Energy production of the summer months is read daily and compared to the one registered.
6) The difference between the two lists of values is due to the DC loss.
7) DC losses are now set in the PVsyst project.
8) The simulation is launched again.
9) Energy production of the winter months is read daily an compared to the one registered.
10) The difference between the two list of values is due to the snow loss.

The methodology can be repeated using values from different years to have a more reliable answer.

The snow loss values can be compared to the results obtained in Chap. 3 to have an indication about the influence of building geometry and panel frames to the theoretical snow loss.

This experimental study could lead to the comprehension of the influence of architectural choice in energy gain. However, the answer would be deeply related to the ZEB Living Lab case study. The study conducted in this Master's thesis is a generic evaluation. Therefore, it can be considered a more useful research than a specific case study.

Appendix

Appendix A

Tab. A.1. Daily average snow depth (cm) in Oslo, Bergen, Trondheim in January and February.

	January				February		
Day	**Oslo**	**Bergen**	**Trondheim**	**Day**	**Oslo**	**Bergen**	**Trondheim**
1	9	6	5	1	16	5	8
2	9	5	5	2	17	4	8
3	9	5	5	3	17	5	8
4	9	4	5	4	16	5	8
5	9	5	4	5	17	4	8
6	9	5	5	6	17	3	8
7	9	5	4	7	17	3	8
8	10	6	4	8	17	4	9
9	10	5	5	9	17	5	9
10	10	4	5	10	17	6	9
11	10	5	5	11	17	5	9
12	11	5	4	12	17	5	9
13	11	5	5	13	17	4	9
14	11	4	4	14	17	3	10
15	10	4	3	15	17	4	8
16	10	5	3	16	17	5	8
17	10	5	4	17	17	5	9
18	10	5	6	18	18	5	11
19	11	4	6	19	19	4	11
20	11	5	6	20	20	4	10
21	11	4	4	21	20	3	11
22	11	4	5	22	21	3	10
23	13	4	5	23	21	3	11
24	14	4	4	24	20	2	11
25	13	5	4	25	19	3	11
26	13	7	5	26	20	2	10
27	13	8	6	27	20	2	10
28	14	7	9	28	20	2	9
29	14	6	9	29	20	3	10
30	15	7	9				
31	15	6	9				

Tab. A.2. Daily average snow depth (cm) in Oslo, Bergen, Trondheim in March and April.

March				April			
Day	**Oslo**	**Bergen**	**Trondheim**	**Day**	**Oslo**	**Bergen**	**Trondheim**
1	20	4	10	1	12	0	0
2	20	4	10	2	11	0	0
3	22	4	10	3	12	1	0
4	23	4	9	4	10	1	0
5	24	3	9	5	9	0	0
6	23	3	11	6	8	0	0
7	21	2	10	7	7	0	0
8	21	2	10	8	6	0	0
9	21	2	11	9	6	0	0
10	20	1	11	10	5	0	0
11	20	1	11	11	5	0	0
12	20	2	10	12	5	0	0
13	19	3	9	13	4	0	0
14	19	5	10	14	4	0	0
15	19	4	10	15	3	0	0
16	20	3	9	16	2	0	0
17	19	3	8	17	1	0	0
18	19	3	8	18	1	0	0
19	18	2	6	19	1	0	0
20	19	1	4	20	1	0	0
21	19	1	3	21	0	0	0
22	19	1	1	22	0	0	0
23	18	2	0	23	0	0	0
24	19	1	0	24	0	1	0
25	18	1	0	25	0	0	0
26	18	1	0	26	0	0	0
27	17	1	0	27	0	0	0
28	17	1	0	28	0	0	0
29	16	0	0	29	0	0	0
30	15	0	0	30	0	0	0
31	14	0	0	31	0	0	0

154

Tab. A.3. Daily average snow depth (cm) in Oslo, Bergen, Trondheim in November and December.

November				December			
Day	**Oslo**	**Bergen**	**Trondheim**	**Day**	**Oslo**	**Bergen**	**Trondheim**
1	1	0	0	1	4	1	0
2	0	0	0	2	4	1	0
3	0	0	0	3	4	0	0
4	0	0	0	4	4	0	0
5	0	0	0	5	3	0	0
6	0	0	0	6	3	0	0
7	0	1	0	7	3	0	0
8	0	0	0	8	3	0	0
9	1	0	0	9	3	0	0
10	1	1	0	10	3	0	0
11	1	0	0	11	3	0	0
12	1	0	0	12	3	0	0
13	1	0	0	13	3	0	0
14	1	0	0	14	3	1	0
15	1	0	0	15	4	1	0
16	0	0	0	16	4	2	0
17	0	0	0	17	4	2	0
18	0	0	0	18	6	1	1
19	2	0	0	19	7	1	1
20	1	0	0	20	8	3	3
21	1	0	0	21	7	6	5
22	1	1	0	22	7	5	6
23	1	1	0	23	8	5	3
24	2	1	0	24	8	5	1
25	3	0	0	25	7	5	3
26	3	0	0	26	8	4	3
27	3	0	0	27	8	6	3
28	3	0	0	28	8	6	3
29	3	1	0	29	9	6	1
30	3	1	0	30	9	5	3
				31	9	6	4

Appendix B

Snow depth values (cm) collected in Leinstrand and Trondheim from November 2015 to March 2016. Highlights values are used for the linear regression showed in the following graph. This data was furnished by NOAA (National Centers for Environmental information in U.S.), accessing to national database of Norwegian Meteorological Institute (eklima.met.no). Many values are missing in Trondheim data.

Tab. B.1. Snow depth values (cm) collected in Leinstrand and Trondheim from November 2015 to December 2015.

November 2015			December 2015		
Day	**Trondheim**	**Leinstrand**	**Day**	**Trondheim**	**Leinstrand**
1	0	0	1	0	0
2	0	0	2	0	3
3	0	0	3	0	0
4	0	0	4	1	0
5	0	0	5	0	0
6	0	0	6	0	0
7	0	0	7	0	0
8	0	0	8	2	0
9	0	0	9	0	0
10	0	0	10	0	0
11	0	0	11	0	0
12	0	0	12	0	0
13	0	0	13	0	0
14	0	0	14	1	1
15	0	0	15	2	0
16	0	0	16	0	0
17	0	0	17	1	0
18	0	0	18	0	0
19	0	0	19		0
20	0	1	20		0
21	0	2	21		0
22	0	3	22		0
23	2	0	23		0
24	0	0	24		0
25	0	0	25		0
26	0	0	26	4	2
27	0	0	27		11
28	0	0	28	13	11
29	2	0	29		7
30	0	0	30		4
			31		1

Tab. B.2. Snow depth values (cm) collected in Leinstrand and Trondheim from January 2016 to March 2016.

	January 2016			February 2016			March 2016	
	Trondheim	Leinstrand		Trondheim	Leinstrand		Trondheim	Leinstrand
1		1	1		6	1		27
2		1	2		26	2		27
3		1	3		25	3		27
4		1	4		32	4		27
5		1	5		30	5	10	27
6		1	6		28	6	0	26
7		1	7	7	24	7	0	27
8		1	8	6	24	8		28
9		1	9	0	14	9	4	28
10		1	10	0	11	10	4	28
11		1	11		14	11		28
12		1	12		15	12	0	28
13		1	13		15	13	0	27
14		1	14		15	14	0	16
15		1	15		17	15	0	17
16	0	1	16	15	18	16	0	17
17		1	17	15	16	17	0	17
18	15	18	18	10	15	18	2	
19	20	19	19	0	12	19	0	7
20	25	24	20	0	9	20	0	5
21	25	30	21	0	9	21	0	4
22	25	30	22	0	9	22	0	4
23	30	34	23	0	9	23	0	2
24	30	34	24	0	14	24	0	2
25	30	28	25	15	16	25	0	
26		26	26	20	26	26	0	
27	7	18	27		24	27	0	0
28		21	28	15	27	28	0	0
29	6	14	29	15	27	29	0	
30		8				30	0	
31	2	8				31	0	

157

Appendix C

Data sheets about:

- Modules
- Inverter
- Inverter monitoring system
- Mounting system

REC

HIGH PERFORMANCE SOLAR MODULES

REC PEAK ENERGY SERIES

REC Peak Energy Series modules are the perfect choice for building solar systems that combine long lasting product quality with reliable power output. REC combines high quality design and manufacturing standards to produce high-performance solar modules with uncompromising quality.
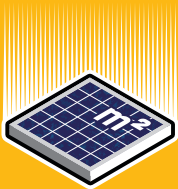
MORE POWER PER M²

ROBUST AND DURABLE DESIGN

ENERGY PAYBACK TIME OF ONE YEAR

OPTIMIZED FOR ALL SUNLIGHT CONDITIONS

REC PEAK ENERGY SERIES

Measurements in mm.

15.8%	**EFFICIENCY**					
10	**YEAR PRODUCT WARRANTY**					
25	**YEAR LINEAR POWER OUTPUT WARRANTY**					

TEMPERATURE RATINGS

Nominal Operating Cell Temperature (NOCT)	45.7°C (±2°C)
Temperature Coefficient of P_{MPP}	-0.40 %/°C
Temperature Coefficient of V_{OC}	-0.27 %/°C
Temperature Coefficient of I_{SC}	0.024 %/°C
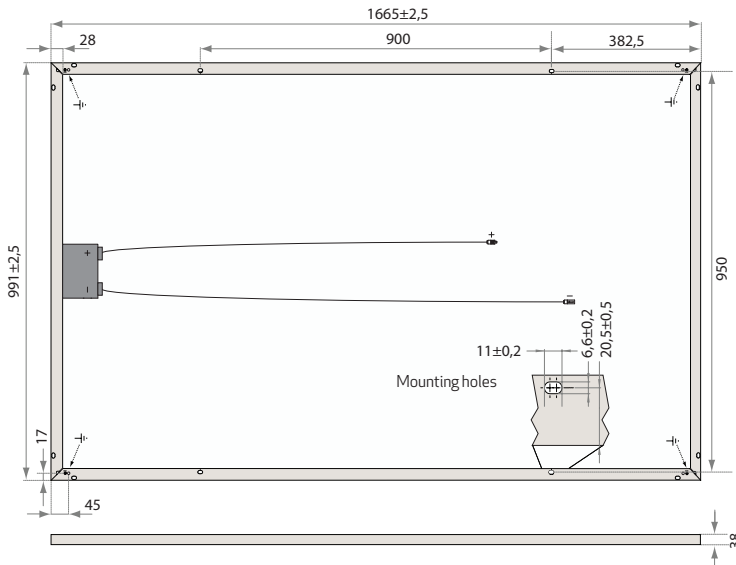
ELECTRICAL DATA @ STC

	REC235PE	REC240PE	REC245PE	REC250PE	REC255PE	REC260PE
Nominal Power - P_{MPP} (Wp)	235	240	245	250	255	260
Watt Class Sorting - (W)	0/+5	0/+5	0/+5	0/+5	0/+5	0/+5
Nominal Power Voltage - V_{MPP} (V)	29.5	29.7	30.1	30.2	30.5	30.7
Nominal Power Current - I_{MPP} (A)	8.06	8.17	8.23	8.30	8.42	8.50
Open Circuit Voltage - V_{OC} (V)	36.6	36.8	37.1	37.4	37.6	37.8
Short Circuit Current - I_{SC} (A)	8.66	8.75	8.80	8.86	8.95	9.01
Module Efficiency (%)	14.2	14.5	14.8	15.1	15.5	15.8

Analysed data demonstrates that 99.7% of modules produced have current and voltage tolerance of ±3% from nominal values.
Values at standard test conditions STC (airmass AM 1.5, irradiance 1000 W/m², cell temperature 25°C).
At low irradiance of 200 W/m² (AM 1.5 and cell temperature 25°C) at least 97% of the STC module efficiency will be achieved.

ELECTRICAL DATA @ NOCT

	REC235PE	REC240PE	REC245PE	REC250PE	REC255PE	REC260PE
Nominal Power - P_{MPP} (Wp)	179	183	187	189	193	197
Nominal Power Voltage - V_{MPP} (V)	27.5	27.7	28.1	28.3	28.5	29.0
Nominal Power Current - I_{MPP} (A)	6.51	6.58	6.64	6.68	6.77	6.81
Open Circuit Voltage - V_{OC} (V)	34.2	34.4	34.7	35.0	35.3	35.7
Short Circuit Current - I_{SC} (A)	6.96	7.03	7.08	7.12	7.21	7.24

Nominal operating cell temperature NOCT (800 W/m², AM 1.5, windspeed 1 m/s, ambient temperature 20°C).

GENERAL DATA

Cell Type:	60 REC PE multi-crystalline 3 strings of 20 cells with bypass diodes
Glass:	3.2 mm solar glass with anti-reflection surface treatment
Back Sheet:	Double layer highly resistant polyester
Frame:	Anodized aluminium (silver)
Junction Box:	IP67 rated 4 mm² solar cable, 0.9 m + 1.2 m
Connectors:	MC4 (4 mm²) MC4 connectable (4 mm²) Radox twist lock (4 mm²)

MAXIMUM RATINGS

Operational Temperature:	-40 ... +80°C
Maximum System Voltage:	1000 V
Maximum Snow Load:	550 kg/m² (5400 Pa)
Maximum Wind Load:	244 kg/m² (2400 Pa)
Max Series Fuse Rating:	25 A
Max Reverse Current:	25 A

CERTIFICATION

IEC 61215 & IEC 61730, IEC 62716 (ammonia resistance) & IEC 61701 (salt mist - severity level 6).

PV CYCLE

Member of PV Cycle

WARRANTY

10 year product warranty
25 year linear power output warranty
(max. degression in performance of 0.7% p.a.)
See warranty conditions for further details.

MECHANICAL DATA

Dimensions:	1665 x 991 x 38 mm
Area:	1.65 m²
Weight:	18 kg

Note! Specifications subject to change without notice.

REC is a leading global provider of solar electricity solutions. With nearly two decades of expertise, we offer sustainable, high-performing products, services and investment opportunities for the solar and electronics industries. Together with our partners, we create value by providing solutions that better meet the world's growing electricity needs. Our 2,300 employees worldwide generated revenues of more than NOK 7 billion in 2012, approximately EUR 1 billion.

REC

www.recgroup.com

SUNNY BOY 3000TL / 3600TL / 4000TL / 5000TL

Economical
- Maximum efficiency of 97 %
- Multi-string technology in all power classes
- Cost saving due to fewer parallel strings
- Shade management with OptiTrac Global Peak

Flexible
- Maximum DC input voltage of 750 V
- Integrated grid management functions and reactive power provision

Simple
- Without fan
- Easier wall mounting
- SUNCLIX DC plug-in system
- Fast connection, no tools required

Communicative
- Simple country configuration
- *Bluetooth*® technology as standard

SUNNY BOY 3000TL / 3600TL / 4000TL / 5000TL with Reactive Power Control

The same. Only better. The universally usable Sunny Boy.

It all remains the best: The new transformerless Sunny Boy is the ideal solution, especially for demanding PV arrays and partly shaded plants. Version 20 of the successful Sunny Boy offers a further array of advantages. It's more flexible in its range of applications, provides even more efficient yields, and it's easier to use. The high DC voltage of 750 V proves to be a cost advantage, since fewer parallel strings are required. In addition, the integrated grid management functions make the devices suitable for universal applications and allow them to actively support the grid.

SUNNY BOY 3000TL / 3600TL / 4000TL / 5000TL
with Reactive Power Control

Technical data	Sunny Boy 3000TL	Sunny Boy 3600TL
Input (DC)		
Max. DC power (@ cos φ = 1)	3200 W	3880 W
Max. input voltage	750 V	750 V
MPP voltage range / rated input voltage	175 V ... 500 V / 400 V	175 V ... 500 V / 400 V
Min. input voltage / initial input voltage	125 V / 150 V	125 V / 150 V
Max. input current input A / input B	15 A / 15 A	15 A / 15 A
Max. input current per string input A / input B	15 A / 15 A	15 A / 15 A
Number of independent MPP inputs / strings per MPP input	2 / A:2; B:2	2 / A:2; B:2
Output (AC)		
Rated power (@ 230 V, 50 Hz)	3000 W	3680 W
Max. apparent AC power	3000 VA	3680 VA
Nominal AC voltage / range	220 V, 230 V, 240 V / 180 V – 280 V	220 V, 230 V, 240 V / 180 V – 280 V
AC power frequency / range	50 Hz, 60 Hz / -5 Hz ... +5 Hz	50 Hz, 60 Hz / -5 Hz ... +5 Hz
Rated power frequency / rated grid voltage	50 Hz / 230 V	50 Hz / 230 V
Max. output current	16 A	16 A
Power factor at rated power	1	1
Displacement power factor, adjustable	0.8 overexcited ... 0.8 underexcited	0.8 overexcited ... 0.8 underexcited
Feed-in phases / connection phases	1 / 1	1 / 1
Efficiency		
Max. efficiency / European weighted efficiency	97 % / 96 %	97 % / 96.3 %
Protective devices		
DC disconnect device	●	●
Ground fault monitoring / grid monitoring	● / ●	● / ●
DC reverse polarity protection / AC short-circuit current capability / galvanically isolated	● / ● / –	● / ● / –
All-pole-sensitive residual-current monitoring unit	●	●
Protection class (according to IEC 62103) / overvoltage category (according to IEC 60664-1)	I / III	I / III
General data		
Dimensions (W / H / D)	490 / 519 / 185 mm (19.3 / 20.4 / 7.3 inches)	
Weight	26 kg (57.3 lb)	26 kg (57.3 lb)
Operating temperature range	–25°C ... +60°C (–13°F ... +140°F)	–25°C ... +60°C (–13°F ... +140°F)
Noise emission (typical)	25 dB(A)	25 dB(A)
Self-consumption (night)	1 W	1 W
Topology	Transformerless	Transformerless
Cooling concept	Convection	Convection
Degree of protection (according to IEC 60529)	IP65	IP65
Climatic category (according to IEC 60721-3-4)	4K4H	4K4H
Maximum permissible value for relative humidity (non-condensing)	100 %	100 %
Features		
DC connection / AC connection	SUNCLIX / Spring clamp terminal	SUNCLIX / Spring clamp terminal
Display	Graphic	Graphic
Interface: RS485 / Bluetooth / Speedwire / Webconnect	○ / ● / ○ / ○	○ / ● / ○ / ○
Multi-function relay / Power Control Module	○ / ○	○ / ○
Warranty: 5 / 10 / 15 / 20 / 25 years	● / ○ / ○ / ○ / ○	
Certificates and approvals (additional on request)	AS 4777, C10/11, CE, CEI 0-21, EN 50438[1], G59/2, G83/1-1, IEC 61727, NRS 097-2-1, PEA, PPC, PPDS, RD1699, RD 661, UTE C15-712, VDE-AR-N 4105, VDE0126-1-1	
Version: March 2013		
● Standard features ○ Optional features – Not available, Data at nominal conditions		
Type designation	SB 3000TL-21	SB 3600TL-21

Efficiency curve SUNNY BOY 5000TL

- Eta (V$_{PV}$ = 175 V)
- Eta (V$_{PV}$ = 400 V)
- Eta (V$_{PV}$ = 500 V)
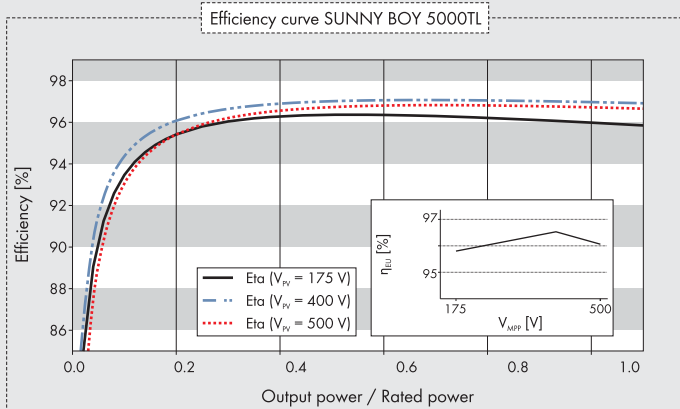
Accessories

RS485 interface
DM-485CB-10

Speedwire/Webconnect
interface SWDM-10

Multi-function relay
MFR01-10

Additional fan kit
FANKIT01-10

Power Control Module
PWCMOD-10

[1] Does not apply to all national appendices of EN 50438
[2] 4600 VA with VDE-AR-N-4105
[3] 4825 W with VDE-AR-N 4105

Technical data	Sunny Boy 4000TL	Sunny Boy 5000TL
Input (DC)		
Max. DC power (@ cos φ = 1)	4200 W	5250 W[3]
Max. input voltage	750 V	750 V
MPP voltage range / rated input voltage	175 V ... 500 V / 400 V	175 V ... 500 V / 400 V
Min. input voltage / initial input voltage	125 V / 150 V	125 V / 150 V
Max. input current input A / input B	15 A / 15 A	15 A / 15 A
Max. input current per string input A / input B	15 A / 15 A	15 A / 15 A
Number of independent MPP inputs / strings per MPP input	2 / A:2; B:2	2 / A:2; B:2
Output (AC)		
Rated power (@ 230 V, 50 Hz)	4000 W	4600 W
Max. apparent AC power	4000 VA	5000 VA[2]
Nominal AC voltage / range	220 V, 230 V, 240 V / 180 V – 280 V	220 V, 230 V, 240 V / 180 V – 280 V
AC power frequency / range	50 Hz, 60 Hz / –5 Hz ... +5 Hz	50 Hz, 60 Hz / –5 Hz ... +5 Hz
Rated power frequency / rated grid voltage	50 Hz / 230 V	50 Hz / 230 V
Max. output current	22 A	22 A
Power factor at rated power	1	1
Displacement power factor, adjustable	0.8 overexcited ... 0.8 underexcited	0.8 overexcited ... 0.8 underexcited
Feed-in phases / connection phases	1 / 1	1 / 1
Efficiency		
Max. efficiency / European weighted efficiency	97 % / 96.4 %	97 % / 96.5 %
Protective devices		
DC disconnect device	●	●
Ground fault monitoring / grid monitoring	● / ●	● / ●
DC reverse polarity protection / AC short-circuit current capability / galvanically isolated	● / ● / –	● / ● / –
All-pole-sensitive residual-current monitoring unit	●	●
Protection class (according to IEC 62103) / overvoltage category (according to IEC 60664-1)	I / III	I / III
General data		
Dimensions (W / H / D)	490 / 519 / 185 mm (19.3 / 20.4 / 7.3 inches)	
Weight	26 kg (57.3 lb)	26 kg (57.3 lb)
Operating temperature range	–25°C ... +60°C (–13°F ... +140°F)	–25°C ... +60°C (–13°F ... +140°F)
Noise emission (typical)	25 dB(A)	25 dB(A)
Self-consumption (night)	1 W	1 W
Topology	Transformerless	Transformerless
Cooling concept	Convection	Convection
Degree of protection (according to IEC 60529)	IP65	IP65
Climatic category (according to IEC 60721-3-4)	4K4H	4K4H
Maximum permissible value for relative humidity (non-condensing)	100 %	100 %
Features		
DC connection / AC connection	SUNCLIX / Spring clamp terminal	SUNCLIX / Spring clamp terminal
Display	Graphic	Graphic
Interface: RS485 / Bluetooth / Speedwire / Webconnect	○ / ● / ○ / ○	○ / ● / ○ / ○
Multi-function relay / Power Control Module	○ / ○	○ / ○
Warranty: 5 / 10 / 15 / 20 / 25 years	● / ○ / ○ / ○ / ○	
Certificates and approvals (additional on request)	AS 4777, C10/11, CE, CEI 0-21, EN 50438[1], G59/2, G83/1-1, IEC 61727, NRS 097-2-1, PEA, PPC, PPDS, RD1699, RD 661, UTE C15-712, VDE-AR-N 4105, VDE0126-1-1	
● Standard features ○ Optional features – Not available, Data at nominal conditions		
Type designation	SB 4000TL-21	SB 5000TL-21

SUNNY SENSORBOX

Reliable

- Rapid error detection via continuous target-actual comparison of plant performance

Informative

- Precise acquisition of irradiation intensity, module temperature, ambient temperature and wind speed values

Easy to install

- Easy installation on the solar generator
- Simple integration into existing PV plants via RS485

- Data analysis on any PC or in the Sunny Portal

SUNNY SENSORBOX

The weather station for PV plants

The Sunny SensorBox is installed directly onto the modules and measures the sun radiation and temperature. In combination with Sunny WebBox and Sunny Portal, it provides a continuous target-actual comparison of plant performance. This makes it possible to detect shade, dirt, and gradually declining performance in a generator and thus maximizes yield security. Additional sensors for optional measurement of ambient temperature or wind speed permit more precise calculations.

SUNNY SENSORBOX

Innovation and precision for your performance monitoring

Complete system monitoring easily installed

The Sunny SensorBox is installed outdoors at the solar generator, and comes with an integrated solar cell, which measures solar irradiation. The module temperature is measured by means of the temperature sensor which is included. From the present solar irradiation level and the module temperature, it is possible to calculate the expected output, and to compare it with the actual measured output of the inverters. Temporary or continuous yield losses caused by unknown failure sources are therefore a thing of the past.

... extendable

Once the Sunny SensorBox has been aligned to the modules, it is simply connected with the inverters to a Sunny WebBox with an RS485 data connection. From there, the data can be transferred to a PC for further processing, or to the Sunny Portal for automatic performance analysis. The Sunny SensorBox also enables the connection of additional sensors, e. g. to measure the ambient temperature or wind speed for calculations which are even more precise. This ensures reliable system monitoring for operators – and maximum yield security.

Typical system design – Cable Transmission

Electricity Generation
1 SUNNY MINI CENTRAL
2 Solar generator

System Monitoring
3 SUNNY SENSORBOX
4 SUNNY WEBBOX
5 SUNNY PORTAL
6 FLASHVIEW
7 SUNNY MATRIX

— RS485
— Local network / Internet
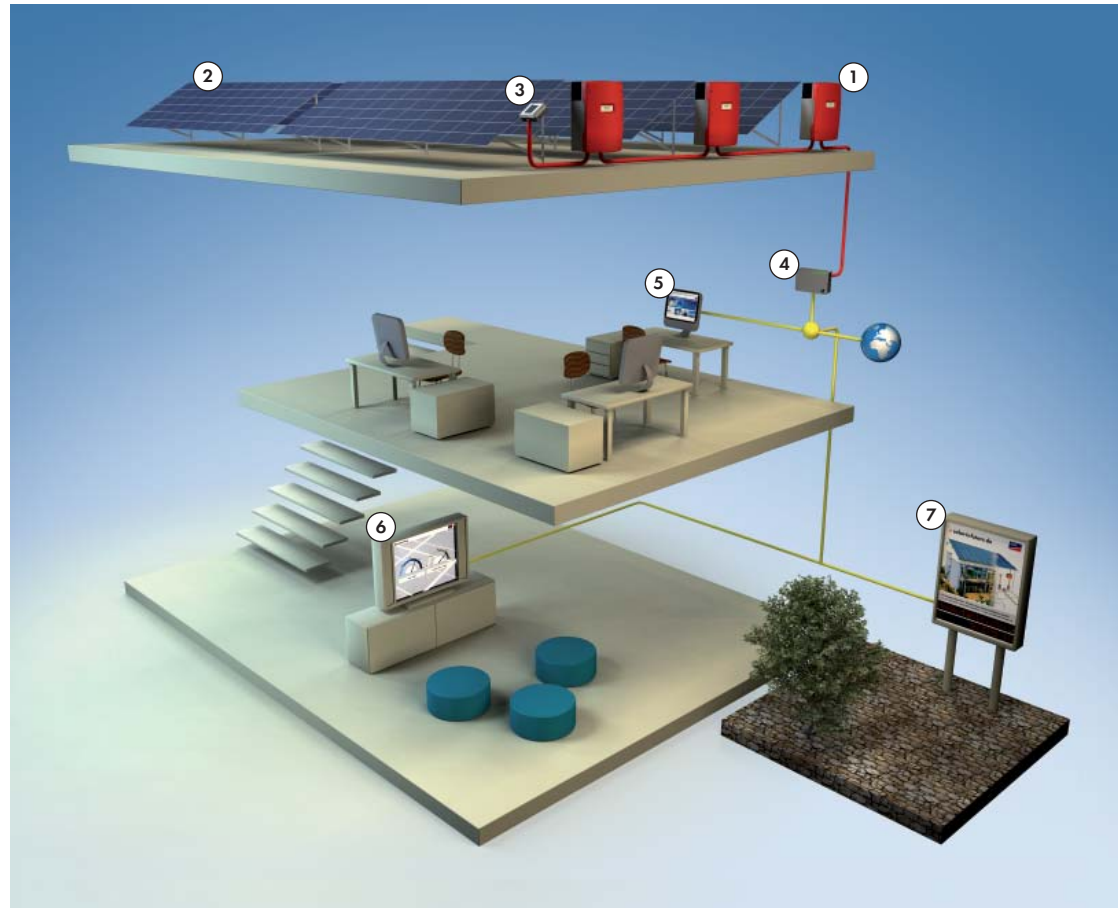
Performance ratio as a quality indicator

Shadowing, defects, surface contamination and gradual malfunctions such as deteriorating modules have a serious impact on the generator yield and the overall performance and are not to be underestimated. Particularly annoying for the operator is the fact that the losses in yield could have been avoided in most cases – if the error had been detected in time. The system efficiency of the PV-plant (performance ratio) is therefore an essential value. The performance ratio indicates the ratio of actual yield to the theoretically possible yield. Since the performance ratio indicates how the irradiated energy on the generator side is exploited, it is the decisive quality factor for the performance of the entire PV system. This is where the

Sunny SensorBox comes into play.

How to determine the performance ratio

You simply divide the actual energy yield through the possible energy yield. While the inverter measures the actual energy, the possible energy yield is determined according to the efficiency of the modules, the module surface and the recorded insolation. Good grid connected PV systems reach performance ratios of between 60 % and 80 % – ratios under this value can indicate malfunctions of the system.

Technical data	Sunny SensorBox	
Communication		
Data logger communication	RS485 or SMA Power Injector with *Bluetooth* to Sunny WebBox	
Interfaces		
Sunny WebBox and Power Injector	1x SMACOM / spring terminals	
Max. communication range		
RS485	1.200 m	
SMA Power Injector with *Bluetooth*	100 m	
Power supply		
Power supply	RS485 Power Injector SMA Power Injector with *Bluetooth*	
Input voltage	100 V – 240 V AC, 50 / 60 Hz	
Power consumption	< 1 W	
Environmental conditions in operation		
Ambient temperature	–25 °C ... +70 °C	
Protection rating (as per EN 60529)	IP65	
General data		
Dimensions (W / H / D) in mm	120 / 50 / 90	
Weight	500 g	
Mounting location	Outdoor	
Deployment options	Mounting plate, roof bracket	
Language versions – manual	German, English, French, Italian, Spanish, Dutch, Czech, Portuguese, Greek. Korean	
Features		
Operation	via the Sunny WebBox interface	
Warranty	5 years	
Certificates and approvals	www.SMA-Solar.com	
Accessories		
Mounting plate	O	
Roof bracket	O	
Wind sensor	O	
Wall mounting bracket for wind sensor	O	
PT100 ambient temperature sensor	O	
PT100 module temperature sensor	●	
RS485 Power Injector	●	
SMA Power-Injector with *Bluetooth*®	O	

● Standard features   O Optional features   — Not available

Communication with the Sunny WebBox via RS485

Continuous **monitoring** of generator performance in Sunny Portal

Measurement of radiation and module temperature (plus optional measurement of ambient temperature and wind speed)

Easy installation data transmission and energy supply via a common cable

www.SMA-Solar.com

SMA Solar Technology AG

User-friendly

- Central management of all customer and plant data
- Easy to understand reporting

- World-wide access via the Internet – via PC and mobile phones

Personalization

- Personalized configuration of pages and diagrams
- Individual yield and event reports sent via e-mail

Informative

- Fully automatic yield comparison of plant devices
- Professional integration into personal website

SUNNY PORTAL

Professional management, monitoring and presentation of PV plants

Whether for small residential systems or a large PV farm, centralized management and system monitoring saves time and money. Through the Sunny Portal, plant operators and installers have access to key data at any time. Pre-configured standard pages can be easily customized or supplemented. Whether as a data table or as a diagram: SMA solutions allow almost infinite options for analyzing measured data or visualizing yields. The yields of all inverters in a plant are compared automatically, allowing for the detection of even the smallest deviations. The powerful reporting functions also provide regular updates via e-mail to help ensure yields.

Technical Data	Sunny Portal
Languages	
Available languages	German, English, Italian, Spanish, French, Dutch, Portuguese, Greek, Korean, Czech, Chinese
System requirements	
Supported operating systems	All / optimized access for mobile devices
Plant information	
Plant description	Overview of the key properties of the PV plant
Annual comparison	Quick yield overview of the entire operating period
Energy balance	Overview of purchased and fed in power and self-consumption, if applicable (power meter integration via Meter Connection Box or Sunny Home Manager required)
Plant log book	Access to messages regarding plant events
Device overview	Properties and parameters of the devices in the PV plant
Software	
Recommended browsers	Firefox, Internet Explorer, version 7 and later, Safari
Other	JavaScript and cookies enabled
Supported data logger	Sunny WebBox, Sunny Home Manager
Access	
Website	www.sunnyportal.com
Smartphone	www.sunnyportal.mobi, Sunny Portal App for iPhone and Android
Plant management	
Sunny Portal Account	One password for all your plants in Sunny Portal
Page design	
Standard pages	Automatic standard pages for the most common plant monitoring and presentation needs
Personalized pages	A variety of templates for page construction
Page modules	Tables, diagrams, custom images, free text, plant overview (CO_2, remuneration, energy)
Visualization of yield and measured values	
Diagram types	Selection of six diagram types for optimum presentation of yield & measured values, bar graphs, area charts, and line charts (with, without, or only tags), as well as XY diagrams
Tables	Individual configuration of charts for all yield and measured values
Time periods	From 5 minutes to 1 year, various time intervals selectable (depending on provided data)
Monitoring	
Inverter comparison	Fully automatic and ongoing inverter yield comparison and e-mail alarms
Communication monitoring	Ongoing monitoring and, when necessary, alarms for the connection between Sunny Portal and Sunny WebBox, the Sunny Home Manager and the Power Reducer Box
Status reports	
Information reports	Daily or monthly reports on energy yield, maximum output, remuneration, CO_2 reduction via e-mail; a self-defined page can also be sent from Sunny Portal
Event reports	Hourly or daily reports on information, warnings, faults and errors, with personalized content and recipients
Report format	Text, PDF, HTML
Individual access	
Publication of specific pages	Access via the public area on Sunny Portal by all Internet users, ideal for personalized presentations on personal Web sites
User roles	Assign roles of "guest", "standard user", "installer" and "plant administrator" to easily determine who has which viewing and configuration rights
Type designation	Sunny Portal

Management of several PV plants from one central location

Monitoring without having to be on-site

Quick overview of measured and yield values of the PV plant

Easy diagnostics through display of measured values and event log

High-performance reporting to help safeguard yields

Personalized access to screen options and functions

Flexible page design for individual presentation of the PV plant

Standard pages for the most common display options

SUNNY WEBBOX

Safe

- Remote monitoring, diagnosis and configuration of the solar power plant from anywhere in the world

- Quick detection of malfunctions and notification in case of a failure via e-mail or text message*
- Powerful data logger for documentation of all important plant data

User-friendly

- Easy remote access via the web browser
- Including free standard access for Sunny Portal for the entire service life of the plant

- Flexible display, evaluation, yield and event reports via Sunny Portal

SUNNY WEBBOX

Remote monitoring and maintenance of large solar power plants

System monitoring, remote diagnosis, data storage and visualization: the Sunny WebBox is the high-performance communication hub for medium- to large-scale solar power plants. It continuously collects all the data from the inverters on the system side, thereby keeping you informed of the system's status at any given time. The Sunny WebBox is a multi-functional, energy-efficient data logger which offers a wealth of options for displaying, archiving and processing data, even in networks with strict security regulations. In case of the event "Error", the WebBox informs you immediately by e-mail or text message*. Even from remote locations where no DSL or telephone connection is available, measurement data can be transmitted to the Sunny Portal via a GSM modem.

*optional with existing GSM modem

SUNNY WEBBOX

Modular system monitoring for commercial solar power systems

Plant management

The Sunny WebBox continuously records and stores all available measured values of up to 50 inverters. In addition, the inverter parameters can be called up and modified. The Sunny WebBox is the single point of operation e.g. for changing the operating parameters of the connected inverters – from anywhere in the world.

The Sunny WebBox allows installers and plant operators to have all information concerning the status of a solar power plant at any time and to detect operational faults at an early stage. In case of an event of the type "Error" you are furthermore alarmed actively by e-mail or optionally by text message*. Wherever you may be – whether at home, in the office or on a business trip: all you need is a PC with internet browser and an internet connection in order to access the data of the Sunny WebBox.

*optional with existing GSM modem

Data management

The Sunny WebBox provides various modern data processing options for professional data management. The recorded performance values, which provide you with detailed information on the performance of your system, are saved in conventional CSV or XML file formats on the Sunny WebBox. The ability to exchange data by FTP allows you to easily transfer these values to the PC. In this way, valuable system data can not only be saved on your computer for the long-term, but can also be displayed according to your preferences using MS Excel, for example, and create straightforward evaluations over the course of the day, month and year. Additionally, it is possible to send plant data – simultaneously to the Sunny Portal – to a freely selectable FTP-server.

Typical plant design

Electricity generation
① SUNNY MINI CENTRAL
② PV generator

System monitoring
③ SUNNY SENSORBOX
④ SUNNY WEBBOX
⑤ SUNNY PORTAL
⑥ FLASHVIEW
⑦ SUNNY MATRIX

— RS485
— Local network / Internet
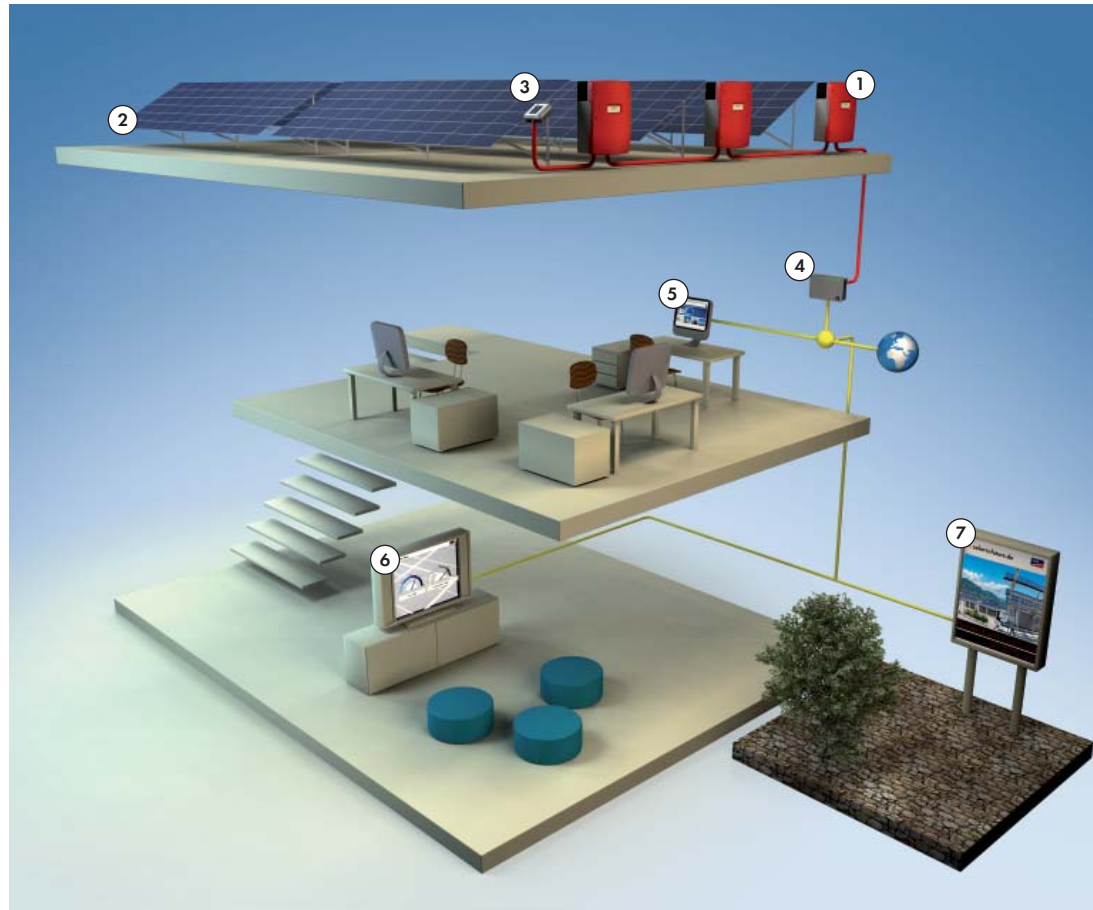
You can just as easily use a SD-card to save your data and transfer it between the Sunny WebBox and your PC. If a SD-card is inserted, the Sunny WebBox will additionally save your data on the removable storage medium. The data read out from the SD-card by a PC provides the identical individual options for processing it as with FTP.

A perfect duo with Sunny Portal

The next step to even more convenience is to use the Sunny WebBox in combination with our free Internet portal.

At www.SunnyPortal.com, we provide you with a completely pre-configured environment in which the data can be archived, processed and displayed automatically. If desired, the Sunny Portal also generates a daily or monthly plant report that you receive by e-mail. In case the Sunny WebBox does not send any data, the Sunny Portal also informs about that. On

request, the online platform automatically compares the yields of all inverters in a system and keeps you informed about potential deviations. Another advantage: the WebBox software can be automatically updated via Sunny Portal. This ensures that your system monitoring is always kept up-to-date with the latest technology.

The combination of Sunny Portal and WebBox results in an invincible team for keeping track of your solar harvest. And with the SMA Service, plant operators and installers get support for the entire service life of a system. Because in case of an event our employees can log in to the plant and support in the troubleshooting.

Technische Daten	SUNNY WEBBOX
Communication	
Inverter communication	RS485, 10/100 Mbit Ethernet (only for Sunny Central)
PC communication	10/100 Mbit Ethernet
Modem	Analog (optional), GSM (optional)
Max. number of SMA devices	
RS485 / Ethernet	50 / 50
Max. communication range	
RS485 / Ethernet	1,200 m / 100 m
Power supply	
Power supply	external plug-in power supply
Input voltage	100 V – 240 V AC, 50 / 60 Hz
Power consumption	Typ. 4 W/ max. 12 W
Environmental conditions in operation	
Ambient temperature	–20 °C to +65 °C
Relative air humidity	5 % to 95 %, non-condensing
Memory	
internal	8 MB circular buffer
external	SD-card 128 MB / 512 MB / 1 GB / 2 GB
General data	
Dimensions (W / H / D) in mm	225 / 130 / 57
Weight	750 g
Installation site	indoor
Deployment options	DIN rail mounting, wall mounting, tabletop device
Status display	LEDs
Language versions - software / manual	German, English, French, Greek, Italian, Korean, Dutch, Portuguese, Spanish, Czech
Features	
Operation	integrated Web server (Internet browser)
Warranty	5 years
Certificates and approvals	www.SMA-Solar.com
Accessories	
Sunny SensorBox / Sunny Matrix	O/O
SD card 128 MB / 512 MB / 1 GB / 2 GB	O/O/O/O
Outdoor GSM antenna / GSM data card	O/O
RS485 communication cable	O

● Standard equipment   O Optional

Direct alarm in case of the event „Error" by e-mail or text message

Presentation of plant data with Sunny Matrix or Flashview

Automatic **visualization** of the measurement data in Sunny Portal - free of charge

SD card slot for optional **memory expansion** and data transfer to a PC

Integrated web server enables **online remote data access** from any web-enabled PC in the world

Integrated FTP server for data transfer and storage on a PC

Individual processing of the measuring data on the PC

Flexible data transfer to freely selectable FTP server parallel to Sunny Portal possible

*optional with existing GSM modem

www.SMA-Solar.com

SMA Solar Technology AG

SMA

Simple

- Straightforward plug-&-play commissioning
- Other SMA devices are not required

Economical

- Reasonable investment costs and low installation effort
- Most favorable way of plant monitoring

Communicative

- Free online monitoring via Sunny Portal
- Clear display of the most important plant data with Sunny Portal

Direct

- Data exchange with Sunny Portal without data logger
- Free Sunny Portal app for data visualization on smartphones

WEBCONNECT

Direct data exchange with Sunny Portal

Ideally suited for online monitoring of small PV plants with a maximum number of up to four inverters: Webconnect provides free access to Sunny Portal without additional data logger – easily via an existing Internet access and a DSL router. After the simple installation of the inverter interface which is optionally available or already integrated at the factory, you can commission the Webconnect. Basically, it's plug-n-play. Once configured, key plant data can be accessed and displayed in a clear format whenever you need it. Moreover, automatic product updates ensure that the device firmware is always up-to-date.

Optional Webconnect interface of data module[1] or Piggy-Back[2] type

SB 240-10 and Sunny Multigate with integrated Webconnect functionality

STP 5000/6000/7000/8000/9000TL-20 with integrated Webconnect functionality

[1] Supported inverters: STP 15000TLEE-10 / 20000TLEE-10, STP 15000TLHE-10 / 20000TLHE-10, STP 10000TL-10 / 12000TL-10 / 15000TL-10 / 17000TL-10, SB 2500TLST-21 / 3000TLST-21, SB 3000TL-21 / 3600TL-21 / 4000TL-21 / 5000TL-21

[2] Supported inverters: SB 1300TL-10 / 1600TL-10 / 2100TL, SB 3300-11 / 3800-11, SMC 6000A-11

Technical data	Inverter with Webconnect functionality	Micro inverter with Webconnect functionality
Communication		
Sunny Portal	SMA Webconnect via Ethernet	
Connections		
Ethernet	RJ45	
Max. radio range		
Ethernet	100 m	
Supported Sunny Portal functions		
Online device updates	●	
Plant and device information		
Live data	●	●
Panel Level Monitoring	–	●
Plant description	Overview of the key properties of the PV plant	
Annual comparison	Quick yield overview of the entire operating period	
System logbook	Access to messages regarding plant events	
Device Overview	Properties and parameters of the devices in the PV plant	
Status reports	E-mail reports provide regular information on plant yields and plant events	
Data management	Data consolidation after two years	
Monitoring		
Inverter comparison	Fully automatic and continuous yield comparison and e-mail alarms	
Communication monitoring	Ongoing monitoring of the connection between Sunny Portal and the PV plant	
Individual access		
Publication of specific pages	Access via the public area on Sunny Portal by all Internet users, ideal for personalized presentations on personal websites	
User roles	By assigning the roles of "guest", "standard user", "installer" and "plant administrator", you can determine viewing and configuration rights of the different roles.	
Access		
Website	www.sunnyportal.com	
Smartphone	www.sunnyportal.mobi, Sunny Portal App for iPhone and Android	

● Standard feature   ○ Optional feature   – Not available

Typical plant design

Power generation
① e.g. Sunny Tripower with Webconnect data module
② PV array

Plant monitoring
③ Sunny Explorer
   Sunny Portal
④ Mobile access

www.SMA-Solar.com

SMA Solar Technology

CSTB
le futur en construction
PASS'INNOVATION
n° 2011-123

*Inter*Sole SE

Produktinformation

Beschreibung / Vorteile

Integriertes Montagesystem für PV-Module in Schrägdächern

InterSole SE ist das ideale Montagesystem für die Integration von gerahmten oder rahmenlosen PV-Modulen auf Schrägdächern. Es wird bereits seit 2003 europaweit erfolgreich installiert. Die PV-Module sind bündig integriert und schaffen so eine perfekte und harmonische Optik mit der Dacheindeckung. Eine ausreichende Hinterlüftung bleibt gewährleistet: der kühlende Luftstrom kann hinter den Modulen zirkulieren und sorgt somit für optimale Energieerträge. Das innovative und durchdachte Design der InterSole sorgt für eine einfache und schnelle Installation.

Das System besteht aus HDPE-Platten (Polyethylen hoher Dichte), sowie Montageschienen, Modulklemmen und Verblechung aus Aluminium. Alle Befestigungselemente sind aus Edelstahl. Das InterSole SE Montagesystem wurde entwickelt um höchste Zuverlässigkeit, Langlebigkeit, einfache Montage und darüber hinaus ein exzellentes Preis-Leistungsverhältnis zu gewährleisten. Es ist TÜV zertifiziert und hat in Frankreich die Pass Innovation Nr. 2011-123 für die "décénale" (10-jährige) Garantie vom Installateur erhalten.

InterSole SE

Einsatzbereich

System	belüftetes, einstufiges Integrationssystem für Dachlatten
Gebäudeart	Wohn- und Industriegebäude mit Dachlatten
Dacheindeckungstypen	Dachpfannen, Schiefer
Material	InterSole Platten in recycletem Polyethylen hoher Dichte (HDPE), Struktur und Verblechung in Aluminium und Befestigungselemente in Edelstahl
Dachneigung	min. 15° (20° wenn Montage ohne untere Esthétivette) max. 70°
Systemhöhe	51 mm (minimaler Abstand zwischen Dachlatten und untere Modulseite)
Verblechung	ja
Lüftungshöhe	49mm (Dicke der Luftschicht unter den Modulen)

Modulkompatibilität

Typ	gerahmte oder rahmenlose PV Module
Stärke	gerahmte Module: 34 ~ 51 mm rahmenlose Module : 3 ~ 25 mm
Modulausrichtung	Hochformat quer
Normen	IEC 61215 oder IEC 61646 / IEC 61730

Komponente

Hintergrund	ca. 2mm stark, lieferbar in Platten 1,1x1,6m (3kg) oder Rollen 1,1x10m (19kg)
Anker	22mm hoch
Montageschiene	27mm hoch, lieferbar in 1,5m, 3m Länge oder Zuschnitt

Leistung

Installationsdauer	ca. 7 Stunden (für eine 3 kWp Anlage, mit 2 erfahrenen Installateure)
Windbelastbarkeit	Windzone 3 bei 12 m Gebäudehöhe (Frankreich, Standardmontage)
Schneebelastbarkeit	Schneezone B2 bei 600 müNN Meereshöhe (EN1991-1-4 : 2004 Eurocode1) alle anderen Zonen bis 200 müMM Meereshöhe

Design

Farben Schienen und Klemmen	pressblank oder schwarz
Farben Verblechung	pressblank (schwarz für 4Q2011 geplant)
Farben wasserfeste Schürze	schwarz oder rot

Zertifizierung

TÜV	Bericht Nr. 21213086
CSTB (FR)	Pass Innovation Nr. 2011-123
Mechanische Belastbarkeit	DIN 1055 (Schnee und Wind)
Regen-Belastbarkeit	PrEN 15601 (Schlagregen)
UV Beständigkeit	ISO 4892-4 (2500 Stunden)
Brandschutz	Broof t1 und t3, ENV 1182 und EN 13501-5

Service und Support

Produktgarantie	10 Jahre
Schulung	auf Anfrage
Web Konfigurator	ja
Support	telefonisch und online, Vor-Ort

Appendix D
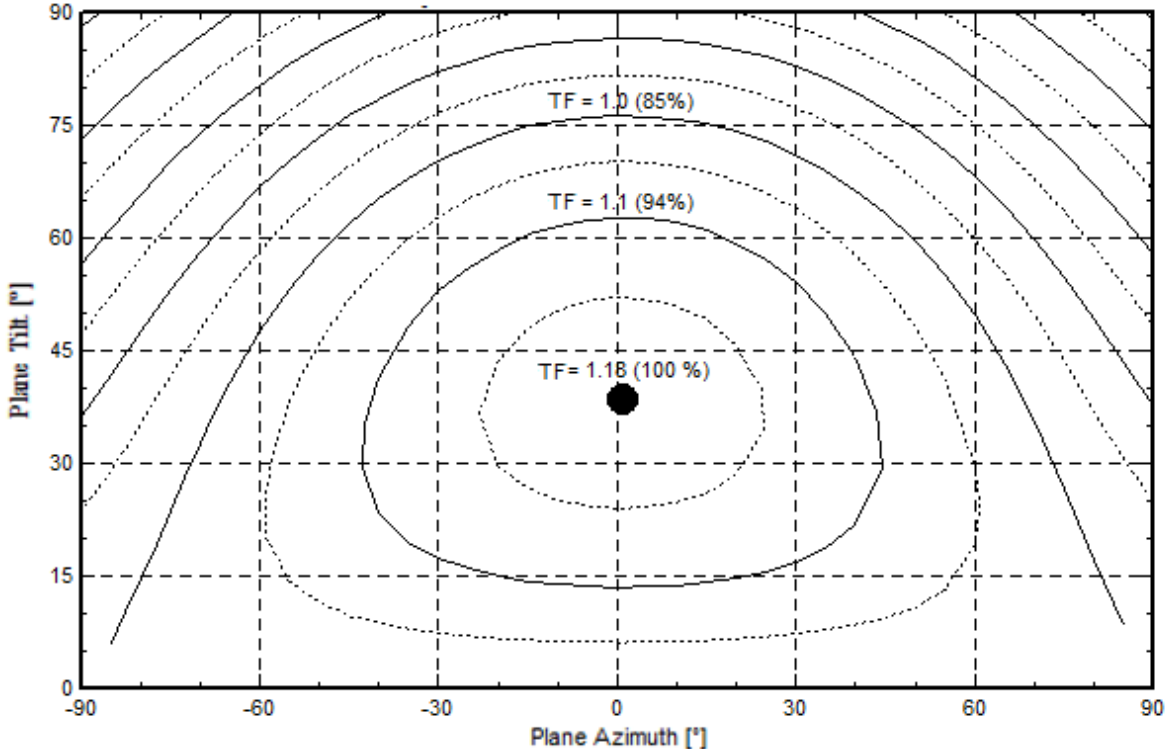
Fig. D.1. Transposition factor variation as function of plane tilt and plane azimuth. Values during the whole year for Oslo (plotted by the author through PVsyst).
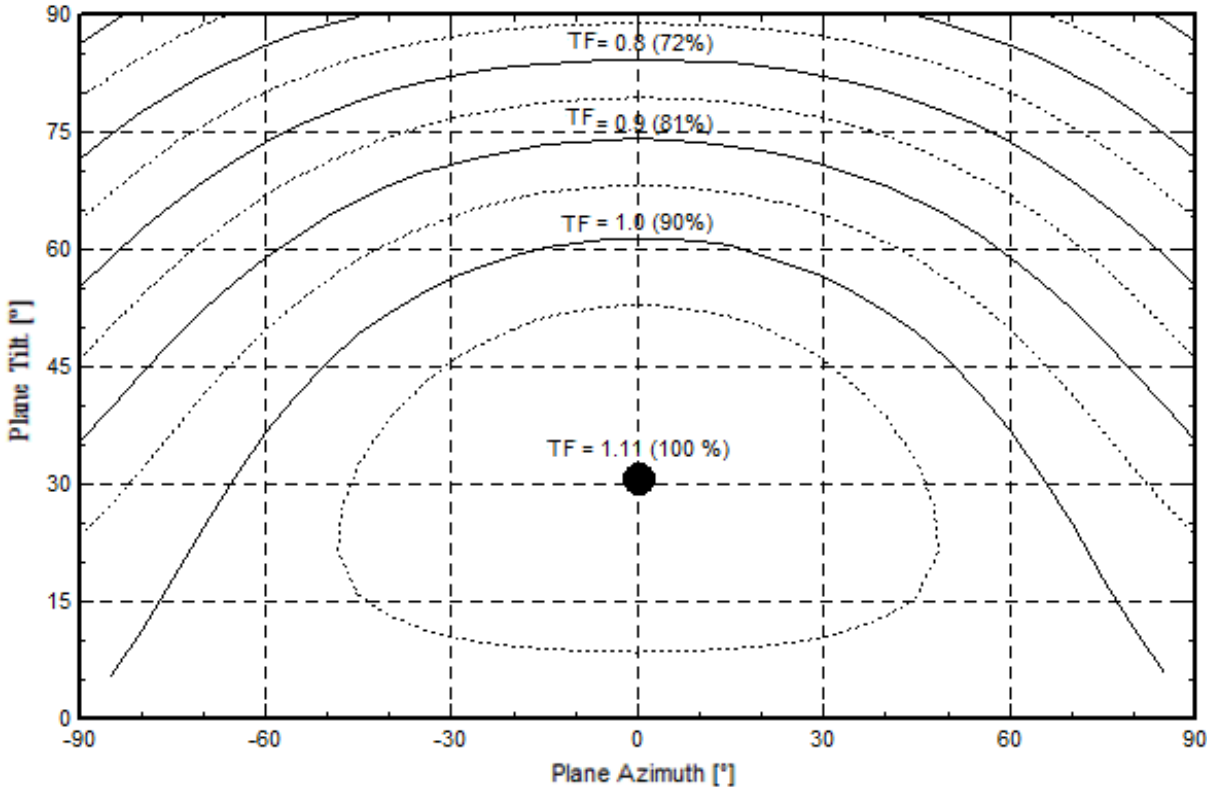
Fig. D.2. Transposition factor variation as function of plane tilt and plane azimuth. Values during the summer for Oslo (plotted by the author through PVsyst).

159
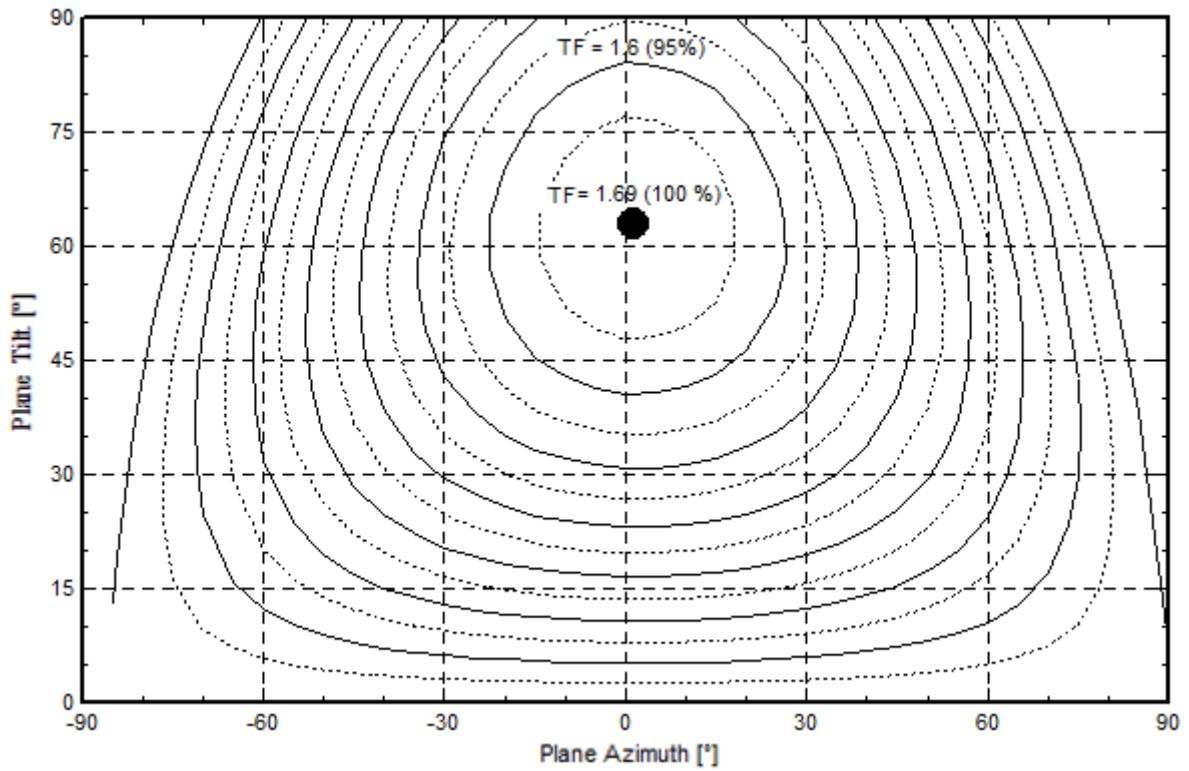
Fig. D.3. Transposition factor variation as function of plane tilt and plane azimuth. Values during the winter for Oslo (plotted by the author through PVsyst).
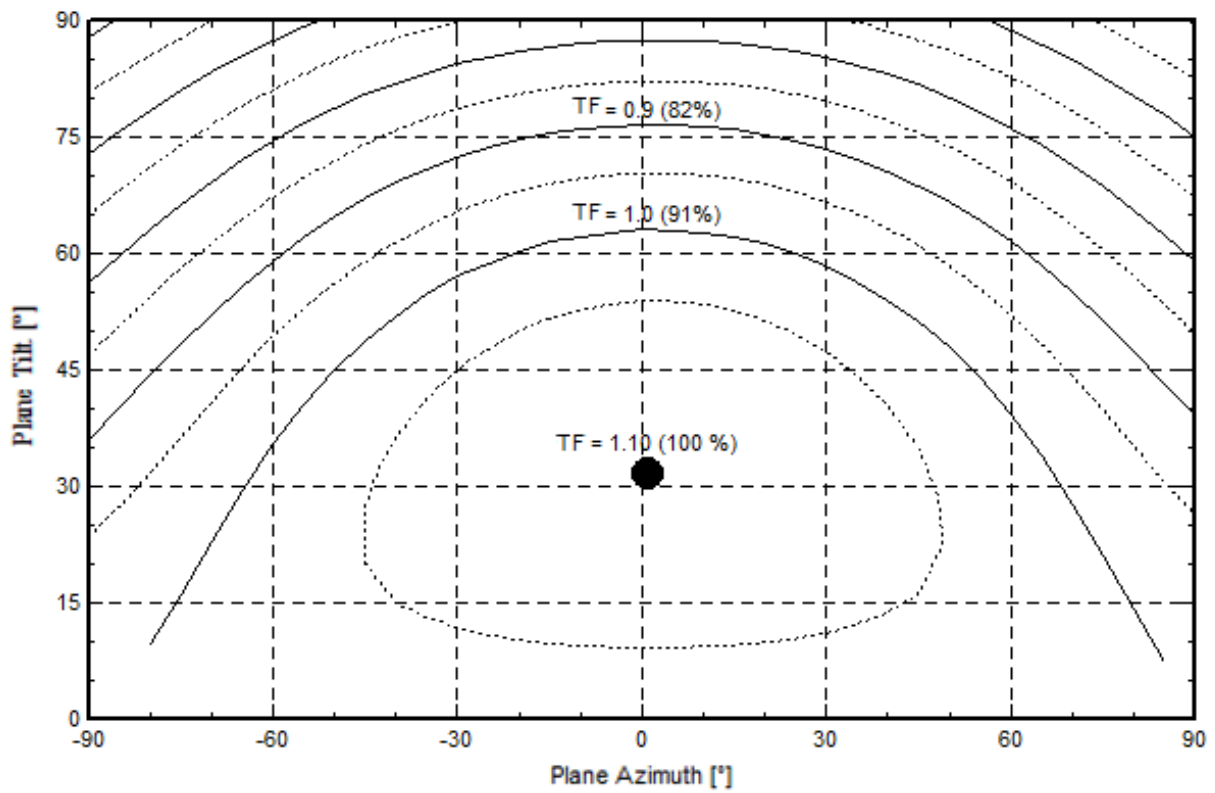
Fig. D.4. Transposition factor variation as function of plane tilt and plane azimuth. Values during the whole year for Bergen (plotted by the author through PVsyst).

160
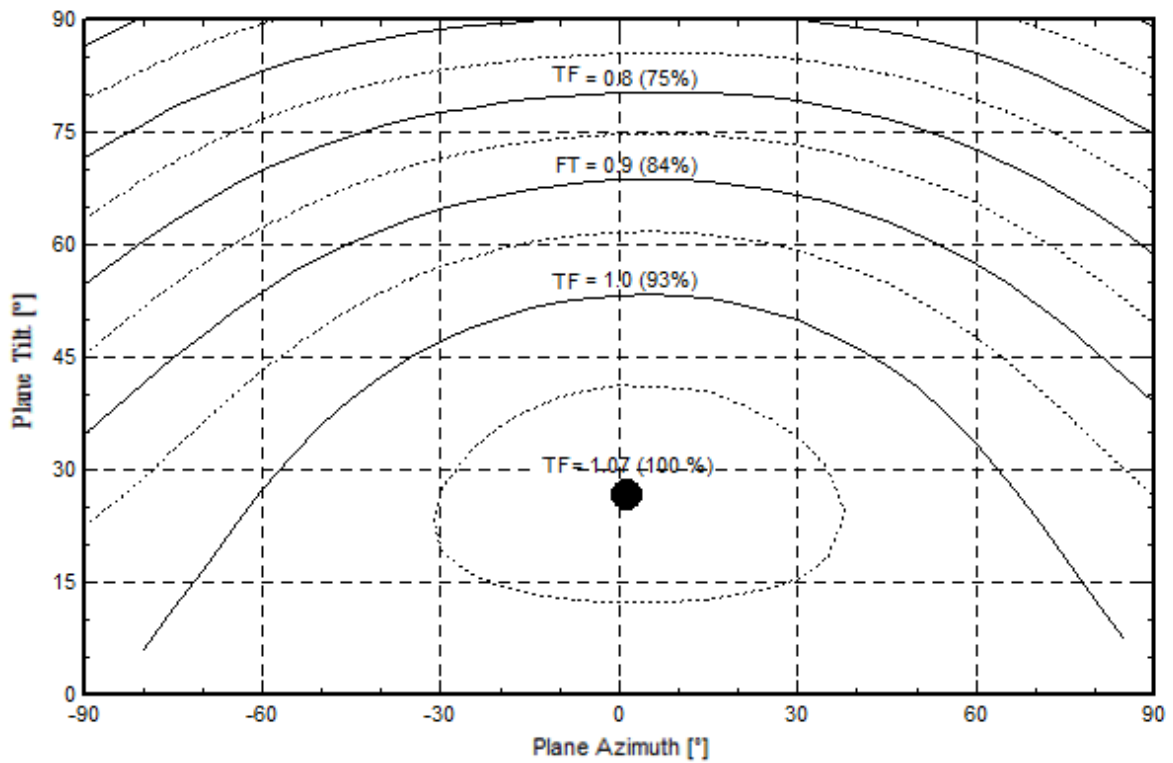
Fig. D.5. Transposition factor variation as function of plane tilt and plane azimuth. Values during the summer for Bergen (plotted by the author through PVsyst).
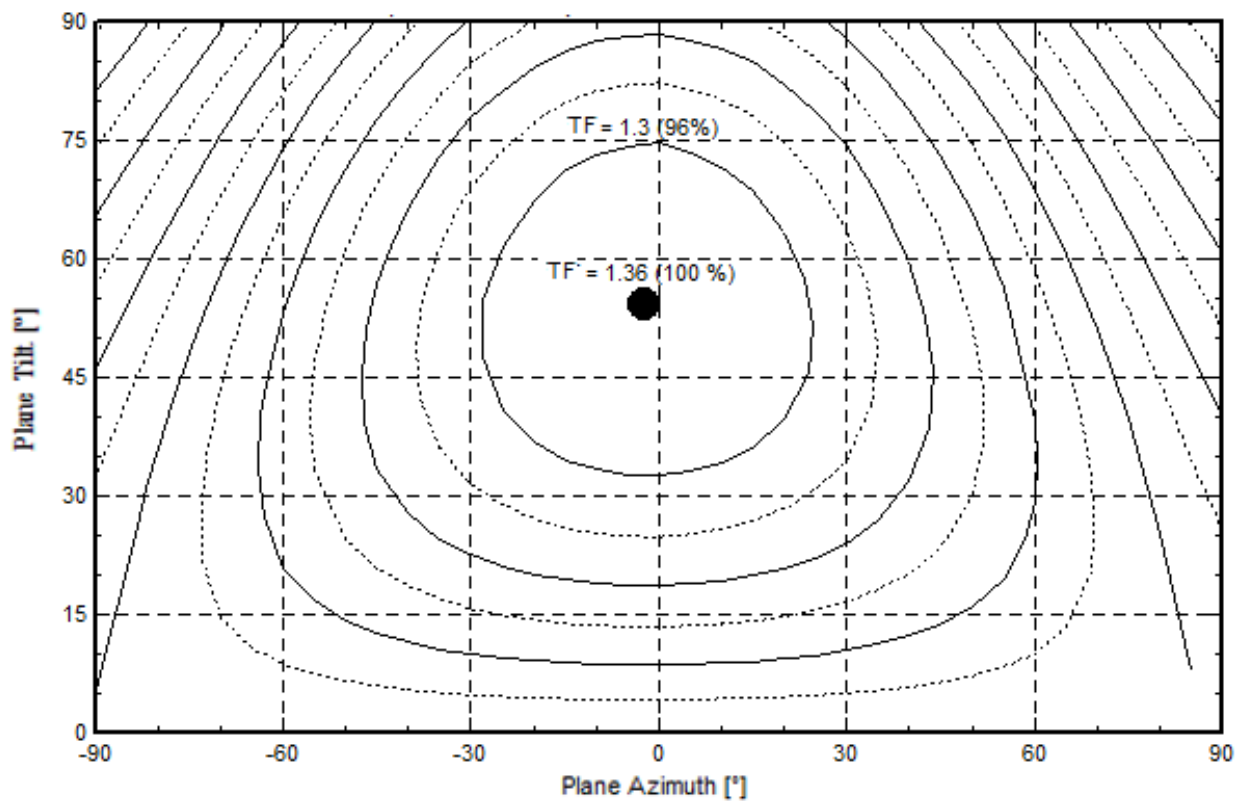
Fig. D.6. Transposition factor variation as function of plane tilt and plane azimuth. Values during the winter for Bergen (plotted by the author through PVsyst).

Appendix E

Screenshots about SAM interface.
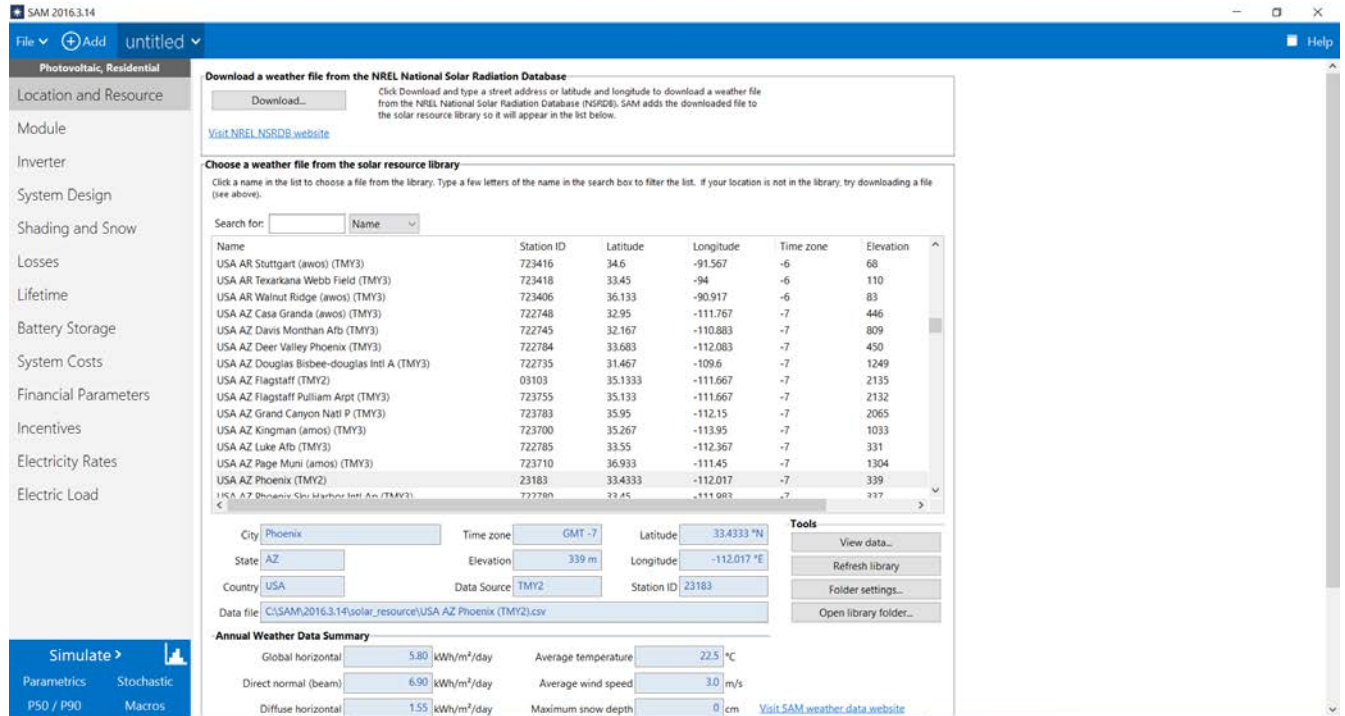
Fig. E.1. Location and Resource.
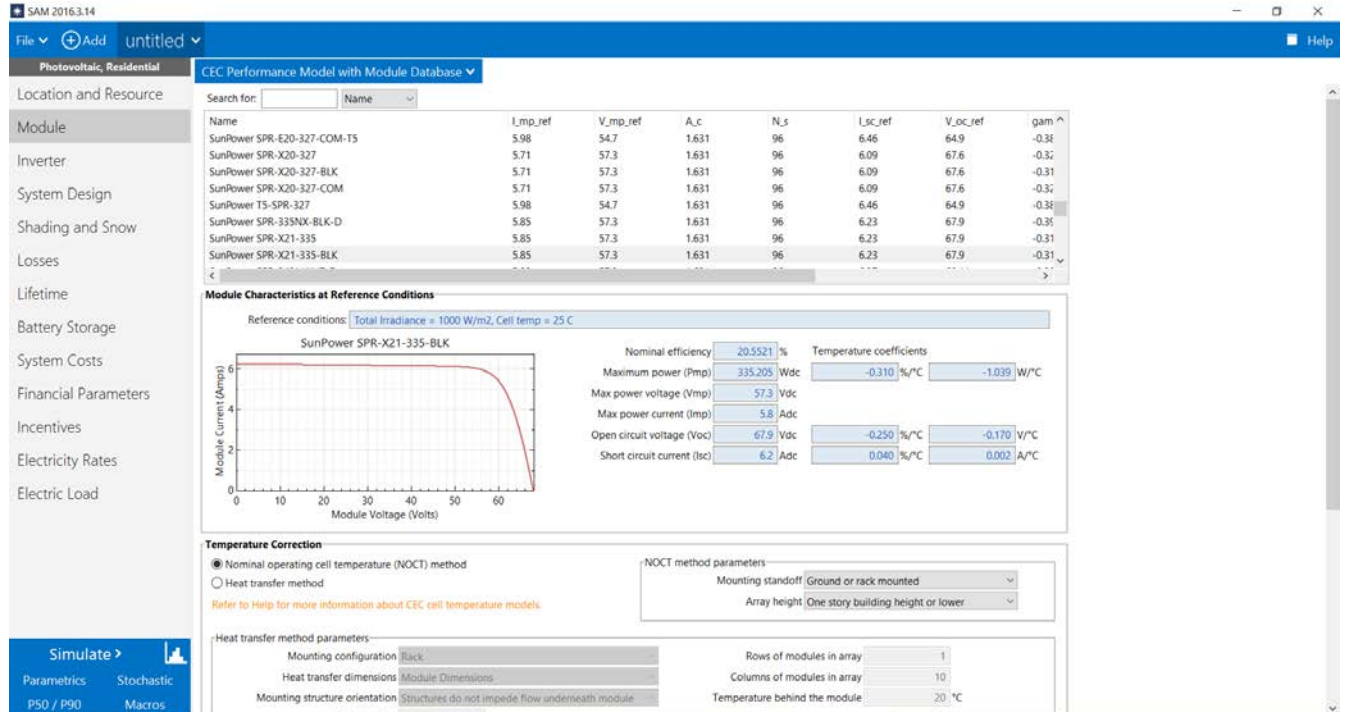
Fig. E.2. Module, CEC Performance with Module Database.
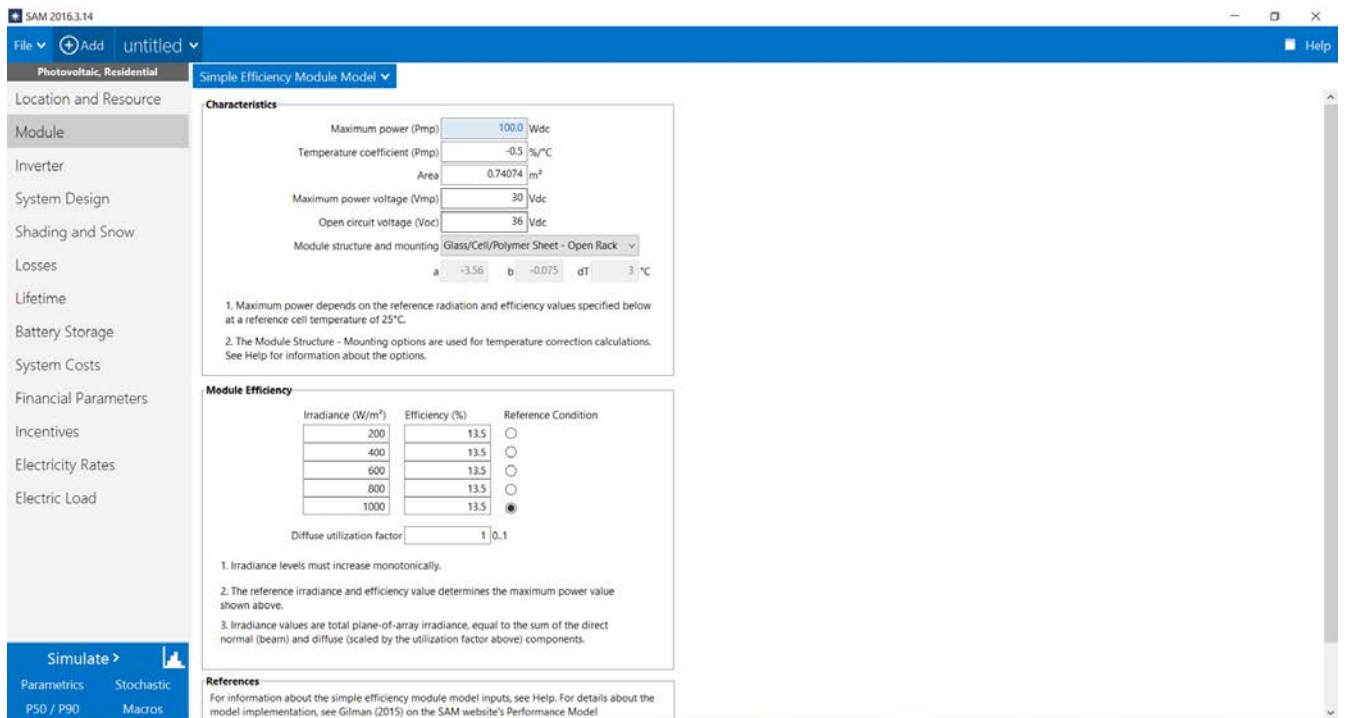
Fig. E.3. Module, Simple Efficiency Module Model.
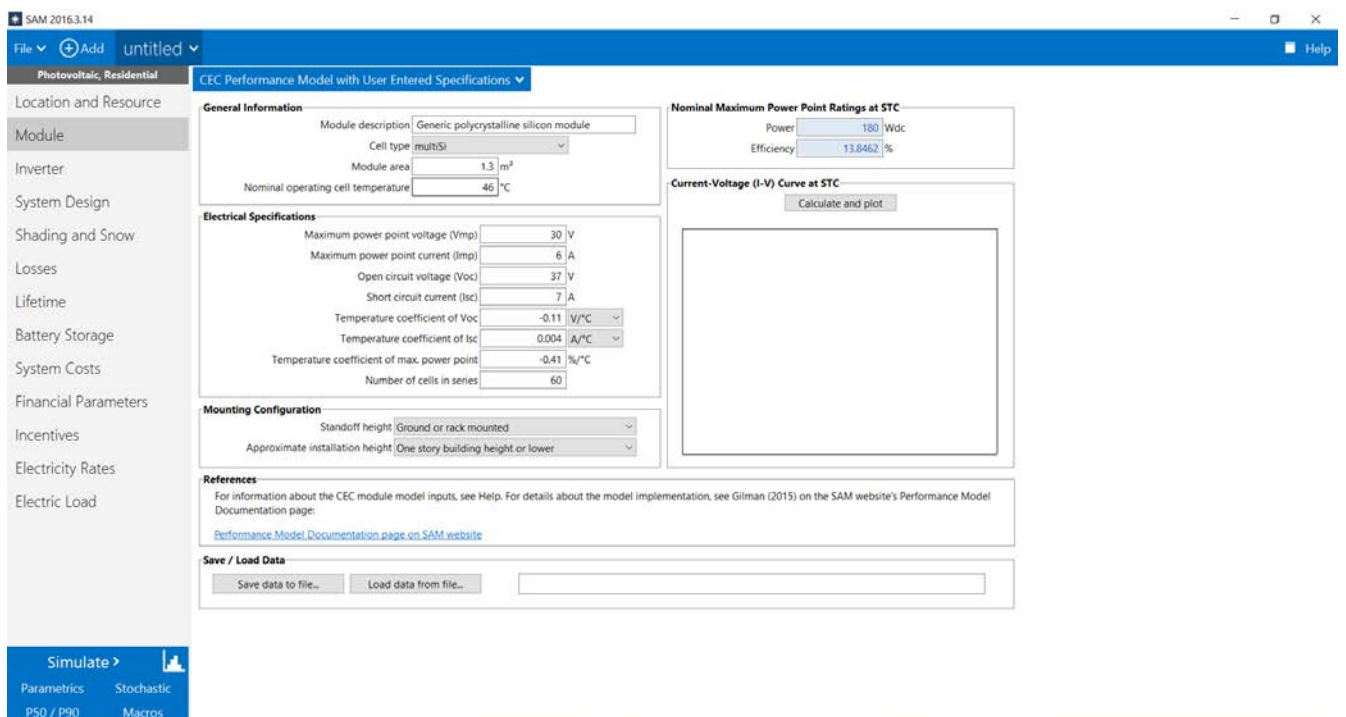
Fig. E.4. Module, CEC Performance Model with User Entered Sperifications.
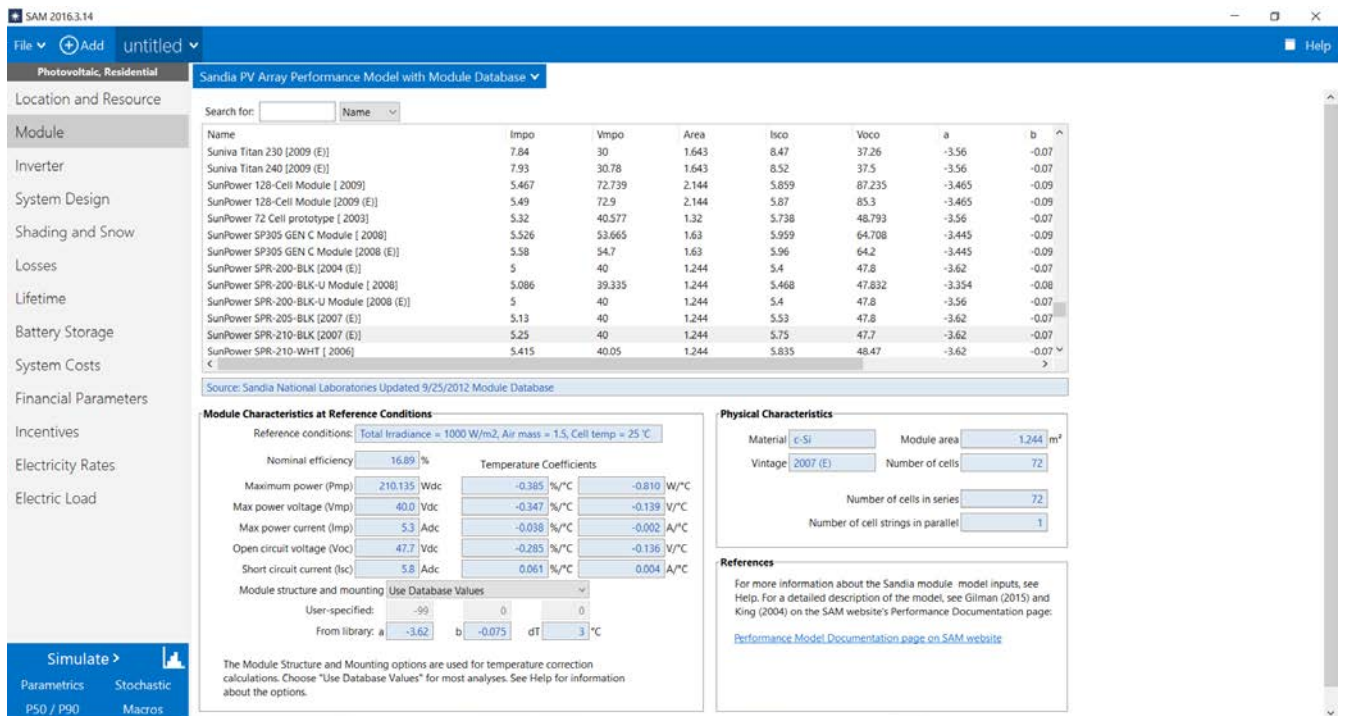
Fig. E.5. Module, Sandia PV Array Performance Model with Module Database.
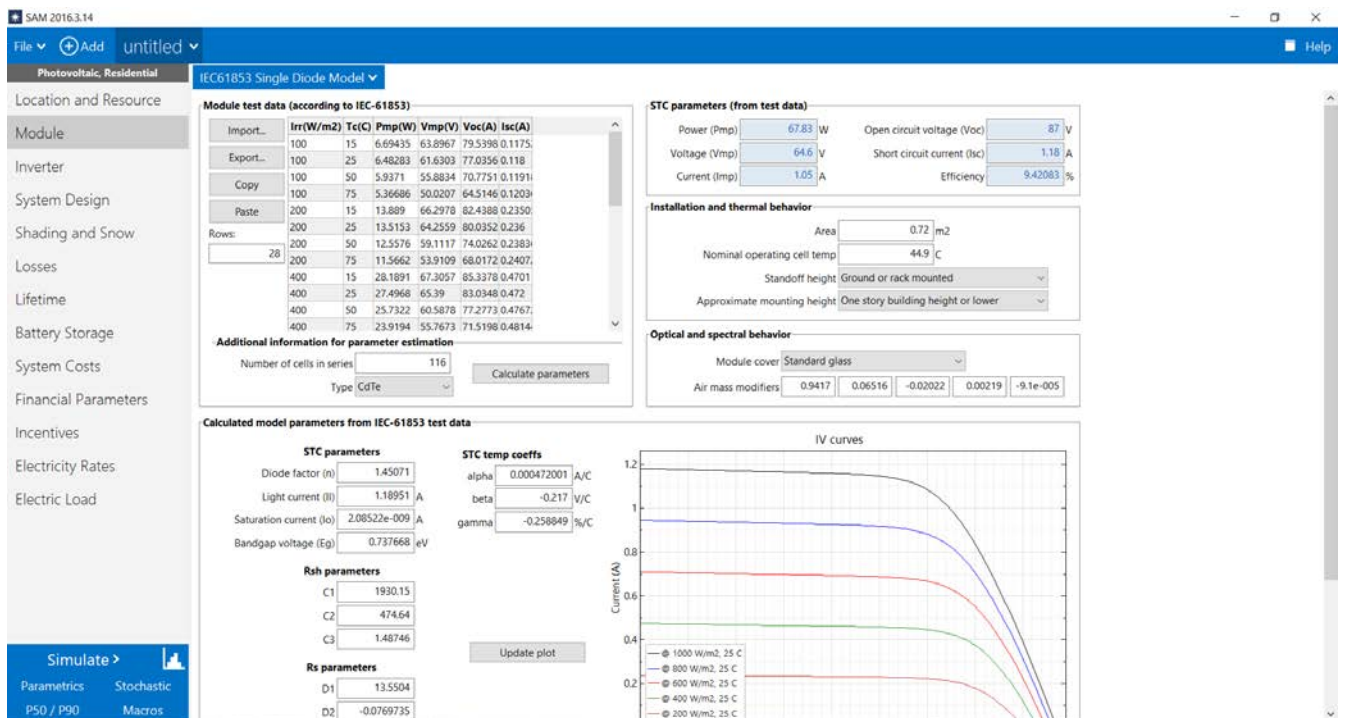
Fig. E.6. Module, IEC61853 Single Diode Model.
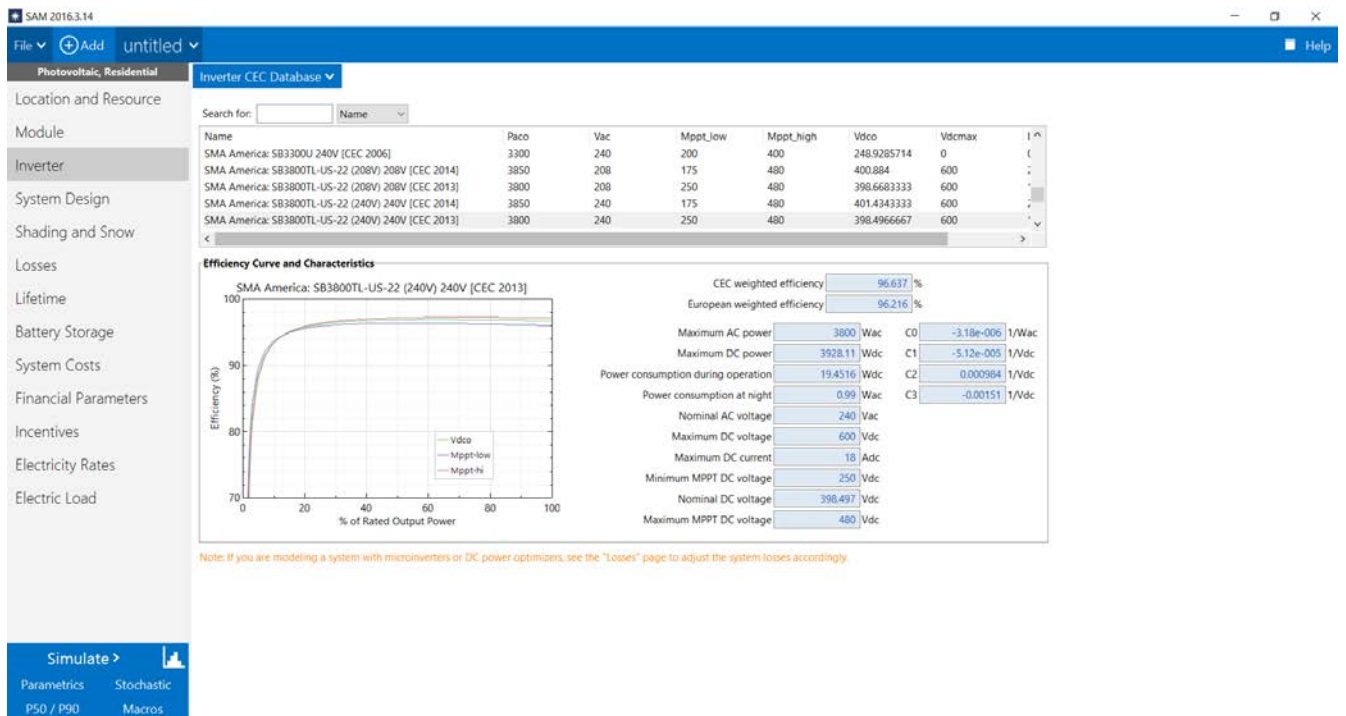
Fig. E.7. Inverter, Inverter CEC Database.
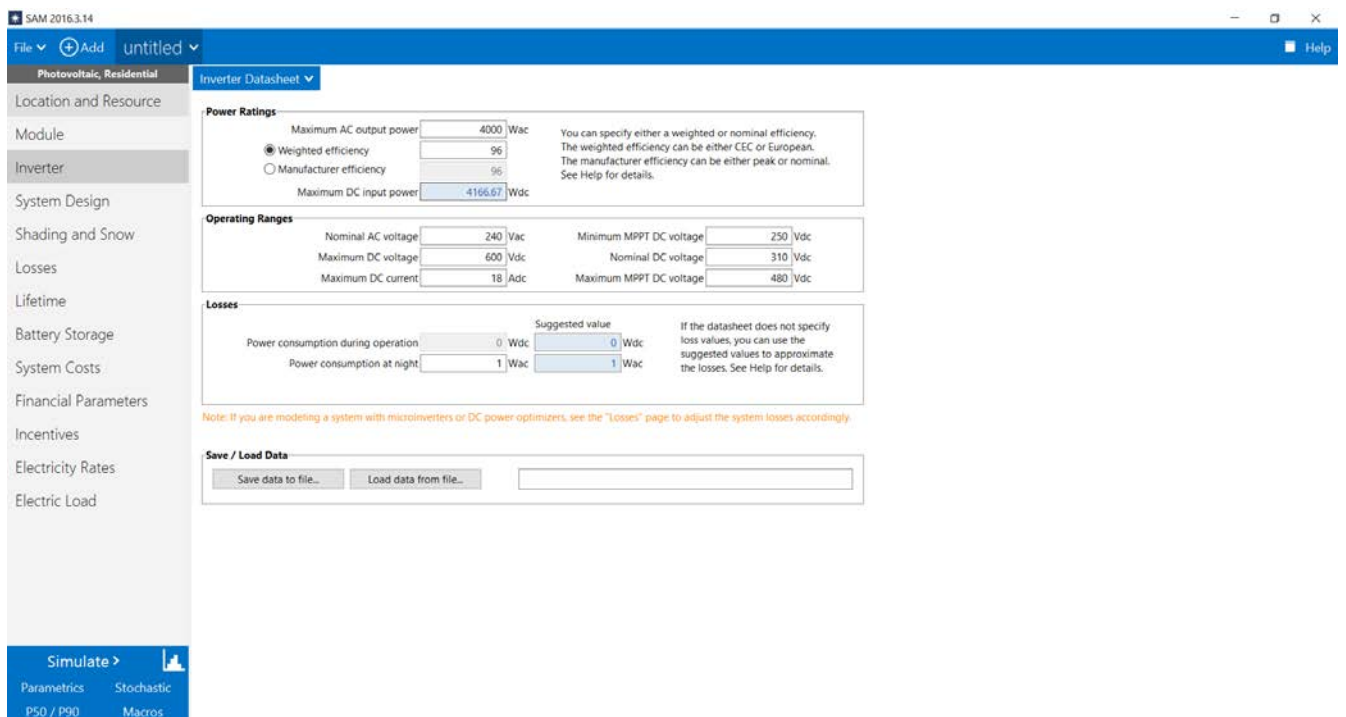
Fig. E.8. Inverter, Inverter Datasheet.
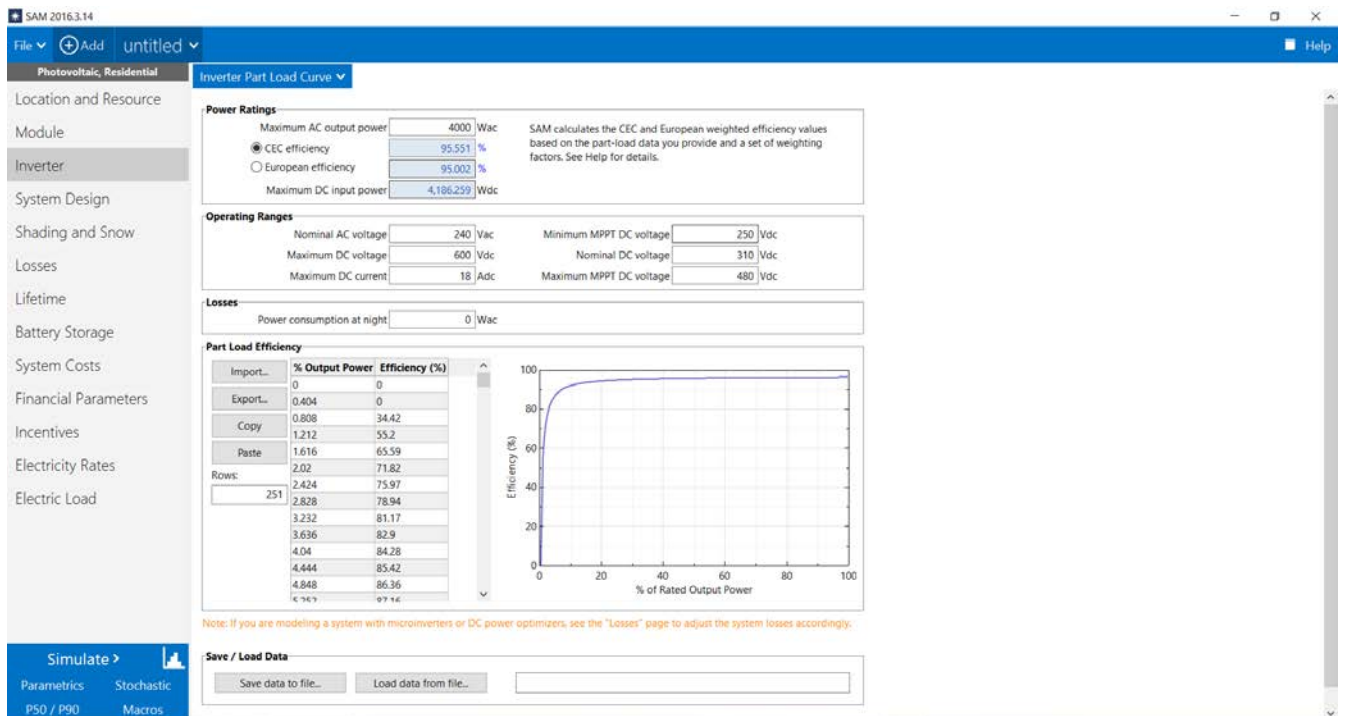
Fig. E.9. Inverter, Inverter Part Load Curve.
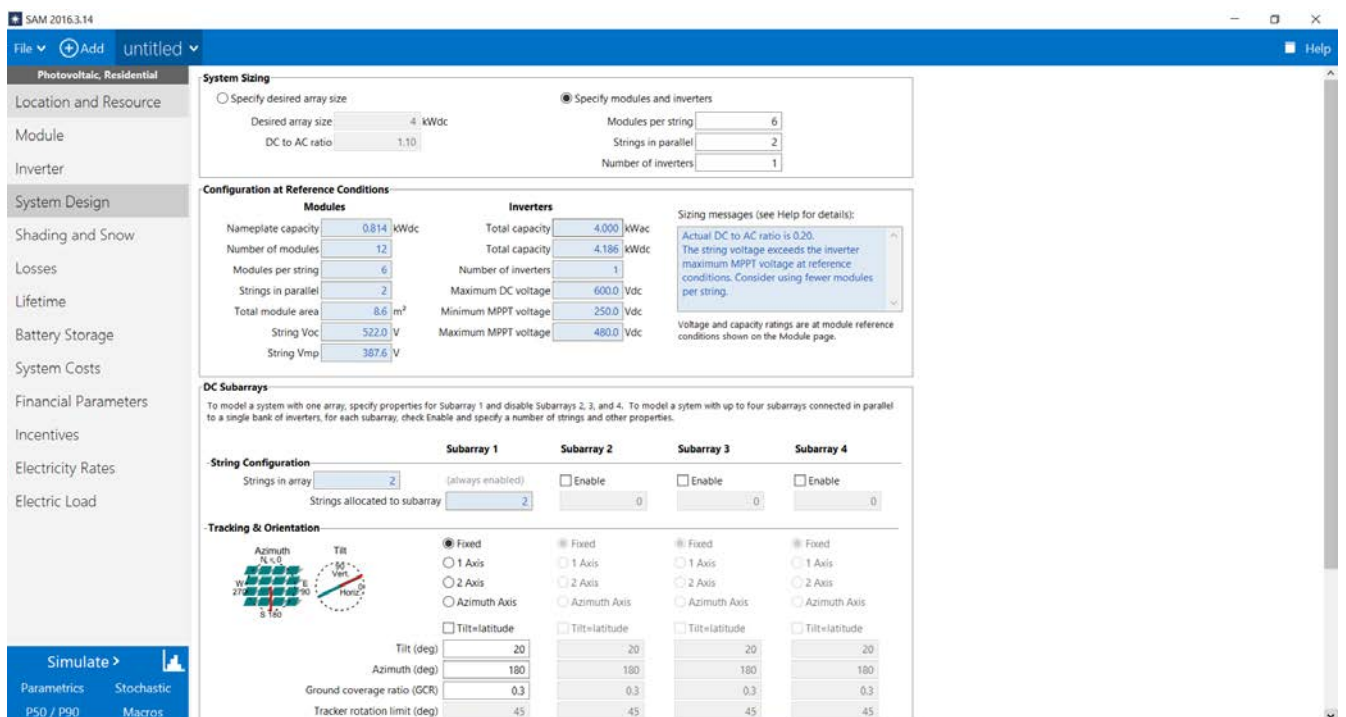
Fig. E.10. System Design.

166
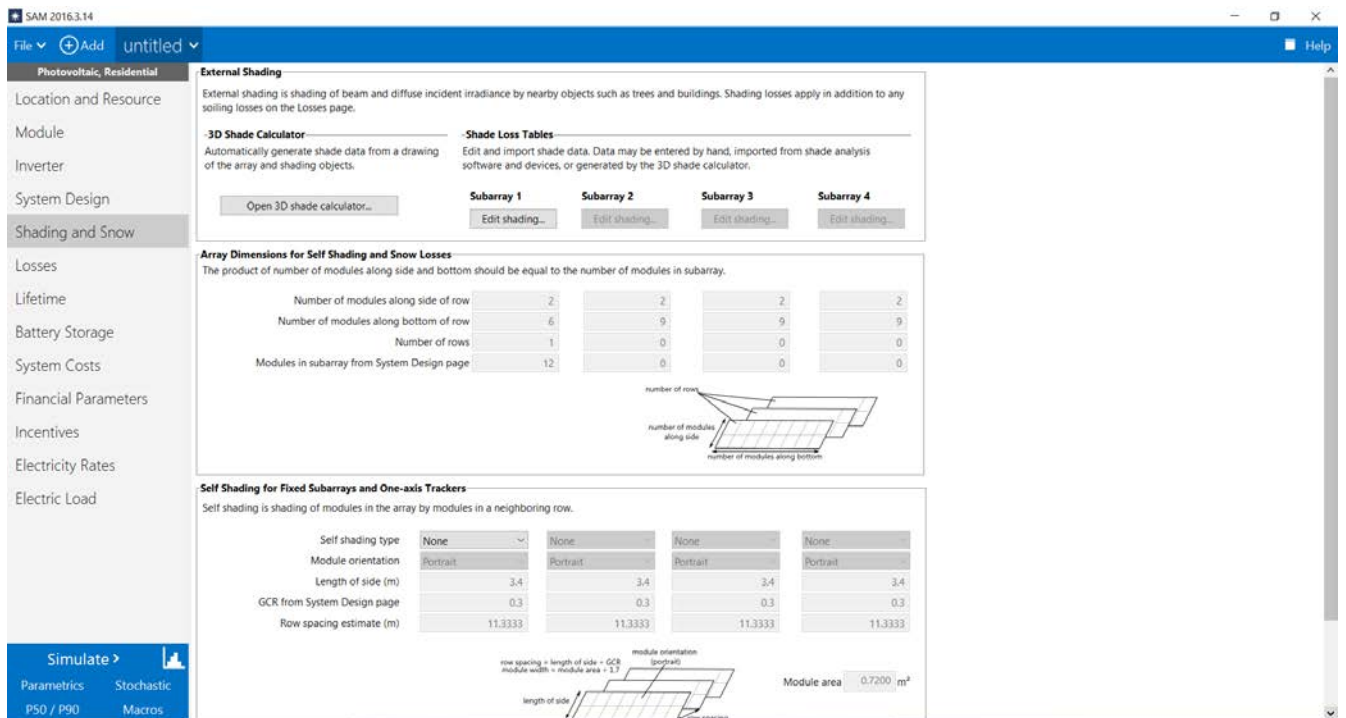
Fig. E.11. Shading and Snow.
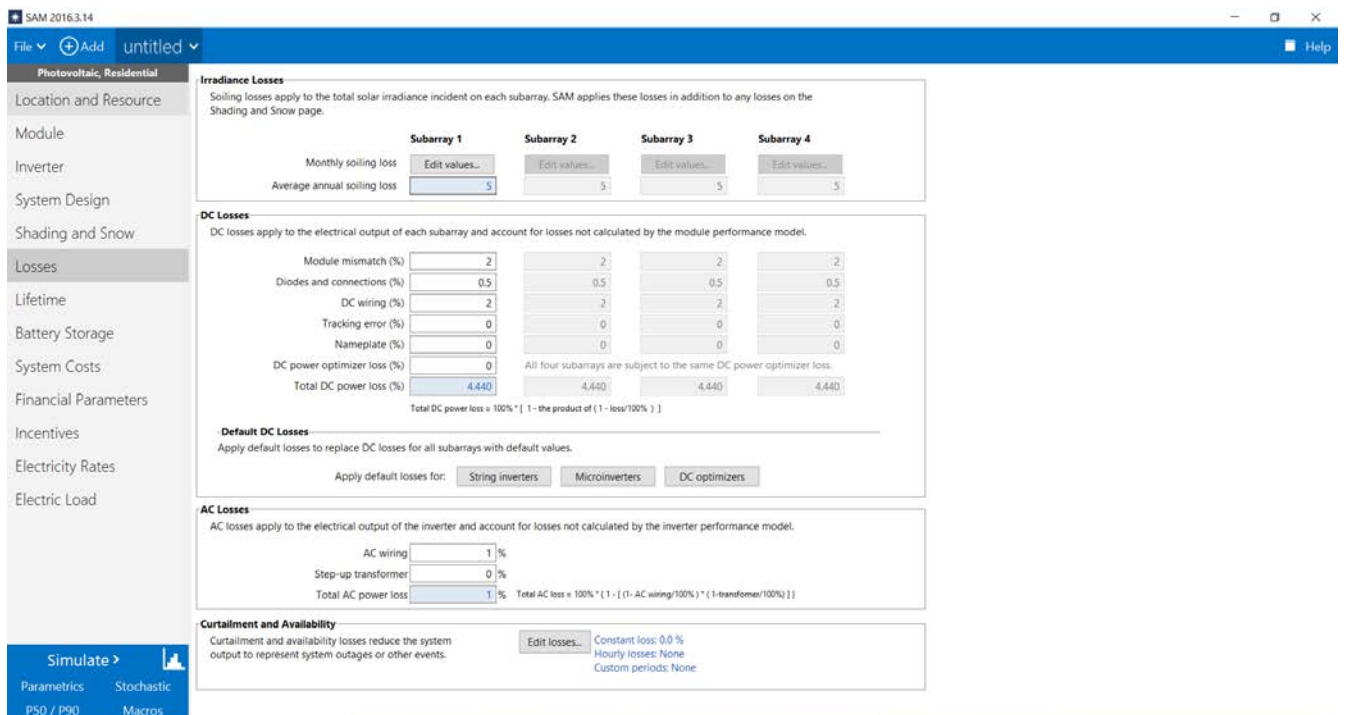
Fig. E.12. Losses.

Appendix F

Screenshots about PVsyst interface.
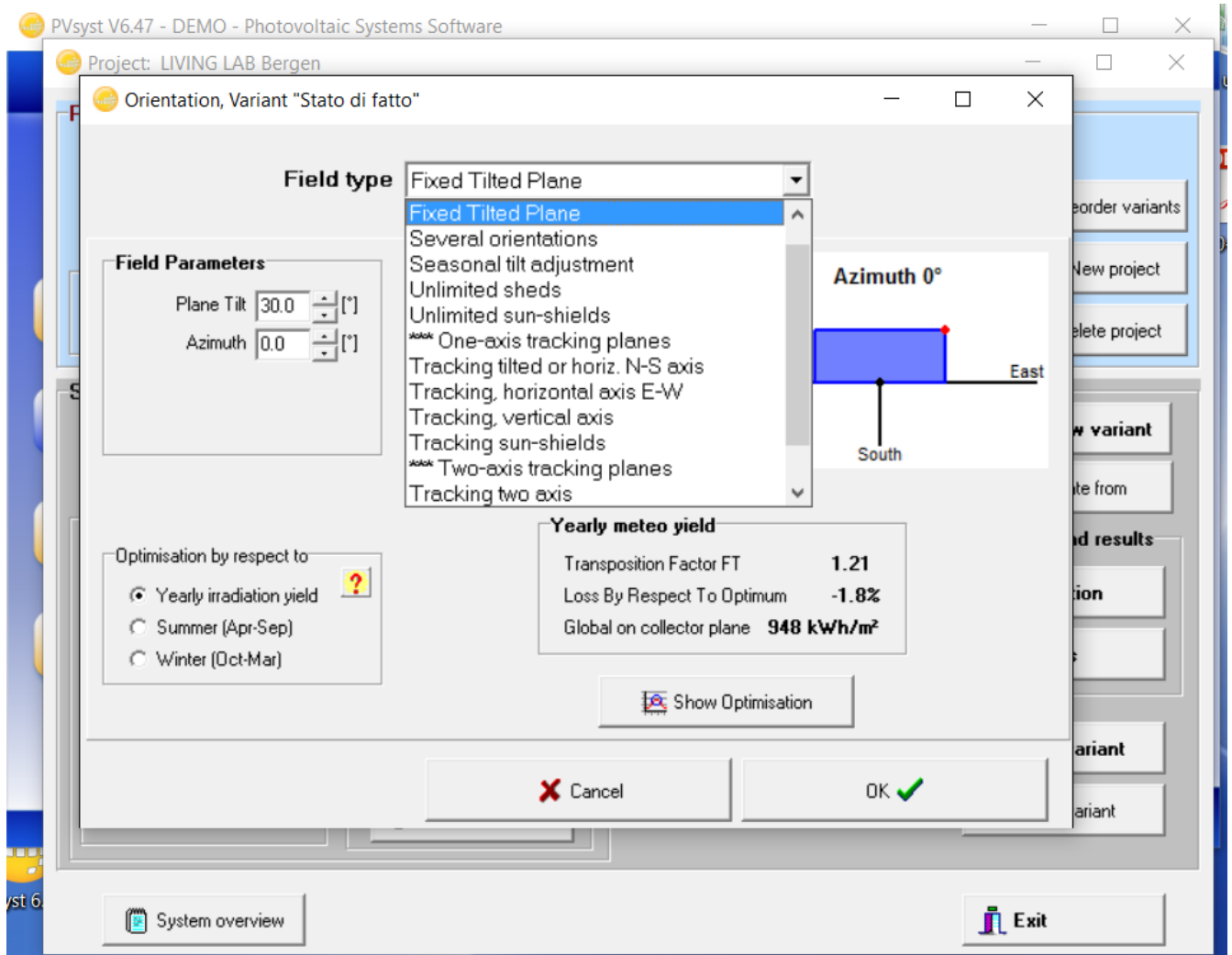
Fig. F.1. Orientation.
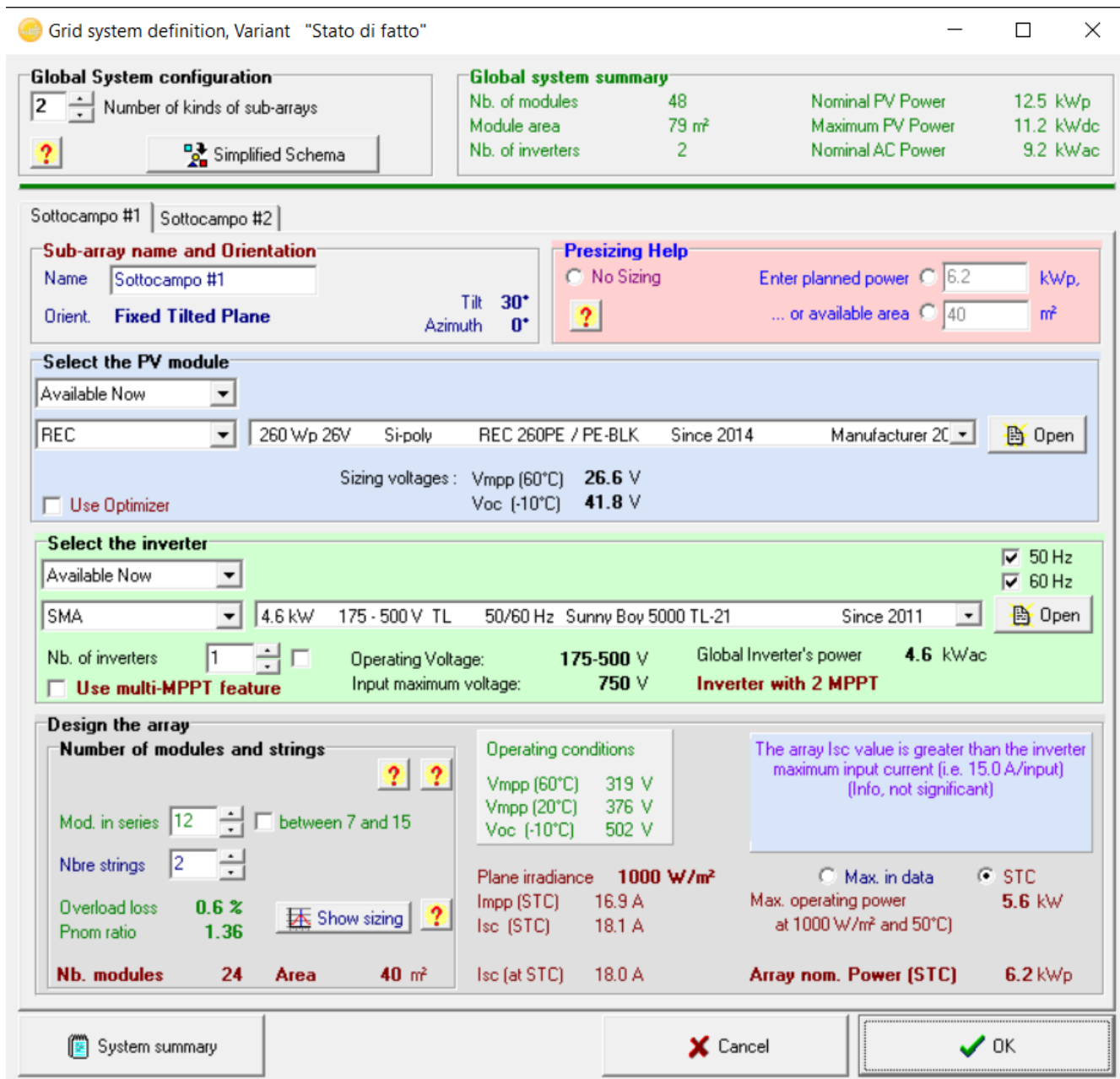
Fig. F.2. System.
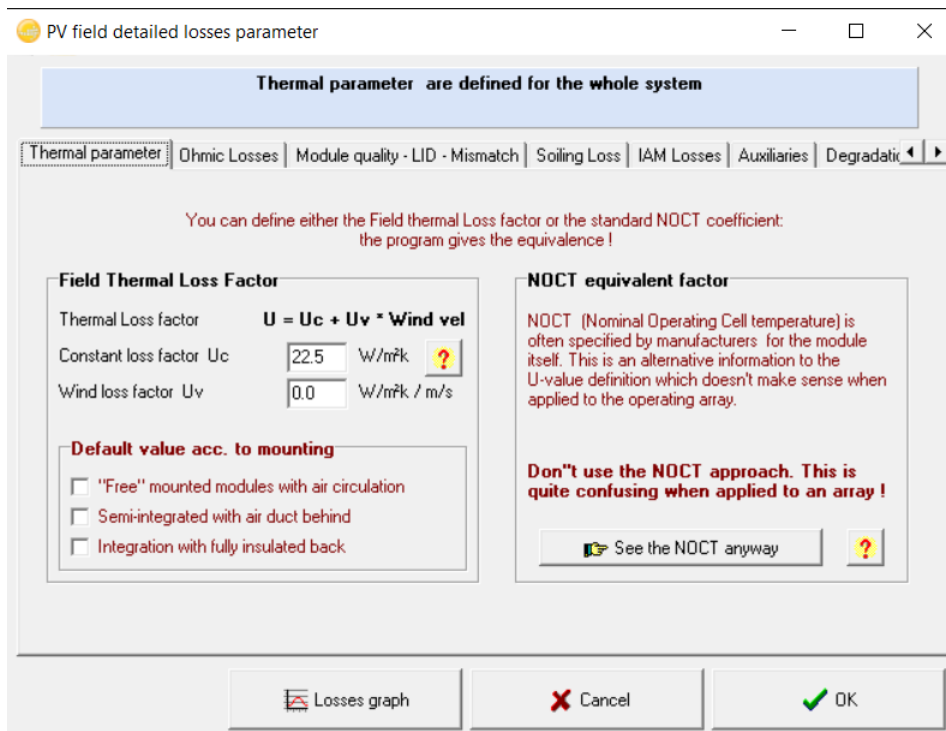
Fig. F.3. Detailed losses, Thermal parameter.
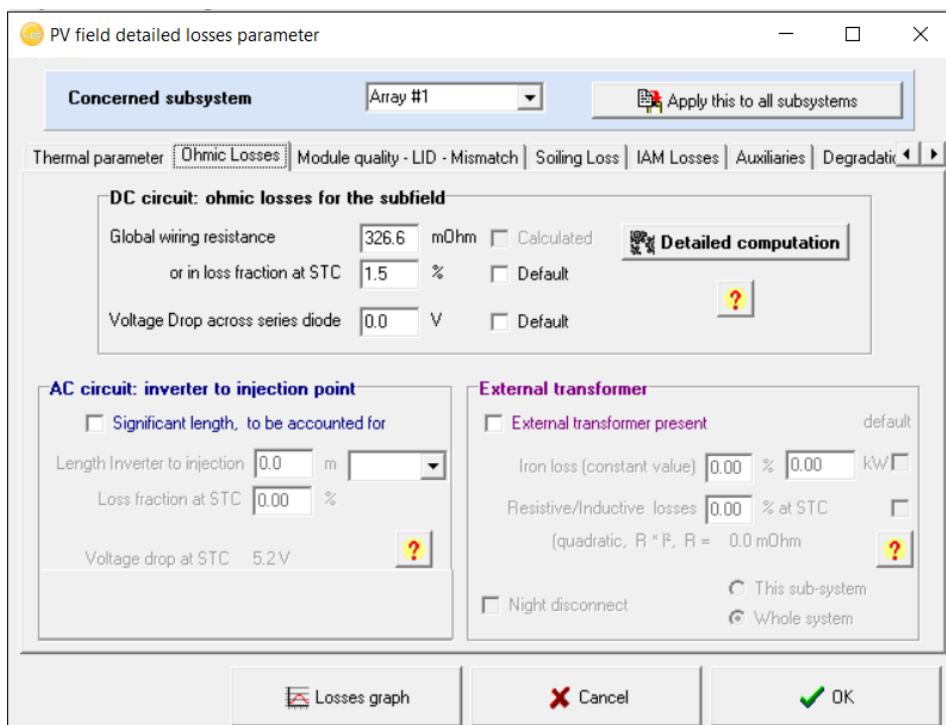
Fig. F.4. Detailed losses, Ohmic losses.
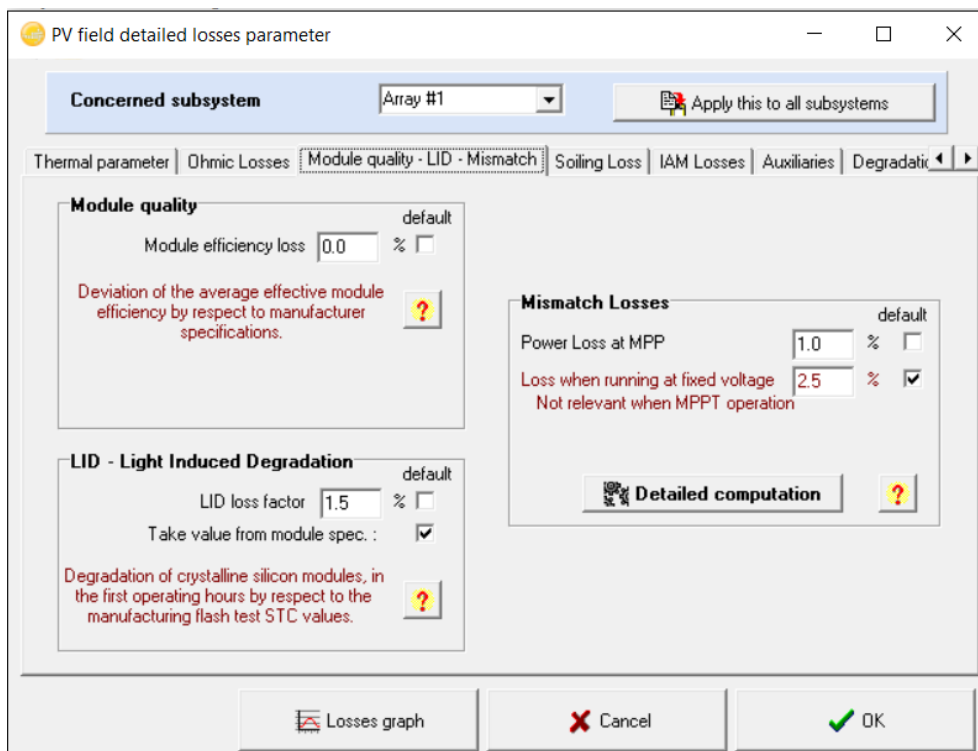
Fig. F.5. Detailed losses, Module quality – LID – Mismatch.
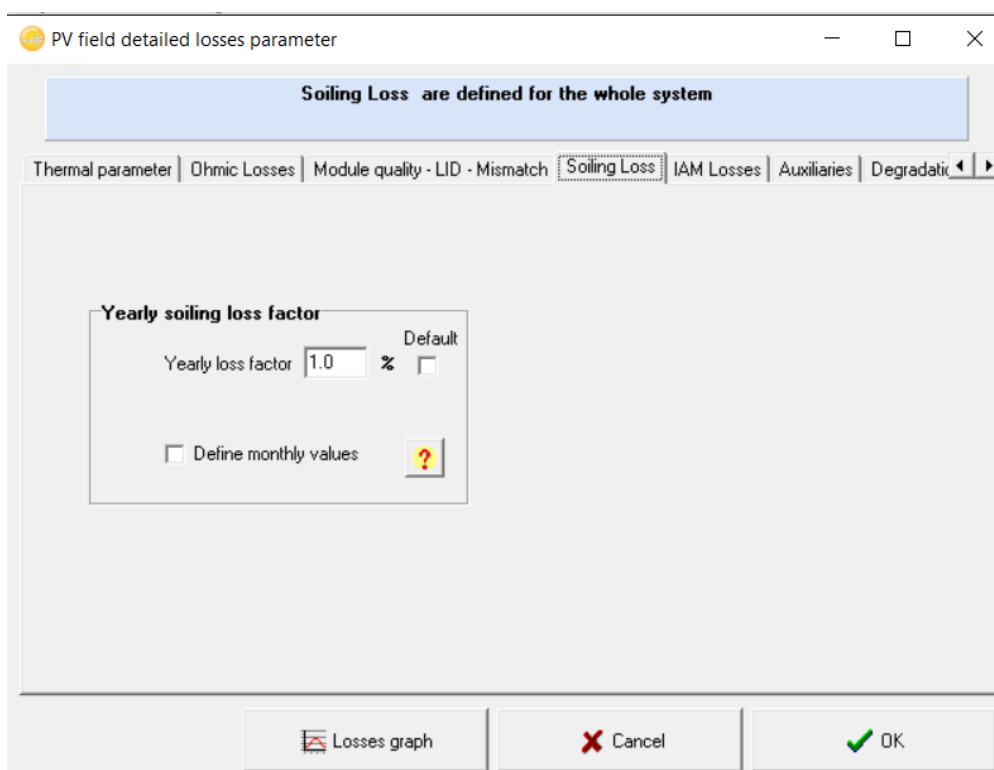
Fig. F.6. Detailed losses, Soiling Loss.
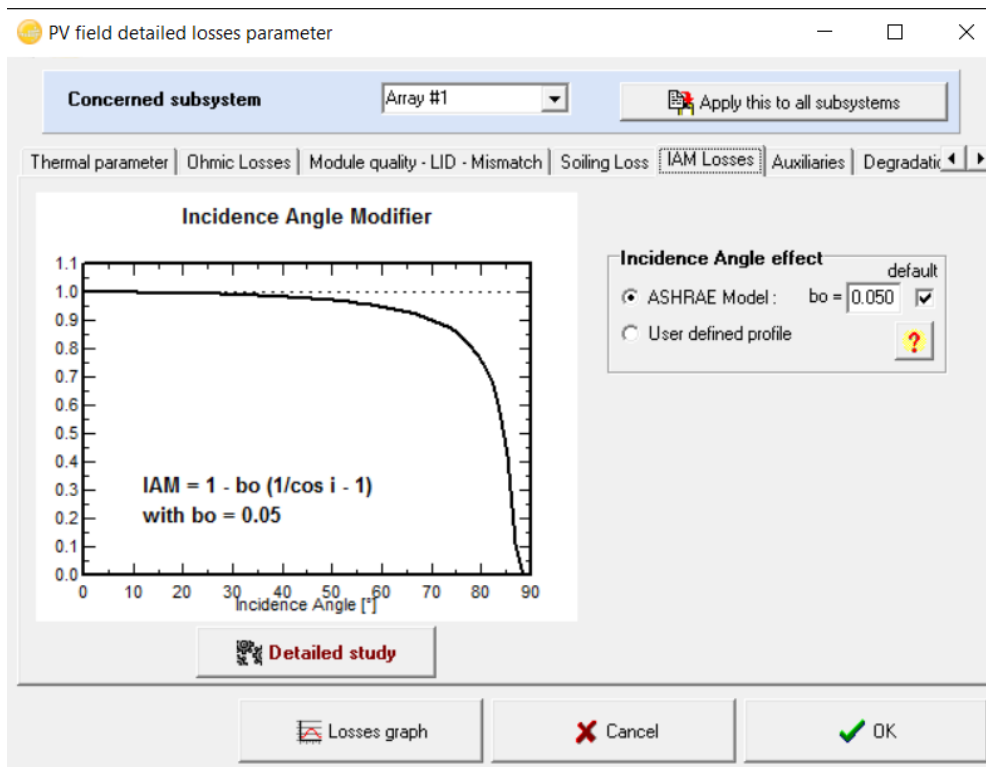
Fig. F.7. Detailed losses, IAM Losses.
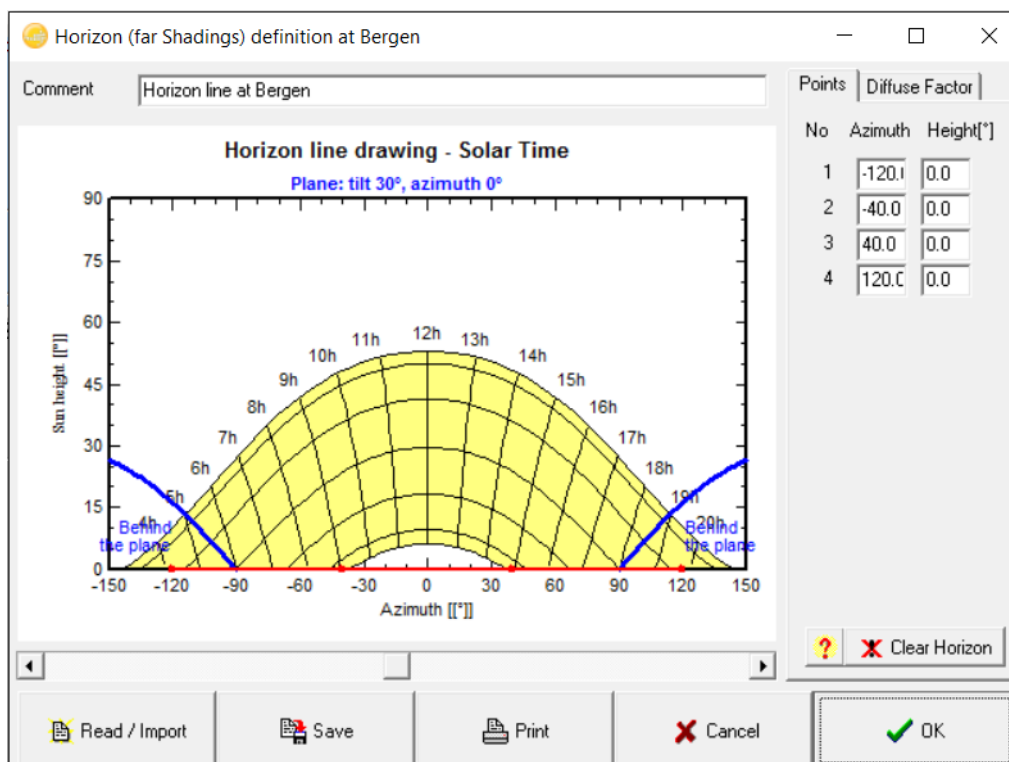
Fig. F.8. Horizon.
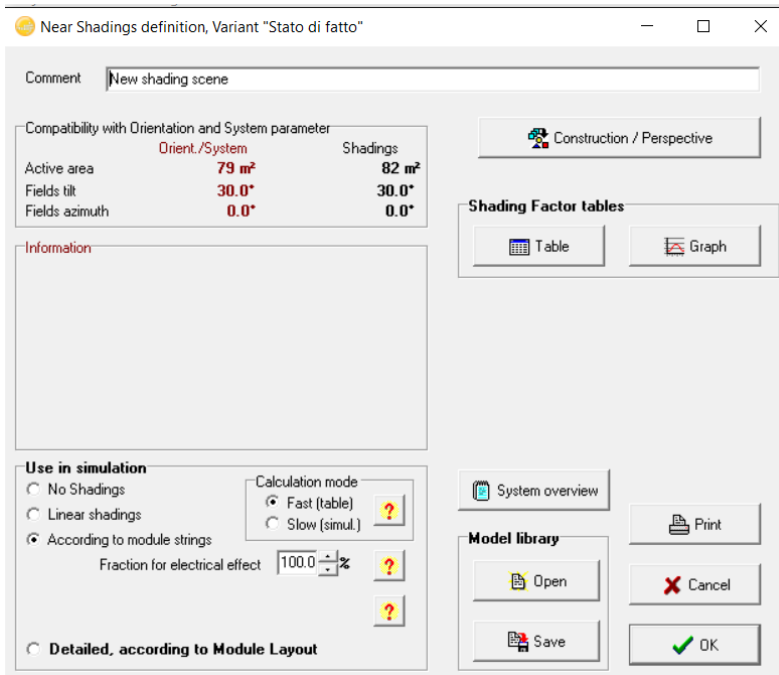
Fig. F.9. Near Shadings.
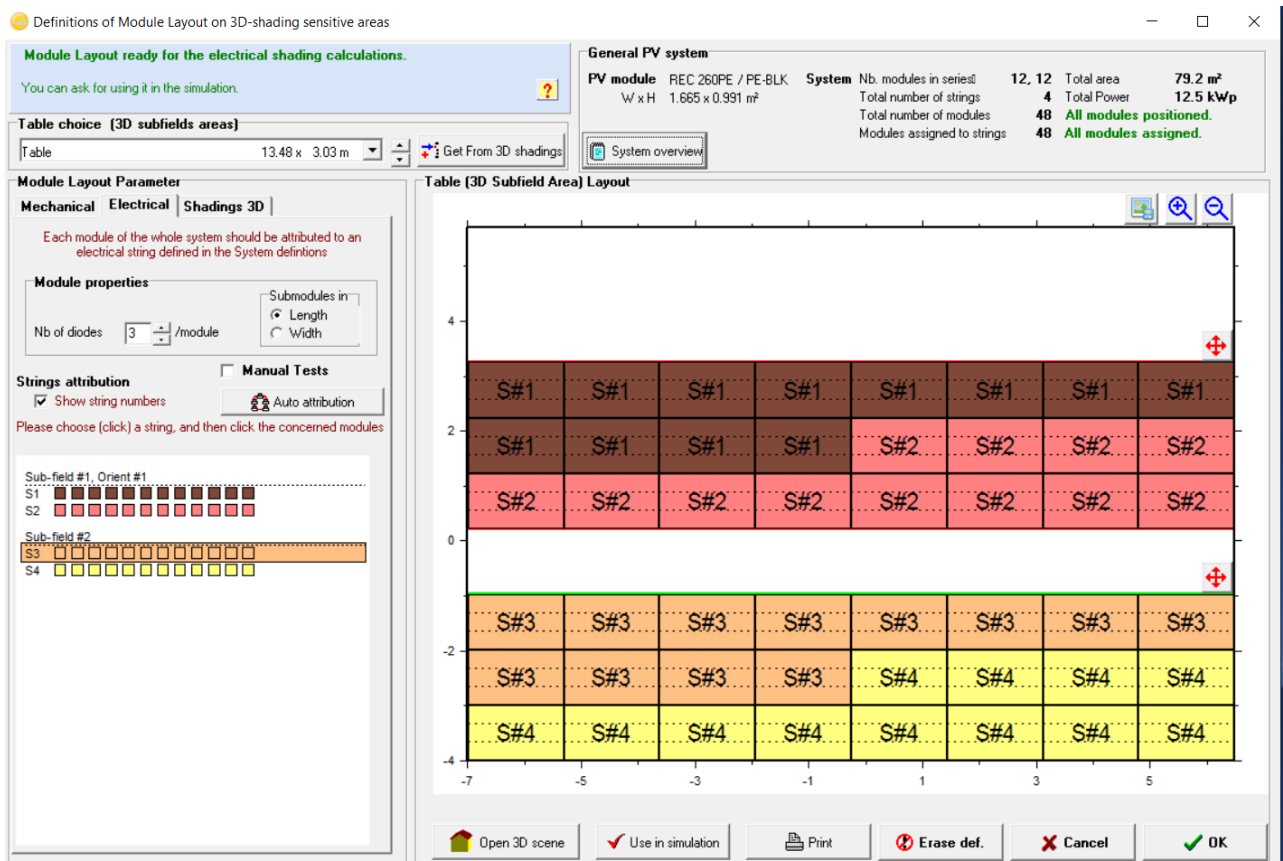
Fig. F.10. Module layout.

Appendix G

PVsyst simulation results for:

- Oslo
- Bergen
- Trondheim

Grid-Connected System: Simulation parameters

Project :   **Living Lab OSLO**

Geographical Site	**Oslo**	Country	**Norway**

Situation   Latitude   59.9°N   Longitude   10.6°E
    Time defined as   Legal Time   Time zone UT+1   Altitude   17 m
Monthly albedo values

	Jan.	Feb.	Mar.	Apr.	May	June	July	Aug.	Sep.	Oct.	Nov.	Dec.
Albedo	0.82	0.82	0.75	0.55	0.20	0.20	0.20	0.20	0.20	0.20	0.20	0.82

Meteo data: **Oslo**   Canada EPW hourly TMY (1953-1995) - TMY

Simulation variant :   **Stato di fatto**

             Simulation date   20/07/16 00h12

Simulation parameters

Collector Plane Orientation	Tilt	30°	Azimuth	0°

Models used   Transposition   Hay   Diffuse   Imported

Horizon   Free Horizon

Near Shadings   According to strings   Electrical effect   100 %

PV Arrays Characteristics   **(2 kinds of array defined)**
PV module   Si-poly   Model   **REC 260PE / PE-BLK**
    Original PVsyst database   Manufacturer   REC

Sub-array "Sottocampo #1"
Number of PV modules   In series   12 modules   In parallel   2 strings
Total number of PV modules   Nb. modules   24   Unit Nom. Power   260 Wp
Array global power   Nominal (STC)   **6.24 kWp**   At operating cond.   5.62 kWp (50°C)
Array operating characteristics (50°C)   U mpp   333 V   I mpp   17 A

Sub-array "Sottocampo #2"
Number of PV modules   In series   12 modules   In parallel   2 strings
Total number of PV modules   Nb. modules   24   Unit Nom. Power   260 Wp
Array global power   Nominal (STC)   **6.24 kWp**   At operating cond.   5.62 kWp (50°C)
Array operating characteristics (50°C)   U mpp   333 V   I mpp   17 A

Total   Arrays global power   Nominal (STC)   **12 kWp**   Total   48 modules
                    Module area   **79.2 m²**   Cell area   70.1 m²

Inverter   Model   **Sunny Boy 5000 TL-21**
    Original PVsyst database   Manufacturer   SMA
Characteristics   Operating Voltage   175-500 V   Unit Nom. Power   4.60 kWac

Sub-array "Sottocampo #1"   Nb. of inverters   1 units   Total Power   4.6 kWac
Sub-array "Sottocampo #2"   Nb. of inverters   1 units   Total Power   4.6 kWac

Total   Nb. of inverters   2   Total Power   9 kWac

PV Array loss factors

Array Soiling Losses   Loss Fraction   1.0 %
Thermal Loss factor   Uc (const)   22.5 W/m²K   Uv (wind)   0.0 W/m²K / m/s
Wiring Ohmic Loss   Array#1   327 mOhm   Loss Fraction   1.5 % at STC
                    Array#2   327 mOhm   Loss Fraction   1.5 % at STC
                    Global   Loss Fraction   1.5 % at STC

Grid-Connected System: Simulation parameters (continued)

LID - Light Induced Degradation   Loss Fraction   1.5 %
Module Quality Loss   Loss Fraction   0.0 %
Module Mismatch Losses   Loss Fraction   1.0 % at MPP
Incidence effect, ASHRAE parametrization   IAM =   1 - bo (1/cos i - 1)   bo Param.   0.05

User's needs :   Unlimited load (grid)

Grid-Connected System: Near shading definition

Project :   **Living Lab OSLO**

Simulation variant :   **Stato di fatto**

Main system parameters	System type	**Grid-Connected**		
Near Shadings	According to strings		Electrical effect	100 %
PV Field Orientation	tilt	30°	azimuth	0°
PV modules	Model	REC 260PE / PE-BLK	Pnom	260 Wp
PV Array	Nb. of modules	48	Pnom total	**12.48 kWp**
Inverter	Model	Sunny Boy 5000 TL-21	Pnom	4600 W ac
Inverter pack	Nb. of units	2.0	Pnom total	**9.20 kW ac**
User's needs	Unlimited load (grid)			

Perspective of the PV-field and surrounding shading scene

Iso-shadings diagram
Living Lab OSLO - Legal Time

Beam shading factor (according to strings) : Iso-shadings curves

Shading loss: 1 %
Shading loss: 5 %
Shading loss: 10 %
Shading loss: 20 %
Shading loss: 40 %

**Attenuation for diffuse: 0.048
and albedo: 0.387**

1: 22 june
2: 22 may - 23 july
3: 20 apr - 23 aug
4: 20 mar - 23 sep
5: 21 feb - 23 oct
6: 19 jan - 22 nov
7: 22 december

Grid-Connected System: Main results

Project :   **Living Lab OSLO**

Simulation variant :   **Stato di fatto**

Main system parameters

	System type	**Grid-Connected**		
Near Shadings	According to strings		Electrical effect	100 %
PV Field Orientation	tilt	30°	azimuth	0°
PV modules	Model	REC 260PE / PE-BLK	Pnom	260 Wp
PV Array	Nb. of modules	48	Pnom total	**12.48 kWp**
Inverter	Model	Sunny Boy 5000 TL-21	Pnom	4600 W ac
Inverter pack	Nb. of units	2.0	Pnom total	**9.20 kW ac**
User's needs	Unlimited load (grid)			

Main simulation results

System Production	**Produced Energy**	**10510 kWh/year**	Specific prod.	842 kWh/kWp/year
	Performance Ratio PR	79.80 %		

Normalized productions (per installed kWp): Nominal power 12.48 kWp
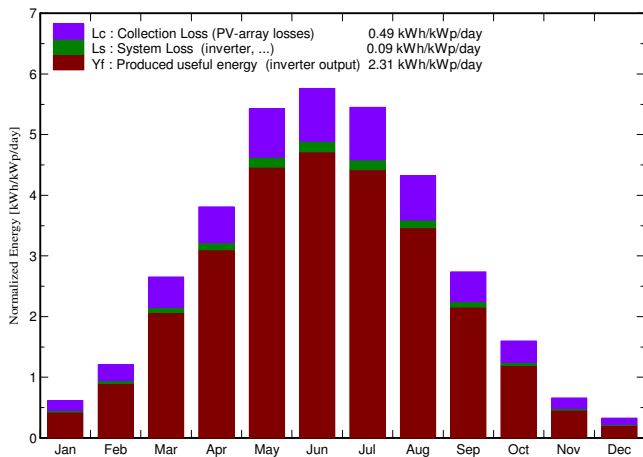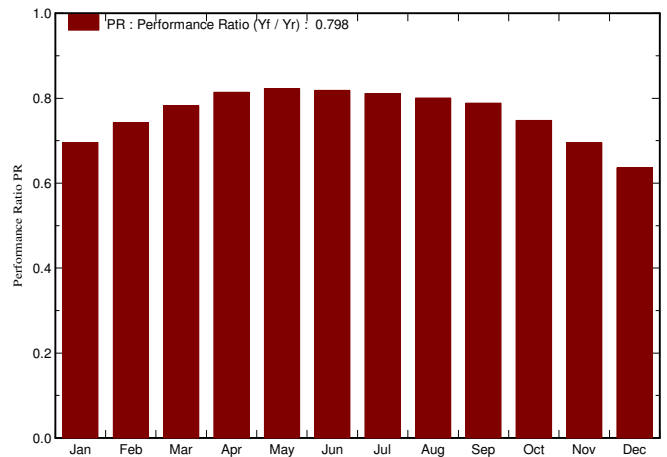
Lc : Collection Loss (PV-array losses)   0.49 kWh/kWp/day
Ls : System Loss (inverter, ...)   0.09 kWh/kWp/day
Yf : Produced useful energy (inverter output)   2.31 kWh/kWp/day

Performance Ratio PR

PR : Performance Ratio (Yf / Yr) : 0.798

Stato di fatto
Balances and main results

	GlobHor	T Amb	GlobInc	GlobEff	EArray	E_Grid	EffArrR	EffSysR
	kWh/m²	°C	kWh/m²	kWh/m²	kWh	kWh	%	%
January	9.1	-3.78	19.1	14.5	177	166	11.69	10.96
February	20.7	-0.85	33.8	27.7	329	313	12.30	11.70
March	57.2	0.92	82.2	71.4	835	803	12.82	12.33
April	92.9	4.60	114.3	104.2	1205	1161	13.32	12.83
May	150.5	11.89	168.3	157.5	1790	1727	13.43	12.95
June	161.3	14.70	172.9	161.1	1831	1767	13.37	12.90
July	155.1	17.48	169.0	157.8	1773	1710	13.25	12.78
August	115.3	16.55	134.1	124.3	1390	1340	13.09	12.62
September	66.5	11.05	82.1	73.9	841	808	12.93	12.42
October	34.3	6.70	49.6	42.4	485	463	12.34	11.79
November	10.9	1.78	19.8	15.6	184	172	11.70	10.95
December	4.8	-1.61	10.1	7.5	88	80	10.94	10.02
Year	878.6	6.66	1055.3	957.8	10927	10510	13.07	12.57

Legends: GlobHor   Horizontal global irradiation   EArray   Effective energy at the output of the array
          T Amb   Ambient Temperature   E_Grid   Energy injected into grid
          GlobInc   Global incident in coll. plane   EffArrR   Effic. Eout array / rough area
          GlobEff   Effective Global, corr. for IAM and shadings   EffSysR   Effic. Eout system / rough area

Grid-Connected System: Loss diagram

Project : **Living Lab OSLO**

Simulation variant : **Stato di fatto**

Main system parameters	System type	**Grid-Connected**		

Near Shadings	According to strings		Electrical effect	100 %
PV Field Orientation	tilt	30°	azimuth	0°
PV modules	Model	REC 260PE / PE-BLK	Pnom	260 Wp
PV Array	Nb. of modules	48	Pnom total	**12.48 kWp**
Inverter	Model	Sunny Boy 5000 TL-21	Pnom	4600 W ac
Inverter pack	Nb. of units	2.0	Pnom total	**9.20 kW ac**
User's needs	Unlimited load (grid)			

Loss diagram over the whole year

879 kWh/m²   **Horizontal global irradiation**

+20.1% **Global incident in coll. plane**

-5.5% Near Shadings: irradiance loss

-2.9% IAM factor on global

-1.0% Soiling loss factor

958 kWh/m² * 79 m² coll.   **Effective irradiance on collectors**

efficiency at STC = 15.76%   PV conversion

11955 kWh   **Array nominal energy (at STC effic.)**

-1.8% PV loss due to irradiance level

-2.0% PV loss due to temperature

-1.8% Shadings: Electrical Loss acc. to strings

-1.5% LID - Light induced degradation

-1.0% Module array mismatch loss

-0.7% Ohmic wiring loss

10949 kWh   **Array virtual energy at MPP**

-3.8% Inverter Loss during operation (efficiency)

-0.2% Inverter Loss over nominal inv. power

0.0% Inverter Loss due to power threshold

0.0% Inverter Loss over nominal inv. voltage

0.0% Inverter Loss due to voltage threshold

10510 kWh   **Available Energy at Inverter Output**

10510 kWh   **Energy injected into grid**

Grid-Connected System: Simulation parameters

Project :   **LIVING LAB Bergen**

| **Geographical Site** | | **Bergen** | | Country | **Norway** |

Situation   Latitude   60.4°N   Longitude   5.3°E
    Time defined as   Legal Time   Time zone UT+1   Altitude   9 m
Monthly albedo values

	Jan.	Feb.	Mar.	Apr.	May	June	July	Aug.	Sep.	Oct.	Nov.	Dec.
Albedo	0.82	0.82	0.75	0.55	0.20	0.20	0.20	0.20	0.20	0.20	0.20	0.82

Meteo data: **Bergen**   Canada EPW hourly TMY (1953-1995) - TMY

Simulation variant :   **Stato di fatto**

                                Simulation date   20/07/16 00h16

Simulation parameters

| **Collector Plane Orientation** | Tilt | 30° | Azimuth | 0° |

Models used   Transposition   Perez   Diffuse   Imported

Horizon   Free Horizon

Near Shadings   According to strings   Electrical effect   100 %

PV Arrays Characteristics   **(2 kinds of array defined)**
PV module   Si-poly   Model   **REC 260PE / PE-BLK**
    Original PVsyst database   Manufacturer   REC

Sub-array "Sottocampo #1"
Number of PV modules	In series	12 modules	In parallel	2 strings
Total number of PV modules	Nb. modules	24	Unit Nom. Power	260 Wp
Array global power	Nominal (STC)	**6.24 kWp**	At operating cond.	5.62 kWp (50°C)
Array operating characteristics (50°C)	U mpp	333 V	I mpp	17 A

Sub-array "Sottocampo #2"
Number of PV modules	In series	12 modules	In parallel	2 strings
Total number of PV modules	Nb. modules	24	Unit Nom. Power	260 Wp
Array global power	Nominal (STC)	**6.24 kWp**	At operating cond.	5.62 kWp (50°C)
Array operating characteristics (50°C)	U mpp	333 V	I mpp	17 A

| **Total** Arrays global power | Nominal (STC) | **12 kWp** | Total | 48 modules |
| | Module area | **79.2 m²** | Cell area | 70.1 m² |

Inverter   Model   **Sunny Boy 5000 TL-21**
    Original PVsyst database   Manufacturer   SMA
| Characteristics | Operating Voltage | 175-500 V | Unit Nom. Power | 4.60 kWac |

| **Sub-array "Sottocampo #1"** | Nb. of inverters | 1 units | Total Power | 4.6 kWac |
| **Sub-array "Sottocampo #2"** | Nb. of inverters | 1 units | Total Power | 4.6 kWac |

| **Total** | Nb. of inverters | 2 | Total Power | 9 kWac |

PV Array loss factors

Array Soiling Losses			Loss Fraction	1.0 %
Thermal Loss factor	Uc (const)	22.5 W/m²K	Uv (wind)	0.0 W/m²K / m/s
Wiring Ohmic Loss	Array#1	327 mOhm	Loss Fraction	1.5 % at STC
	Array#2	327 mOhm	Loss Fraction	1.5 % at STC
	Global		Loss Fraction	1.5 % at STC
LID - Light Induced Degradation			Loss Fraction	1.5 %
Module Quality Loss			Loss Fraction	0.0 %
Module Mismatch Losses			Loss Fraction	1.0 % at MPP

Grid-Connected System: Simulation parameters (continued)

Incidence effect, ASHRAE parametrization   IAM =   1 - bo (1/cos i - 1)   bo Param.   0.05

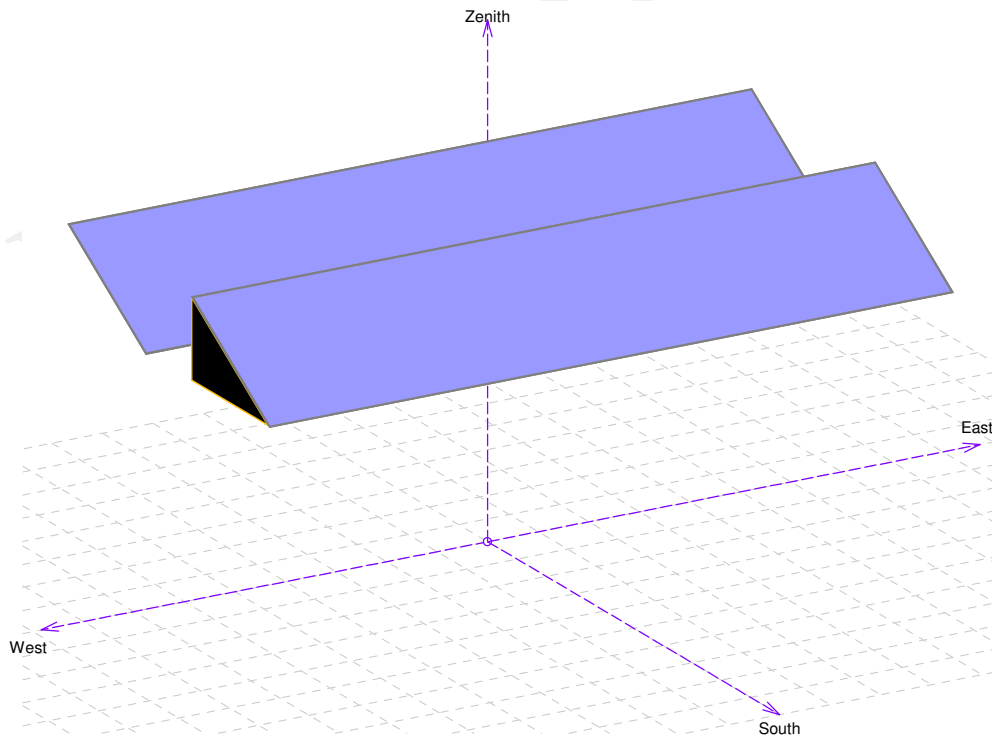**User's needs :**   Unlimited load (grid)

Grid-Connected System: Near shading definition

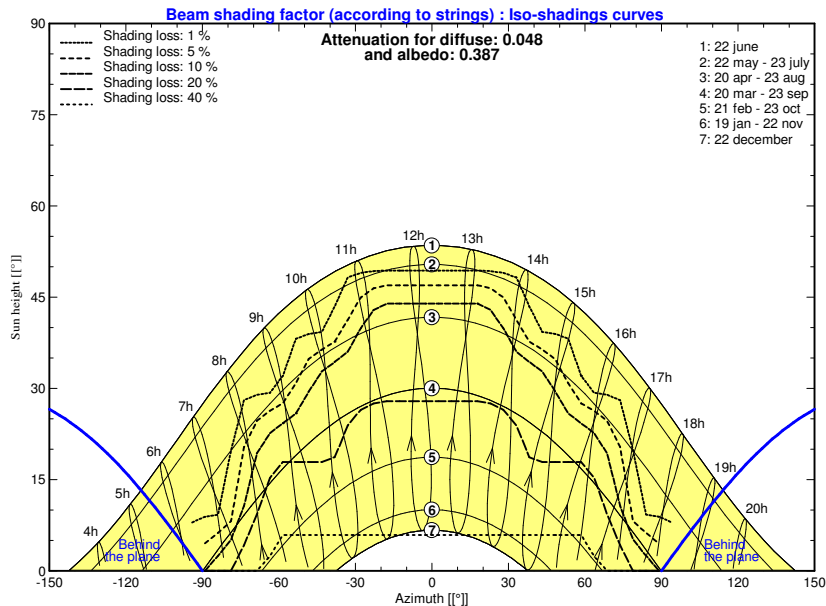**Project :**   **LIVING LAB Bergen**

Simulation variant :   **Stato di fatto**

Main system parameters	System type	**Grid-Connected**		
Near Shadings	According to strings		Electrical effect	100 %
PV Field Orientation	tilt	30°	azimuth	0°
PV modules	Model	REC 260PE / PE-BLK	Pnom	260 Wp
PV Array	Nb. of modules	48	Pnom total	**12.48 kWp**
Inverter	Model	Sunny Boy 5000 TL-21	Pnom	4600 W ac
Inverter pack	Nb. of units	2.0	Pnom total	**9.20 kW ac**
User's needs	Unlimited load (grid)			

Perspective of the PV-field and surrounding shading scene

Iso-shadings diagram

LIVING LAB Bergen - Legal Time

Beam shading factor (according to strings) : Iso-shadings curves

Shading loss: 1 %
Shading loss: 5 %
Shading loss: 10 %
Shading loss: 20 %
Shading loss: 40 %

**Attenuation for diffuse: 0.048
and albedo: 0.387**

1: 22 june
2: 22 may - 23 july
3: 20 apr - 23 aug
4: 20 mar - 23 sep
5: 21 feb - 23 oct
6: 19 jan - 22 nov
7: 22 december

Grid-Connected System: Main results

Project : **LIVING LAB Bergen**

Simulation variant : **Stato di fatto**

Main system parameters
System type **Grid-Connected**

Near Shadings	According to strings	Electrical effect	100 %
PV Field Orientation	tilt 30°	azimuth	0°
PV modules	Model REC 260PE / PE-BLK	Pnom	260 Wp
PV Array	Nb. of modules 48	Pnom total	**12.48 kWp**
Inverter	Model Sunny Boy 5000 TL-21	Pnom	4600 W ac
Inverter pack	Nb. of units 2.0	Pnom total	**9.20 kW ac**
User's needs	Unlimited load (grid)		

Main simulation results

System Production | **Produced Energy** | **8555 kWh/year** | Specific prod. | 686 kWh/kWp/year
Performance Ratio PR | 80.88 %

Normalized productions (per installed kWp): Nominal power 12.48 kWp
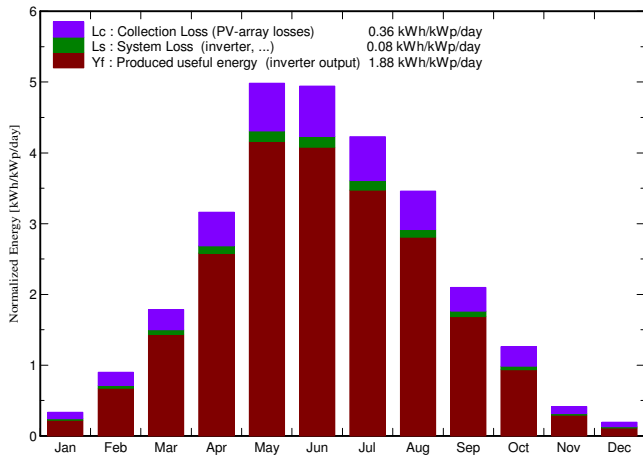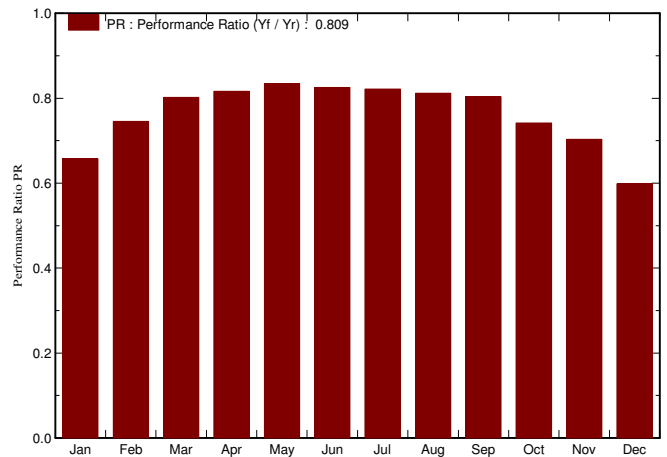
Lc : Collection Loss (PV-array losses)   0.36 kWh/kWp/day
Ls : System Loss (inverter, ...)   0.08 kWh/kWp/day
Yf : Produced useful energy (inverter output) 1.88 kWh/kWp/day

Performance Ratio PR

PR : Performance Ratio (Yf / Yr) : 0.809

Stato di fatto
Balances and main results

	GlobHor	T Amb	GlobInc	GlobEff	EArray	E_Grid	EffArrR	EffSysR
	kWh/m²	°C	kWh/m²	kWh/m²	kWh	kWh	%	%
January	6.5	2.00	10.4	8.1	94	85	11.43	10.36
February	17.7	1.05	25.2	21.1	249	235	12.46	11.74
March	44.6	2.66	55.4	48.6	581	555	13.23	12.64
April	80.7	5.31	94.8	85.9	1005	966	13.38	12.87
May	138.3	9.01	154.5	144.1	1668	1609	13.63	13.15
June	141.1	12.13	148.3	137.3	1585	1528	13.50	13.01
July	124.3	13.74	131.1	120.9	1396	1344	13.44	12.94
August	97.6	13.95	107.2	98.7	1129	1086	13.30	12.79
September	55.3	10.64	63.0	56.6	660	632	13.23	12.66
October	28.0	7.53	39.1	33.3	381	362	12.29	11.68
November	8.9	4.04	12.5	10.2	119	110	12.06	11.08
December	3.7	2.78	6.0	4.5	50	45	10.64	9.43
Year	746.7	7.11	847.5	769.5	8917	8555	13.28	12.75

Legends:	GlobHor	Horizontal global irradiation	EArray	Effective energy at the output of the array
	T Amb	Ambient Temperature	E_Grid	Energy injected into grid
	GlobInc	Global incident in coll. plane	EffArrR	Effic. Eout array / rough area
	GlobEff	Effective Global, corr. for IAM and shadings	EffSysR	Effic. Eout system / rough area

Grid-Connected System: Loss diagram

Project :   **LIVING LAB Bergen**

Simulation variant :   **Stato di fatto**

Main system parameters	System type	**Grid-Connected**		

Near Shadings	According to strings		Electrical effect	100 %
PV Field Orientation	tilt	30°	azimuth	0°
PV modules	Model	REC 260PE / PE-BLK	Pnom	260 Wp
PV Array	Nb. of modules	48	Pnom total	**12.48 kWp**
Inverter	Model	Sunny Boy 5000 TL-21	Pnom	4600 W ac
Inverter pack	Nb. of units	2.0	Pnom total	**9.20 kW ac**
User's needs	Unlimited load (grid)			

Loss diagram over the whole year

747 kWh/m² **Horizontal global irradiation**

+13.5% **Global incident in coll. plane**

-5.3% Near Shadings: irradiance loss

-3.1% IAM factor on global

-1.0% Soiling loss factor

769 kWh/m² * 79 m² coll. **Effective irradiance on collectors**

efficiency at STC = 15.76% PV conversion

9604 kWh **Array nominal energy (at STC effic.)**

-2.4% PV loss due to irradiance level

-0.5% PV loss due to temperature

-1.2% Shadings: Electrical Loss acc. to strings

-1.5% LID - Light induced degradation

-1.0% Module array mismatch loss

-0.6% Ohmic wiring loss

8939 kWh **Array virtual energy at MPP**

-4.0% Inverter Loss during operation (efficiency)

-0.3% Inverter Loss over nominal inv. power

0.0% Inverter Loss due to power threshold

0.0% Inverter Loss over nominal inv. voltage

0.0% Inverter Loss due to voltage threshold

8555 kWh **Available Energy at Inverter Output**

8555 kWh **Energy injected into grid**

Grid-Connected System: Simulation parameters

Project : **Living Lab meteonorm**

| **Geographical Site** | **Trondheim** | Country | **Norway** |

Situation Latitude 63.6°N Longitude 10.4°E
  Time defined as Legal Time Time zone UT+1 Altitude 359 m
Monthly albedo values

	Jan.	Feb.	Mar.	Apr.	May	June	July	Aug.	Sep.	Oct.	Nov.	Dec.
Albedo	0.82	0.82	0.75	0.55	0.20	0.20	0.20	0.20	0.20	0.20	0.20	0.82

Meteo data: **Trondheim** Canada EPW hourly TMY (1953-1995) - TMY

Simulation variant : **Stato di fatto**

  Simulation date 30/05/16 09h47

Simulation parameters

Collector Plane Orientation Tilt 30° Azimuth 0°

Models used Transposition Perez Diffuse Imported

Horizon Free Horizon

Near Shadings According to strings Electrical effect 100 %

PV Arrays Characteristics (2 kinds of array defined)
PV module Si-poly Model **REC 260PE / PE-BLK**
  Original PVsyst database Manufacturer REC
Sub-array "Sottocampo #1"
Number of PV modules In series 12 modules In parallel 2 strings
Total number of PV modules Nb. modules 24 Unit Nom. Power 260 Wp
Array global power Nominal (STC) **6.24 kWp** At operating cond. 5.62 kWp (50°C)
Array operating characteristics (50°C) U mpp 333 V I mpp 17 A

Sub-array "Sottocampo #2"
Number of PV modules In series 12 modules In parallel 2 strings
Total number of PV modules Nb. modules 24 Unit Nom. Power 260 Wp
Array global power Nominal (STC) **6.24 kWp** At operating cond. 5.62 kWp (50°C)
Array operating characteristics (50°C) U mpp 333 V I mpp 17 A

Total Arrays global power Nominal (STC) **12 kWp** Total 48 modules
  Module area **79.2 m²** Cell area 70.1 m²

Inverter Model **Sunny Boy 5000 TL-21**
  Original PVsyst database Manufacturer SMA
Characteristics Operating Voltage 175-500 V Unit Nom. Power 4.60 kWac

Sub-array "Sottocampo #1" Nb. of inverters 1 units Total Power 4.6 kWac
Sub-array "Sottocampo #2" Nb. of inverters 1 units Total Power 4.6 kWac

Total Nb. of inverters 2 Total Power 9 kWac

PV Array loss factors

Array Soiling Losses Loss Fraction 1.0 %
Thermal Loss factor Uc (const) 22.5 W/m²K Uv (wind) 0.0 W/m²K / m/s
Wiring Ohmic Loss Array#1 327 mOhm Loss Fraction 1.5 % at STC
  Array#2 327 mOhm Loss Fraction 1.5 % at STC
  Global Loss Fraction 1.5 % at STC
LID - Light Induced Degradation Loss Fraction 1.5 %
Module Quality Loss Loss Fraction 0.0 %
Module Mismatch Losses Loss Fraction 1.0 % at MPP

Grid-Connected System: Simulation parameters (continued)

Incidence effect, ASHRAE parametrization   IAM = $1 - bo (1/\cos i - 1)$ bo Param.   0.05

User's needs :   Unlimited load (grid)

Grid-Connected System: Near shading definition

Project :   **Living Lab meteonorm**

Simulation variant : **Stato di fatto**

Main system parameters	System type	**Grid-Connected**		
Near Shadings	According to strings		Electrical effect	100 %
PV Field Orientation	tilt	30°	azimuth	0°
PV modules	Model	REC 260PE / PE-BLK	Pnom	260 Wp
PV Array	Nb. of modules	48	Pnom total	**12.48 kWp**
Inverter	Model	Sunny Boy 5000 TL-21	Pnom	4600 W ac
Inverter pack	Nb. of units	2.0	Pnom total	**9.20 kW ac**
User's needs	Unlimited load (grid)			

Perspective of the PV-field and surrounding shading scene

Iso-shadings diagram
Living LabLegal Time

Beam shading factor (according to strings) : Iso-shadings curves

Shading loss: 1 %
Shading loss: 5 %
Shading loss: 10 %
Shading loss: 20 %
Shading loss: 40 %

Attenuation for diffuse: 0.048
and albedo: 0.387

1: 22 june
2: 22 may - 23 july
3: 20 apr - 23 aug
4: 20 mar - 23 sep
5: 21 feb - 23 oct
6: 19 jan - 22 nov
7: 22 december

Grid-Connected System: Main results

Project : **Living Lab meteonorm**

Simulation variant : **Stato di fatto**

Main system parameters
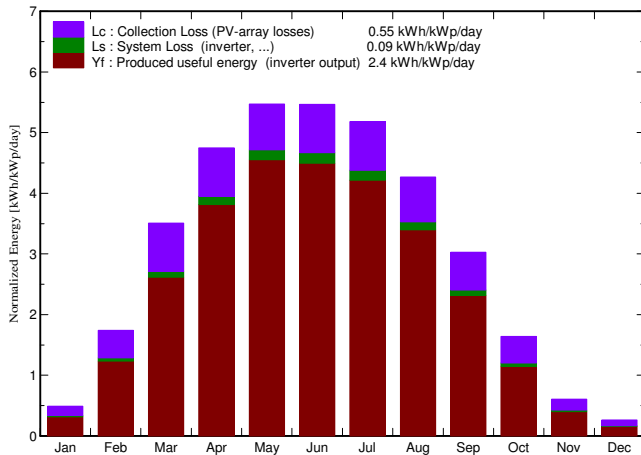
	System type	**Grid-Connected**	
Near Shadings	According to strings	Electrical effect	100 %
PV Field Orientation	tilt 30°	azimuth	0°
PV modules	Model REC 260PE / PE-BLK	Pnom	260 Wp
PV Array	Nb. of modules 48	Pnom total	**12.48 kWp**
Inverter	Model Sunny Boy 5000 TL-21	Pnom	4600 W ac
Inverter pack	Nb. of units 2.0	Pnom total	**9.20 kW ac**
User's needs	Unlimited load (grid)		

Main simulation results

System Production	**Produced Energy**	**10910 kWh/year**	Specific prod.	874 kWh/kWp/year	
	Performance Ratio PR	78.8 %			

Normalized productions (per installed kWp): Nominal power 12.48 kWp
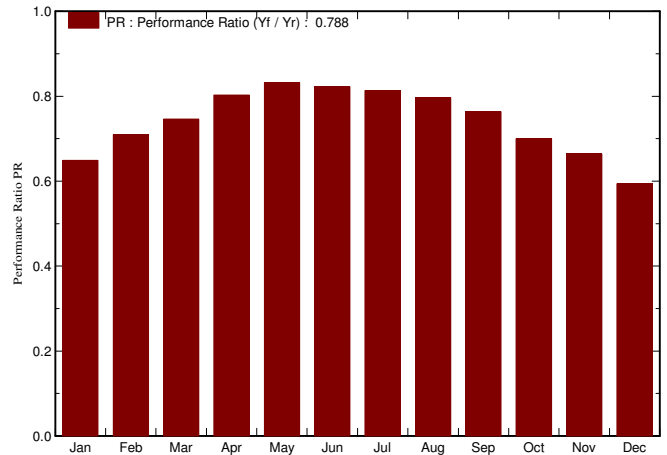
Lc : Collection Loss (PV-array losses)   0.55 kWh/kWp/day
Ls : System Loss (inverter, ...)   0.09 kWh/kWp/day
Yf : Produced useful energy (inverter output)   2.4 kWh/kWp/day

Performance Ratio PR

PR : Performance Ratio (Yf / Yr) : 0.788

Stato di fatto
Balances and main results

	GlobHor	T Amb	GlobInc	GlobEff	EArray	E_Grid	EffArrR	EffSysR
	kWh/m²	°C	kWh/m²	kWh/m²	kWh	kWh	%	%
January	5.4	-1.18	15.2	11.1	131	123	10.85	10.22
February	21.8	-1.46	48.8	38.0	450	432	11.64	11.17
March	63.4	0.04	108.8	92.1	1050	1013	12.19	11.76
April	108.0	4.30	142.4	129.1	1479	1428	13.11	12.65
May	152.4	7.96	169.6	157.8	1826	1761	13.59	13.11
June	156.9	11.33	164.1	152.6	1749	1684	13.46	12.96
July	151.9	14.00	160.7	149.4	1694	1631	13.31	12.82
August	114.1	13.88	132.3	122.1	1366	1315	13.04	12.55
September	66.1	10.38	90.9	80.5	901	867	12.51	12.04
October	28.8	5.50	50.9	41.7	466	444	11.55	11.03
November	7.4	1.53	18.1	13.5	159	150	11.10	10.47
December	2.4	-1.52	8.2	5.6	65	61	10.06	9.36
Year	878.7	5.44	1110.0	993.4	11336	10910	12.89	12.41

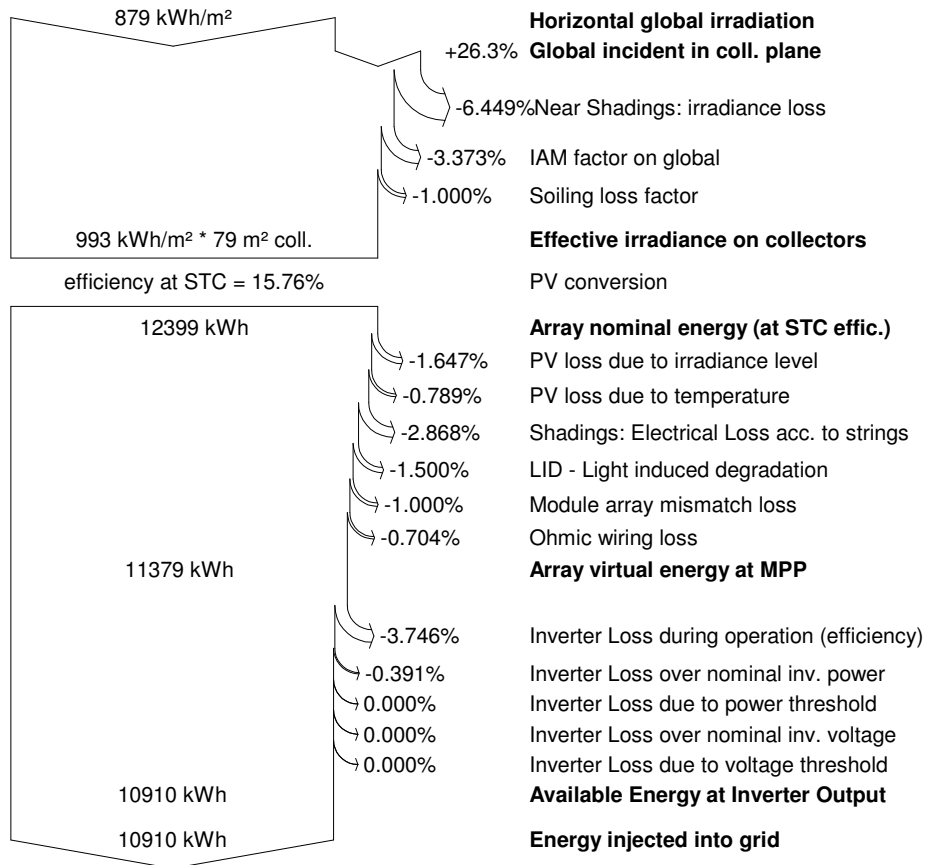| Legends:	GlobHor	Horizontal global irradiation	EArray	Effective energy at the output of the array
	T Amb	Ambient Temperature	E_Grid	Energy injected into grid
	GlobInc	Global incident in coll. plane	EffArrR	Effic. Eout array / rough area
	GlobEff	Effective Global, corr. for IAM and shadings	EffSysR	Effic. Eout system / rough area

Grid-Connected System: Loss diagram

Project : **Living Lab meteonorm**

Simulation variant : **Stato di fatto**

Main system parameters	System type	**Grid-Connected**	

Near Shadings	According to strings	Electrical effect	100 %
PV Field Orientation	tilt	30°	azimuth	0°
PV modules	Model	REC 260PE / PE-BLK	Pnom	260 Wp
PV Array	Nb. of modules	48	Pnom total	**12.48 kWp**
Inverter	Model	Sunny Boy 5000 TL-21	Pnom	4600 W ac
Inverter pack	Nb. of units	2.0	Pnom total	**9.20 kW ac**
User's needs	Unlimited load (grid)		

Loss diagram over the whole year

879 kWh/m²	**Horizontal global irradiation**
+26.3%	**Global incident in coll. plane**
-6.449%	Near Shadings: irradiance loss
-3.373%	IAM factor on global
-1.000%	Soiling loss factor
993 kWh/m² * 79 m² coll.	**Effective irradiance on collectors**
efficiency at STC = 15.76%	PV conversion
12399 kWh	**Array nominal energy (at STC effic.)**
-1.647%	PV loss due to irradiance level
-0.789%	PV loss due to temperature
-2.868%	Shadings: Electrical Loss acc. to strings
-1.500%	LID - Light induced degradation
-1.000%	Module array mismatch loss
-0.704%	Ohmic wiring loss
11379 kWh	**Array virtual energy at MPP**
-3.746%	Inverter Loss during operation (efficiency)
-0.391%	Inverter Loss over nominal inv. power
0.000%	Inverter Loss due to power threshold
0.000%	Inverter Loss over nominal inv. voltage
0.000%	Inverter Loss due to voltage threshold
10910 kWh	**Available Energy at Inverter Output**
10910 kWh	**Energy injected into grid**

Appendix H

Data sheets about icephobic coatings by:

- NEI Corporation
- NuSil
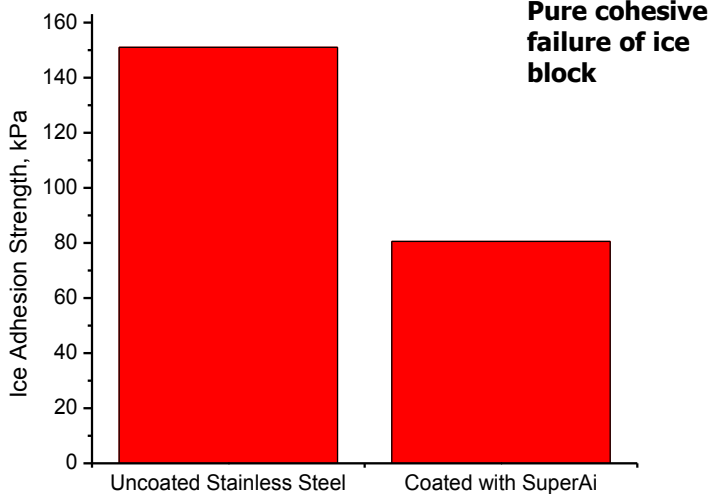- MicroPhase Coatings
- Fraunhofer

NANOMYTE® SuperAi
Durable, Corrosion Resistant, Anti-Ice Coating
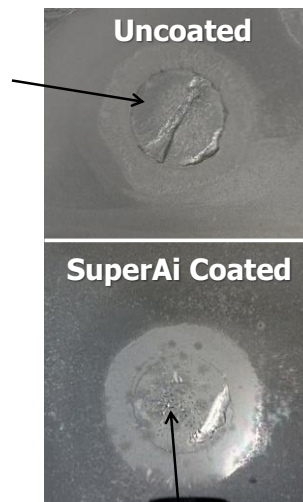
NEI Corporation

NANOMYTE® SuperAi is a nanocomposite coating that imparts anti-icing properties to the underlying substrate. The transparent coating also provides a hard, dense, and smooth finish. Surfaces treated with SuperAi exhibit reduced ice adhesion, thereby preventing ice buildup. SuperAi is a versatile coating that can be applied directly on a variety of substrate materials, including plastics, metals, glass, concrete and ceramics. SuperAi cures under ambient conditions.

In independent tests performed at multiple sites, it has been shown that NANOMYTE® SuperAi reduces the adhesion strength of ice by as much as 60%, compared to bare metal and painted surfaces. This in turn leads to reduced ice accretion. The use of SuperAi in applications such as wind turbines, overhead high voltage power lines, transportation, marine, and others enhances productivity and energy efficiency, thereby providing a good return on investment.

The coating can be applied by brushing, spraying or wiping. The dry film thickness can be adjusted to be in the range of 5 – 15 microns (1/5th to 3/5th of a mil). Only one coat is required to cover the substrate. The liquid coating solution is available in liter and gallon quantities.

FEATURES

- Decreases ice adhesion by 40 to 60%
- Transparent and glossy finish, with low haze
- Dries thin: < 1 mil
- Low VOC
- Product can be applied to a variety of substrates
- Low viscosity formulation spreads quickly – even over complex surfaces

BENEFITS

- **Weather Resistant –** Hydrophobic surface repels water and reduces ice build up
- **Easy-to-Clean –** Lower friction, slippery surface makes it resistant to contamination and easier to clean up
- **Easy Application –** Can be applied by brush, spray, or wipe, with no primer or curing required
- **Durability –** Increases the service life of coating by preserving protective functions
- **Cost Savings –** Reduces raw material, labor, and energy cost of repainting or recoating
- **Maintenance –** Eliminates the need to frequently repaint or replace damaged coatings

Pure cohesive failure of ice block

Uncoated

SuperAi Coated

Mostly adhesive failure on substrate

Left: Stainless Steel coated with NANOMYTE® SuperAi exhibits up to a 60% reduction in ice adhesion. Right: Uncoated surface shows a cohesive failure within ice, while stainless steel coated with SuperAi had adhesive failure at the interface.

PRODUCT DESCRIPTION

NANOMYTE® SuperAi is a nanocomposite coating that imparts anti-icing properties to the underlying substrate. The transparent coating also provides a hard, dense and smooth finish. Surfaces treated with SuperAi exhibit reduced ice adhesion, thereby preventing ice buildup. SuperAi can be applied to a variety of substrates, including plastics, metals, glass, and ceramics. In some instances, a suitable primer may be required for maximum adhesion of the anti-ice coating. The coating can be cured at room temperature.

TECHNICAL DATA

Color:	Clear
Curing Temperature:	20° − 150 °C
Cured Film Thickness:	5 − 15 µm
Coverage:	110 m^2 (1200 ft^2) / gallon
Solids Content:	18 − 20 %
Water Contact Angle:	100 − 105°

SURFACE PREPARATION

Ensure surfaces to be coated are clean, dry, and in sound condition. Before applying SuperAi, remove all oil, grease, dust, dirt and other foreign material by using an appropriate cleaner. To ensure that the surface is completely free of oil and grease, use a lint-free white cloth with a solvent such as alcohol or acetone, and wipe the surface. If the cloth remains white, the surface is clean; if the cloth turns dark, continue cleaning until it remains white. Once clean, SuperAi can be applied by following the instructions below.

COATING APPLICATION

It is recommended that coating application be performed in a clean environment to minimize surface defects. The coating can be applied by immersion, spraying, rolling, or brushing. Only one coat is required to cover the substrate. Under ambient conditions (25°C / 77°F, 50% RH), a single coat is 5 − 15 µm (0.2 - 0.6 mil) thick. Dilute with isopropanol as needed.

Spraying:

When surface preparation is complete and surface is dry and free of dust, begin application using a high volume, low pressure (HVLP) spray gun with a 1.0 size tip and the pressure set at approximately 25 to 30 psi. On a separate piece of cardboard, first spray a test pattern to achieve a 6" to 8" elongated pattern approximately 1½" wide in the middle and fluid enough to cover but not puddle. If there is high wind, this will affect the quality of the finish as blowing wind can disrupt the spray pattern from your HVLP. It can also contribute to contamination of the finish with blowing dust. It may be necessary to erect a windscreen to protect the area. Once the spray pattern is achieved on the test cardboard, spray one coat in a cross-pattern; left to right, then up and down. This will provide sufficient coverage and will help prevent holes in coverage. Desired wet film thickness (WFT) is approximately 2.0 to 2.5 mils (spraying undiluted solution).

If using spray application method in an enclosed space, make certain to tent off the area being sprayed with plastic tarps to avoid spray dust from traveling and contaminating other surfaces with overspray dust. Tented and enclosed areas always require to be positively supplied with fresh air and have ventilated exhaust to outside using fans. Never spray near any open flame or any possible source of ignition such as pilot light, or anything that may spark, as this may cause ignition and explosion of the fumes and vapors.

Rolling:

Make certain the surface is clean as per preparation instructions. Using a white, ultra-smooth high-density foam roller, pour SuperAi into a roller pan and completely saturate the roller. Apply in a cross-pattern; left to right, then up and down as quickly as possible as the coating dries fast. Avoid down pressure on the roller to achieve a better looking finish.

Brushing:

Make certain the surface is clean as per preparation instructions. Select the appropriate size brush width based on the surface area being coated. Using only a good quality China bristle brush, apply SuperAi in a cross-pattern; up and down, then left and right. To obtain the best results, do not overwork the coating as it dries fairly quickly. Do not bear down with the brush. Use light strokes using the tip of the brush to smooth out the coating. Desired wet film thickness (WFT) is approximately 2.0 to 2.5 mils.

CURING

Ambient Curing:

Under ambient conditions (25°C / 77°F, 50% RH), a single coat will be dry to the touch in 1 hour and completely cured in 24 hours.

Accelerated Curing: In order to accelerate curing, let the coated surface dry in ambient air for 10 minutes and then heat to at least 105°C for a minimum of 5 minutes, preferably ~15 minutes. An oven, blow dryer, or heat gun may be used (maximum temperature is 150°C).

CLEAN UP

Clean tools and flush equipment immediately after application is completed with acetone thoroughly before product dries. Once coating is dry, the tools will not clean with acetone or any other solvent.

STORAGE & HANDLING

Precautions for Safe Handling:
Appropriate personal protective equipment should be used at all times. Provide good ventilation or extraction. Avoid prolonged or repeated breathing of vapor. Avoid contact with eyes, skin and clothing. Keep away from heat, sparks, flames and other sources of ignition. Wash hands thoroughly after handling.

Conditions for Safe Storage (including any incompatibilities):
Avoid storage over 100° F and contamination with incompatible materials. Keep containers tightly closed in a cool, well ventilated place. Protect from moisture. Residual vapors might explode on ignition. Do not apply heat, cut, drill, and grind or weld on or near this container.

Refer to SDS for complete information on the safe handling of this product.

ADDITIONAL INFORMATION

NEI Corporation believes that the information in this technical data sheet is an accurate description of the typical use of the product. However, NEI disclaims any liability for incidental or consequential damages, which may result from the use of their products that are beyond its control. Employers should use this information only as a supplement to other information gathered by them and should make independent judgment of suitability of this information to ensure proper use and protect the health and safety of employees. Therefore, it is the user's responsibility to thoroughly test the product in their particular application to determine its performance, efficacy, and safety. Nothing contained herein is to be considered as permission or a recommendation to infringe any patent or any other intellectual right.

# Polymer Systems Technology Limited

UK & Ireland Distributor
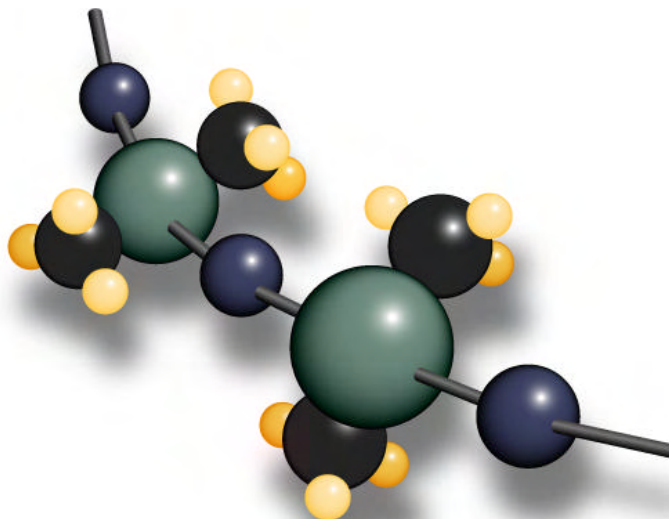
Silicone Ice-phobic Coatings

Ice build up has major economic impact on the aircraft industry, resulting in multiple efforts to understand and resolve the problem. When compared to other commercially marketed ice-phobic coatings and non-stick materials such as Teflon®, NuSil's silicone coatings show significantly improved reduction in ice adhesion when applied on aluminum surfaces. In addition, new silicone materials have been developed that cure at room temperature and add fuel resistance.
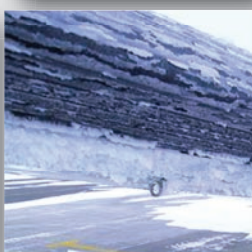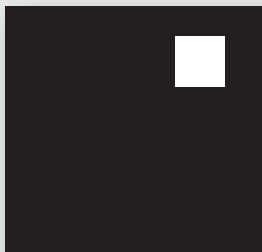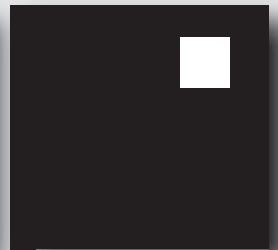
NuSil Technology is the cutting edge manufacturer of silicone products for the aircraft industry requiring precise and predictable materials. NuSil's silicone materials deliver adhesives, potting compounds, encapsulants, and fast-curing silicones.

ISO 9001 certified since 1994, and AS 9100 certified since 2008, NuSil operates state-of-the-art laboratories and processing facilities in North America and provides on-site, in-person application engineering support worldwide.

www.nusil.com

Ice Adhesion Testing

Department of the Army, Engineer Research and Development Center, Cold Regions Research and Engineering Laboratory (CRREL) tested ice adhesion to several new NuSil ice-phobic coatings using the Zero-Degree Cone test. Ice is grown in a gap between two concentric, cylindrical surfaces. The force required to push the inner cylinder out of the ice collar is measured to determine the adhesive strength of the ice to the coating. Samples are frozen at -10 ºC for 48 hours and the nominal shear stress for ice release is calculated from the measured maximum load divided by the surface area of the coated pin/ice interface.
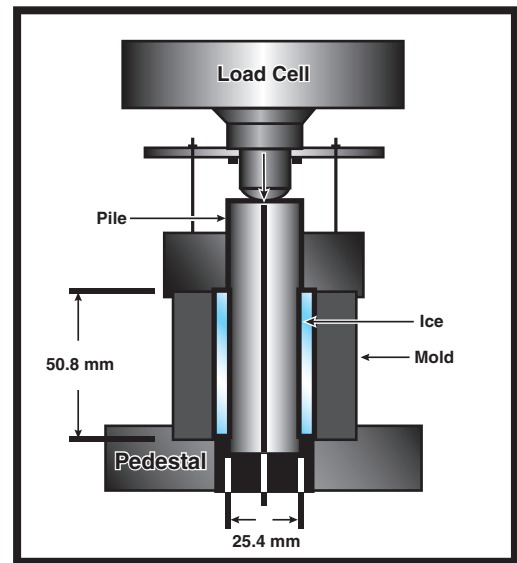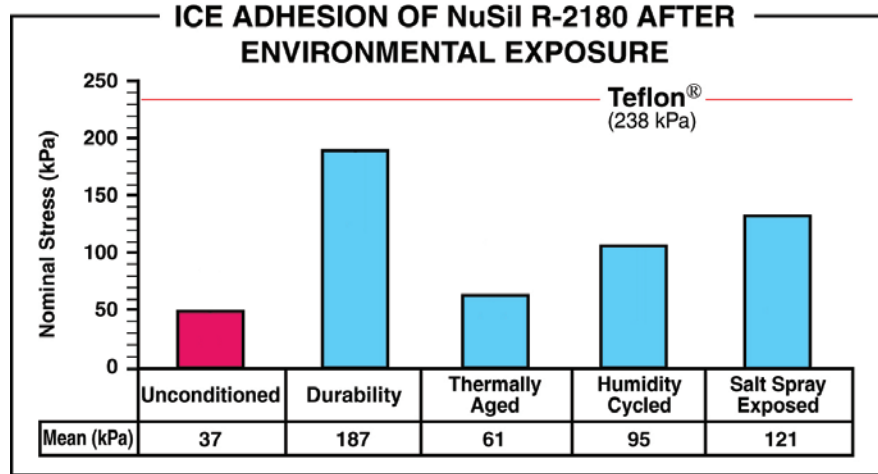

Ice Adhesion Test Results

All of NuSil's materials demonstrate much lower stress compared to the standard Teflon® (238 kPa). Bare Aluminum stress is also referenced at 1520kPa. Coating thickness of the material tested is 0.010 inches.

Mean Stress (kPa)

	R-1009	R-1082	R-3930	R-3975	R-2180
	8	27	47	22	37
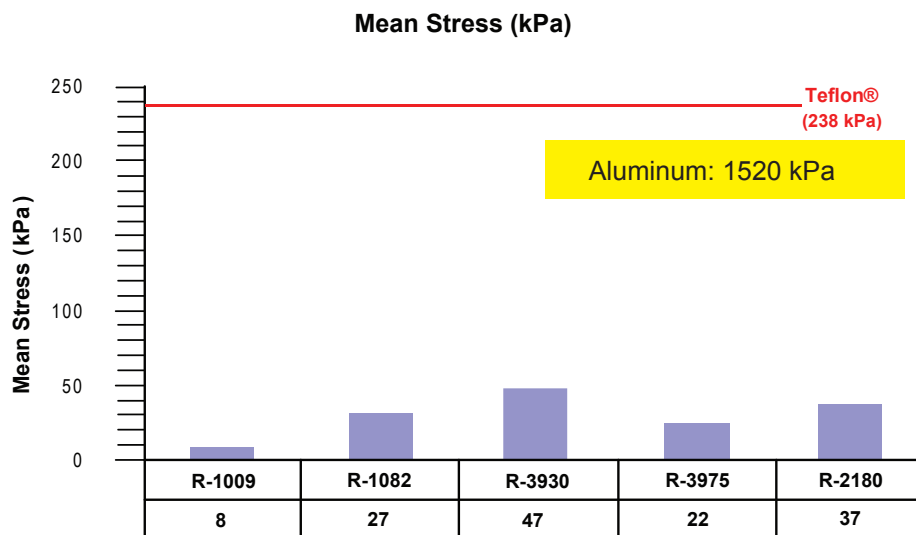
Environmental Exposure

Evaluation of a coating after exposure to extreme environmental conditions and wear is important to measure when considering material for your application. NuSil's R-2180 shows favorable performance after exposure to wear, heat, humidity, and salt water spray compared to the industry standard Teflon®.

ICE ADHESION OF NuSil R-2180 AFTER ENVIRONMENTAL EXPOSURE

Mean (kPa)	Unconditioned	Durability	Thermally Aged	Humidity Cycled	Salt Spray Exposed
	37	187	61	95	121

Teflon® (238 kPa)

Material Properties

The below table shows the typical material properties in the uncured and cured state of the NuSil products referenced in this study.

Typical Properties	R-1009 RTV Silicone Coating	R-1082 RTV Silicone Coating	R-3930 RTV Fuel Resistant Coating	R-3975 RTV Fuel Resistant Coating	R-2180 Heat Curing Silicone Coating
Uncured:					
Viscosity	6,500 cPs 6,500 mPas	700 cPs 700 mPas	735 cPs 735 mPas	1,625 cPs 1,625 mPas	3,075 cPs 3,075 mPas
Non-Volatile Content	33%	29%	60%	60%	20%
Work Time	>72 hours	N/A	N/A	N/A	>72 hours
Solvent	VM&P Naptha (R-1001)	Xylene (R1-1001)	Tert Butyl Acetate (R2-1001)	Tert Butyl Acetate (R2-1001)	Xylene (R1-1001)
Cured:					
Cure Schedule (days @ ambient)	7	5	3	3	*See Below
Specific Gravity	1.10	1.09	1.36	1.29	N/A
Durometer, Type A	40	25	30	25	40
Tensile Strength	1200 psi 8.3 MPa	1,425 psi 9.8 MPa	750 psi 5.2 MPa	425 psi 2.9 MPa	1,700 psi 11.7 MPa
Tear Strength	95 ppi 16.8 N/mm	125 ppi 22.0 kN/m	40 ppi 7.1 kN/m	Min. 35 ppi 6.2 kN/m	300 ppi 52.9 kN/m
% Elongation	650%	950%	400%	400%	1,050%
Contact Angle	113°	115°	107°	111°	116°
Recommended NuSil Primer**	SP-120 SP-121	SP-120 SP-121	SP-120 SP-121	SP-120 SP-121	SP-270

*30 min @ 25°C (77°F), 45 min @ 75°C (167°F), and 135 min @ 150°C (302°F)
**Some bonding applications may require use of a primer. NuSil Technology recommends the primers listed in the above table.
RTV = Room Temperature Vulcanizing

References

• EM 1110-2-1612, Engineering and Design – Ice Engineering, U.S. Army Corps of Engineers, Department of the Army, October 20, 2002, UPDATE VERSION September 2006.
• Mulherin, ND, RB Haehnel, JF Jones (1998) Toward developing a standard shear test from ice adhesion. Proceedings, 8th International Workshop on Atmospheric Icing Structures, Reykjavik, Iceland, June 8-11, 1998. IWAIS '98.
• Laboratory Ice Adhesion test Results for Commercial Icephobic Coatings for NuSil, June 2009, CRREL.

NuSil SILICONE TECHNOLOGY
Creative Partners in a Material World

Corporate Headquarters
NuSil Technology - USA
1050 Cindy Lane
Carpinteria, CA 93013
+1 (805) 684-8780
+1 (805) 566-9905 Fax
silicone@nusil.com
www.nusil.com

NuSil Technology - Europe
Parc d'Activités de Sophia Antipolis
Le Natura Bt2
1198, avenue Maurice Donat
06250 MOUGINS France
+33 4 92 96 93 31
+33 4 92 96 06 37 Fax
nusil.sophia@nusil.com

NuSil SILICONE TECHNOLOGY
Creative Partners in a Material World

2539 Asher View Ct.
Raleigh NC, 27606

MicroPhase Coatings, Inc.

PH 919.779.7679
FAX 919.779.1109
www.microphasecoatings.com

MPCI Product Data Sheet
Revision Date: April 2011
This data sheet refernces batches made after
April 4, 2011. Batch number reference is
PhaseBreak ESL-Master-20110404

PhaseBreak ESL
Icephobic Coating

PRODUCT DESCRIPTION

PhaseBreak ESL is a two-part epoxy silicate ambient cure coating that reduces ice particle adhesion (icephobicity) via freezing point depressants. The coating is VOC compliant and easy to apply by spray, brush or roll. A more aggressive version, PhaseBreak ESL2X, is also available. The best choice between standard ESL and ESL2X and coating life before refinishing is determined experimentally for a particular application. This family coatings was originally designed as an icephobic coating for the USAF B-2 aircraft. As such, the coating has passed a rigorous set of criteria required for use on this aircraft.

FEATURES

- Excellent ice release properties
- Good rain erosion
- Low VOC
- Environmentally friendly
- Good spray/brush/roll properties

USES

- General ice prevention and ice shedding
- Architectural, bridges, etc.
- Protecting aircraft engines from ice foreign object debris (FOD)
- Radar domes and transmission lines
- Wind turbine generator blades
- Shipboard antennas
- Helicopter engine inlets

SUBSTRATES AND SURFACE PREPARATION

General

Surfaces must be clean and dry (SSPC #2 minimum). Employ adequate methods to remove dirt, dust, oil and all other contaminants that could interfere with adhesion of the coating. Steel, aluminum, titanium and other metals require a primer tie coat to get good adhesion.

Polymer Coatings and Surfaces

PhaseBreak ESL has good adhesion to various organic coatings and to epoxy-based composites. Because of the wide variety of coatings available, adhesion tests should be conducted with these coatings as part of the qualification process.

APPLICATION EQUIPMENT

Spray Application (General)

This is a high solids coating and may require adjustments in spray techniques. Wet film thickness is easily and quickly achieved. The following spray equipment has been found suitable and is available from manufacturers such as Binks, DeVilbiss and Graco.

Conventional Spray

Pressure pot equipped with dual regulators, 3/8" I.D. minimum material hose, 0.070" I.D. fluid tip and appropriate air cap.

Airless Spray

Pump Ratio:	30-1 (min)	Tip Size:	0.015" – 0.031"
GPM Output:	3.0 (min)	Output PSI:	2100 – 2300
Material Hose:	3/8" I.D. (min)	Filter Size:	50 mesh

MIXING AND THINNING

Mixing

Power mix separately, then combine and power mix. DO NOT MIX PARTIAL KITS. Wait 10 minutes before applying.

Ratio:	**3:5 (A to B)**	**Cure-to-touch:**	**4 hrs**
Thinning :	**None**	**Hard:**	**24 hrs**
Pot Life:	**2 hrs @ 72ºF**	(Complete cure:	7 days)

CLEANUP AND SAFETY

Cleanup

Use isopropyl alcohol, MEK, or acetone. In case of spillage, absorb and dispose per local regulations.

Safety

Follow all caution statements on this product data sheet and on the MSDS for this product. Employ normal workmanlike safety precautions. Wear appropriate Personnel Protective Equipment.

Caution

Flammable material – keep away from sparks and open flames. All electrical equipment and installations should be made and grounded in accordance with the National Electric Code. In areas where explosion hazards exist, workmen should be required to use non-ferrous tools and wear conductive and non-sparking shoes.

PACKAGING, HANDLING & STORAGE

Packaged as 1 quart or 1 gallon kits
Store indoors at 32ºF to 100ºF
Shelf Life: 6 months at 75ºF

2539 Asher View Ct,
Raleigh, NC 27606

MicroPhase Coatings, Inc.

PH 919.779.7679
FAX 919.779.1109
www.microphasecoatings.com

MPCI Product Data Sheet
Revision Date: July 2011

PhaseBreak Flex MPD
Icephobic Coating

PRODUCT DESCRIPTION

PhaseBreak Flex MPD is a two-part tough siloxane coating that reduces ice particle adhesion (icephobicity). The coating is a unique formulation of siloxanes, silanes, and freezing point depressants that enable an ambient cure system. The coating is easy to apply by air or airless spray equipment, or by brush. This coating was designed to shed ice from static surfaces, such as power equipment, satelite dishes, and steel structures.

The coating reduces ice adhesion using two approaches. First, the coating is formulated with a specialty oil that significantly reduces inherent ice adhesion. Secondly, freezing point depressants are formulated into the coating to melt ice at the surface of the coating. These freezing point depressants are non-toxic and environmentally safe. The resultant coating has good durability, and excellent resistance to ice formation.

FEATURES

- Excellent ice release properties
- Good rain erosion
- Multi-year service life
- Environmentally friendly
- Good spray properties

USES

- Protecting aircraft engines from ice foreign object debris (FOD)
- Radar domes
- Power transmission equipment
- Wind turbine generator blades
- Shipboard antennas
- Helicopter engine inlets

SUBSTRATES AND SURFACE PREPARATION

General

Surfaces must be clean and dry (SSPC #2 minimum). Employ adequate methods to remove dirt, dust, oil and all other contaminants that could interfere with adhesion of the coating. Adhesion is excellent on steel, aluminum, and titanium. Plastic or painted surfaces will require PhaseCoat Primer to achieve good adhesion.

PACKAGING, HANDLING & STORAGE

Packaged as 1 quart or 1 gallon kits
Store indoors at 32ºF to 100ºF
Shelf Life: 6 months at 75ºF

APPLICATION EQUIPMENT

Spray Application (General)

This is a high solids coating and may require adjustments in spray techniques. Wet film thickness is easily and quickly achieved. The following spray equipment has been found suitable and is available from manufacturers such as Binks, DeVilbiss and Graco.

Conventional Spray

Pressure pot equipped with dual regulators, 3/8" I.D. minimum material hose, 0.070" I.D. fluid tip and appropriate air cap. Spray gun and pot pressure should be 40 P.S.I. Nozzle size of 1.8 mm is ideal.

Airless Spray

Pump Ratio:	30-1 (min)	Tip Size:	0.015" – 0.031"
GPM Output:	3.0 (min)	Output PSI:	2100 – 2300
Material Hose:	3/8" I.D. (min)	Filter Size:	50 mesh

MIXING AND THINNING

Mixing

Pour contents of Part A into Part B and mix using a mechanical stirring device. DO NOT MIX PARTIAL KITS. Wait 5 minutes before applying.

Cure-to-touch:	**2-5 hrs**		
Thinning :	**Naptha**	**Survice ready:**	**24 hrs**
Pot Life:	**3 hrs @ 75ºF**	(Complete cure:	7 days)

Oven Curing

Heat coated article to 150ºF for 30 minutes.

Room Temperature Curing

For room temperature cure applications use PhaseBreak Part C Accelerator. This is a dibutyl tin dilaurate catalyst that will accelerate the chemistry.

CLEANUP AND SAFETY

Cleanup

Use isopropyl alcohol, MEK, or naptha. In case of spillage, absorb and dispose per local regulations.
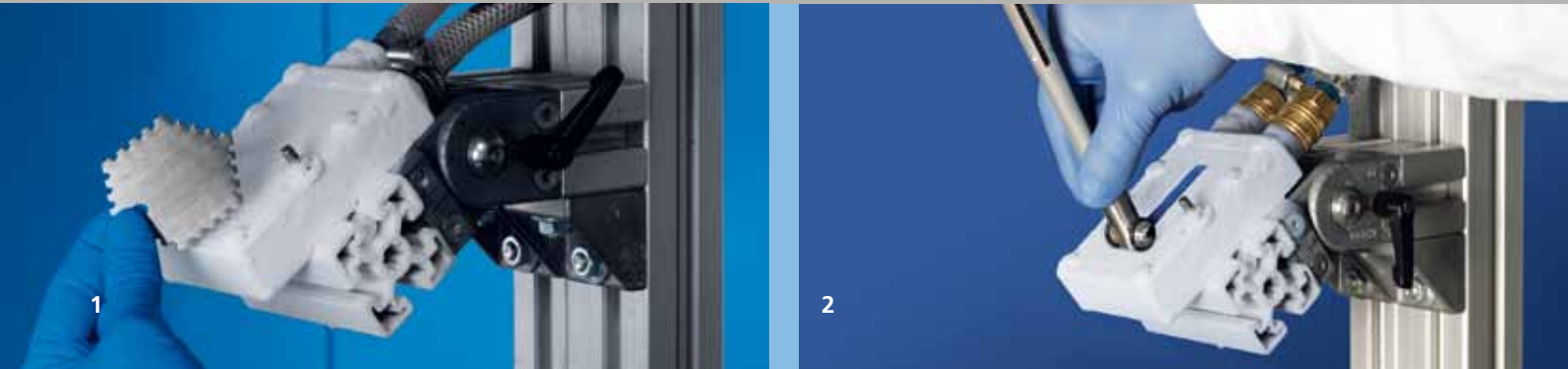
Safety

Follow all caution statements on this product data sheet and on the MSDS for this product. Employ normal workmanlike safety precautions. Wear appropriate Personnel Protective Equipment.

Caution

Flammable material – keep away from sparks and open flames. All electrical equipment and installations should be made and grounded in accordance with the National Electric Code. In areas where explosion hazards exist, workmen should be required to use non-ferrous tools and wear conductive and non-sparking shoes.

July 2011

Fraunhofer

IFAM

FRAUNHOFER INSTITUTE FOR MANUFACTURING TECHNOLOGY AND ADVANCED MATERIALS IFAM

1 *Analysis of the rime layer using a measuring comb.*

2 *Evaluation of rime adhesion using the rime adhesion test developed at Fraunhofer IFAM.*

Fraunhofer Institute for Manufacturing Technology and Advanced Materials IFAM – Adhesive Bonding Technology and Surfaces –
Wiener Strasse 12
28359 Bremen | Germany

Institute director
Prof. Dr. Bernd Mayer

Contact

Paint/Lacquer Technology
Dr. Volkmar Stenzel
Phone +49 421 2246-407
volkmar.stenzel@ifam.fraunhofer.de

www.ifam.fraunhofer.de

© Fraunhofer IFAM

ANTI-ICING COATINGS

Ice formation on surfaces – A challenge

The icing of surfaces is a widespread problem that incurs high costs and impairs functionality and safety. For example, icing can adversely affect aircraft, ships, rail vehicles, cars, roller shutters, cooling systems, and wind turbines. The deposition of ice on surfaces leads to higher energy consumption, lower energy output, e.g. for wind turbines, and an increased risk of accidents. Icing also causes increased maintenance and downtimes, negatively impacting the efficiency of the relevant equipment.

Development of anti-icing coatings at Fraunhofer IFAM

New techniques for the nano-structuring of surfaces and their anti-icing effect

The topography of a surface has a major influence on the run-off of water and hence on the adhesion of ice and rime. Fraunhofer IFAM has investigated a variety of approaches for structuring surfaces.

Hydrophobic and superhydrophobic coatings

Hydrophobic coatings change the wetting of a surface by water via chemical and topographic effects. In the ideal situation the water droplets then run off the surface before they freeze. In addition, ice and rime adhesion is minimized. This reduces icing and facilitates ice removal.

Heatable coatings

The heatable coatings developed at Fraunhofer IFAM are based on the principle of resistance heating. Electrically conducting particles are incorporated into the coating and applied to the surface using conventional spraying or brushing methods. In contrast to heated mats, the material is easy to apply and repair.

3

4

Anti-icing tests for coatings

→ Icing chamber at Fraunhofer IFAM

The icing chamber developed at Fraunhofer IFAM is used to simulate the effects of freezing rain and rime formation on surfaces and coatings.

→ Icing laboratory with integrated wind tunnel at Fraunhofer IFAM

Realistic icing tests on wing sections and rotor blades can be performed in the icing laboratory with integrated wind tunnel at Fraunhofer IFAM. In addition, functional tests can be carried out on technical equipment, sensors, and wind/ice measuring devices.

▌ Air temperatures down to -30 °C
▌ Maximum wind speeds up to 350 km/h
▌ Icing due to supercooled water droplets

→ Icing test stand – Testing under real conditions

Coating systems that have been successfully tested in the icing chamber are exposed to the outside weather in an endurance test. This icing test stand is located on the Brocken in the Harz Mountains at a height of 1141 meters.

Biomimetic anti-icing coatings based on anti-freeze proteins

▌ Mimicking nature, so-called anti-freeze proteins can be attached to the surface of coatings. Under certain conditions, these proteins then protect the surface from icing.

Temporary anti-icing coatings

▌ This approach involves freezing point suppressors being washed out of a coating in order to prevent icing of the surface. The coating material must be regularly renewed to maintain the anti-icing effect.

Surface icing – Current research

Icing tests under realistic conditions

Fraunhofer IFAM has developed its own icing chamber (Fig. 3) for performing icing tests with clear ice and rime. Methods have also been developed for quantifying the adhesion of clear ice and rime to surfaces. Since mid 2014, Fraunhofer IFAM additionally has run an icing laboratory with integrated wind tunnel (Fig. 4) which has been developed in the frame of the EU-funded project JediAce. Realistic icing tests at temperatures down to -30 °C and at wind speeds up to 350 km/h can be undertaken on wing sections and rotor blades. For example, supercooled water droplets can be simulated and the formation of runback ice investigated. In additon, functional tests can be performed on technical equipment, sensors, and wind/ice measuring devices.

New R&D strategies

The Paint/Lacquer Technology department at Fraunhofer IFAM is currently working on a variety of strategies for minimizing ice formation. Our extensive knowledge of surface pre-treatment, coating development and testing is being utilized for this work, along with internal Fraunhofer IFAM expertise in the area of plasma technology for modifying surfaces. Complementing the aforementioned tests, computer-aided simulation methods are also being used to evaluate the adhesion and detachment mechanisms of ice and rime on coating surfaces. The findings are allowing acceleration and optimization of development work.

3 *Icing chamber developed at Fraunhofer IFAM.*

4 *Icing wind tunnel at Fraunhofer IFAM.*